PSL UNIVERSITÉ PARIS

THÈSE DE DOCTORAT

DE L'UNIVERSITÉ PSL

Préparée à Mines Paris-PSL

Microstructure-properties relationship in AISI 316L stainless steel produced by wire additive manufacturing (WAAM & WLAM): experimental study and simulation

- -

Microstructure et propriétés de l'acier 316L élaboré par fabrication additive par dépôt de fil (WAAM et WLAM) : caractérisation expérimentale et modélisation.

Soutenance par

Damien ARTIÈRES

Prévue le 11 Avril 2025

École doctorale n°621

Ingénierie des Systèmes, Matériaux, Mécanique, Énergétique

Spécialité

Sciences et Génie des Matériaux

Composition du jury :

Angéline POULON	Maître de conférence HDR, Univ. de Bordeaux	*Rapporteure*
Helmut KLÖCKER	Directeur de recherche, Mines Saint-Étienne	*Rapporteur*
Muriel CARIN	Professeure des universités, Univ. Bretagne Sud	*Examinatrice*
Julien ZOLLINGER	Professeur des universités, Univ. de Lorraine	*Examinateur*
Sylvain DÉPINOY	Chargé de recherche, Mines Paris - PSL	*Examinateur*
Serge PASCAL	Ingénieur de recherche, CEA Saclay	*Examinateur*
Vladimir ESIN	Professeur des universités, Univ. de Lorraine	*Directeur de thèse*
Diogo GONÇALVES	Ingénieur de recherche, EDF R&D	*Invité*
Nicolas HERVÉ	Ingénieur de recherche, Framatome	*Invité*

MINES PARIS | PSL

Contents

Nomenclature

Table 1. Used symbols and units.

Notation	Significance	Units
General notations		
$\underline{e_x}$	Manufacturing direction	m
$\underline{e_z}$	Deposition direction	m
$\underline{e_y}$	Transverse direction	m
$\underline{X}$	Vector value	–
$\underline{\underline{X}}$	Second-order tensor value	–
$\underline{\underline{\underline{X}}}$	Fourth-order tensor value	–
$\underline{x}, \underline{x_s}$	Points of space $(\underline{e_x}, \underline{e_y}, \underline{e_z})$	–
$\underline{n}$	Normal vector	–
T	Temperature	K
Process parameters		
d_w, v_w	Wire diameter, wire feed rate	$m, m.s^{-1}$
s	Deposition speed	$m.s^{-1}$
Q_{exp}	Experimental heat source power	W
t_{int}	Interlayer cooling times	s
T_{int}	Interlayer targeted temperature	K
T_0	Room reference temperature	K
l	Argon flow rate	$m^3.s^{-1}$
L_{wall}, H_{wall}	Lenght, height of the wall	m
N_{layers}	Number of deposited layers	–
δz	Layer height	m
d_{rate}	Deposition rate	$kg.s^{-1}$
E_l	Applied linear energy	$J.m^{-1}$
S	Volume of material per unit of length	m^2
E_v	Volume energy density	$J.m^{-3}$
G	Thermal gradient	$K.m^{-1}$
R	Solidification speed	$m.s^{-1}$
$\dot{T}$	Cooling rate	$K.s^{-1}$
Geometry		
w	Width of the deposited bead	m
h	Height of the deposited bead	m
d	Dilution	–
Finite elements (FE) mesh		
Ω^e	Finite element domains	m^3
$\partial\Omega^e_R$	FE-air boundary	m^2
$\partial\Omega^e_T$	FE-table boundary	m^2
V_{Ω^e}	Volume of Ω^e	m^3
e_1, e_2	Fine, coarse mesh size	m
e_3	Material addition step size	m
δt	Computing time step	s

Properties of 316L steel		
T_{fus}	Liquidus temperature	K
H_{mass}	Enthalpy of melting	$J.kg^{-1}$
ϵ	Emissivity coefficient	$-$
σ_B	Stefan-Boltzmann constant	$W.m^{-2}.K^{-4}$
I	Irradiance	$W.m^{-2}$
$c(T)$	Heat capacity	$J.K^{-1}.kg^{-1}$
$\rho(T)$	Density	$kg.m^{-3}$
$\lambda(T)$	Thermal conductivity	$W.m^{-1}.K^{-1}$
σ_y	Yield strength	MPa
Thermal analysis		
$\underline{T}$	Nodal temperature	°C
$\underline{q}$	Heat flux density	$W.m^{-2}$
Q_{comp}	Thermal applied power	W
Q_{heat}	Required power to heat the wire	W
Q_{melt}	Required power to melt the wire	W
$s^Q(\underline{x}, \underline{x}^s)$	Heat power distribution	$W.m^{-3}$
R_0, Z_0	Gaussian radii	m
η_{Source}	Heat source efficiency	$-$
η_{Num}	Heat source numerical correction	$-$
H_1, H_2	Convective exchange coefficients with the air, the work table	$W.m^{-2}.K^{-1}$
$H_R\left(T^3\right)$	Thermal radiation equivalent "convective coefficient"	K^3
Mechanical analysis		
$\underline{U}$	Nodal displacements	m
$\underline{\underline{\sigma}}, \underline{\underline{\varepsilon}}$	Stress, strain tensors	$Pa, -$
$\underline{\underline{\varepsilon}}^e, \underline{\underline{\varepsilon}}^e, \underline{\underline{\varepsilon}}^{th}$	Elastic, plastic, thermal strains	$-$
$\underline{\underline{\alpha}}(T)$	Linear thermal expansion	K^{-1}
$\underline{\underline{\underline{\underline{\mathcal{C}}}}}^e(T)$	Hook's tensor	$N.m^{-1}, Pa$
$\underline{\underline{\underline{\underline{K}}}}^s$	Clamping elastic stifness	$N.m^{-1}$
$R(p)$	Isotropic hardening variable	Pa
$f\left(\underline{\underline{\sigma}}, R\right)$	Plasticity criterion	Pa
$\mathcal{J}_2\left(\underline{\underline{\sigma}}\right)$	Second invariant of $\underline{\underline{\sigma}}$	Pa

Introduction

This thesis presents a research project conducted between October 2021 and February 2025 at the Assembly Technology Laboratory (LTA, Laboratoire des Technologies d'Assemblage) of the CEA [1] in collaboration with the Centre des Matériaux of Mines Paris.

The study focused on the microstructure–properties relationship in AISI 316L stainless steel produced by two wire-based additive manufacturing processes, WAAM & WLAM, through experimental analysis and simulation. The WLAM (Wire Laser Additive Manufacturing) and WAAM (Wire Arc Additive Manufacturing) processes correspond to the family of directed energy deposition (DED) processes using a metallic wire as material feedstock (Figure 1).

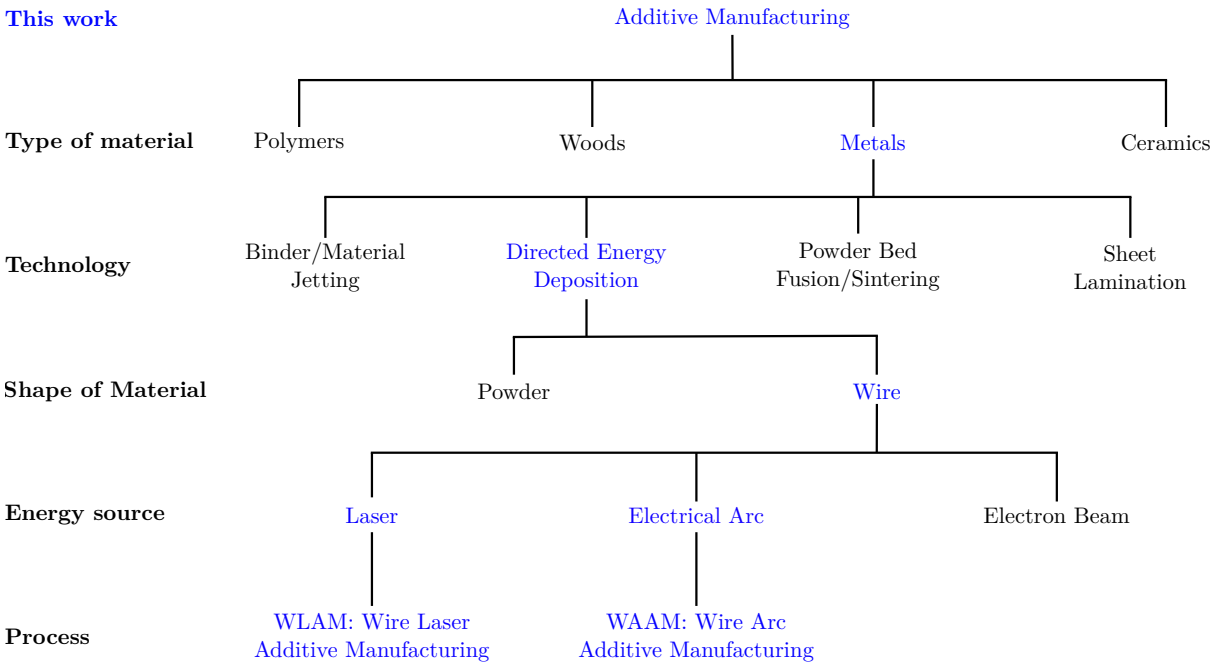

Figure 1. Simplified classification of additive manufacturing processes based on the type of material, the used technology, the shape of the material and the energy source.

Compared to traditional manufacturing techniques, additive manufacturing is the most cost-efficient for producing moderately to highly complex components at low production volumes [2]. Wire additive manufacturing also promotes more sustainable production, as it minimizes material wastes [3, 4].

While Powder Bed Fusion processes prioritize high geometric accuracy with an average deposited bead thickness of approximately 100 µm [3], wire-based Directed Energy Deposition focuses on maximizing the deposition rate, achieving bead thicknesses ranging from 1 to 10 mm [3]. This makes WAAM and

WLAM processes particularly well-suited for manufacturing large-scale components with moderately complex geometries.

Several examples of components produced by WAAM and WLAM are presented in Figure 2, including a ship propeller and a bicycle frame produced by WAAM and a blisk and a pipe manifold produced using WLAM.

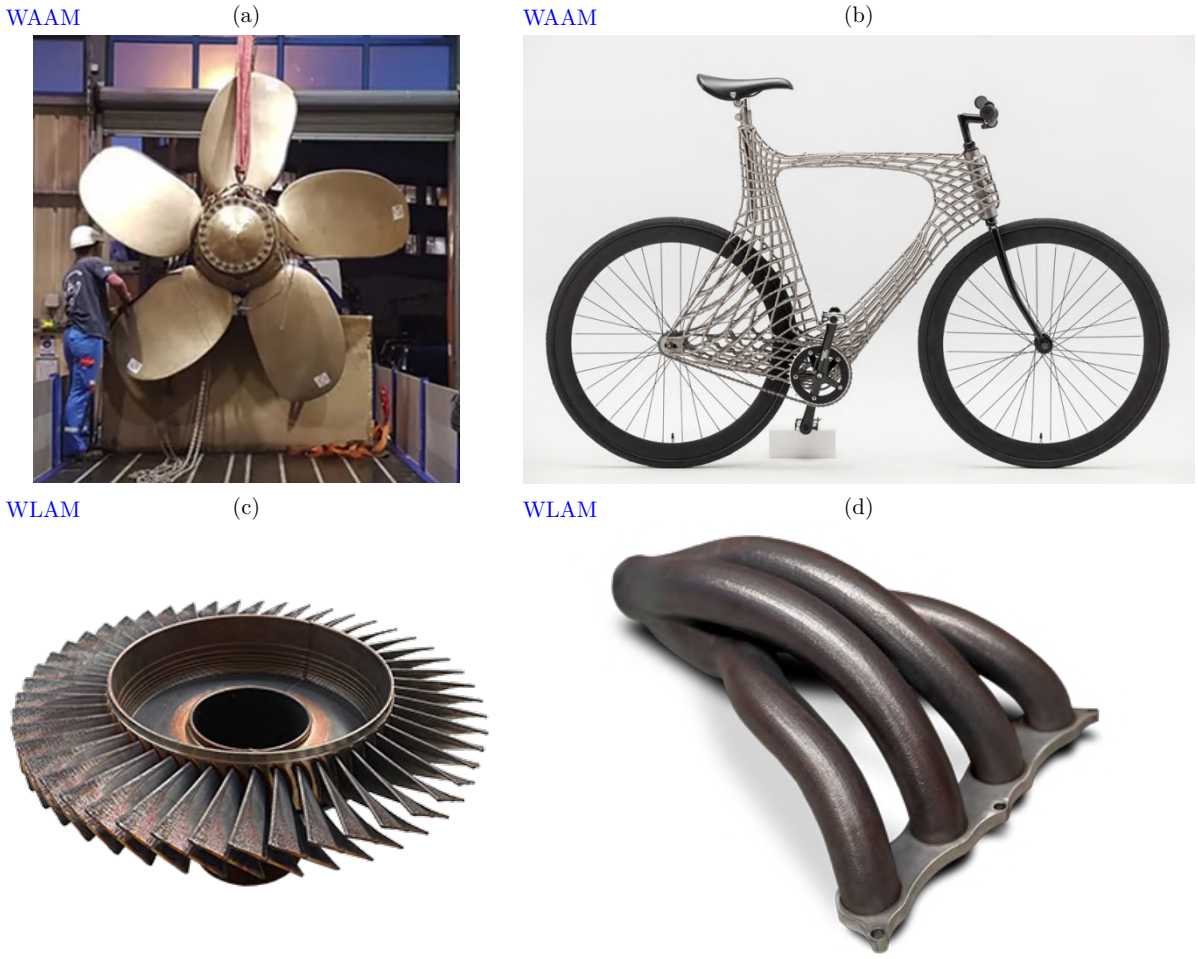

Figure 2. Applications of components produced by wire additive manufacturing: (a) Propeller of the ship Andromède, manufactured by NavalGroup with WAAM process [5]; (b) Bicycle achieved by MX3D using stainless steel and the WAAM process [6]; (c) Blisk made of 316L produced by WLAM by Meltio [7]; (d) Pipe manifold made of 316L produced by WLAM by Meltio [7].

In this context, the CEA is investigating Wire Additive Manufacturing to determine potential applications in nuclear power plants, particularly for manufacturing 316L stainless steel components used in structural applications outside the reactor core [8]. More specifically, this thesis aims to better understand the relationship between various complex effects (thermal, fluid, mechanical, metallurgical) occurring during WAAM and WLAM manufacturing and the final microstructure and properties of model components made of 316L steel. The effect of post-processing heat treatment on microstructure evolution and/or stability is also investigated. Particular attention is paid to the modeling of both WAAM and WLAM manufacturing at different scales to better understand the phenomena operating during the components processing and, as will be shown, to optimize several processing parameters.

Accurate manufacturing requires careful selection of numerous interdependent parameters. Therefore, the experimental part of this work investigated the effect of processing conditions on microstructure and the

appearance of various defects. Numerical modeling has been developed to simulate WAAM and WLAM processes at microscopic and macroscopic scales to reveal critical factors for defect formation, such as stress and solidification kinetics.

Therefore, this work aims more precisely to assess the influence of the parameters of WAAM and WLAM processes used to manufacture 316L austenitic stainless steel components (single beads, single-bead walls and tiles) on (i) their geometrical regularity, (ii) their microstructure, (iii) their mechanical properties and (iv) their thermal stability.

The thesis is divided into five chapters:

- A literature review is presented in Chapter 1, describing the Wire Additive Manufacturing processes, their advantages and drawbacks and the applied parameters. In addition, the microstructure and the mechanical properties are described. Finally, a highlight is made on the current applications of numerical modeling of wire additive manufacturing.
- Chapter 2 presents the employed Wire Additive Manufacturing platforms, the initial state of 316L steel used in this work, the processing using WAAM and WLAM and the methods used for characterizing the microstructure and the mechanical properties of the manufactured components.
- Chapter 3 aims to find the optimal manufacturing conditions leading to defect-free components with regular geometry. The influence of the process parameters on the geometry of single beads is also determined. The parameters are adapted to the manufacturing of single-bead walls and multilayer tiles. One set of parameters per process is ultimately selected.
- Chapter 4 investigates the microstructure of 316L components produced using the WAAM and WLAM processes based on the selected parameters in Chapter 3. The microstructure in the as-built state is examined for single beads, single-bead walls and tiles. Additionally, the mechanical properties of the single-bead walls are determined. Finally, heat treatments were conducted to assess the stability of the as-built microstructure in single-bead walls.
- Chapter 5 presents a new finite element thermomechanical model applied to manufacturing single-bead walls with WAAM and WLAM processes, aiming to better understand experimental results detailed in Chapters 3 and 4.

Introduction en français

Cette thèse est réalisée au Laboratoire des Technologies d'Assemblage du CEA en collaboration avec le Centre des Matériaux des Mines de Paris. Le travail porte sur l'étude de la microstructure et des propriétés de pièces réalisées en acier 316L par fabrication additive par dépôt de fil (WAAM et WLAM), au travers de caractérisations expérimentales et numériques.

Les procédés WAAM et WLAM sont adaptés à la production de pièces de grandes dimensions aux géométries moyennement complexes. Le CEA étudie ces procédés afin de monter en compétence sur leur utilisation (par la fabrication de géométries d'étude) et déterminer des champs d'applications.

La thèse vise à évaluer l'effet des paramètres des procédés WAAM et WLAM utilisés pour fabriquer des pièces en acier austénitique inoxydable 316L (monocordons, murs ou blocs) sur (i) leur régularité géométrique, (ii) leur microstructure, (iii) leurs propriétés mécaniques et (iv) leur stabilité microstructurale sous l'effet de la température.

This page was intentionally left blank.

Chapter 1

Bibliographic overview

Contents

Résumé en français du chapitre 1 : revue bibliographique

Les procédés de fabrication additive permettent la production de pièces à la géométrie complexe tout en minimisant la quantité de matériau utilisée. Différentes technologies de fabrication additive ont été développées (Figure 1.1): la fusion laser sur lit de poudre (L-PBF), le dépôt de matière sous énergie concentrée avec emploi de poudre (DED-poudre) et le DED avec emploi de fil (DED-fil). En particulier, les procédés WAAM (Figure 1.3) et WLAM (Figure 1.4) sont basés sur la technologie DED-fil avec fusion du fil métallique par un arc électrique et un laser, respectivement.

La technologie L-PBF est adaptée à la fabrication de pièces de petites dimensions avec une géométrie complexe, étant donné que le procédé possède une grande précision géométrique. A l'inverse, les procédés WAAM et WLAM permettent la fabrication de pièces de grande taille de par leur taux de dépôt élevé et le plus faible coût du fil comparé à la poudre. Le procédé WLAM a l'avantage de combiner un taux de dépôt relativement important et une bonne précision géométrique.

Plusieurs problèmes doivent encore être résolus avant que la fabrication additive par dépôt de fil ne puisse être utilisée dans l'industrie (Figure 1.6). La littérature indique que la porosité, les inclusions, les déformations macroscopiques et des taux élevés de contraintes résiduelles sont les principaux défauts influents sur la qualité des pièces fabriquées.

Les principaux paramètres influents sur la géométrie des cordons déposés par WAAM et WLAM sont la puissance de la source d'énergie, la vitesse de dépôt et la vitesse d'apport de fil. Ils contribuent à modifier l'énergie linéique appliquée ainsi que le volume de métal déposé par unité de longueur, ce qui revient à faire varier la densité volumique d'énergie. Une densité d'énergie trop faible ou trop élevée entraîne le dépôt de cordons à la géométrie irrégulière (Figures 1.8 et 1.9). De plus, dans le cas de la fabrication de pièces constituées de plusieurs cordons, un mauvais contrôle de la stratégie de dépôt et du temps de refroidissement interpasse peut provoquer des irrégularités locales et des pertes de hauteur dans les pièces fabriquées (Figures 1.13 et 1.15).

L'acier inoxydable austénitique 316L, utilisé dans plusieurs secteurs industriels y compris le nucléaire, a été utilisé dans ce travail. Les pièces en 316L fabriquées par WAAM et WLAM possèdent une microstructure constituée de grains colonnaires dans la direction du gradient thermique (Figure 1.18), avec des orientations cristallines résultantes des phénomènes d'épitaxie (le grain formé à l'interface solide-liquide reprend l'orientation du grain déjà solidifié) et de compétition de croissance (les grains ayant leur direction $\langle 001 \rangle$ orientée parallèlement au gradient thermique sont favorisés).

Pour les murs monocordons (Figure 1.19), le gradient thermique est unidirectionnel et parallèle à la direction de fabrication $\underline{e_z}$. Cela conduit a la formation de grains colonnaires allongés sur plusieurs dizaines de passes, associés à une texture en $\langle 001 \rangle_{\parallel \underline{e_z}}$ correspondant à la direction de croissance préférentielle.

Dans le cas de blocs multicouches (Figure 1.20), la forme différente des bains de fusions entre les pièces réalisées par WAAM et par WLAM conduit à des microstructures distinctes. Dans le cas du WAAM, des grains colonnaires dans la direction de fabrication $\underline{e_z}$ et une texture selon $\langle 001 \rangle_{\parallel \underline{e_z}}$ sont observés aux extrémités des cordons, tandis que des grains plus petits et une texture selon $\langle 011 \rangle_{\parallel \underline{e_z}}$ sont observés au centre des cordons. Dans le cas du WLAM, la microstructure est majoritairement texturée selon $\langle 011 \rangle_{\parallel \underline{e_z}}$ en raison de la forme convexe des bains de fusion, de manière similaire aux pièces obtenues avec le procédé L-PBF.

Dans des conditions de solidification typique des procédés WAAM et WLAM, la microstructure des

pièces en 316L est austéno-ferritique, avec une ferrite sous forme vermiculaire formée au cours d'une solidification de type FA (Figure 1.22, la ferrite est la première phase formée à partir du métal liquide). De plus, dans certaines conditions, le cyclage thermique subi par les pièces fabriquées par WAAM peut permettre la précipitation de la phase intermétallique σ (Figure 1.24), néfaste aux propriétés mécaniques du matériau.

Les propriétés en traction uniaxiale des pièces fabriquées par WAAM et WLAM sont légèrement anisotropes entre leur direction de fabrication $\underline{e_z}$ et leur direction de dépôt $\underline{e_x}$ (Table 1.4). Ces propriétés dépassent néanmoins les normes imposées pour du 316L produit de manière conventionnelle.

Des traitements thermiques peuvent être utilisés pour induire la relaxation des contraintes résiduelles dans les pièces, la recristallisation et la dissolution de la ferrite (Figure 1.25).

Enfin, divers modèles numériques ont été développés afin d'étudier les échelles de la pièce fabriquée, du cordon déposé et son bain de fusion, et de la microstructure. Les modèles sont basés sur la prise en compte de plusieurs phénomènes physiques, tels que la thermique, la mécanique, la formation de la géométrie, la mécanique des fluides dans le métal liquide ou les lois de germination et de croissance cristalline (Figures 1.28, 1.30, 1.32 et 1.34).

Les modèles ont permis une description de l'évolution de la température dans les pièces pendant la fabrication, de leur déformation finale, des contraintes résiduelles, de la forme des cordons déposés et des bains de fusion, ainsi que de la microstructure. Ils peuvent être utilisés afin d'identifier un mauvais contrôle des paramètres des procédés, en mettant en évidence par exemple de l'accumulation de chaleur dans les pièces, et conduire à l'optimisation de ces paramètres.

1.1 Wire Additive Manufacturing processes and challenges

The scientific interest in additive manufacturing has increased significantly since the 90s. Particularly, research has risen exponentially since 2010 as the processes are reaching a good maturity level and now have various application fields [9].

Additive manufacturing offers the possibility to design complex geometries [10, 11]. It also enables the manufacturing of materials with chemical composition gradients or the designing of alloys directly during the manufacturing, which is difficult to achieve with conventional processes [12]. It can also reduce production costs under certain conditions, as mentioned by Pinkerton and Andrew [13]. Unlike conventional manufacturing, the unit cost of a component produced using additive manufacturing does not increase with its complexity and production volume. Oppositely, the cost of a component manufactured using conventional processes decreases with the production volume but increases with the complexity. Thus, additive manufacturing reduces the costs for low-volume production of complex components. Finally, several authors mentioned that components processed using additive manufacturing can have improved properties compared to components produced using conventional manufacturing [14, 15, 16].

Different technologies for additive manufacturing have been developed to optimize either the deposition rate of the process or the geometrical quality of the manufactured components [17]. The different additive manufacturing processes, as well as their application fields and challenges, are presented in this section.

1.1.1 Additive manufacturing technologies for metallic components

The production of a component with additive manufacturing is achieved based on a computer-aided design geometry, which is sliced to determine a layer-by-layer trajectory of material deposition. Post-process machining can be achieved to modify the surface state or to adjust the geometrical dimensions [18, 19].

Additive manufacturing applied to metals can be divided into three technological families:

- **sheet lamination** technology, in which thin metal sheets are joined using a welding energy source. This technology is rarely employed due to its limited applications [20].
- **powder bed** technology, most often represented by the Laser-Powder Bed Fusion (L-PBF) process (Figure 1.1a), in which a layer of powder is deposited using a rake and further locally melted with a laser. Layers of powder are successively deposited while lowering the level of the building tray [21].
- **directed energy deposition (DED)** technology, in which the material is directly deposited on a melt pool on top of a substrate. The deposited material can be used in the form of powder (Figure 1.1b) or wire (Figure 1.1c). The process using the DED technology and blown powder focused on a laser source, presented in Figure 1.1b, is often referred to as DED in the literature [11]. To differentiate it from the DED technology, we will refer to it in this document as the DED-powder process. When a wire is employed as material feedstock (Figure 1.1c), the used energy source to melt the wire can be an electrical arc (WAAM, Wire-Arc Additive Manufacturing), a laser (WLAM, Wire-Laser Additive Manufacturing) or an electron beam (WEBAM, Wire-Electron Beam Additive Manufacturing) [15].

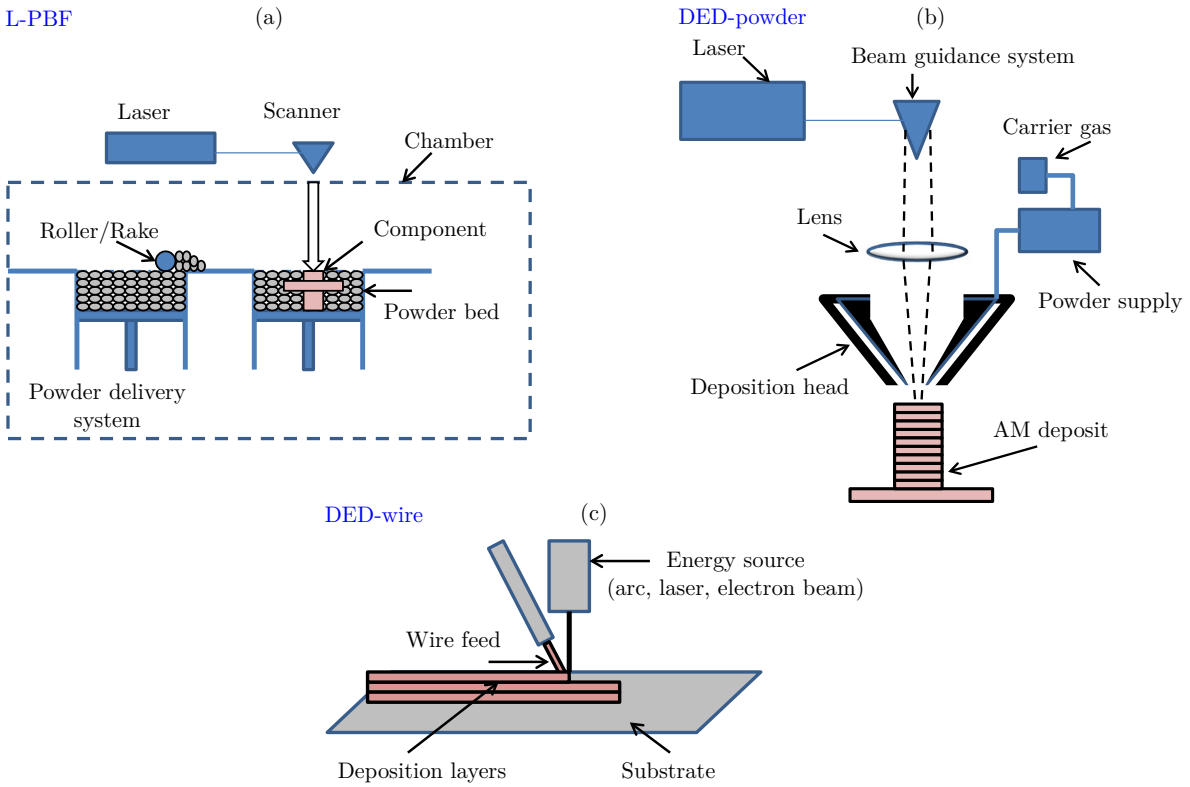

Figure 1.1. Schematic drawing of the different metallic additive manufacturing technologies: (a) powder bed system; (b) DED-powder feed system; (c) DED-wire feed system. Adapted from Frazier [21].

Table 1.1 compares different parameters of L-PBF, DED-powder and DED-wire processes. DED-wire process, compared to the two others, has the advantage of using wire instead of powder, which limits the health risks for the operator [22], reduces the production costs as the wire is ten times cheaper than powder [21] and maximizes the buy-to-fly ratio (ratio between material delivery rate and deposition rate) to 100%. In contrast, the buy-to-fly ratio is only around 30% in the DED-powder process [23] as not all the powder is used to produce the component.

Table 1.1. Comparison between additive manufacturing processes: L-PBF, DED-powder and DED-wire. Numbers in red indicate the ranking of one process with the other two on the defined criterion.

Property	L-PBF	DED-powder	DED-wire
Buy-to-fly ratio	3.	2. $\approx 30\%$ [23]	1. 100% [22]
Heat input [24]	1. $10^{-1} - 1$ J/mm	2. $10^{1} - 10^{2}$ J/mm	3. 10^{3} J/mm
Layer width [24]	1. $0.05 - 0.5$ mm	2. $0.5 - 5$ mm	3. $1 - 10$ mm
Deposition rate [17]	3. $10^{-2} - 10^{-1}$ g/s	2. 10^{-1} g/s	1. $10^{-1} - 1$ g/s

The DED-wire process has the highest deposition rate, the highest heat input and produces the largest layers compared to the DED-powder and the L-PBF processes [24, 17]. However, according to Ding *et al.* [22], an increase in the deposition rate is made to the detriment of the geometrical resolution. As a result, components produced using the DED-wire process will have poor geometrical accuracy and surface finish compared to components produced using DED-powder and L-PBF processes [25]. The L-PBF process is, therefore, better suited to the production of small components with good geometric accuracy. In contrast, the DED-wire process is more suitable for the manufacturing of large components with moderately complex geometries [26, 27]. Due to the lower safety constraints imposed by the use of wire compared to powder, DED-wire processes are not restricted, unlike L-PBF, to a maximum build chamber size. Furthermore, the use of metal powder diminishes in relevance as the size of the components increases due to the production costs associated with using powder (more expensive than wire) and also knowing that larger geometric tolerances are generally accepted for larger components. The DED-powder process is positioned as an intermediary between these two processes.

The higher heat input in the DED-wire process compared to that of the L-PBF process [28] will induce differences in the solidification conditions and thus different microstructures (thermal gradient and growth rate of the liquid-solid interface for a given material [24]). Figure 1.2a compares the thermal gradient and the growth rate in components manufactured with the L-PBF, the DED-powder and the DED-wire processes. Mukherjee *et al.* [24] reported that the highest thermal gradients and growth rates are measured during the L-PBF process, while the DED-wire process results in the lowest ones. The effect of these thermal gradients and growth rate on the microstructure will be further discussed in the next section.

Figure 1.2b compares the obtained cooling rates and the heat input of each process. The lowest thermal gradients and growth rates experienced during the manufacturing of a component with the DED-wire process result in obtaining the lowest cooling rate of about 10^{2} °C/s, against $10^{3} - 10^{4}$ °C/s for DED-powder and $10^{6} - 10^{7}$ °C/s for L-PBF, potentially influencing the solidification path [29].

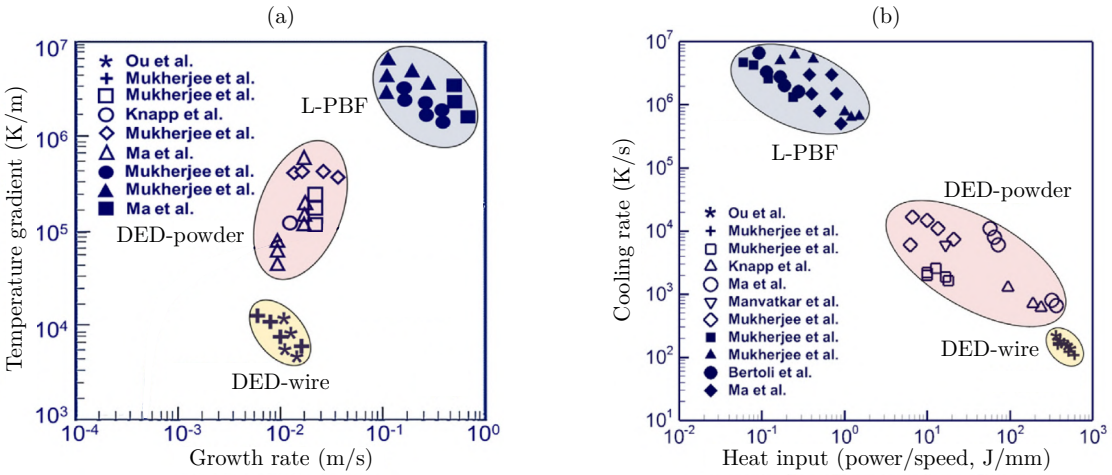

Figure 1.2. (a) Dependence between temperature gradient and growth rate and (b) variations of the cooling rate with respect to the linear heat input for the different additive manufacturing processes, using 316 stainless steel. Adapted from Mukherjee et al. [24].

Finally, components produced using the DED-wire process exhibited the highest residual stresses, six times higher than those produced using the L-PBF process, due to the intense heat input applied with this process [17]. A more precise description of the WAAM and WLAM processes employed in this work is proposed in the next section.

1.1.2 Wire Additive Manufacturing processes

Wire-Arc Additive Manufacturing (WAAM)

The WAAM process is based on arc welding technology, widely used in the industry [30]. Three arc welding processes are mainly employed, depending on the way the electrical arc is generated:

- the **Gas-Metal Arc Welding (GMAW)** process, also referred to as the Metal Inert Gas/Metal Active Gas (MIG/MAG) process [31], uses the wire as the electrode to generate the electrical arc (Figure 1.3a). In this figure and the rest of this document, $\underline{e_z}$ denotes the manufacturing direction (in which the layers are stacked), $\underline{e_x}$ the deposition direction (in which the deposition head is moving during the manufacturing) and $\underline{e_y}$ corresponds to the transverse direction. The wire is then brought coaxially into the melt pool. Shielding gas is blown through a nozzle to protect the melted metal from atmosphere contamination [30]. The applied current can both be pulsed or continuous [30]. According to Costello *et al.* [31], the GMAW process is the most widely used for arc generation in WAAM. A process derived from GMAW is the Cold Metal Transfer (CMT) process, in which the wire oscillates to control the generation of the arc [32, 22]. The push and pull cycles of the wire are calibrated with the current pulsations. This process limits the heat amount introduced in the component [33].
- the **Gas-Tungsten Arc Welding (GTAW)** process, also referred to as the Tungsten Inert Gas (TIG) process, uses a non-fusible tungsten electrode to generate the arc (Figure 1.3b). The wire is brought laterally at the front or the side of the melt pool [34, 35]. A variant of GTAW is the TopTIG process, where the wire is brought coaxially to the electrical arc [31].
- the **Plasma Arc Welding (PAW)** process is similar to GTAW, except that the electrical arc is restricted into a plasma created by blown ionized gas. This process allows for reaching the highest

temperatures, as the electrical arc can go up to 11,000 °C. Among the three arc welding processes, PAW generates the thinnest electrical arc.

The GTAW process was employed in this work. Unless otherwise indicated, the expression "WAAM process" refers to the GTAW-WAAM process.

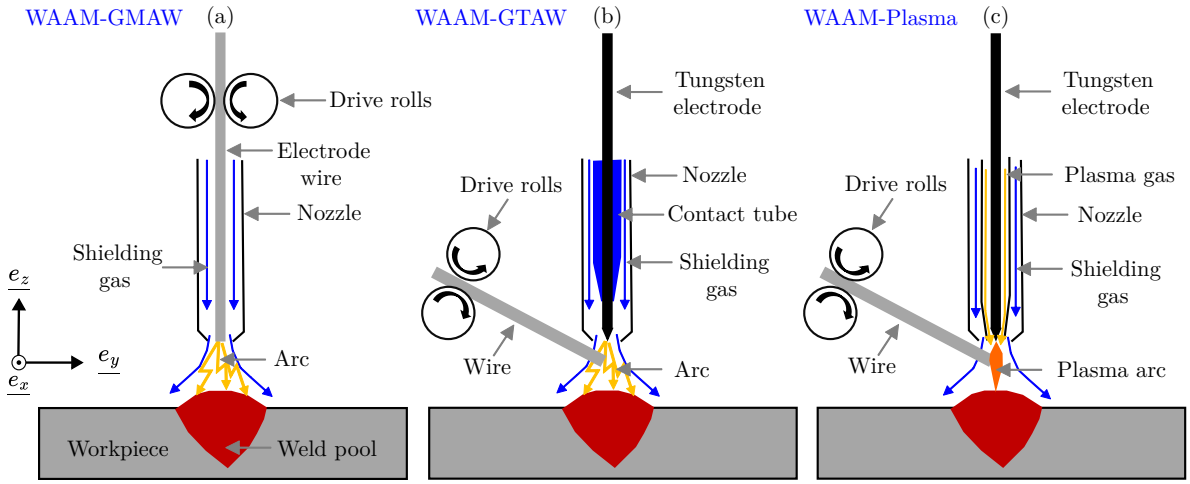

Figure 1.3. Schematic drawing of Wire Additive Manufacturing with different methods for electric arc generation: (a) gas metal arc welding (GMAW); (b) gas tungsten arc welding (GTAW); (c) plasma arc welding (PAW). Adapted from Ding et al. [22].

Wire Laser Additive Manufacturing (WLAM)

The WLAM process uses either a single fiber laser or several diode lasers to melt a metallic wire inside a melt pool. The required laser power is of the order of 1 kW [36, 37]. Both pulsed or continuous lasers can be employed [38], and the laser can be brought laterally [39] or coaxially [37]:

- if the wire is brought laterally (Figure 1.4a), front feeding allows for regular deposition [35];
- if the wire is brought coaxially (Figure 1.4b), the laser has to be split and refocused [37].

The laser beam is enlarged to improve the formation of the melt pool, using ring-shaped (Figure 1.4c [37]), three-point shaped (Figure 1.4c [40]) and donut-shaped (Figure 1.4c [37]) geometries. According to Schulz *et al.* [36], the laser spot should have the size of the deposited melt pool to prevent oxidation. The focusing should be correctly made to ensure proper deposition:

- if it is too high, the wire is susceptible to melt prior to reaching the melt pool;
- if it is too low, the wire is susceptible not to being correctly melted [41].

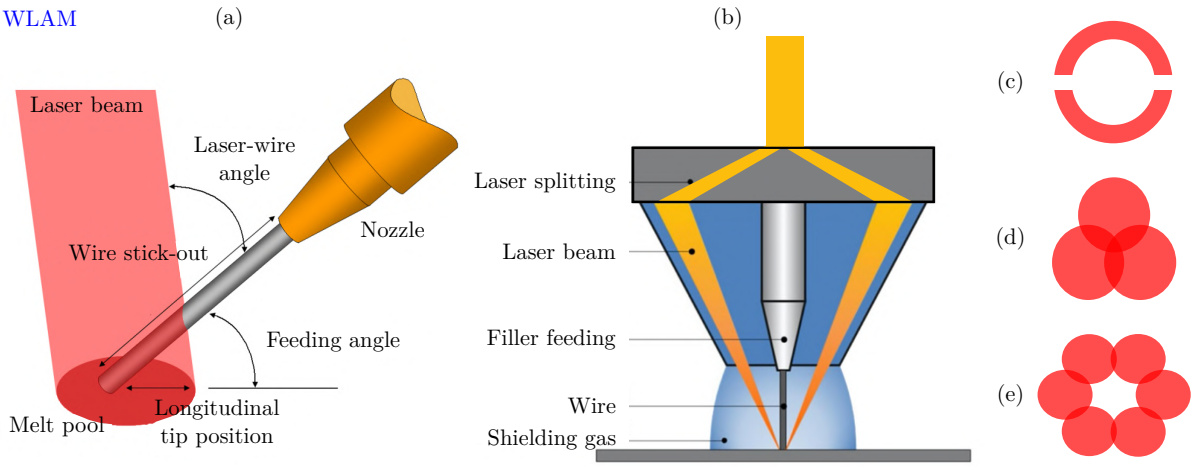

Figure 1.4. Schematic drawing of Wire Laser Additive Manufacturing in different configurations: (a) lateral wire supply, adapted from Heralic [39]; (b) coaxial wire supply, adapted from Bambach et al. [37]; (c) ring-shaped laser beam [37]; (d) three-point laser beam [40]; (e) donut-shaped laser beam [37].

1.1.3 Comparison of wire additive manufacturing processes

Among the Wire Additive Manufacturing processes, WAAM is the cheapest as a platform can be built for less than 90 k£ (108 k€) according to Williams *et al.* [42]. Anzalone *et al.* [43] even obtained a proof-of-concept WAAM platform for less than 2 k$ (1.9 k€). Conversely, the WEBAM process is the most expensive to set up [44].

According to Elmer *et al.* [15], the WAAM process is the most energy-efficient as the efficiency of the electrical arc is about 90% compared to efficiencies of 2-5% for the laser and 15-20% for the electron beam. The highest energy input is experienced by components achieved by WEBAM, followed by those produced by WAAM and by WLAM (750, 370 and 70 J/mm, respectively). The WLAM process, then, is an interesting option for limiting the amount of heat introduced into the component.

The WAAM process has the highest deposition rate (1-4 kg/h), where the highest value is obtained with PAW and the lowest one with GTAW [45]. The WLAM process has a slightly lower deposition rate, which can still be in the same magnitude for high-power laser values [46]. Components produced using the WAAM process have the poorest surface state and geometrical accuracy compared to those produced using WLAM, in which the size of the layers is limited by the width of the laser [22]. Indeed, the WLAM process is an interesting compromise between a high deposition rate and a good geometrical accuracy of the produced components, as mentioned by Valentin *et al.* [47].

WEBAM operates under vacuum, which prevents the contamination of the liquid metal by the atmosphere and limits the formation of inclusions compared to WAAM and WLAM [15].

Lastly, lower residual stresses were observed in components manufactured by WLAM compared to those manufactured by WAAM (200 MPa versus 500 MPa at maximum), as the consequence of the lower heat input in WLAM compared to WAAM [48].

Figures 1.5a, b and c present components elaborated using WAAM [49], WLAM [41] and WEBAM [44], respectively. The component obtained with WEBAM had the highest layer thickness. In contrast, the component obtained with WAAM was manufactured using the highest deposition rate, and the WLAM component had the thinnest layers. Each component was achieved with a satisfying surface state and

geometry accuracy with respect to the dimensions of the components.

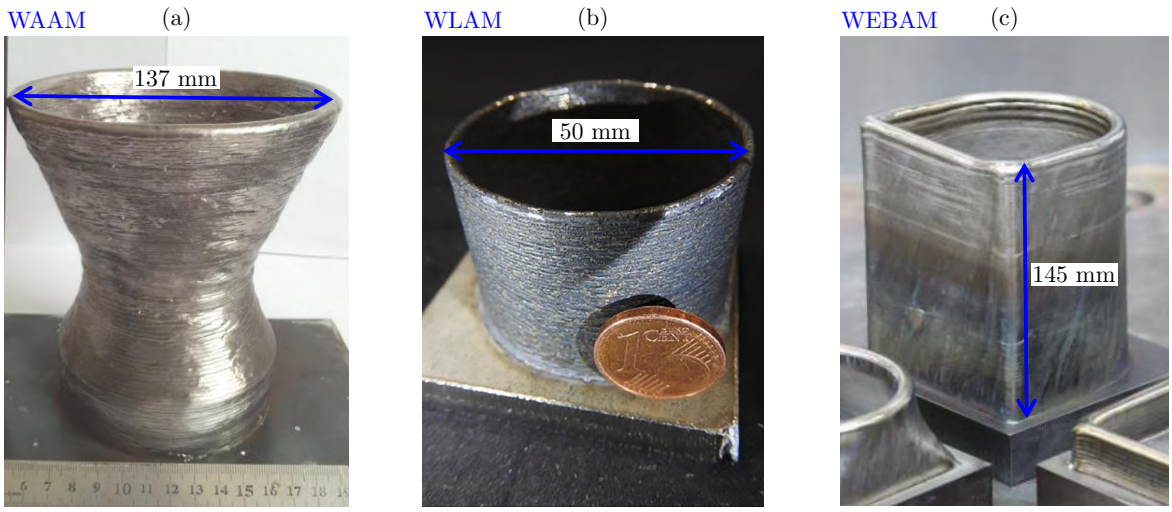

Figure 1.5. Examples of components produced using wire additive manufacturing processes: (a) WAAM [49]; (b) WLAM [41]; (c) WEBAM [44].

1.1.4 Applications and challenges of Wire Additive Manufacturing

Additive Manufacturing has shown great interest in various fields such as:

- the aerospace industry as it ensures optimum material use, especially for expensive Ti-based and Ni-based alloys, by limiting machining [33];
- the automotive industry by reducing the production costs and favoring the manufacturing of new geometries to reduce the weight while maintaining the mechanical quality [22, 26];
- the medical field through the manufacturing of on-demand geometries adapted to each patient [26].

More generally, DED additive manufacturing has applications in various fields, including nuclear power, transport, energy and tooling [33], enabling the production of complex geometries without joining [26] or the design of chemical composition gradient materials (for DED-powder [2] or WAAM using two wires [50]). The DED technology also allows for the repairing of components directly on-site [51].

However, many scientific challenges in DED technology remain to be addressed. Several authors identified the most critical defects induced by DED additive manufacturing, among which:

- **porosity** (Figure 1.6a) damaging the mechanical properties of the manufactured components [16, 14]. Intralayer pores, spherical and randomly distributed, are caused by gas entrapment in the liquid metal. Interlayer pores, irregular and located between two adjacent beads, result from a lack of fusion [52];
- the presence of **inclusions** (Figure 1.6b) results from contamination of the liquid metal by the atmosphere [33] and damages the mechanical and corrosion properties of the components [31];
- **deposition issues** causing irregularities in the geometry of the achieved layers, referred to as dripping and stubbing in WLAM [53, 54], and balling and humping (Figure 1.6c) in WAAM [55, 3]. They are the consequences of improper calibration of the process parameters;
- **residual stresses** (Figure 1.6d) are the consequence of the inherent elevated thermal gradients during additive manufacturing [14]. They induce strains, causing geometrical distortions and, in some cases, cracks in the achieved components [34];

- **geometrical issues** (Figure 1.6e) caused by incorrect deposition strategies for geometrical specificities in the achieved components, such as "T"-shaped section, angles, crossings or start and stop sequences [56, 54];
- **macroscopic collapses** due to the curvature of the deposited beads (stair-stepping effect, Figure 1.6f). A layer deposited on top of another will normally be smaller or of the same size as the one below, as the liquid metal needs to be deposited on a relatively flat surface to keep it from flowing due to gravity. The accumulation of the stair-stepping effect as the number of deposited layers increases can result in significant variations between the actual and desired dimensions of the manufactured components [22]. Heat accumulation caused by insufficient cooling [33] also lead to wrong geometry [56];
- **delamination** of two successive layers due to incomplete melting or insufficient remelting of the previous layer [57];
- changes in the **chemical composition** due to vaporization of alloying elements during the melting of the metal [17]. These changes influence the mechanical properties of the achieved components and can cause corrosion [31].

In addition, according to Debroy *et al.* [9], economic, technological and health challenges must also be addressed in DED additive manufacturing through the determination of standards, study of the market, definition of qualifications, certifications and scale-up to the industry. Risks exist when using wire as material feedstock, as "welding fumes" containing nickel and chromium are known carcinogens. These risks are less pronounced than for metallic powder, which can be a source of explosion or affect the operator's lungs, and must be manipulated carefully.

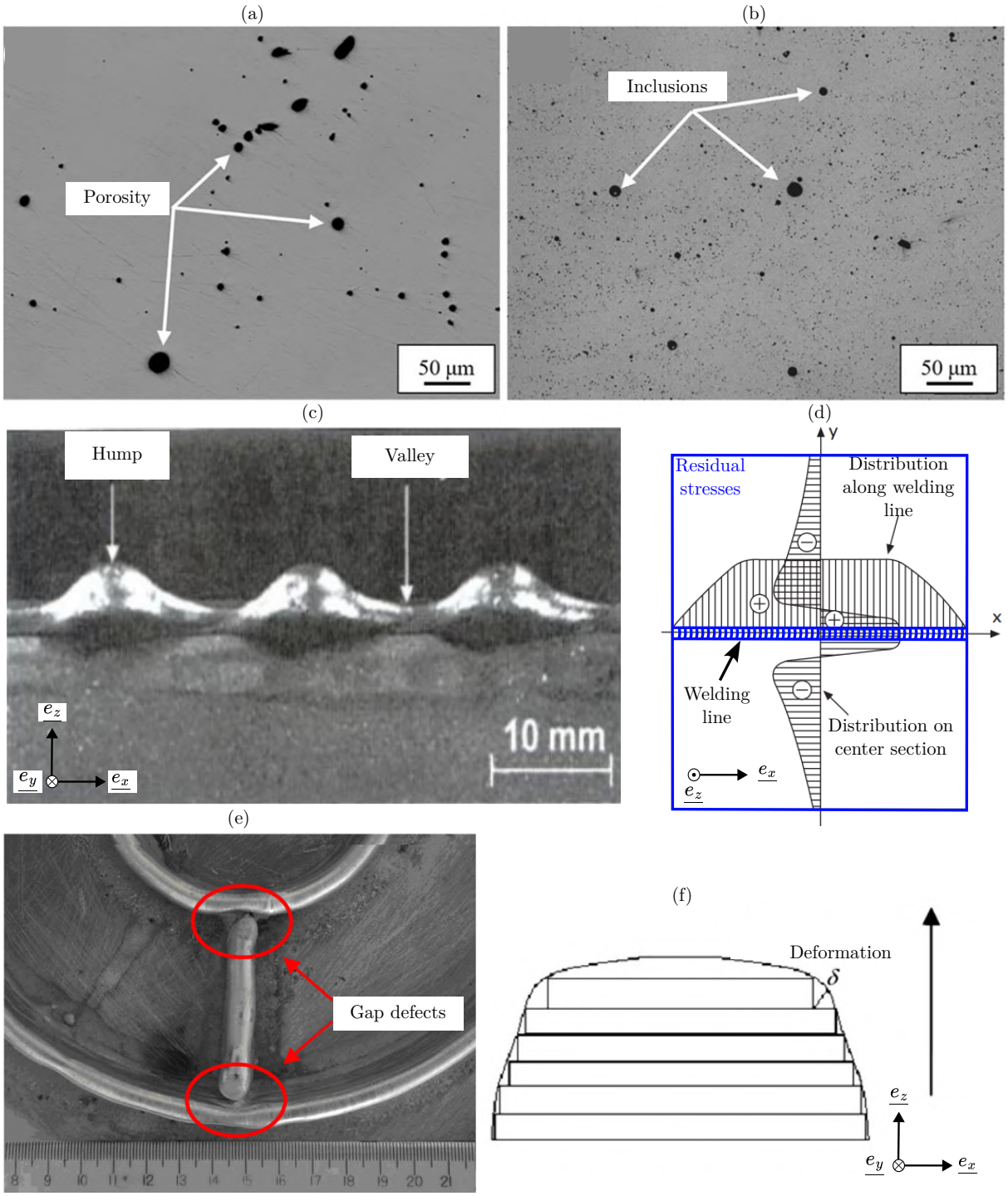

Figure 1.6. Typical defects during additive manufacturing: (a) porosities and (b) inclusions in 316L steel achieved with DED-powder [58]; (c) humping phenomenon during the deposition of carbon steel with GTAW welding process [59]; (d) distribution of the residual stresses in the welding direction (x-axis) [48]; (e) gap defects during the deposition of a "T-shaped" geometry with WAAM process [60]; (f) schematic drawing of the "stair stepping" deformation effect [22].

1.2 Processing conditions

Ahn [11] established an exhaustive list of process parameters associated with producing a component with wire additive manufacturing, as presented in Figure 1.7. The process parameters are differentiated based on whether they influence the thermal energy, the material, the wire feeding, or the motion and path of the deposition head.

According to Baghdadchi *et al.* [61], a complex component usually has thin and thick sections and angles, although the preliminary calibration for further manufacturing might be established based on the study of single beads, single-bead walls, tiles and geometrical components.

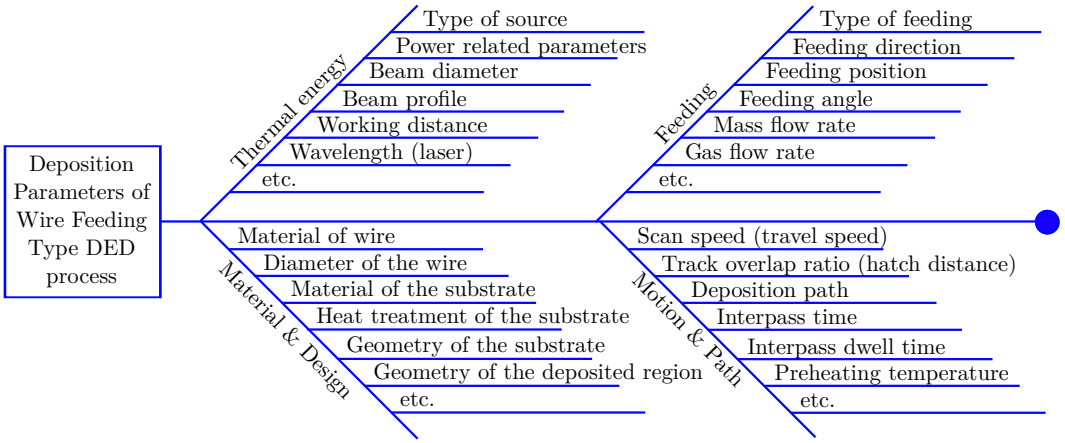

Figure 1.7. List of processing conditions of wire additive manufacturing. Adapted from Ahn [11].

Many authors have calibrated their process parameters based on the characterization of single beads to:

1. ensure continuous deposition with consistent height and width regularity [62];
2. prevent porosity formation in the manufactured components [52];
3. maintain the wetting angle between the deposited layer and the substrate below 90°. Oliari *et al.* [63] reported that an excessively high wetting angle can lead to intralayer porosities.

Based on these criteria, several geometric parameters were analyzed to assess the shape of the deposited bead, including the width/height ratio, the dilution (the ratio between the height of the deposited layer and the depth of penetration into the substrate or previous layer) and the wetting angle [52].

Optimal values for these parameters were determined based on different considerations:

- **Geometrical accuracy of the component:** Aldalur [64] determined that the optimal wetting angle for single beads manufactured using the WAAM process is 30°. Dass and Moridi [52] established that the ideal dilution ratio of single beads manufactured with DED-powder is between 10% and 30% and the ideal width/height ratio is 3.5.
- **Efficiency:** Le *et al.* [65] maximized the bead height and width while minimizing the heat input while manufacturing single beads with the WAAM process.
- **Production rate:** To optimize deposition efficiency, the goal is to maximize the bead size while ensuring consistent deposition. This involves maximizing bead width and height while minimizing the dilution ratio [66, 67] or reducing as much as possible the width/height ratio [68].

1.2.1 Effect of processing conditions on the geometry

Ding *et al.* [22] mentioned that the main process parameters influencing the geometry of single beads deposited with wire additive manufacturing processes are the power of the heat source Q_{exp}, the wire feed rate v_w and the deposition speed s. Many studies were conducted to assess the influence of these parameters on the geometrical specificities of the beads. The following conclusions were reported:

- increase in the wire feed speed increases the width w of the beads in WAAM [56], but not in WLAM, where w remains constant as it is mainly determined by the width of the laser [69];
- increase in the wire feed speed increases the height of both WAAM and WLAM single beads [70, 69];
- increase in the deposition speed decreases the width and the height of both WAAM and WLAM single beads [56, 71];
- increase in power increases the width of single beads manufactured by WAAM and WLAM [70, 69];
- increase in power results in a decrease of the height of the WAAM bead [70], but not of the WLAM bead [69], as the wire absorbs the power and shields the melt pool;
- increase in power also increases the depth of the melt pool in WAAM and WLAM process [70, 72].

In the WAAM process, the arc power has the most important effect on the width, while the deposition speed has the most important effect on the height of the achieved single beads [62]. Similarly, in the WLAM process, the laser power has the most important effect on the width, while the deposition speed influences the height of the achieved single beads [22].

1.2.2 Volume energy density

The applied volume energy density is the main physical parameter influencing the morphology of the deposited single beads [46]. This volume energy density E_v can be expressed as the fraction of the linear energy E_l (proportional to the ratio of the power of the heat source and the deposition speed, *i.e.* $E_l \propto \frac{Q_{exp}}{s}$) and the deposited volume of metal per unit of length S (proportional to the ratio of the wire feed and the deposition speeds *i.e.* $S \propto \frac{v_w}{s}$) [73]. The volume energy density is then expressed as $E_v = \frac{E_l}{S} \propto \frac{Q_{exp}}{v_w}$.

Figure 1.8a presents various examples of single beads obtained for a nickel alloy with increasing volume energy density with WLAM process [74]. Irregular morphologies of single beads were obtained when applying a too low or a too high volume energy density. These phenomena are known as wire stubbing and wire dripping, respectively. In the case of wire stubbing (Figure 1.8b), the energy is too low to melt the substrate properly, and the wire goes against the solid substrate, leading to wire deformations and irregular deposition [41]. Wire stubbing is also known to result in the formation of interlayer pores [73]. In the case of wire dripping (Figure 1.8c), excessively high applied energy causes premature melt of the wire. As a result, the metal droplets of wire are not correctly deposited onto the substrate [75].

Similarly, Figure 1.9 presents various single beads made of nickel alloy with WAAM process using increasing volume energy density [70]. Again, irregular morphologies were obtained for too low or too high volume energy densities. These phenomena are known as balling and humping, respectively. In the case of balling, insufficient volume energy density limits the correct wetting of the melt pool on top of the substrate, resulting in the formation of metallic droplets [70]. In the case of humping, an excess of volume energy density causes surface waving as a consequence of the increased fluid flow effects in the liquid metal due to the intense thermal gradients at its surface and the larger dimensions of the melt pool, resulting in irregular deposition [76].

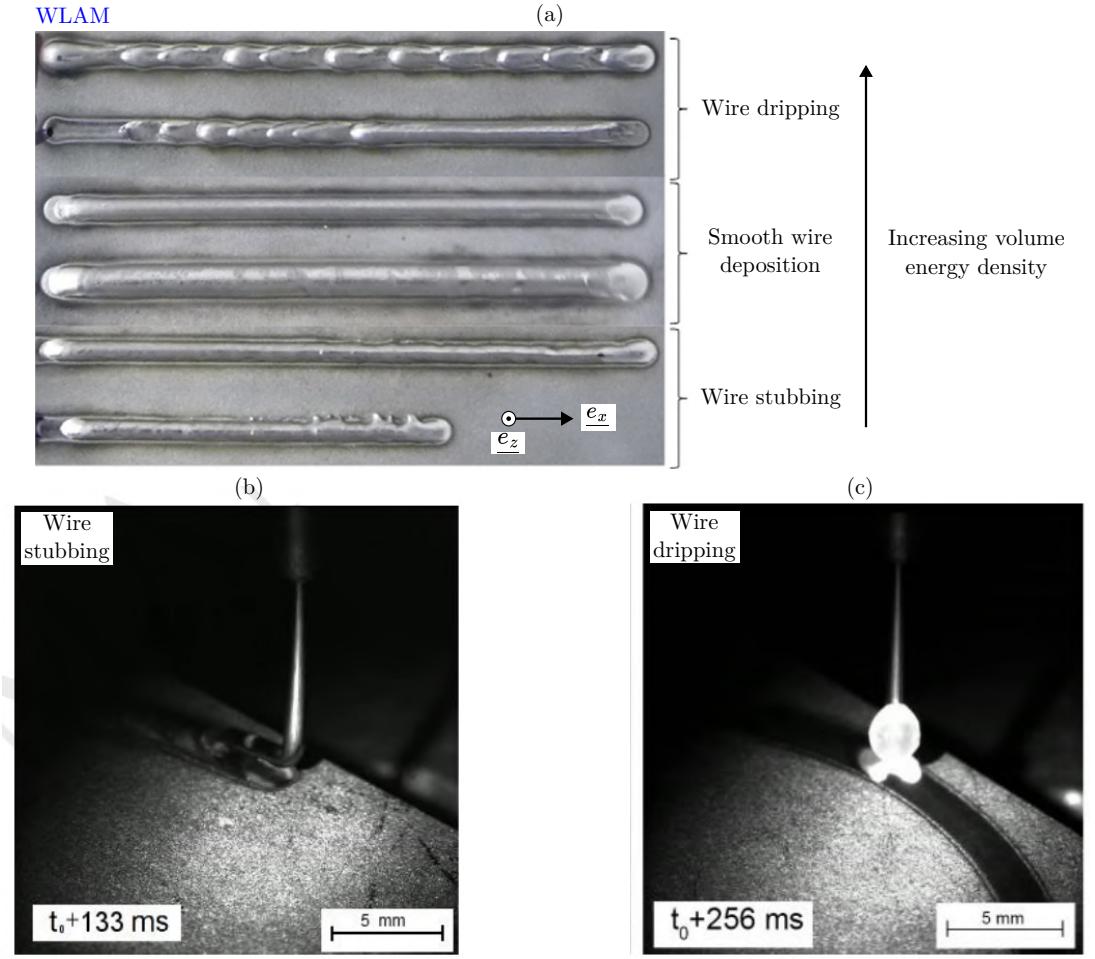

Figure 1.8. (a) Inconel 625 (nickel alloy) single beads manufactured with WLAM and increasing volume energy density [74]. Photographs of (b) wire stubbing effect and (c) wire dripping effect in WLAM, acquired using a rapid camera [41].

Figure 1.9. Hastelloy X (nickel alloy) single beads manufactured with WAAM and increasing volume energy. Adapted from Dinovitzer et al. [70].

According to Long *et al.* [77], the process parameters in wire additive manufacturing can influence the microstructure of the achieved components by modifying the applied linear energy E_l and, subsequently, the thermal gradients and solidification cooling rates. In addition, the volume energy density has to be controlled to prevent the formation of porosity within the manufactured layers:

- interlayer pores (Figure 1.10a) are the consequence of lack-of-fusion between two consecutive beads

caused by insufficient volume energy density or non-adapted deposition path causing overlapping issues between two successive beads;

- intralayer pores (Figure 1.10b) result from gas entrapments in the melt pool caused by an excessive volume energy density. For DED-powder processes, these pores are reported to be formed in "keyhole" mode, in which the energy density is sufficient to vaporize the liquid metal, creating a hole associated with important dilution of the melt pool.

Thus, the authors mentioned that, theoretically, there exists an optimum volume energy density minimizing both the intra- and interlayer pores (Figure 1.10c).

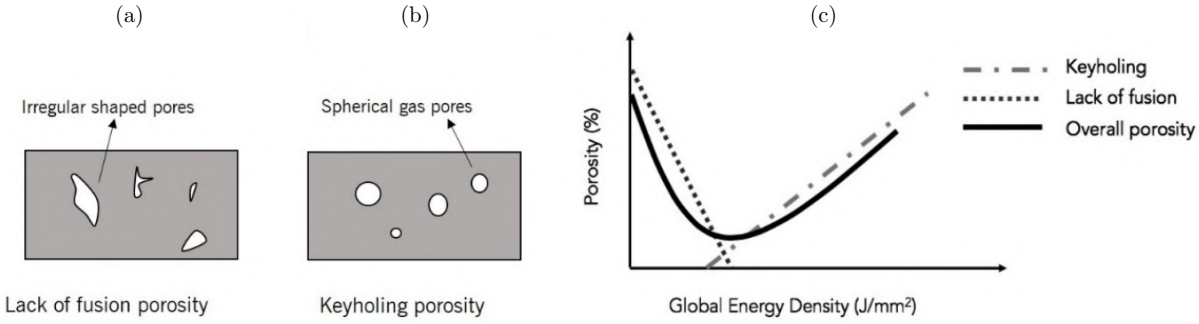

Figure 1.10. Schematic drawing of (a) lack-of-fusion interlayer porosity, (b) keyholing intralayer porosity and (c) the effect of the volume energy density on the fraction of inclusions in the achieved components [52].

1.2.3 Deposition strategy

The deposition strategy has to be optimized to avoid geometrical defects. Angles, crossings, "T"-shape joining and closed loops are the main geometrical features that can lead to height irregularities [78]. An angle in the geometry of a manufactured component changes the local deposition speed and usually increases the applied linear energy. In addition, the surface curvature of the components can influence the cooling rates and impact the microstructure [79].

The manufacturing of an X-shaped component with WAAM (Figure 1.11a) results in material excess at the crossing area [80]. A correction should be applied to limit the amount of crossings, as schematized in the deposition path. Another option could be to limit the amount of wire injected at the crossing to compensate for the height excess.

Next, the manufacturing of a "T"-shape component with WAAM resulting in lack-of-height issues is presented in Figure 1.11b [81]. The authors compensated for this lack of height by adding a bead near the joining area every four layers (Figure 1.11c).

The deposition of a single bead with WAAM and WLAM can be achieved using two deposition strategies: linear deposition strategy, presented in Figures 1.12a and b, and overlapping deposition strategy, presented in Figures 1.12c and d [64, 30]. According to Ayed [46], the overlapping deposition strategy is preferred for the manufacturing of large components with the WAAM process, as it improves the control of the width of the bead. The overlapping strategy presented satisfying results in terms of height regularity and surface state of manufactured components, as for the wall presented in Figure 1.12e [82].

However, several authors mentioned that the overlapping deposition strategy causes variations in the microstructure compared to linear deposition and induces the formation of strong crystal texture in the achieved components due to the flatness of the bead [83, 84]. This variation in microstructure is

susceptible to influence the mechanical properties [83].

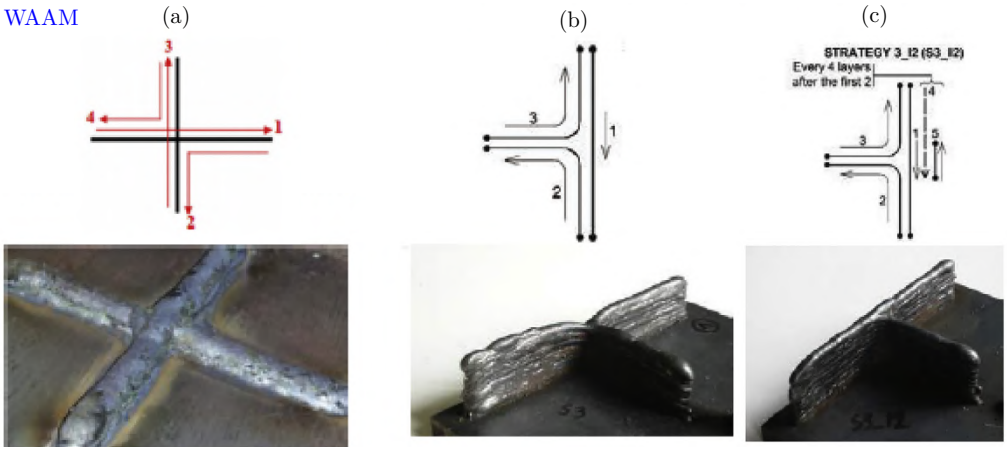

Figure 1.11. (a) Height "excess" during the manufacturing of a "X-shaped" component with WAAM using carbon steel [80]. (b) "Lack" of height during the manufacturing of a "T-shaped" component with WAAM using 308 steel and (c) corrected deposition strategy [81]. Adapted from Jafari et al. [56].

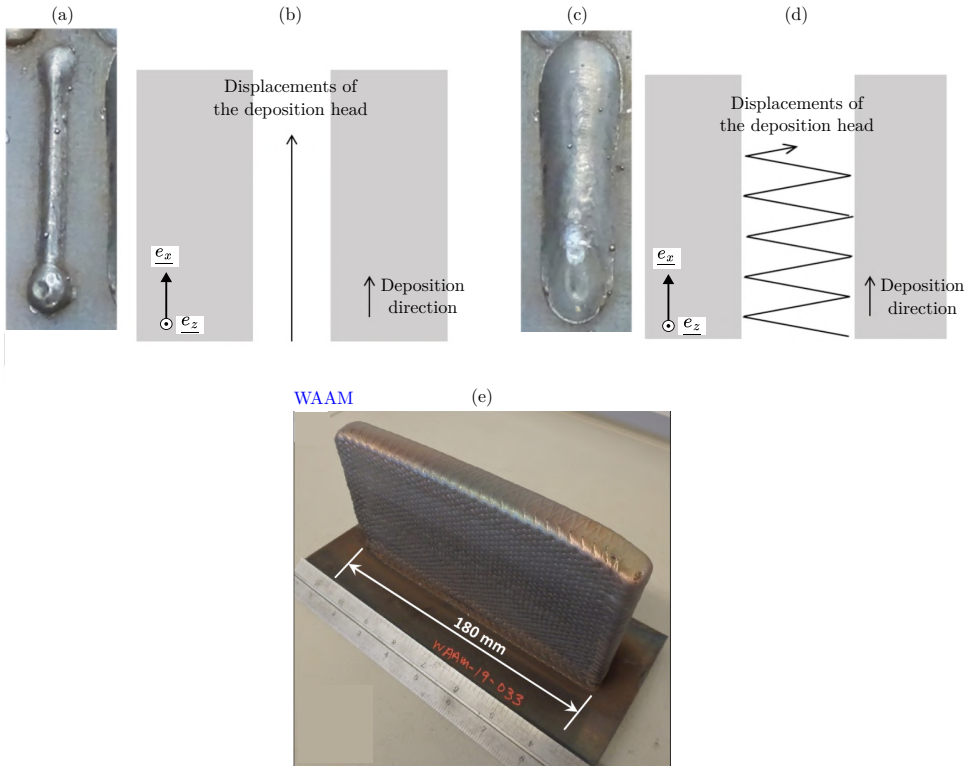

Figure 1.12. Mild steel single beads deposited by WAAM using (a) a linear deposition strategy and (c) an "overlapping" deposition strategy [64]. Schematic drawing of (b) linear and (d) overlapping deposition strategies, adapted from Marsac [30]. (e) P91 single-bead wall achieved by WAAM using an overlapping deposition strategy [82].

When stacking beads vertically during the manufacturing of single-bead walls with Wire Additive Manufacturing, two deposition strategies can be used: a one-way deposition strategy where all the beads are deposited in the same direction (raster), and a two-way deposition strategy where the beads are deposited in alternating directions (zigzag) [55] (Figure 1.13). Raster results in macroscopic collapse at one of the edges, attributed to heat accumulation in this part of the component. Conversely, the zigzag deposition

strategy formed a regular wall in height, successfully distributing the heat in the component.

Generally, when manufacturing a complex component, the deposition path must be designed to distribute the heat throughout the component [85]. Several deposition strategies have been developed for depositing multilayer components using a linear, spiral or fractal path [86].

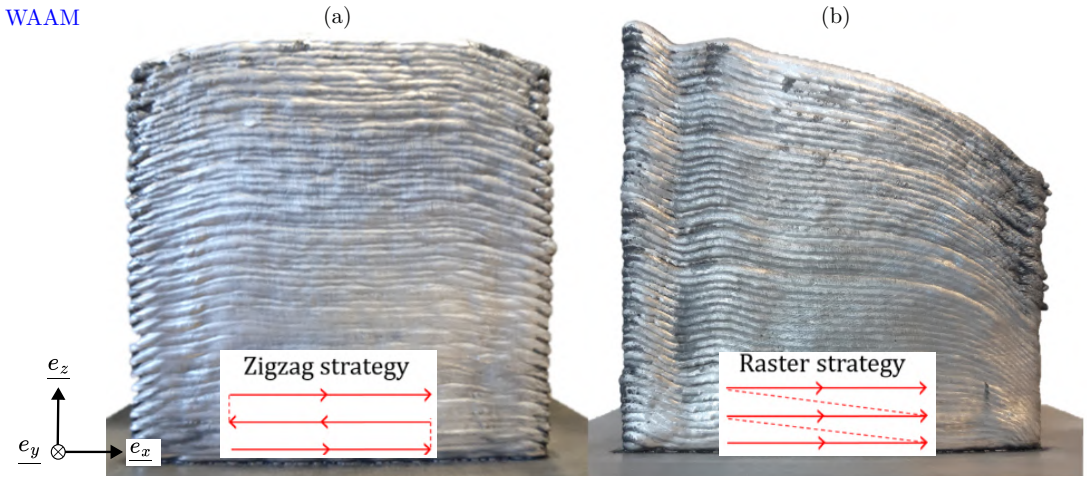

Figure 1.13. Comparison of the height regularity in single-bead walls made of aluminum alloy with WAAM process using (a) a two-way (zigzag) and (b) a one-way (raster) deposition strategy [55].

During the manufacturing of a multilayer component, calibration of the distance between two successive beads has to be ensured to obtain the flattest possible surface [4]. Suryakumar *et al.* [87] studied the overlapping of two consecutive beads, as presented in Figure 1.14. To obtain a flat surface, the authors mentioned that the valley between the two beads has to have the same size as the overlapped volume (Figure 1.14a). If the overlap increment is too high, the overlapping volume will be less than the volume of the valley, which will not be filled (Figure 1.14b). If the overlap is too small, the overlapped volume will be more than the volume of the valley, resulting in excessive layer height (Figure 1.14d). Finally, Ding *et al.* [4] mentioned that the theoretical overlap increment required to perfectly fill the valley and obtain a flat surface (Figure 1.14c) has to be 0.738 times the width of the beads.

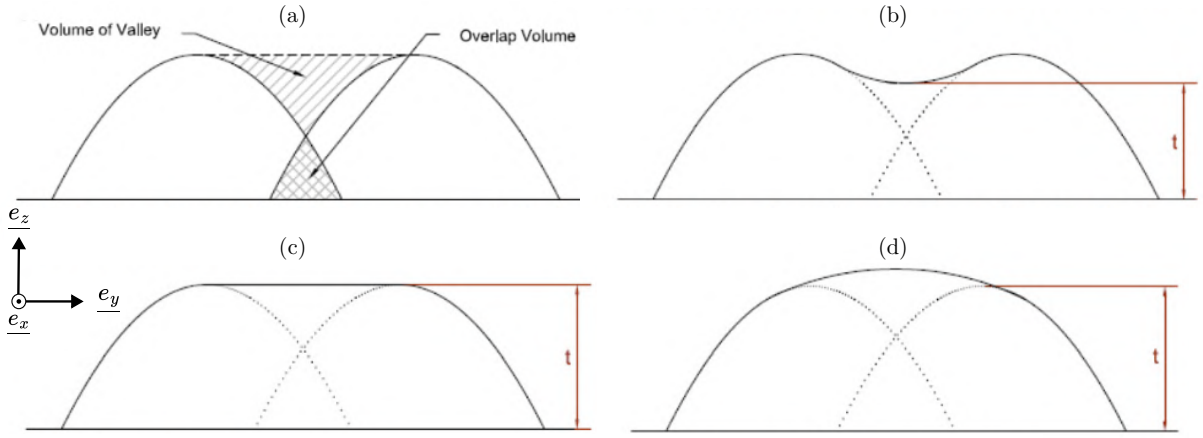

Figure 1.14. Schematic drawing of the overlapping of two consecutive single beads, adapted from Suryakamar et al. [87]: (a) overlapped volume and available valley between the beads; (b) insufficient overlapping (the overlapping volume is less than the volume of the valley); (c) adequate overlapping (the overlapping volume equals the volume of the valley); (d) excessive overlapping (the overlapping volume exceeds the volume of the valley).

1.2.4 Interlayer cooling time

Interlayer cooling time affects the effective volume energy density. If the interlayer cooling time does not allow the component to cool completely, the remaining heat will be added to the effective energy applied during the processing. While manufacturing single-bead walls, several authors mentioned that the temperature in the components at the end of each cooling cycle increases if the interlayer cooling time is kept constant [88]. This heat accumulation leads to the loss of height of the deposited beads and an increase in their width [89]. Figures 1.15a and b present respectively the transverse cross-sections of 316L single-bead walls achieved by WAAM with an interlayer cooling time of 0 and 60 s [90]. The wall manufactured without interlayer cooling presented an irregular profile in terms of width. According to Treutler *et al.* [91], heat accumulation is the consequence of the fact that, in the first layers, the heat is free to distribute by conduction into the substrate (Figure 1.15c), whereas it is constrained to go in the previous layers as the number of layer increases, resulting in heat accumulation if the cooling is not handled properly [92] (Figure 1.15d).

Heat accumulation caused by insufficient interlayer cooling time causes an increase in surface roughness [93] and creates heterogeneous properties in terms of hardness and tensile resistance [94].

However, excessive interlayer cooling times can damage the properties of the achieved materials, as they increase the distortions in the component [85]. A compromise must thus be found between sufficient cooling time to prevent geometrical deformations but without affecting the mechanical properties [22].

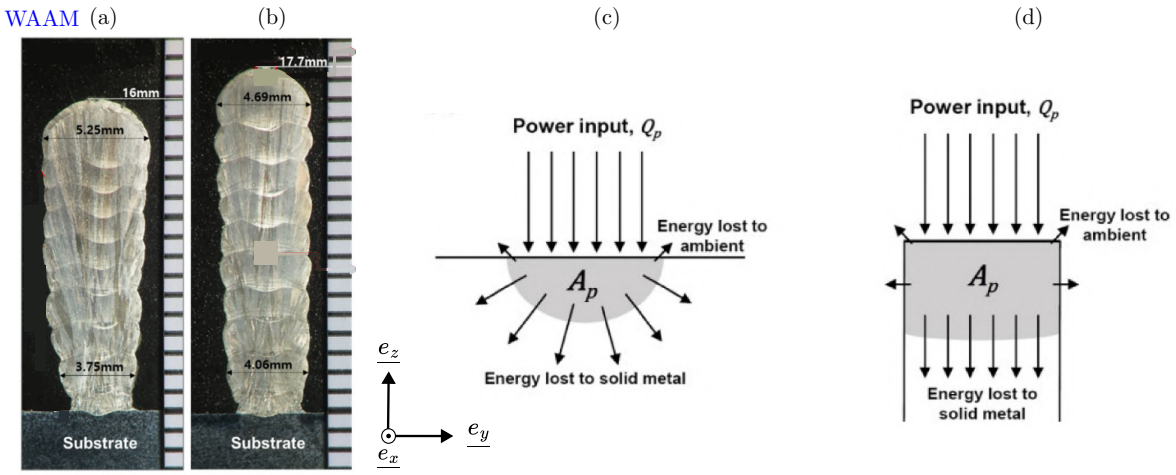

Figure 1.15. (a) and (b) transverse cross-sections of 316L single-bead walls manufactured by WAAM with an interlayer cooling time of 0 and 60 s, respectively [90]. Schematic drawing of heat transfer from (c) the first layer to the substrate and (d) the last layer to the previous layers [91].

1.3 316L stainless steel processed by WAAM and WLAM

1.3.1 Composition

Stainless steels are composed by definition of at least 10.5 wt.% of chromium to give them their corrosion resistance properties by forming a protective oxide layer at the interface between the metal and the oxidative environment. Other chemical elements, such as nickel, can be added in various proportions, resulting in different microstructures for the stainless steels: austenitic, ferritic, martensitic, duplex and precipitation hardened [95].

The austenitic stainless steels (with a face-centered cubic crystal structure) are referred to using the nomenclature 3xx, as presented in Figure 1.16 [96, 95]. The typical chemical composition of the austenitic stainless steels mentioned in this work is also given in Table 1.2. 304 stainless steel is the reference alloy, with its two main alloying elements being chromium (in rates between 18.0 and 20.0 wt.%) and nickel (between 8.0 and 10.5 wt.%). The other alloys of the 3xx series are obtained by varying the rate of these elements or by adding new alloying elements (such as S, Nb, Mo, or Si) to improve one specific material property (weldability, corrosion resistance, heat resistance...). In particular, 316 is a specific stainless steel in which molybdenum is added to improve the corrosion resistance and the material strength at high temperatures, making it suitable for applications in the nuclear field [96].

The amount of carbon in the 316 steel can be reduced to improve its corrosion resistance and weldability. Such an alloy is referred to as 316L if the rate of carbon is under 0.03 wt.%. Similarly, 316N and 316H correspond to 316 alloys with added nitrogen and carbon, respectively. This section focuses on determining the microstructure and mechanical properties of the **316L austenitic stainless steel** employed in this thesis.

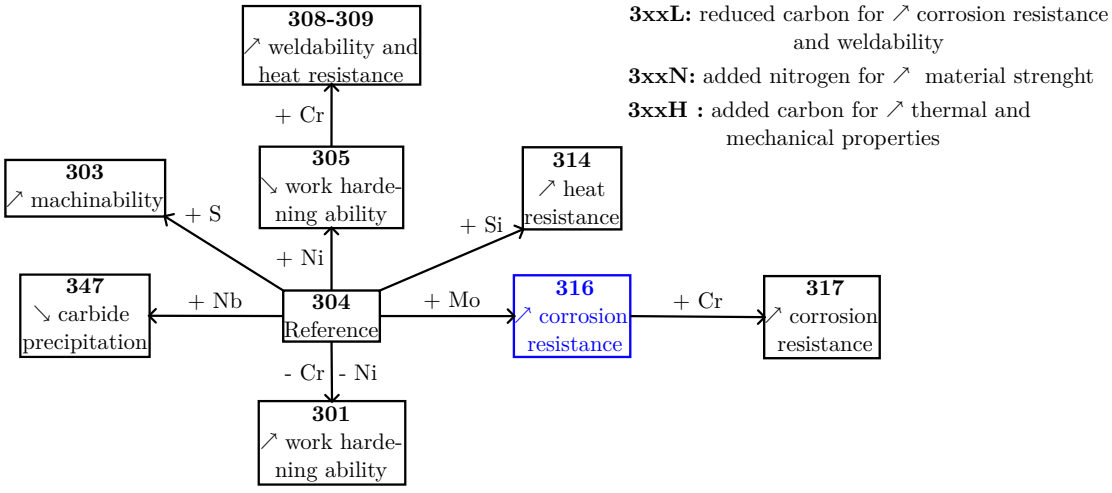

Figure 1.16. Simplified classification of 3xx austenitic stainless steels [96, 95].

Table 1.2. Typical chemical composition of austenitic stainless steels [95].

Steel (wt.%)	C	Mn	Si	Cr	Ni	P	S	Other
304	0.08	2.0	1.00	18.0-20.0	8.0- 10.5	0.045	0.03	...
308	0.08	2.0	1.0	19.0-21.0	10.0-12.0	0.045	0.03	...
316	0.08	2.0	1.00	16.0-18.0	10.0-14.0	0.045	0.03	2.0-3.0 Mo
316L	< 0.03	2.0	1.00	16.0-18.0	10.0-14.0	0.045	0.03	2.0-3.0 Mo

1.3.2 Grain structure

The components achieved by additive manufacturing experience elevated thermal gradients at the liquid-solide interface G and solidification rate R during the process. The ratio between the thermal gradient and the solidification rate indicates whether the solidification mode is planar, columnar dendritic (the solidifying front is split into dendrites growing in the direction of the thermal gradient) or equiaxed (the dendrites grow according to all space directions) [97]. In addition, the product between the thermal gradient and the solidification rate (*i.e.* the cooling rate) determines the size of the solidification structure: large grains and dendrites for low cooling rates. Peyre and Charkaluk [98] have qualitatively placed the different additive manufacturing processes on the mapping of solidification modes (Figure 1.17). Each additive manufacturing process is expected to experience columnar dendritic solidification. However, the WAAM process, which operates with the lowest thermal gradient and solidification rates compared to other processes, is susceptible to experiencing equiaxed dendritic solidification under specific conditions. Baumard [99] reported columnar grains perpendicular to the melt pool boundaries in single beads achieved by L-PBF (Figure 1.18a), which indicated dendritic solidification along with the thermal gradient (perpendicular to the liquid-solid interface). Columnar solidification was also reported for WLAM and WAAM [100, 35]. In addition, the microstructure was coarser in WAAM than in WLAM due to the lower cooling rate. The author also reported that the G/R ratio decreases from the boundary to the center of the bead. In addition, the thermal gradient is lower at the top of the bead (end of solidification) than at the melt pool boundaries (start of solidification), which resulted in a transition in solidification modes from columnar to equiaxed solidification (white line in Figure 1.18a). Then, the shape of the melt pool controls the microstructure by influencing the direction of elongation of the grains. Debroy *et al.* [3] mentioned that the shape of the melt pool is influenced by the applied linear energy E_l. (Figures 1.18b,c,d). When it increases, the rear of the melt pool becomes inclined, which results in a modification of the direction of the thermal gradient (Figure 1.18d).

The unidirectional solidification causes additional specificities governing the formation of the microstructure. The crystal orientation of the grains is determined using the existing orientations below the melt pool boundaries, resulting in an epitaxial solidification [30]. In addition, several crystal orientations are favored. In cubic crystals (such as austenite and ferrite), ⟨001⟩ is the preferential growth direction [98]. Growth of grains with a ⟨001⟩ orientation along the thermal gradient will be favored compared to grains with other orientations, which is susceptible to creating texture in the achieved component.

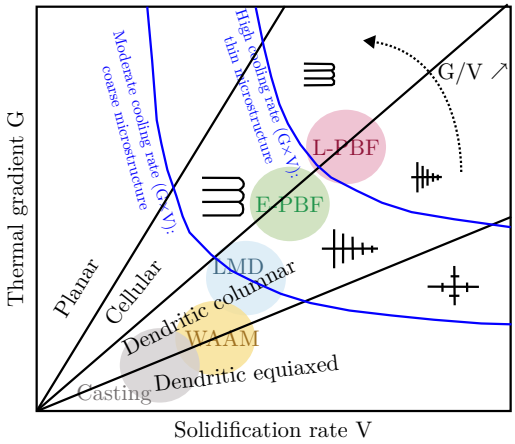

Figure 1.17. Mapping of solidification modes depending on the temperature gradient and the speed of the solidification front for different metal additive manufacturing processes [98].

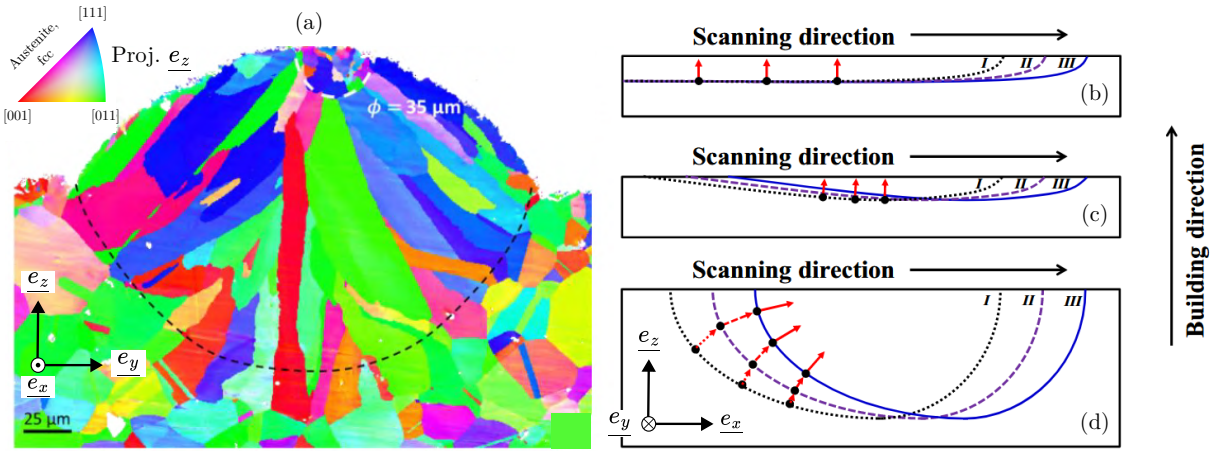

Figure 1.18. (a) EBSD map projected in the building direction of the transverse cross-section of a single bead made of 316L manufactured by L-PBF [99]. Schematic drawing of the growth direction of the grains in (b) a vertical melt boundary, typical of L-PBF, (c) a nearly vertical melt boundary, typical of L-PBF with relatively lower cooling rates and (d) an inclined melt boundary, typical of DED processes [3].

Single-bead walls

In single-bead walls manufactured using DED, the thermal gradient is usually oriented in the manufacturing direction $\underline{e_z}$, from the bottom to the top of the walls, which results in the formation of elongated grains through multiple layers [101, 102]. Cambon *et al.* [103] observed the crystal orientations using EBSD in a single-bead wall made of 316L steel manufactured by WAAM (Figure 1.19a). Similarly, Xu *et al.* [104] performed EBSD characterizations in a single-bead wall made of 316L achieved by WLAM. Both studies reported elongated grains in the manufacturing direction (from the bottom to the top of the walls). However, the grains observed with WLAM are smaller than those observed with WAAM due to the smaller size of the melt pool associated with the faster cooling rate in WLAM [105]. In addition, a $\langle 001 \rangle_{\parallel \underline{e_z}}$ predominant texture is observed in the single-bead wall achieved by WAAM, as a result of epitaxial growth and crystal orientation selection [99]. This texture is not visible in the study of Xu *et al.* [104]. However, similar trends to WAAM were observed during the manufacturing of 316L steel single-bead walls using additive manufacturing processes with higher cooling rates: DED-powder [106] and L-PBF [107]. The elongation of grains and crystal texture can lead to anisotropic properties of the manufactured single-bead components [101].

As the number of deposited layers increases, the cooling rate decreases due to heat accumulation (if interlayer cooling time is not optimized). Wang *et al.* [105] observed the presence of equiaxed grains at the top of the last deposited bead with the WAAM process since the cooling rate decreases between the first and the last deposited layer. Similar observations were made by Su *et al.* [108] for the WLAM process. However, these equiaxed grains at the top of the layers are susceptible to being remelted during the deposition of the next layer [103].

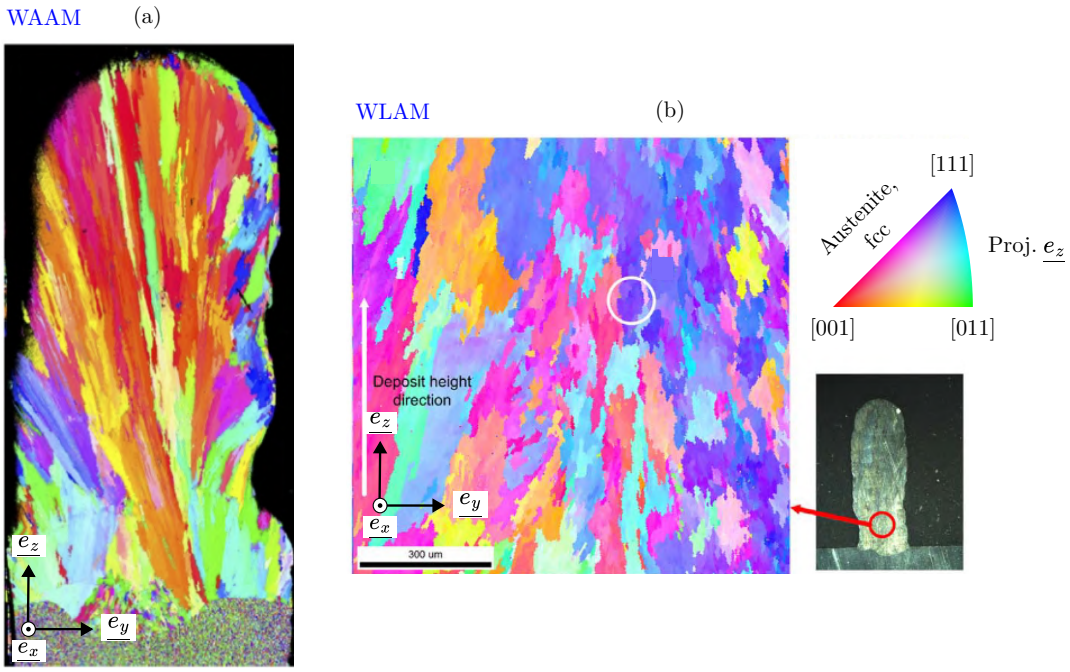

Figure 1.19. Orientation maps obtained by EBSD and projected in the manufacturing direction of transverse cross-sections of 316L single-bead walls achieved by (a) WAAM [103] and (b) WLAM [104].

Multilayer tiles

Akbari *et al.* [109] characterized the microstructure of 316L tiles manufactured by WLAM and noted that the grains in tiles were less elongated and thinner than those observed in single-bead walls. Goland *et al.* [110] studied the microstructure of a tile made of 316L, manufactured by WLAM (Figure 1.20a). Elongated grains were noted and the component exhibited a $\langle 110 \rangle_{\parallel \underline{e_z}}$ texture. This texture resembles the one observed for 316L tiles manufactured by L-PBF. Andreau *et al.* [111] reported that the manufactured tiles with L-PBF exhibit a predominating $\langle 110 \rangle_{\parallel \underline{e_z}}$ caused by the shape of the melt pool, except in the center of the beads where a $\langle 001 \rangle_{\parallel \underline{e_z}}$ texture is observed associated with grain elongation in the manufacturing direction (Figure 1.21).

Monier [28] (Figure 1.20b), Palmeira Belotti *et al.* [112] and Wang *et al.* [113] analyzed the microstructure of tiles made of 316L steel with the WAAM process. Two zones with distinct microstructures characterized the tiles:

- At the edges of the bead (overlapping area OR), the fact that the melt pool is almost flat and perpendicular to the manufacturing direction led to the formation of a $\langle 001 \rangle_{\parallel \underline{e_z}}$ texture. Large columnar grains elongated with the manufacturing direction were reported, similar to single-bead walls.
- In the center of the beads (center of fusion zone CFZ), a $\langle 110 \rangle_{\parallel \underline{e_z}}$ texture was reported. The grains in this area are thinner than in the OR.

Palmeira Belotti *et al.* [112] noted that the elongation direction of the grains in the OR is deviated towards the outside of the layer for the single beads deposited at the edges of the layers, resulting from the inclined thermal gradient. Finally, Wang *et al.* [113] reported that the two zones would exhibit variations in mechanical properties due to their different grain size and texture.

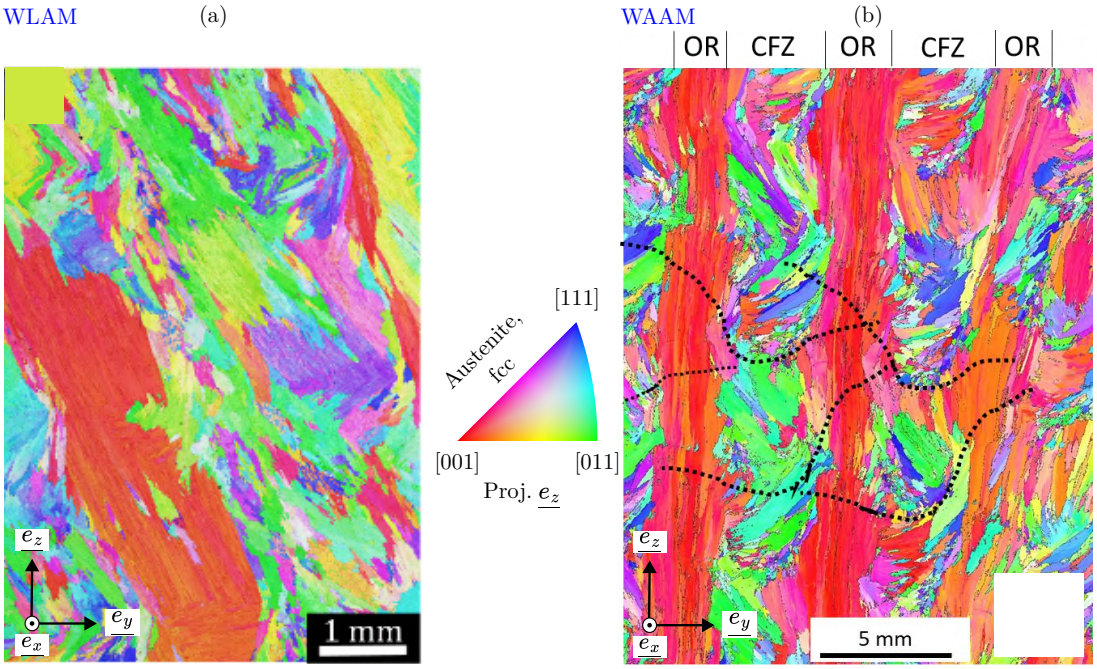

Figure 1.20. Orientation maps obtained by EBSD and projected in the manufacturing direction of transverse cross-sections of 316L tiles achieved by (a) WLAM [114] and (b) WAAM [28].

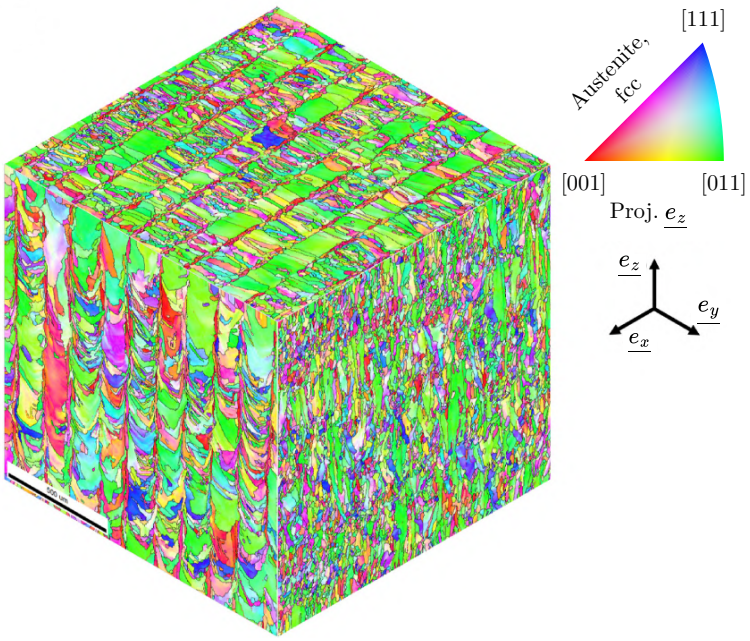

Figure 1.21. 3D-representation of orientation maps obtained by EBSD and projected in the manufacturing direction of a 316L tile manufactured using the L-PBF process [111].

1.3.3 Main phases

Schaeffler [115] approximated the 316L steel to a three-element alloy by regrouping the alloying elements favoring the Face-Centered Cubic (FCC) austenite phase (γ stabilizers: Ni, C, N, Mn) and those favoring the Body-Centered Cubic (BCC) ferrite phase (ferritizers: Cr, Mo, Si, Nb), under equivalent weight percentages $wt.\%Ni_{eq}$ and $wt.\%Cr_{eq}$, after ponderation of their contribution (Equations 1.1 and 1.2).

$$wt.\%Cr_{eq} = \ wt.\%Cr \ + \ wt.\%Mo \ + \ 1.5 \times wt.\%Si \ + \ 0.5 \times wt.\%Nb \tag{1.1}$$

$$wt.\%Ni_{eq} = \ wt.\%Ni \ + \ 30 \times wt.\%C + \ 30 \times wt.\%N \ + \ 0.5 \times wt.\%Mn \tag{1.2}$$

By using these ratios, Schaeffler *et al.* [115] estimated that austenitic 316L stainless steels cooled under the solidification conditions of welding will contain between 5 and 10 vol.% of ferrite, depending on the exact chemical composition. The typical conditions of solidification of WAAM and WLAM processes also promote the formation of an austenitic-ferritic microstructure for 316L steel, according to Astafurov and Astafurova [29]. Oppositely, in the L-PBF process, 316L steel exhibited a fully austenitic structure due to higher solidification rates [116]. Therefore, austenitic-ferritic 316L steel will experience reduced corrosion resistance compared to fully austenitic 316L. Given that chromium and molybdenum are ferritizers, the predominant austenite phase will be depleted of these elements [117].

Suutala *et al.* [118] indicated that two different solidification paths can occur based on the chemical composition of the alloy (ratio between γ stabilizers and ferritizers, $\frac{wt.\%Cr_{eq}}{wt.\%Ni_{eq}}$), as schematized in Figure 1.22:

- the **AF solidification mode** ($1.37 < \frac{wt.\%Cr_{eq}}{wt.\%Ni_{eq}} < 1.48$), in which the alloy primarily solidifies as austenite and ferrite is formed between the dendrites due to the decrease of the amount of γ stabilizer elements in the liquid. The remaining ferrite between the dendrites in AF mode is thus called "interdendritic";
- The **FA solidification mode** ($1.48 < \frac{wt.\%Cr_{eq}}{wt.\%Ni_{eq}} < 1.95$), in which the metal first solidifies as ferrite and is re-transformed into austenite except at the core of the dendrites where residual ferrite remains. This ferrite is referred to as "lathy" or "vermicular".

Suutala *et al.* [119] mentioned that an increase in the deposition speed can also promote AF solidification mode instead of FA mode, depending on the chemical composition of the alloy. Astafurov and Astafurova reported that both solidification modes were observed in WAAM and WLAM components made of 316L steel, even if the FA solidification mode is the most common.

Figures 1.23a and b present the phase microstructure of 308L components (with close chemical composition to 316L, Table 1.2) manufactured using WAAM and WLAM processes, respectively [15]. Both components exhibited vermicular and lathy ferrite within the austenite, indicating FA solidification.

The ferrite fraction in 316L steel manufactured using WAAM and WLAM processes was reported to be between 4 vol.% and 10 vol.% [28, 90, 114, 120], which is agreement with Schaeffler *et al.* [115] for 316L steel solidified under the cooling conditions of welding. Long *et al.* [77] noted that the ferrite fraction increases with the cooling rate using the WAAM-CMT process, which was also noted by Goland [114] for 316L specimens made by WLAM and WAAM. Rodriguez *et al.* [121] reported that the amount of chromium and molybdenum in the ferrite phase of 316L steel increases with the applied energy input, indicating that processes using high linear energy while promoting the formation of austenitic-ferritic

microstructure will produce a component with reduced corrosion resistance.

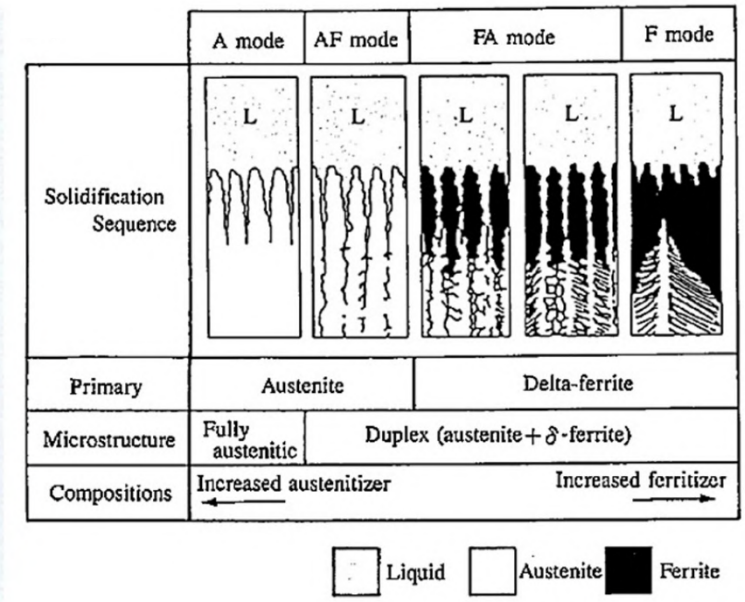

Figure 1.22. Different solidification modes of austenitic-ferritic steels depending on their chemical composition [118, 97].

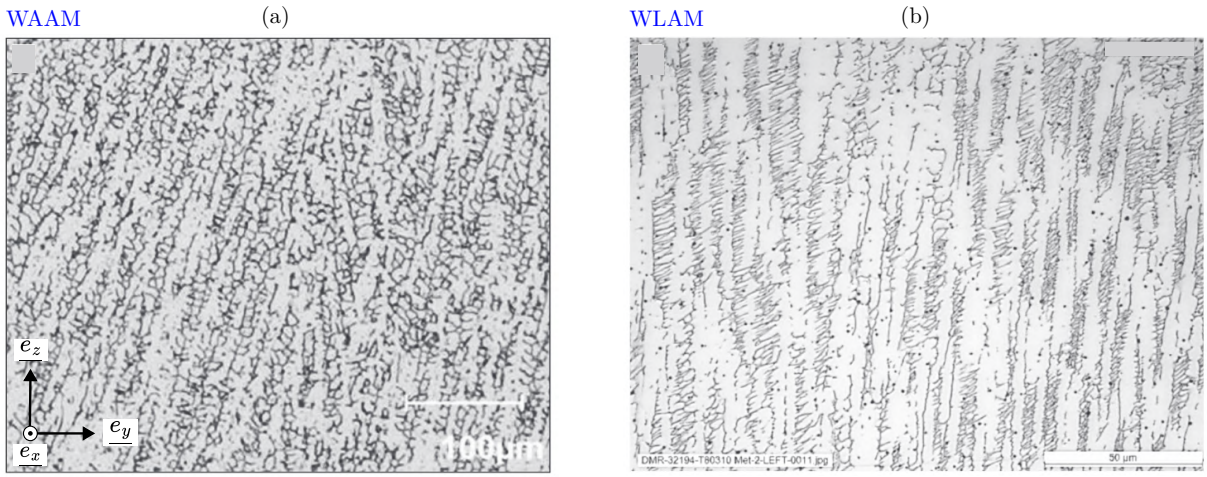

Figure 1.23. Micrographs of the austenitic-ferritic microstructure of 308L stainless steel components produced with (a) WAAM and (b) WLAM processes [15].

Elmer *et al.* [15] noted that the dendrite size is smaller in components manufactured by WLAM compared to those produced by WAAM, as it is linked to the solidification cooling rate. Reciprocally, the dendrite size can be used to estimate the cooling rate at solidification in the achieved components [122]. Table 1.3 reviewed the estimated cooling rates during components manufacturing with WAAM and WLAM processes. The WLAM process resulted in higher cooling rates, in the magnitude of 10^3 °C/s, than the WAAM process (10^2 °C/s).

Table 1.3. Literature review of the cooling rates observed for WLAM and WAAM processes.

Process	Reported cooling rates (°C/s)	Reference
WLAM	500 – 3 000	Bernauer *et al.* [123]
	1 000 – 4 000	Akbari *et al.* [109]
	1 000	Goland *et al.* [114]
WAAM	100	Goland *et al.* [114]
	100	Gudur *et al.* [124]
	1000	Monier [28]
	68 – 690	Park *et al.* [125]
	10	Rodriguez *et al.* [126]

As mentioned by de Sonis [116], the observed as-built microstructure is not as-solidified because the component experienced successive heating and cooling cycles caused by the deposition of new layers. Several authors reported that these heating cycles are susceptible to promoting the σ phase, which is an intermetallic phase detrimental to the mechanical properties of the material [127, 114]. Figure 1.24 illustrates the precipitation of the σ phase in a 316L tile manufactured using the WAAM process. σ phase was reported in the as-built state of components manufactured using WAAM with low solidification cooling rates [114, 128], located in the ferrite [129] as this phase allows for rapid formation of σ phase as compared to austenite [130].

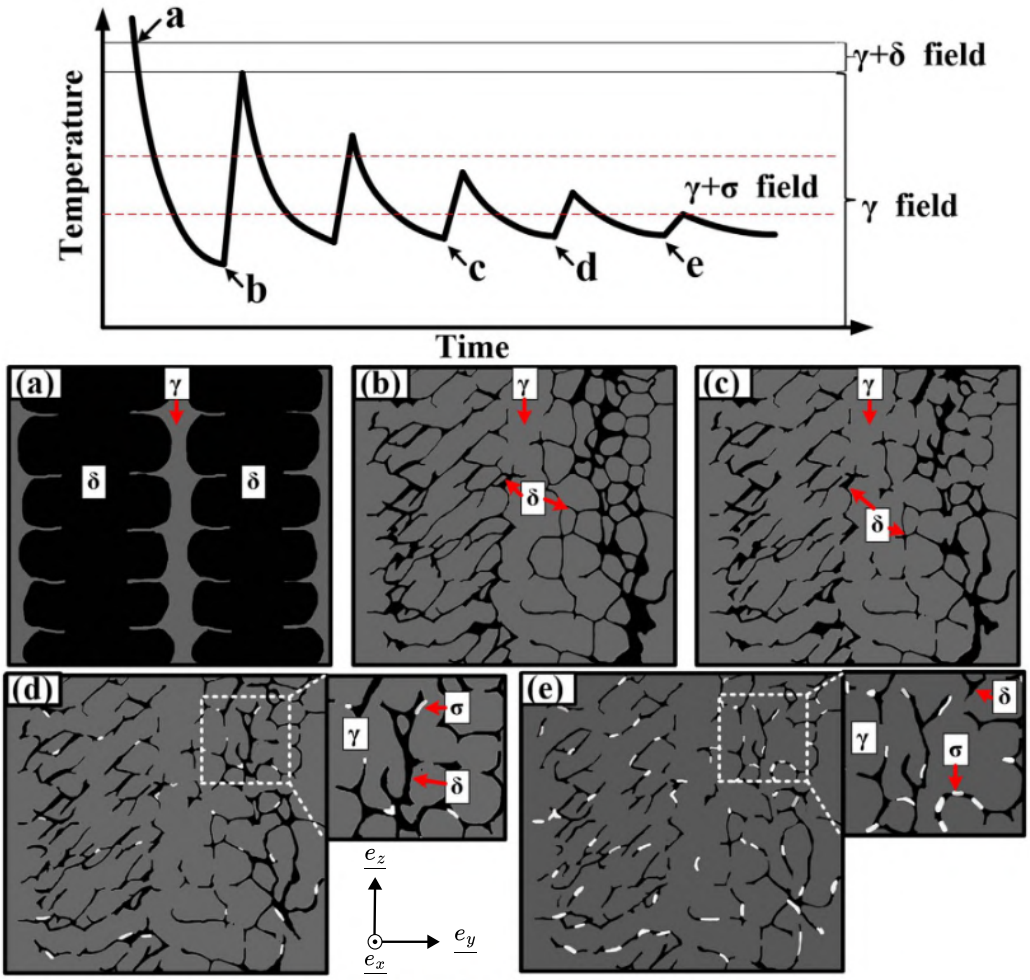

Figure 1.24. Schematic illustration proposed by Chen et al. [127] of σ phase formation within the ferrite during the successive thermal cycles of the manufacturing of a 316L tile with WAAM process.

1.3.4 Mechanical properties

Frazier *et al.* [21] reviewed the mechanical properties of components produced using additive manufacturing processes, highlighting that anisotropy can hardly be avoided due to columnar grain structure. In addition, compared to the materials manufactured using conventional processes, the components manufactured by additive manufacturing exhibited higher tensile strength and yield stress [51, 97]. Laghi *et al.* [131] reported that the mechanical properties are similar in the manufacturing and deposition direction of a component manufactured by WAAM. However, higher values of tensile strength and yield stress were reported with a specimen taken diagonally at 45° to the manufacturing direction due to the columnar and textured microstructure.

Table 1.4 summarizes the determined mechanical properties for 316L components manufactured using different additive manufacturing processes (WAAM with the three different arc-generation methods (GMAW, GTAW and PAW), WLAM, DED-powder and L-PBF). Higher tensile strengths were reported for the components achieved by powder processes than in those produced by wire processes. Bertsch *et al.* [132] mentioned that the successive thermal cycles during the production of a component with additive manufacturing cause strain cycles limited by the geometrical constraints. As a result, it can induce dislocations in the microstructure [116], causing hardening of the material. The authors also indicated that the dislocation density increases with the cooling rate, meaning that more dislocations are expected for L-PBF than for DED-wire processes; and for WLAM than for WAAM.

Moreover, comparable mechanical properties were observed for the components manufactured using WAAM with the three arc-generation methods. For all the processes, some anisotropy is reported between the manufacturing and deposition directions, but in a less significant way for wire processes compared to DED-powder and L-PBF. Lastly, it can be concluded that all the processes allowed to fulfill the requirements imposed by the ASTM A473-15 standard for wrought 316L steel [133].

Table 1.4. Summary of mechanical properties of 316L stainless steel fabricated by additive manufacturing compared to that processed by standard wrought route. V denotes a tensile test achieved in the manufacturing direction, and L denotes a tensile test achieved in the deposition direction.

Process	Orientation	Properties			Reference
		Yield stress (MPa)	Tensile strength (MPa)	Elongation (%)	
WAAM-GMAW	V	235	533	48	Chen *et al.* [127]
	V	235	533	48	Chen *et al.* [129]
	L	286	586	39	Goland *et al.* [114]
WAAM-CMT-continous	V	336.9	574.1	42.0	Rodriguez *et al.* [126]
	L	364	577	43	
WAAM-CMT-pulsed	V	331.7	536.0	45.6	Rodriguez *et al.* [126]
	L	374	588	45	
WAAM-PAW	V	342	539	56	Suarez *et al.* [134]
	L	384	586	40	
WAAM-GTAW	V	322	540	43	Rodriguez *et al.* [126]
	L	365	590	42	
WLAM	L	400	600	34	Bernauer *et al.* [123]
	L	391	634	28	Goland *et al.* [114]
DED-powder	V	479	703	46	Zietala *et al.* [135]
	L	576	776	33	
L-PBF	V	280	580	62	Yu *et al.* [136]
	L	490	685	51	
Wrought requirements	-	**170**	**450**	**40**	ASTM A473-15 [133]

Higher hardness values were also reported in components made of stainless steel manufactured by WAAM and WLAM compared to conventional wrought state (250-270 $HV_{0.2}$ for WLAM [71] and 212-208 HV_1 for WAAM [28]). Consistently with Table 1.4, the hardness of components manufactured by WLAM is reported to be higher than that of a component manufactured by WAAM due to the difference in heat inputs between both processes, which induces more thermal distortions, resulting in an increased dislocation density [137]. In addition, several studies mentioned that, under certain conditions, the hardness of the components manufactured by WAAM and WLAM decreases from the bottom of the wall to the top [123, 138].

Lastly, Li *et al.* [139] and de Sonis [116] studied the fracture of stainless steel samples manufactured by WLAM and WAAM, respectively. Both studies mentioned that the fracture surface exhibited dimples, synonymous with the ductile behavior of the material.

1.4 Heat treatments

Several heat treatments were applied in the literature to components produced by wire additive manufacturing, targeting different objectives :

1. stress-relief to remove the residual stresses;
2. recrystallization, aiming to decrease dislocation density and to eliminate the columnar and textured microstructure caused by the manufacturing [131];
3. phase transformation, aiming, for 316L, in removing the residual ferrite within the austenite (as this phase is not stable at high temperatures), which could be detrimental to the corrosion resistance of the material [121].

Rodrigues *et al.* [121] reported that a heat treatment at 400 °C allowed for the reduction of the amount of residual stresses in a 316L component achieved by WAAM without influencing the microstructure. As a mean of comparison, Luecke *et al.* [140] mentioned that, for stainless steels manufactured using the L-PBF process, a stress-relief heat treatment at 650 °C for 1 h increases the tensile strength and reduces the yield stress.

Several heat treatments were conducted aiming at recrystallizing the microstructure of WAAM and WLAM components made of 316L steel (Figure 1.25), applying temperatures between 1000 and 1200 °C for durations from 30 min to 4 hours:

- Goland *et al.* [114] achieved heat treatments at 1200 °C during 3 hours in a tile manufactured by WAAM, showing only very limited recrystallization (Figures 1.25a and b). Oppositely, Monier [28] mentioned a complete recrystallization in a tile manufactured by WAAM after heat treatment at 1200 °C after only 30 mins, obtaining isotropic grains with a size of about 1 mm (Figure 1.25c).
- Chen *et al.* [129] studied the influence of heat treatments at 1200 °C in single-bead walls achieved by WAAM (Figures 1.25d-f). After 4 hours, millimetric equiaxed grains were obtained.
- Goland *et al.* [114] achieved heat treatments at 1200 °C for 3 hours in a tile manufactured by WLAM, showing complete recrystallization and equiaxed grains with a size of about 400 µm (Figures 1.25g and h).

Wang *et al.* [141] also mentioned that recrystallization is easier in the center of the fusion zone than in the overlapped region. The authors successfully recrystallized the CFZ after heat treatment at 1100 °C, whereas the recrystallization temperature increased to 1200 °C for the OR. The authors also mentioned

that recrystallization heat treatment removes the anisotropy of properties, increasing tensile strength and decreasing yield stress.

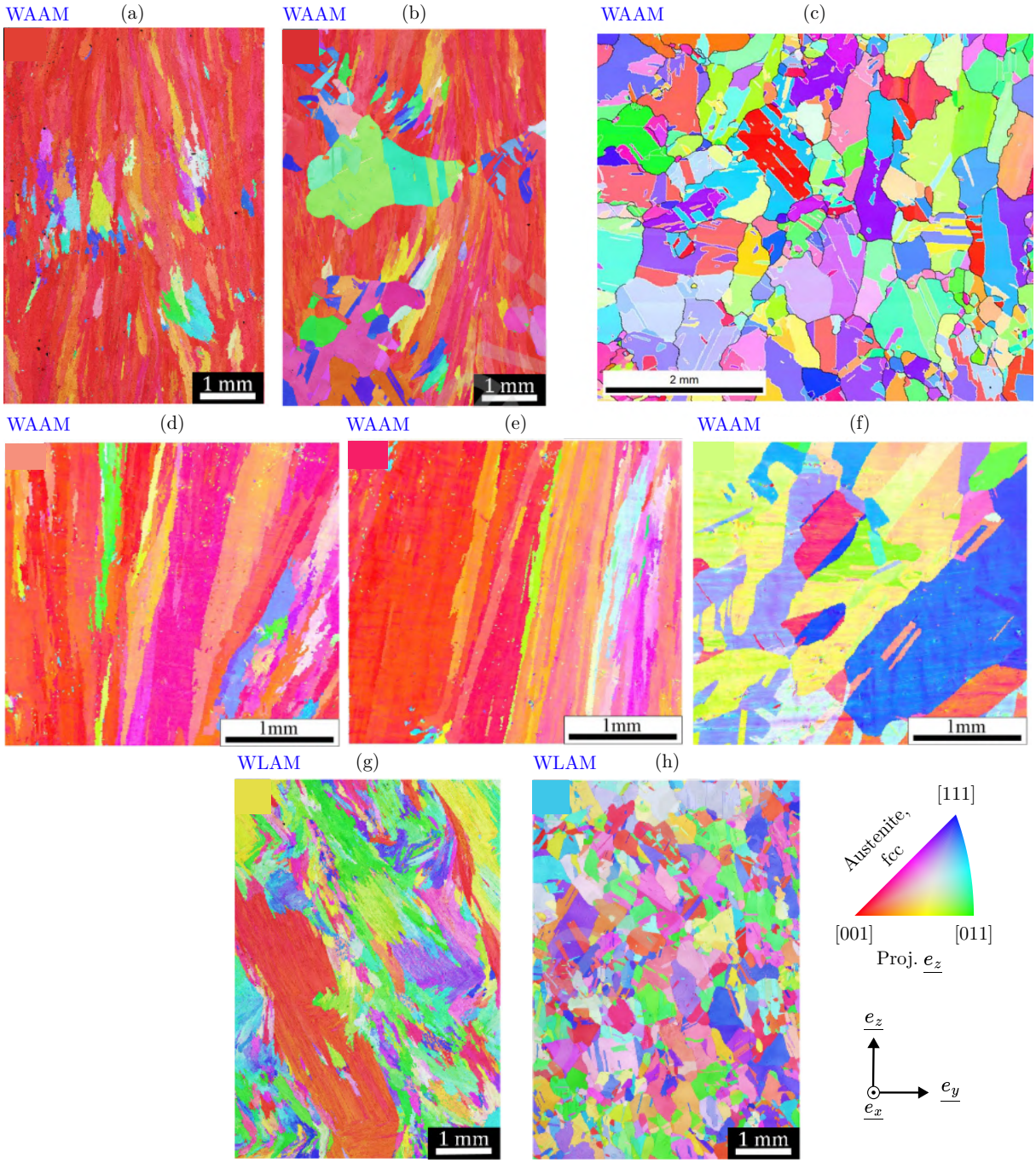

Figure 1.25. Orientation maps obtained by EBSD and projected in the manufacturing direction of transverse cross-sections of 316L components before and after heat treatments followed by water quenching: (a) tile manufactured by WAAM in as-built state [114]; (b) tile manufactured by WAAM after stress relief (400 °C for 2 hours) and solution annealing (1200 °C for 3 hours) [114]; (c) tile manufactured by WAAM after stress relief (600 °C for 1 hour) and solution annealing (1200 °C for 30 mins) [28]; (d) single-bead wall manufactured by WAAM in as-built state [129]; (e) single-bead wall manufactured by WAAM after treatment at 1200 °C for 1 hour [129]; (f) single-bead wall manufactured by WAAM after treatment at 1200 °C for 4 hours [129]; (g) tile manufactured by WLAM in as-built state [114]; (h) tile manufactured by WLAM after stress relief (400 °C for 2 hours) and solution annealing (1200 °C for 3 hours) [114].

Several heat treatments were conducted in tiles manufactured by WAAM to transform the ferrite into austenite:

- After temperature exposure below 1000 °C, several authors mentioned that the heat treatment resulted in the formation of σ phase in the initial ferrite (Figure 1.26) [28, 121, 129].
- After heat treatment above 1000 °C, Chen *et al.* [129] mentioned that the ferrite transforms into austenite, remaining with "globular" ferrite in different amounts depending on the applied treatment (Figure 1.26c and d), even if the grains did not recrystallize. No σ phase was observed. Chen *et al.* [129] reported that this heat treatment resulted in a decrease in both the tensile strength and the yield stress and increased the maximal elongation.

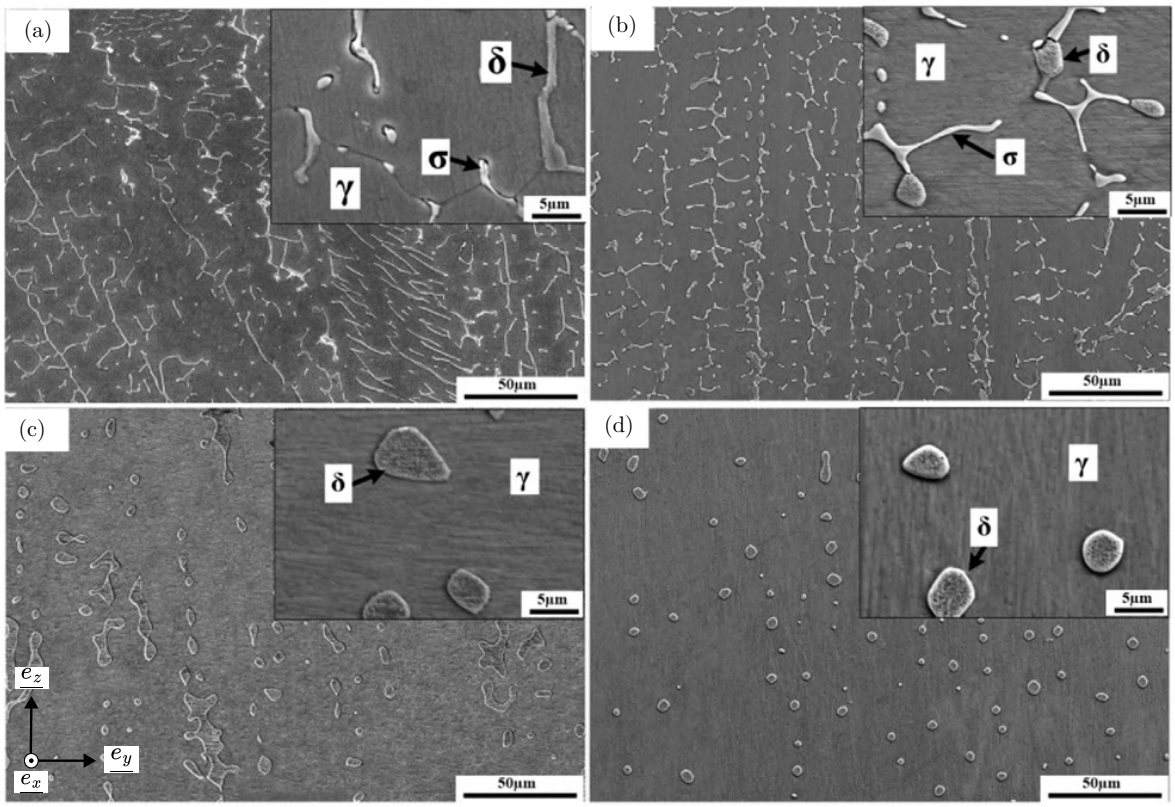

Figure 1.26. Microstructure of 316L tiles manufactured by WAAM (a) in as-built state and after 1 hour heat treatments followed by water quenching at (b) 1000, (c) 1100 and (d) 1200 °C [129].

1.5 Numerical modeling of wire additive manufacturing

The use of a finite element model could allow an increase in the understanding of additive manufacturing processes while reducing the amount of experimental work [142]. It can further lead to the manufacturing of components with better quality in shorter times and lower costs. Thermal, mechanical and metallurgical problems are the main physical phenomena that can be considered in a finite element modeling of additive manufacturing, as presented in Figure 1.27 [143]).

1. The thermal phenomena influence the microstructure of the components through the thermal gradient and the solidification cooling speed;
2. Reciprocally, the phase transformations responsible for microstructure formation influence the temperature evolution through latent heat during the transition from solid to liquid states.
3. The microstructure has a direct effect on mechanical properties.
4. The mechanical state (for example, residual stresses and strains) influences the kinetics of phase transformations.
5. The thermal evolution influences the mechanical properties (as the physical parameters of the material are dependent on the temperature).
6. Lastly, the heat can be dissipated by mechanics-related phenomena.

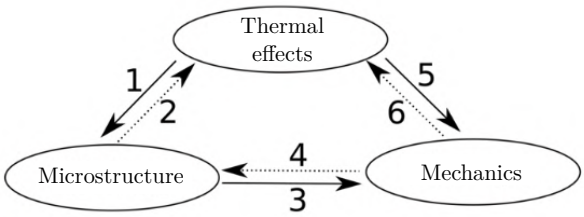

1. Phase transformations
2. Latent heat
3. Mechanical properties dependent on the microstructure
4. Mechanical stresses
5. Non-uniform thermal stresses, temperature-dependent mechanical properties
6. Heat dissipation

Figure 1.27. Coupling between the different physical phenomena involved in wire additive manufacturing. Adapted from Cambon [143].

One of the main challenges in the modeling of additive manufacturing is to reproduce the material deposition during the manufacturing, modifying the geometry, as mentioned by Cambon [143] and Hilal [144]. Several methods have been proposed:

- the activation of elements, in which the finite elements that are not physically deposited already numerically exist with assigned negligible physical parameters. This process can result in errors caused by high thermal gradients between the inactive and active elements.
- the addition of elements, in which the global mesh is updated with new finite elements at regular time steps to reproduce the deposition.
- the tracking of the interface between the component and the ambient air in the meshed geometry, using the Level Set approach. This method allows for modeling the most accurate metal deposition, although it requires elevated computing times.

Several methods have been used to model the heat supply of the energy source during the deposition. Hilal [144] mentioned that the energy source could be modeled as imposed temperatures, input flux, surface heat source or volume heat source. However, this last approach has been demonstrated to be the most accurate for modeling wire additive manufacturing processes [145]. The volume energy distribution can be Gaussian, as in the work of Depradeux [146], allowing a correct prediction of the thermal field in the manufactured components, or adapted to the elongated shape of the melt pool, using a distribution referred to as Goldak distribution [147], as in the works of Cambon [143], Baumard [99] and Engel [107].

Most studies applied an elastoplastic model with hardening to describe the material behavior. Muransky *et al.* [148] mentioned that this hardening can be modeled as both isotropic or kinematic. The authors mentioned that the isotropic hardening tends to overestimate the induced stresses and strains, while the kinematic one underestimates them. A mixed isotropic-kinematic hardening model, referred to as the Chaboche model, is recommended to obtain the most accurate prediction [149].

Lastly, concerning the geometry of the achieved components, Prajadhiama *et al.* [150] mentioned that the rectangular shape modeling to approximate the shape of the beads leads to the lowest error in the prediction of the thermal field compared to arc-shaped modeling of the deposited beads while decreasing the computing times.

1.5.1 Thermal modeling

Several finite element studies were conducted to determine the thermal field during the processing of components with additive manufacturing, as presented in Figure 1.28a for WAAM using 316L steel [151] or in the study of Kiran *et al.* [152] for DED-powder process using 316L steel. The prediction of the thermal field allowed for the determination of thermal cycles induced by successive deposition of layers. Figure 1.28b compares the predicted and experimental thermal field during the manufacturing of a 10-layer component made of 316L with WAAM [90]. The numerical model presented a good accuracy.

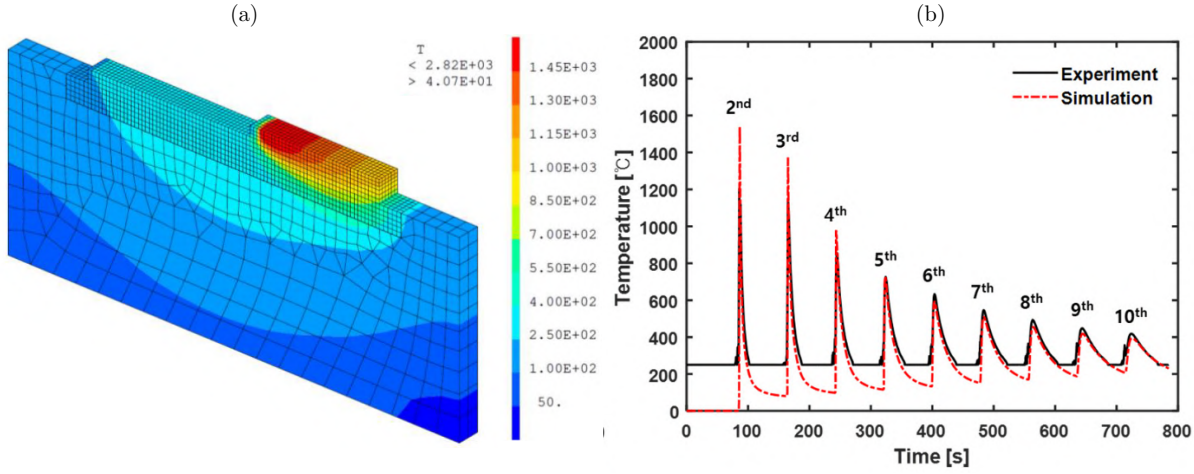

Figure 1.28. Modeling of temperature evolution during additive manufacturing: (a) estimated thermal field during the manufacturing of a single-bead wall with WAAM process using 316L steel [151]; (b) comparison between experimental (pyrometer, black line) and numerical (red dashed line) data of the temperature measured near the bottom of a single-bead wall manufactured using WAAM and 316L steel with an interlayer cooling time of 60 s [90].

The modeling was used to estimate local cooling rates [128]. Lee *et al.* [90] studied the manufacturing of a component made of 316L with the WAAM process without applying interlayer cooling (Figure 1.29a). The authors reported that the temperature at the beginning of deposition of each new bead increases as the number of deposited layers increases, highlighting heat accumulation in the component. As a result, they obtained that the cooling rate decreases as the number of layers increases, causing an increase in dendrite size. Mohebbi *et al.* [153] also determined that an increase in the minimal temperature reached at the end of the interlayer cooling time during the manufacturing of a wall made of steel using the WAAM process is linked to a decrease of the layer height, indicating that heat accumulation will cause geometrical deformations.

Gokhale *et al.* [154] achieved the thermal modeling of a component manufactured with the WAAM process using low-carbon steel, determining that the angles in the deposition path are more likely to experience heat accumulation than the rest of the component.

Park *et al.* [125] used a numerical model to study the thermal gradient and the solidification speed during the manufacturing of a component made of 316L with the WAAM process. Cooling rates at solidification were estimated in the components. The authors also reported that the cooling rates decrease as the number of deposited layers increases. Their model thus allowed for the prediction of the microstructure before manufacturing.

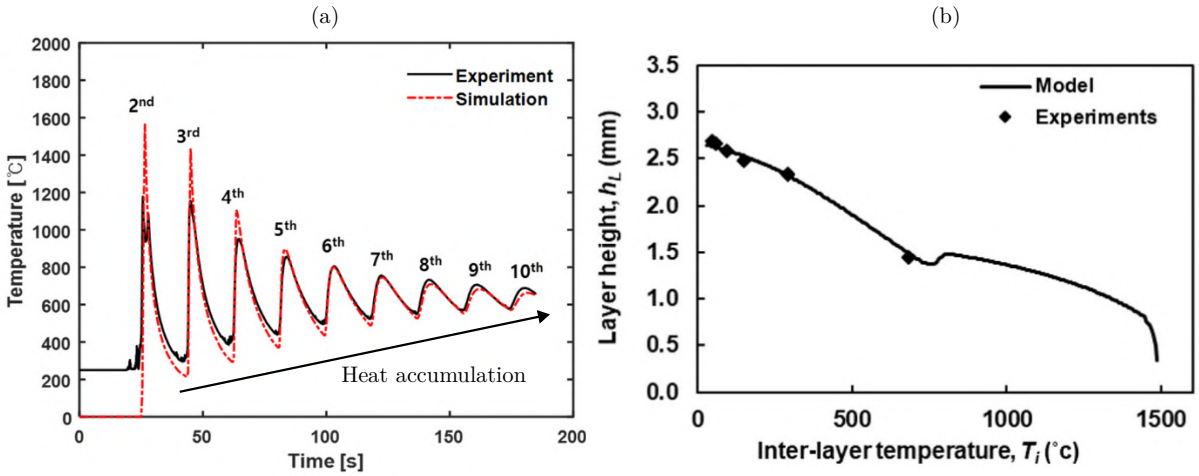

Figure 1.29. Examples of thermal analyses using finite element modeling: (a) comparison between experimental (pyrometer, black line) and numerical (red dashed line) data of the temperature measured near the bottom of a single-bead wall manufactured using WAAM without applying interlayer cooling [90]; (b) estimation of the layer height depending on the experienced interlayer temperature during the manufacturing of a single-bead wall with WAAM [153].

1.5.2 Mechanical modeling

Mechanical models were developed to estimate the distortions in components produced using additive manufacturing. Pascal *et al.* [151] followed the evolution of the deflection of a substrate clamped at one edge and unclamped at the other during the manufacturing of a 316L single-bead wall with WAAM process (Figure 1.30). The authors mentioned that successive deposition led to strain formation during manufacturing. At the end of the deposition, the final cooling is responsible for the most important deflection of the substrate, about 0.8 mm. This indicates that clamping is required to avoid geometrical distortions during manufacturing. Lee *et al.* [155] mentioned that the distortion of a component made of

Ti-6Al-4V and manufactured by WLAM decreases as the interlayer cooling time decreases. In addition, a complete clamping of the substrate reduced the amount of distortion in the component compared to partial clamping at the four edges of the substrate. Mughal *et al.* [156] studied the substrate deformations based on the applied deposition strategy of multilayer tiles made of mild steel and deposited using the WAAM process. A deposition path starting with the outer parts of a component and going through the center caused fewer distortions.

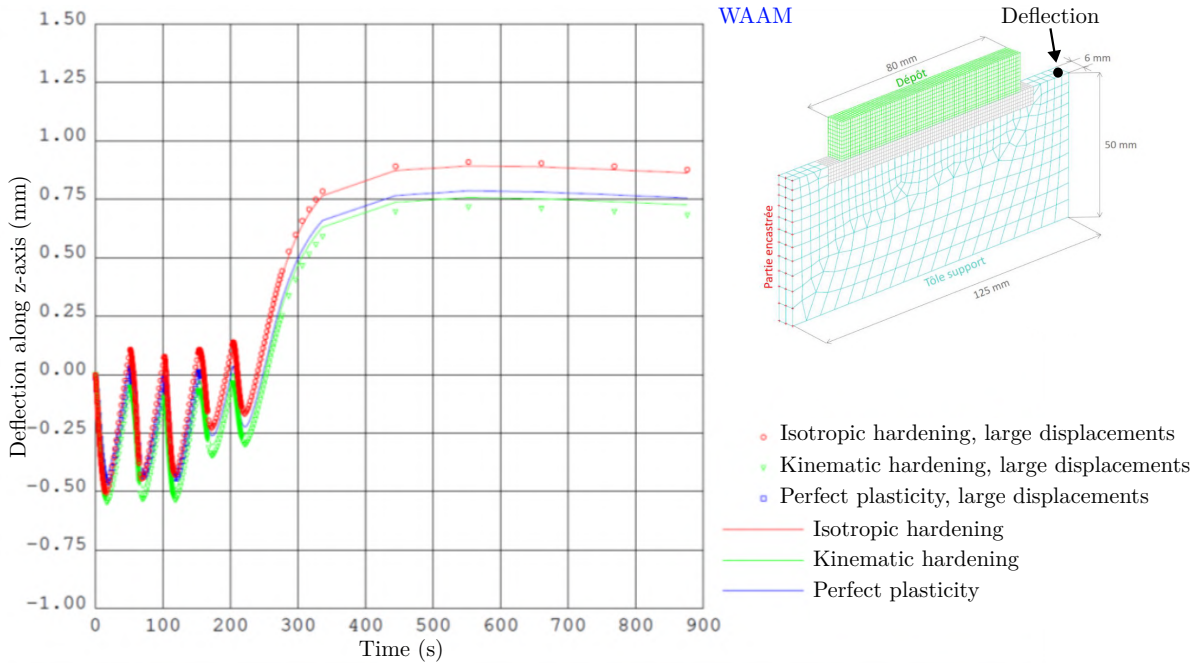

Figure 1.30. Numerical estimation of the displacements of one unclamped extremity of the substrate during the manufacturing of a 5-layer single-bead wall with WAAM process and 316L steel, using different hardening models (perfectly plastic, isotropic hardening and kinematic hardening) and displacements hypotheses (large displacements and small displacements) [151].

Mechanical models also allowed for estimating the residual stresses in the produced components. Figure 1.31a and b present the estimated distribution of the residual stresses in tiles manufactured using the WAAM and the DED-powder process with 316 steel, respectively [17]. High residual stresses were reported, especially for WAAM at the bottom of the wall. This is consistent with the observations of Biegler *et al.* [157] for modeling of DED-powder manufacturing using 316L and Cambon *et al.* [158] for WAAM using 316L. These residual stresses are compressive at the bottom of the manufactured components and progressively evolve to tensile at the top of the components, reaching quite high values up to 400 MPa depending on the used process [159, 152]. Hilal [144] mentioned that the deposition strategy does not impact the residual stresses.

Finally, Wang *et al.* [160] studied the influence of the applied clamping on the residual stresses in the component and the substrate (Figures 1.31c and d) during the manufacturing of a single bead wall made of aluminum alloy using the WAAM process. It was shown that clamping at the center of the ridges (Figure 1.31d) led to smaller residual stresses in the manufactured components compared to corner clamping (Figure 1.31c).

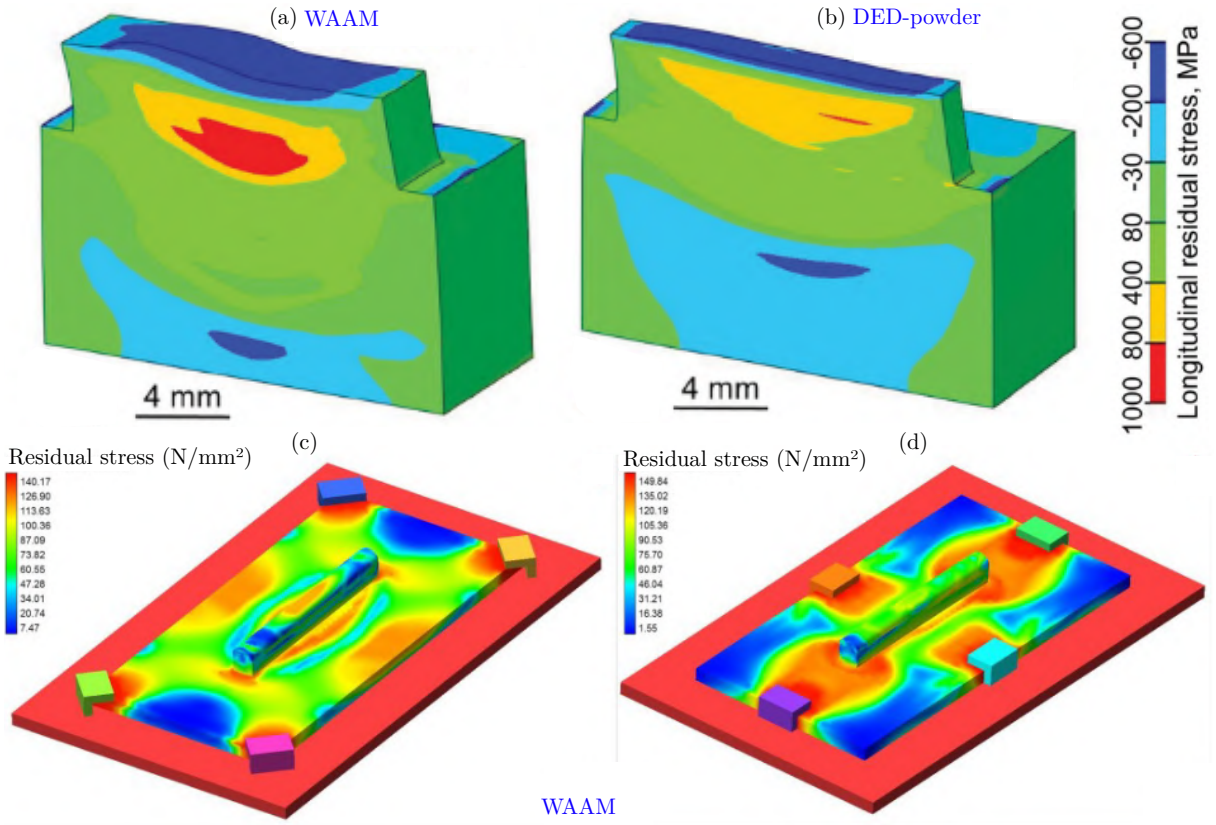

Figure 1.31. Distribution of the residual stresses in a 316L tile manufactured using (a) WAAM process and (b) DED-powder process [17]; (c) and (d): residual stresses in the substrate at the end of the manufacturing of a single-bead wall with WAAM using aluminum alloy, depending on the shape of the clamping (at the edges and the centers of the lines of the substrate, respectively) [160].

1.5.3 Geometry of the melted area

Depradeux *et al.* [146] mentioned that considering the fluid flow phenomena is mandatory to correctly estimate the shape of the melt pools resulting from additive manufacturing.

Several numerical models were implemented using fluid flow hypotheses to estimate the shape of the melt pool. Four forces cause the convection of the liquid metal in the bath [30]: (i) the buoyancy force due to differences in density, (ii) the Lorentz force from the magnetic field, (iii) the Marangoni force related to variations in surface tension and (iv) the shear force caused by the pressure of the electric arc on the liquid metal. Force (i) makes the pool less penetrating, while force (ii) has the opposite effect. Marangoni force (iii) causes both the width and the penetration of the pools to increase. Finally, force (iv) causes the pool to widen [161].

Using the defined fluid flow hypotheses, Ou *et al.* [162] obtained a correct prediction of the shape of single beads obtained with WAAM using H13 steel (Figure 1.32a). The authors also used this accurate local prediction of the thermal field to determine cooling rates, solidification speeds, and the directions of the thermal gradients.

Cadiou *et al.* [163] estimated the thermal field during the manufacturing of a component made of 304 steel with WAAM process by modeling the wire supply considering heat transfer, fluid flows and electromagnetic forces (Figure 1.32b). The authors have indicated, however, that the calculation times are the limit of their study: 15 days of calculation are necessary to model 6 seconds of the process.

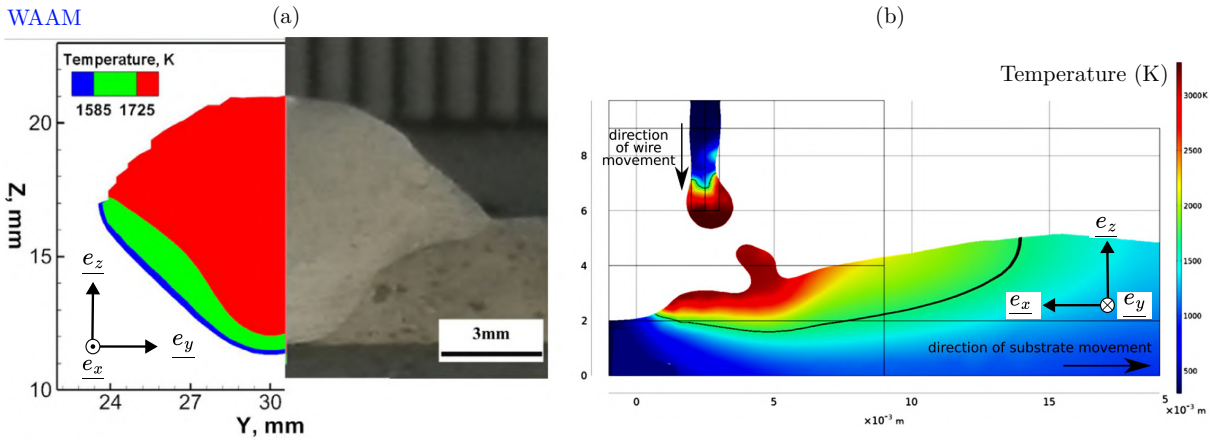

Figure 1.32. (a) Comparison between the calculated and experimental shape of the transverse cross-section of a single bead manufactured by WAAM (H13 steel) using heat transfer and fluid flow hypotheses [162]. (b) Estimation of the thermal field on the longitudinal cut of a single bead manufactured with WAAM (304 steel) using heat transfer, fluid flow and electromagnetic assumptions. The black line represents the melting temperature [163].

To reduce the computing times, several authors used geometrical assumptions to estimate the shape of the deposited beads. Ding *et al.* [4] mentioned that a parabola function could accurately represent the shape of a single bead manufactured by WAAM.

Mohebbi *et al.* [153] modeled the shape of the deposited beads made of EN440 steel with WAAM process using capillarity and gravity assumptions (Figure 1.33a), based on the applied process parameters. The model provides curvature angles (depicted in Figure 1.33a) indicating the shapes of the beads. The authors use it to assess the influence of the process parameters on the geometry of the resulting beads, noting, for instance, that both the height and the width of the bead decrease as the deposition speed increases.

Finally, Ou *et al.* [162] estimated the shape of deposited layers after overlapping by considering the pool as a drop seeking to adapt to the surrounding geometry (Figure 1.33b).

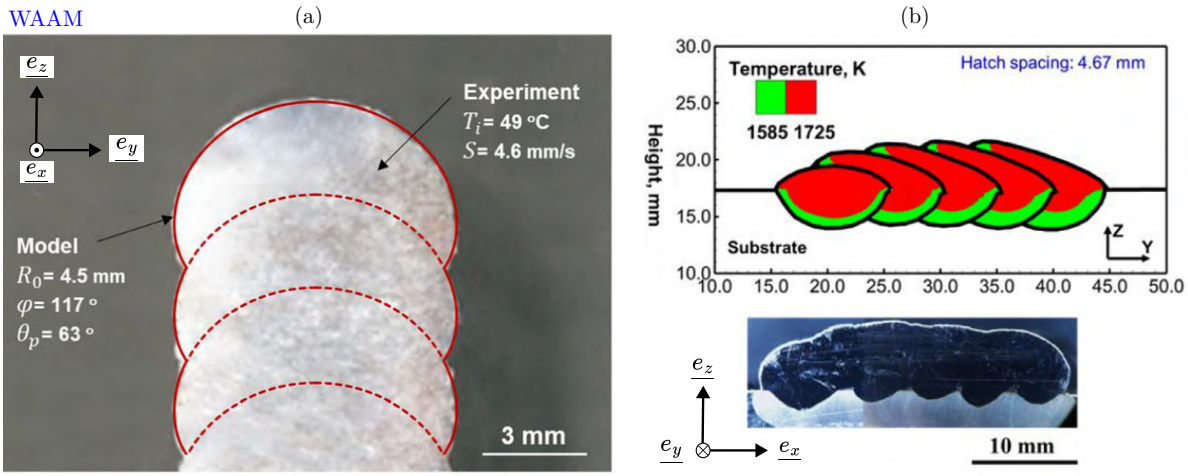

Figure 1.33. (a) Predicted and experimental geometry of a single-bead wall made of EN440 steel manufactured by WAAM using thermo-capillary-gravity assumptions. The different numbers indicate the applied parameters to calibrate the numerical model [153]. (b) Comparison between the calculated and experimental cross-section of a 5-bead layer made of H13 steel manufactured with WAAM [162].

1.5.4 Microstructure modeling

Cellular Automata and Finite Element (CA-FE) models were developed to predict the microstructure in components produced by additive manufacturing. CA-FE combines a dendritic growth law and a nucleation law with modeled thermal conditions. The shape of the deposited beads is adapted using a Goldak volume energy distribution for the heat source [147]. Engel [107] obtained similar experimental and modeled microstructure in transverse cross-sections of single-bead walls made of 316L manufactured by L-PBF (Figure 1.34a and b, respectively).

Phase field models can be used as well to predict the microstructure in components manufactured by WAAM using 316LSi wire, as presented by Herbeaux *et al.* [164] (Figure 1.34c and d, experimental and numerical, respectively). By using the shape of the melt pool determined experimentally, the authors obtained the microstructure using a hypothesis of grain continuity between two successive passes. This method involves much lower computing times than the CA-FE method, allowing it to be used to determine the microstructure depending on several variations in the shape of the deposited beads.

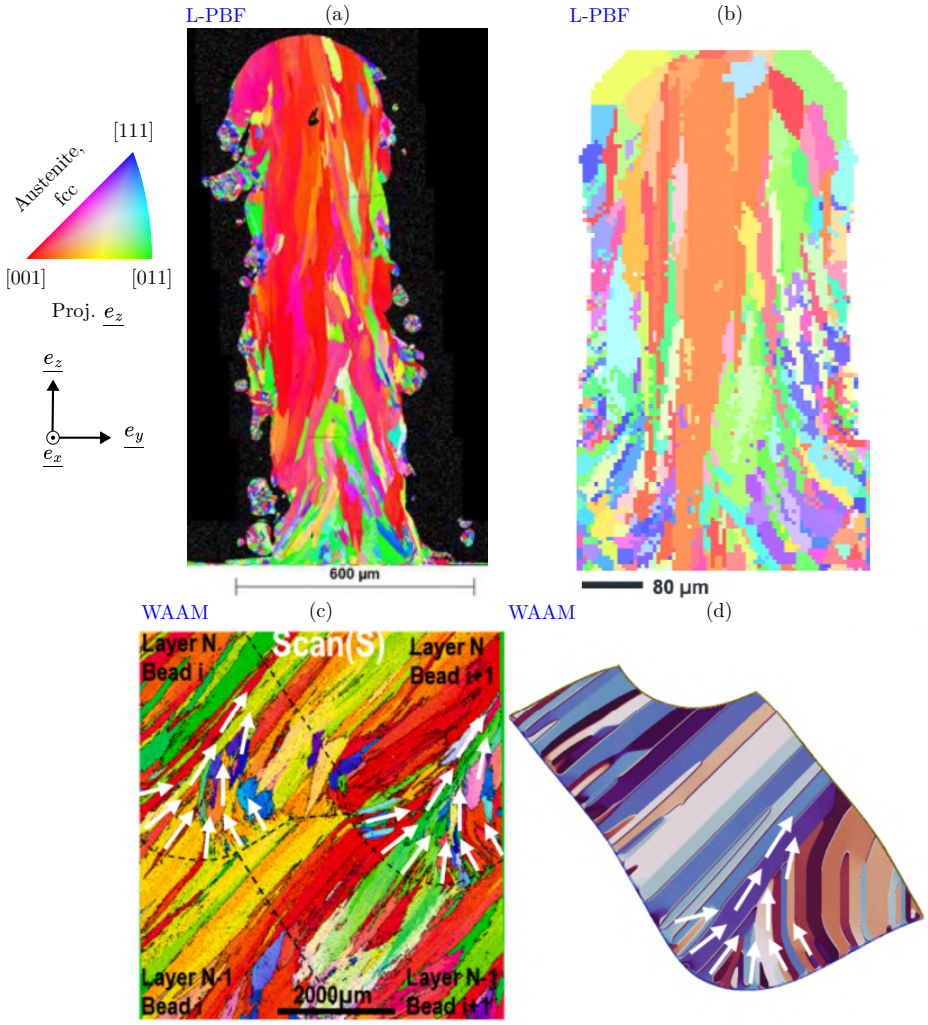

Figure 1.34. Comparison between (a) experimental and (b) modeled microstructure of the transverse cross-section of a single-bead wall made of 316L achieved with L-PBF using a coupled cellular automata/finite element model [107]. Comparison between (c) experimental and (d) modeled microstructure of tiles manufactured with WAAM process using 316LSi steel based on phase field assumptions [164].

1.6 Conclusion to Chapter 1

Additive manufacturing is a promising method for producing parts with complex geometries while minimizing material usage. Each technology, powder bed fusion (L-PBF), directed energy deposition with powder (DED-powder) and directed energy deposition with wire (DED-wire: WAAM and WLAM) is suitable for different applications. L-PBF allows the manufacturing of small components with complex geometries and high geometrical precision. At the same time, WAAM and WLAM show high deposition rate and allow thus the manufacturing of larger components. WLAM, in particular, combines a relatively fast deposition rate and sufficient geometrical precision. Therefore, among the various techniques, those utilizing wire as the material supply offer relatively short manufacturing times and enable the construction of large-scale components. This makes wire-based additive manufacturing particularly attractive for industrial applications.

Despite decades of intensive research on additive manufacturing, wire-based techniques have received significantly less attention compared to powder-based methods, such as L-PBF. Therefore, several issues still need to be addressed before wire additive manufacturing can be widely adopted. Namely, according to literature data, producing a component by additive manufacturing implies the control of porosity, inclusions, macroscopic deformations and the level of residual stresses to have the desired geometry and properties.

From a practical point of view, to get the desired geometry, the power of the energy source, the deposition rate and the wire feed rate have to be carefully chosen. These parameters modify the volume energy density and, thus, the applied linear energy or the volume of metal deposited per unit of length. Too low or too high energy densities lead to the formation of beads with irregular geometry. In addition, particular attention has to be paid to the deposition strategy and the interlayer cooling time since poor control of these parameters can cause local irregularities in the height of the manufactured components.

The processing parameters have to be carefully chosen not only to obtain a component with the desired geometry but also to avoid microstructure defects. The effect of additive manufacturing on microstructure was studied using various metallic alloys. One commonly used material is austenitic stainless steel 316L, which is widely applied in different industries, including the nuclear sector. This steel is also used in the present work.

The 316L components manufactured by WAAM and WLAM present a columnar grain structure with crystal orientations induced by epitaxial growth and/or preferential growth directions depending on the temperature gradient. Under typical solidification conditions in the WAAM and WLAM processes, the microstructure of components made of 316L consists of austenite and ferrite, with lathy and vermicular ferrite resulting from an FA solidification, where ferrite is the first solid phase formed from the liquid. Moreover, under certain conditions, the thermal cycling induced by the WAAM process can allow the precipitation of the intermetallic σ phase in the ferritic zones, which is detrimental to the mechanical properties. For single-bead walls, the thermal gradient is unidirectional (parallel to the direction of manufacturing $\underline{e_z}$). For WAAM and WLAM, this leads to the formation of elongated grains in this direction over several passes, associated with a texture according to $\langle 001 \rangle_{\parallel \underline{e_z}}$, the preferential growth direction. In the case of multilayer components, the different shape of the melt pools between WAAM and WLAM leads to different microstructures. In WAAM, columnar grains and $\langle 001 \rangle_{\parallel \underline{e_z}}$ texture are observed at the edges of the beads (overlapped region). Thinner grains and $\langle 011 \rangle_{\parallel \underline{e_z}}$ texture are observed at the center of the beads (center of fusion zone). In WLAM, the microstructure is mainly textured according to $\langle 011 \rangle_{\parallel \underline{e_z}}$ due to the convex shape of the melt pools, similar to L-PBF. In addition, the

components produced by WAAM and WLAM have anisotropic mechanical properties that differ between the deposition and manufacturing directions. It is worth noting, however, that the mechanical (mostly tensile) properties of 316L components produced by WAAM and WLAM can be better than those imposed by standards for conventionally produced 316L. Post-processing heat treatments have been used to induce relaxation of the components (reduction of the residual stresses), recrystallization and dissolution of the ferrite in 316L steel. The presented literature review highlighted that single-bead walls and tiles manufactured by WAAM and WLAM were not exhaustively investigated. Different microstructures were reported in single-bead walls and tiles made by WAAM and WLAM. Still, most of the works focused on the mechanical properties and the effect of heat treatments on tiles rather than single-bead walls.

Finally, various numerical models were proposed to investigate different phenomena operating during additive manufacturing. These models can be divided into different studied scales: (i) the scale of the manufactured component, (ii) that of the melt pool (deposited bead) and (iii) that of the microstructure. All models are based on hypotheses concerning thermal transfer, mechanical behavior, the geometry of the component, fluid mechanics or crystal growth. The models have enabled the accurate description of the temperature evolution in the components during manufacturing, their final deformation and residual stresses, the shape of the deposited beads and weld pools, and the microstructure. Thermal analysis revealed heat accumulation zones (related to poor control of the interlayer cooling time). Heat accumulation can result in a height collapse as compared to the desired geometry. Therefore, such a thermal model can be used to optimize interlayer cooling time to avoid geometry issues during manufacturing. The mechanical models were applied to calculate strains and residual stresses induced, for example, by the substrate clamping. It was shown that complete clamping minimizes the strains in the component. Moreover, residual stresses are inevitable during the manufacturing process and can evolve with the amount of applied energy and their description is of high importance. The WAAM process, with the highest linear energy, leads to components with the highest residual stresses. Modeling the shape of the melt pools and beads has enabled accurate estimation of the thermal gradient and solidification rate fields, which govern the microstructure formation. Finally, the microstructure modeling highlighted the columnar and textured grains intrinsic to additive manufacturing processes. The literature lacks, however, models that can be valid for both WAAM and WLAM processes to describe the heat transfer and mechanical state. Moreover, most models are valid for one specific scale (that of the microstructure, that of the deposited bead, that of the component) and are not easily transferable from one scale to another due to the used hypotheses.

This page was intentionally left blank.

Chapter 2

Materials and methods

Contents

Résumé en français du Chapitre 2 : Matériaux et Méthodes

Les cellules WAAM et WLAM du CEA/LTA (Figure 2.1) ont été utilisées pour la fabrication de monocordons, de murs et de blocs en acier inoxydable austénitique 316L. Ces plateformes intègrent un robot composé d'un bras à six axes, équipé d'une tête de dépôt spécifique (Figure 2.2) avec un apport de fil coaxial pour le WLAM et transverse pour le WAAM. Le procédé WAAM repose sur la méthode de soudage TIG, dans laquelle une électrode en tungstène sert à générer l'arc électrique. Lors des premières fabrications, la plateforme WAAM n'étant pas encore opérationnelle, un banc de soudage semi-automatique a été utilisé (Figure 2.3). La répétabilité des essais entre ce banc et la plateforme WAAM a ensuite été vérifiée. Les plateformes ont été instrumentées avec des dispositifs d'observation visuelle et thermique (caméras, caméras thermiques, pyromètres, thermocouples) permettant de suivre le processus de fabrication et d'analyser le champ de température. L'émissivité des pièces, nécessaire aux mesures par caméra thermique, a été calibrée à 0,3 pour le WAAM et 0,4 pour le WLAM, ce qui est en accord avec les valeurs rapportées dans la littérature.

La composition chimique du fil d'apport a été déterminée par ICP-AES (Spectrométrie à plasma à couplage inductif) et analyse élémentaire (Table 2.1) et correspond à celle d'un acier inoxydable 316L, à l'exception du chrome qui est volontairement ajouté en léger excès afin de favoriser la formation de ferrite dans les pièces. Une analyse du fil par microsonde de Castaing a révélé la présence de deux types d'inclusions : des sulfures de manganèse et des oxydes complexes ($Al_2O_3 - MnO - MgO - TiO_2 - SiO_2 - CaO$). Ces inclusions sont susceptibles d'être transférées dans les pièces fabriquées étant donné que la température de fusion des oxydes peut ne pas être atteinte lors de la fusion du métal et peuvent altérer leurs propriétés.

Des caractérisations microstructurales ont été réalisées afin d'analyser les grains, les dendrites de solidification et les défauts cristallins (dislocations). L'imagerie au microscope électronique à balayage (MEB) a été effectuée à l'aide des détecteurs d'électrons secondaires et d'électrons rétrodiffusés. La composition chimique locale a été évaluée au MEB par spectroscopie de rayons X à dispersion d'énergie (EDS), tandis que l'orientation cristallographique des grains a été déterminée par la méthode de diffraction d'électrons rétrodiffusés (EBSD).

Les échantillons ont été préparés selon un protocole de polissage standard. Une attaque chimique à l'eau régale a permis de révéler la morphologie des bains de fusion, tandis qu'une attaque électrolytique a été utilisée pour observer la ferrite et les dendrites. Un polissage fin à l'OPS a été réalisé pour les analyses EBSD. L'espacement interdendritique a été mesuré au microscope optique et a permis d'estimer la vitesse de refroidissement dans différentes régions des pièces à l'aide d'équations empiriques issues de la littérature (Equations 2.2 et 2.3). Une méthodologie pour le traitement des analyses EBSD a été définie, fixant un seuil d'angle pour les joints de grains à 5° et évaluant la densité de sous-joints (2–5°), la présence de macles et la désorientation intragranulaire (GOS).

Les défauts cristallins (dislocations) ont été observés par microscopie électronique en transmission (MET). Le MET a également été utilisé pour déterminer la composition chimique locale des phases austénitiques et ferritiques par analyse EDS.

Des traitements thermiques ont été appliqués sur des échantillons issus des murs fabriqués par WAAM et WLAM à 1100 et 1200 °C pendant 30 minutes, suivis d'une trempe à l'eau. Le temps de montée en température n'a pas été inclus dans la durée du traitement.

Enfin, les propriétés mécaniques des pièces ont été établies grâce à des essais de traction à vitesse de déformation constante (10^{-3} s^{-1}) réalisés sur des éprouvettes plates (Figure 2.10), prélevées selon différentes orientations dans les murs fabriqués. Ces essais ont permis d'évaluer la limite d'élasticité, la contrainte maximale et l'allongement à la rupture des pièces. Des mesures de microdureté et de dureté Vickers ont également été effectuées, en appliquant respectivement des charges de 0,1 kgf et 10 kgf.

2.1 WAAM and WLAM manufacturing

2.1.1 Experimental setups

Components with simplified geometries, including single beads, single-bead walls and thick multilayer tiles, were manufactured using WAAM and WLAM platforms of CEA/LTA.

The WLAM platform (Figure 2.1a) operates with a remote control system and incorporates a fiber laser with a maximum power of 4 kW and a wavelength of 1065 nm (YPG-4000). The setup consists of a 6-axis robot (D) equipped with a wire-laser deposition head (E) and a wire feeder (C), manufacturing components on a static testing table (F). During the manufacturing, a movable venting system (A) is positioned near the components to evacuate welding fumes. At the deposition head (Figure 2.2b), the laser beam is divided into three points and refocused at the tip of the head, allowing the wire to be fed coaxially. Finally, pure argon is delivered near the melt pool at a flow rate of 15 L/min to minimize oxygen contamination through a nozzle positioned just above the wire.

Similarly, the WAAM platform (Figure 2.1b) operates with a remote control system and features a 6-axis robot (G). This platform supports GMAW (B), GTAW (D) and plasma (E) processes, though only the GTAW equipment was employed for this work. As with the WLAM platform, a movable venting system (A) was used to evacuate welding fumes. The WAAM platform is also equipped with two wire feeders (C), enabling the fabrication of components with chemical composition gradients when using wires made from different materials. However, only one feeder was employed in this study to feed the 316L wire under the electrical arc. Unlike the WLAM platform, the WAAM platform includes a 2-axis table, allowing for the manufacturing of components with complex geometries. When applying an alternating deposition strategy, the table was rotated rather than the deposition head (G), ensuring consistent deposition direction and facilitating the observation. A close-up of the WAAM-GTAW deposition head is shown in Figure 2.2b. The head employs a non-consumable tungsten electrode with a diameter of 3.2 mm and a tip diameter of 0.8 mm. The wire is fed laterally under the electrode at a 65° angle opposite the deposition direction. Finally, pure argon is blown near the deposition area at a flow rate of 30 L/min to create an inert atmosphere around the melt pool, double that used in the WLAM process.

Initially, the WAAM platform was unavailable to manufacture the first components. Consequently, several components were produced using a semi-manual GTAW welding device, shown in Figure 2.3. This system mainly operates similarly to the WAAM platform, although with some differences. In the semi-manual setup, the deposition head is mounted on a 2-axis traveling ramp (H) and the components are produced on a static testing table (B). This configuration permits only up-down and front-forward movements, significantly limiting the range of geometries that can be achieved. We ensured that the GTAW welding device and the WAAM platform were equivalent by manufacturing similar components with both devices.

(a)

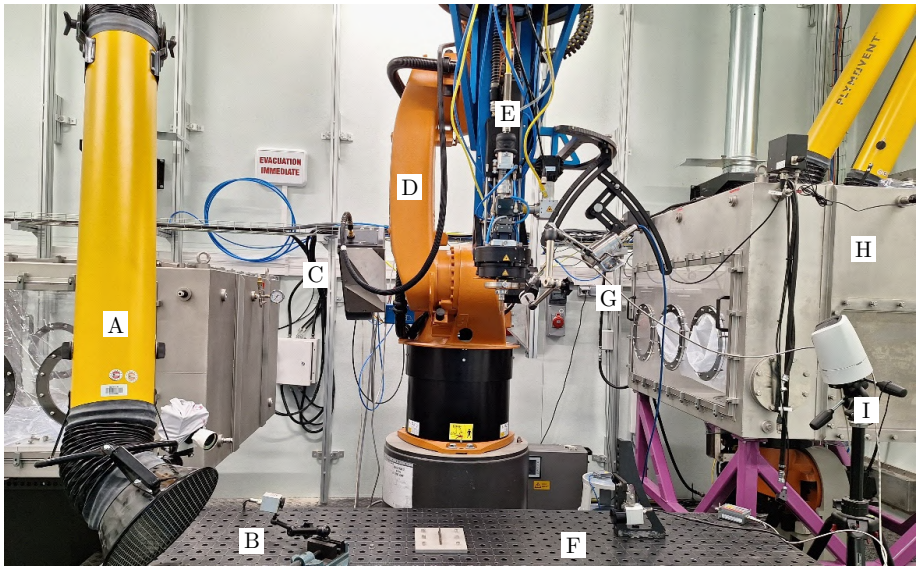

A: venting system
B: thermal camera
C: wire feeder
D: 6-axis robot
E: deposition head
F: static testing table
G: thermal pyrometer
H: inerting chamber
I: viewing camera

(b)

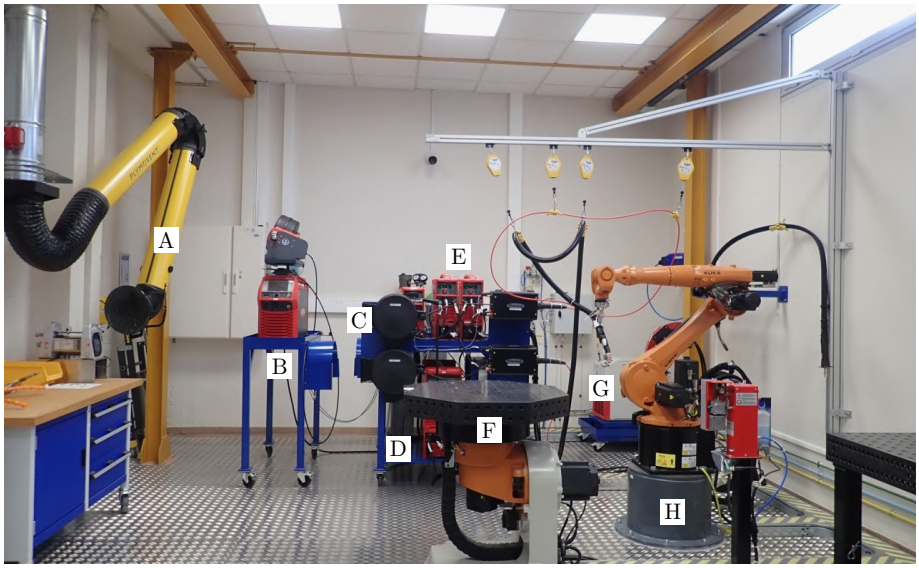

A: venting system
B: WAAM-GMAW monitor
C: wire feeders
D: WAAM-GTAW monitor
E: WAAM-plasma monitor
F: 2-axis testing table
G: deposition head
H: 6-axis robot

Figure 2.1. Platforms of CEA/LTA used in this work for sample processing: (a) WLAM and (b) WAAM.

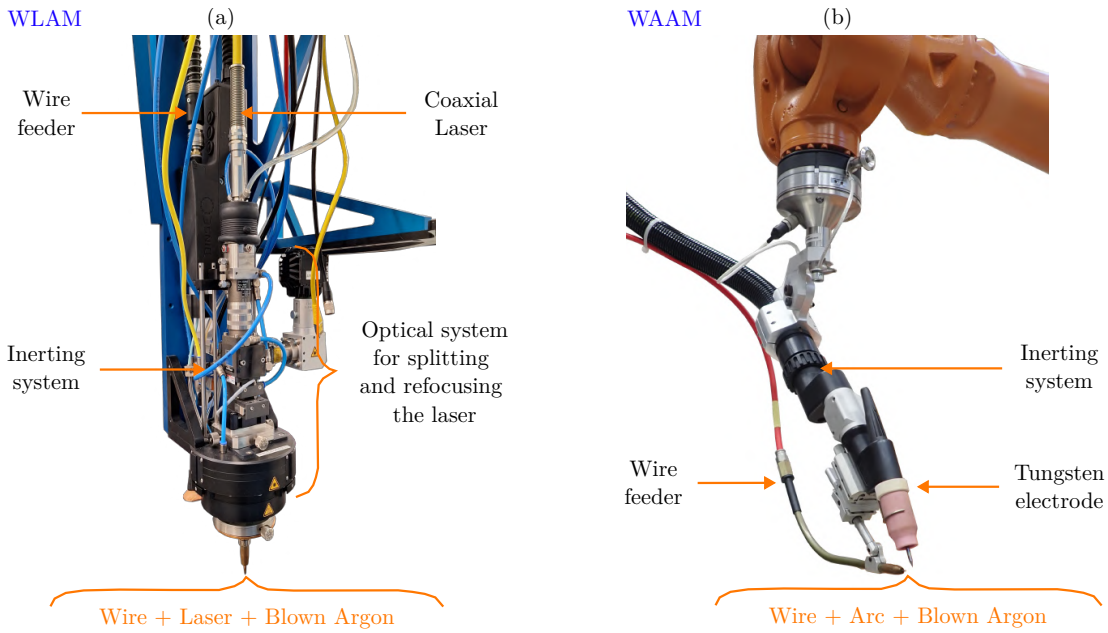

Figure 2.2. (a) WLAM and (b) TIG-WAAM deposition heads, used in this work as an alternative to the WAAM platform, unavailable at the beginning of the project.

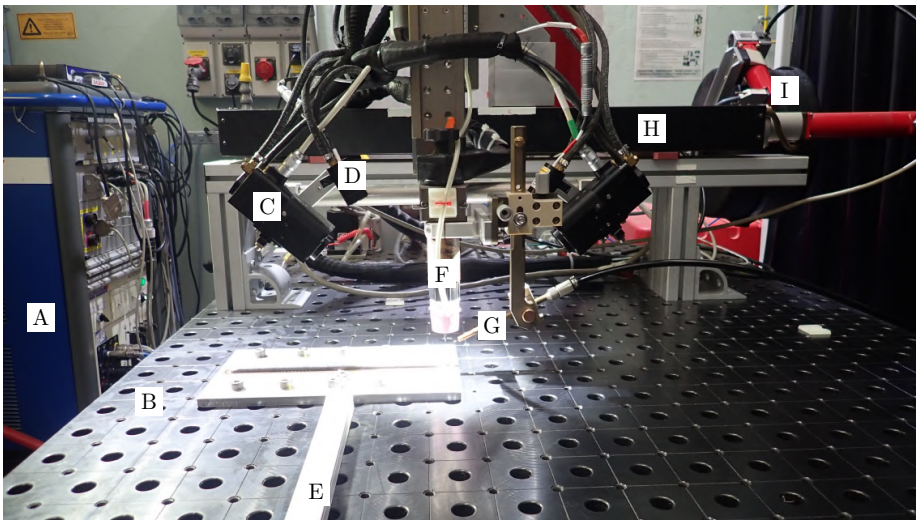

A: GTAW monitor
B: static testing table
C: welding camera
D: white light lamp
E: thermocouples
F: tungsten electrode and inerting nozzle
G: wire
H: 2-axis travelling ramp
I: wire feeder

Figure 2.3. GTAW semi-manual welding device used in this work.

The three devices were equipped with visual and thermal monitoring systems. Viewing cameras ((I) in Figure 2.1a and (C) in Figure 2.3) were set up. Adequate lighting was provided using a white light lamp ((D) in Figure 2.3). This optical equipment ensures the correct introduction of the wire into the melt pool (Figures 2.4a and b for the WAAM and WLAM processes, respectively). At the beginning of this work, video visualization for the WLAM process was unavailable. This capability was later implemented by H. Rosso [165], with Figure 2.4b being a part of his work. Several thermal devices were also set up, such as thermal cameras placed on the testing table ((B) in Figure 2.1a), pyrometers attached to the deposition head ((G) in Figure 2.1a), or K-type thermocouples placed at the surface of the substrate near the deposition ((E) in Figure 2.3).

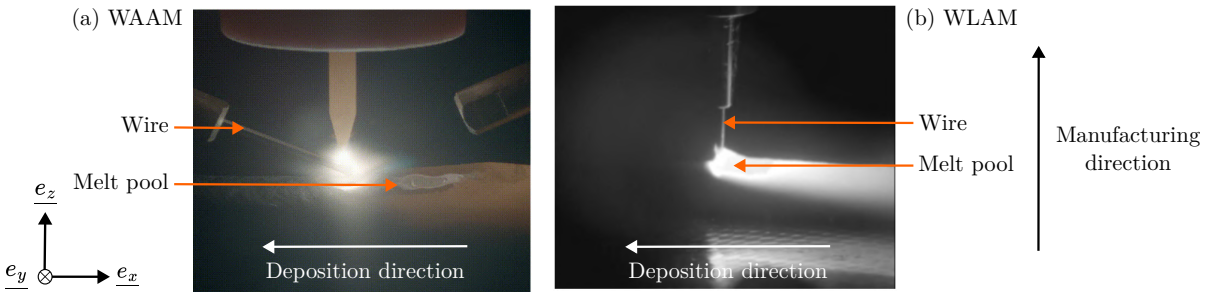

Figure 2.4. Visualisation of the melt pool in (a) GTAW-WAAM and (b) WLAM processes [165].

2.1.2 Temperature measurements

K-type thermocouples and infrared cameras were used to measure the temperature at different locations during the manufacturing of walls using WAAM and WLAM. Thermocouples were positioned on the substrate surface at 2, 4 and 6 mm from the first bead edge, near the middle of the deposition path, as presented in Figure 2.5. Temperature was recorded every 0.1 s during the manufacturing and the interlayer cooling. Temperature of the part was monitored using Optris PI160 infrared camera for WAAM and PI08M for WLAM. The PI160 camera detects infrared radiation in the 8-14 µm range with an optical resolution of 160 × 120 pixels. Conversely, the PI08M camera operates in a narrower band between 780 and 800 nm, which is suitable for laser applications due to its exclusion of the laser wavelength. It provides a higher optical resolution of 382 × 288 pixels, making it appropriate for the smaller dimensions of WLAM-deposited beads. The temperature measurement ranges were from 200 to 1500 °C for the PI160 (WAAM) and from 575 to 1900 °C for the PI08M (WLAM).

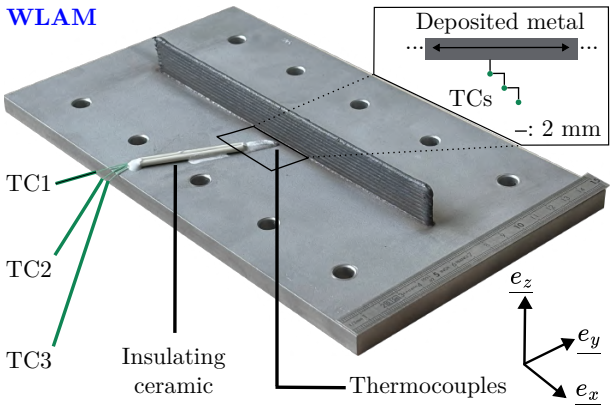

Figure 2.5. WLAM specimen and three K-type thermocouples (TCs: TC1, TC2 and TC3) placed on the substrate at respectively 2 mm, 4 mm and 6 mm from the deposition area. $\underline{e_x}$ denotes the deposition direction, $\underline{e_z}$ the manufacturing direction and $\underline{e_y}$ the transverse direction.

The emissivity for 316L steel (used by infrared cameras to estimate the temperature, Equation 2.1) was not initially known as it varies with temperature, used wavelength range, emission direction, and surface state including oxidation.

For the calibration of the emissivity, the first measurements were conducted considering an arbitrary value of $\epsilon_{0.5} = 0.5$. Our calibration method assumes that emissivity is lower for liquid than for solid metal, as reported by Terrazas-Najera *et al.* [166]. Thus, assuming constant emissivity leads to underestimating the melted pool temperature. In our study, the measured temperature profiles along the deposition direction in WAAM and WLAM showed an initial rise, a maximum (assumed to represent the fusion

isotherm), followed by a decrease under the electrical arc, corresponding to the liquid metal zone with lower emissivity. The emissivity was recalibrated using Equation 2.1 to reach a maximum temperature of 1450 °C, corresponding to the liquidus temperature of 316L steel, before the observed decrease due to the liquid metal. Pichler *et al.* [167] used a similar calibration approach, although they did not report considered emissivity values. We finally obtained emissivities of 0.3 and 0.4 for the WAAM and WLAM processes, respectively.

$$I = \epsilon \cdot \sigma_B \cdot {T_{fus}}^4 = \epsilon_{0.5} \cdot \sigma_B \cdot T_{fus}(\epsilon_{0.5})^4 \Leftrightarrow \epsilon = \epsilon_{0.5} \cdot \left(\frac{T_{fus}(\epsilon_{0.5})}{T_{fus}} \right)^4 \tag{2.1}$$

Balat-Pichelin *et al.* [168] measured the spectral emissivity of 316L stainless steel at various incidence angles. The emissivity of 316L stainless steel at an incidence angle of 0° is a good approximation of the emissivity of the material, according to Barnett *et al.* [169], and corresponds to our acquisition setup, as the cameras are far from the manufactured components, limiting the viewing angle. At 0° incidence, their emissivity values range from 0.35 at a 1 µm wavelength to 0.15 in the 8-14 µm range. The value of 0.35 is close to the values identified in this work. However, the value of 0.15 is slightly lower. This difference may be due to oxidation during WAAM and WLAM manufacturing, which increases emissivity at all wavelengths. Kraus [170] measured a total emissivity of 0.4 for a 316L melt pool obtained by TIG-welding, similar to our PI08M measurements but at higher temperature ranges. Finally, Fu *et al.* [171] reported that total emissivity for steel samples with comparable roughness to those in WAAM and WLAM processes increases with temperature, from 0.25 at 277 °C to 0.36 at 827 °C. This last value is close to the one we obtained for the PI08M camera. The emissivity for low-temperature ranges is slightly underestimated because we kept the emissivity value constant and calibrated it only at a high temperature, around the fusion isotherm.

Our approach to calibrate the emissivity was considered satisfactory for measuring the thermal field at the scale of the manufactured component. If the actual emissivity were 0.5 instead of 0.4, a measured temperature of 1000 °C with the 0.4 emissivity would be overestimated by 54 °C. Conversely, if the actual emissivity were 0.3 instead of 0.4, a measured temperature of 1000 °C would be underestimated by 75 °C. At 100 °C, the overestimation would be 5 °C if the emissivity were 0.5 instead of 0.4. These differences are acceptable for a correct temperature estimation for our applications while manufacturing components with WAAM and WLAM processes.

2.2 Initial 316L wire

2.2.1 Chemical composition

A 316L stainless steel wire with a diameter of 1.2 mm, provided by Voestalpine Böhler Welding, was utilized for the WAAM and WLAM processes. The chemical composition of the wire, measured by ICP-AES and elementary analysis, is in agreement with typical values for 316L stainless steel and agrees with the EN 10088-1 standard [172] (Table 2.1). While the nickel content is within the limits of the standard, the measured chromium content slightly exceeds the upper bound, which was intentionally made to promote ferrite formation in the manufacturing component. Significant amounts of Manganese and Molybdenum (>1 wt.%) were also detected, closely matching reference values. The Carbon content is minimized (<0.030 wt.%) to prevent carbide precipitation, such as $Cr_{23}C_6$, which can damage mechanical properties and reduce passivation potential [96]. The Oxygen content, which could impact mechanical properties through oxide formation [173], was below the ICP-AES detection limit (<0.005 wt.%). Sulfur was detected above the reference limits for 316L stainless steel, potentially causing sulfide precipitation in the austenite matrix [173]. Other elements, including Nitrogen, Silicon, Copper, and Phosphorus, were present in trace amounts.

Table 2.1. Chemical composition (wt. %) of the AISI 316L filler wire. (a) Reference chemical composition for AISI 316L stainless steel in agreement with EN 10088-1 standard [172]. (b) Chemical analysis made by ICP-AES and elementary analysis (C, N and O). (c) Voestalpine Böhler Welding data for the "3Dprint AM 316L" wire.

wt.%	Cr	Ni	Mo	Mn	C	N	Si	Cu	Co	P	S	Al	O
(a) EN 10088-1	16.5-18.5	10.0-13.0	2.00-2.50	2.00	0.030	0.10	1.00	-	-	0.045	0.015	-	-
(b) ICP-AES	19.20	12.66	2.88	1.78	0.016	0.045	0.46	0.042	0.031	0.013	0.007	0.005	-
(c) Manufacturer	18.5	12.3	2.6	1.7	0.02	-	0.5	-	-	-	-	-	-

2.2.2 Inclusions

Several inclusions in the austenite matrix were identified and characterized using Scanning Electron Microscopy (SEM), Wavelength Dispersive Spectroscopy (WDS) with Electron Probe Micro Analysis (EPMA), and Energy Dispersive Spectroscopy (EDS) in SEM. These inclusions are shown in the micrographs obtained at various scales in Figures 2.6a and b. Two distinct families of inclusions were identified. Family A corresponds to elongated inclusions aligned with the wire axis, with widths less than 1 µm. They are frequently observed as bands of multiple similar inclusions (Figure 2.6a). Family B corresponds to spherical inclusions and varies in size, with radii typically larger than 1 µm. While they are often isolated in the austenite matrix, observations at a larger scale (Figure 2.6a) showed that these inclusions can also appear in bands aligned with the wire axis due to the wire extrusion process.

Chemical compositions of several inclusions from Families A and B were determined using WDS analysis (Table 2.2). The analyses were conducted using the Cameca SX-100 EPMA, with a tension of 15 kV and an intensity of 133 nA. Inclusions of family A corresponded probably to copper/manganese sulfides. In contrast, inclusions of family B should be complex oxides like $Al_2O_3 - MnO - MgO - TiO_2 - SiO_2 - CaO$, which may result from the introduction of liquid or powder slags during the processing to reduce the oxygen content [174, 175].

According to WDS maps, the core inclusion from Family B primarily consists of aluminum, magnesium, manganese and oxygen, while titanium, silicon, and calcium are mainly located at the borders in smaller amounts (Figure 2.7). Similar inclusions were observed by Park and Todokori [174], and are referred to as

"aluminosilicate droplets whose primary phase is $[MgO - Al_2O_3]$ spinels". It suggests that these inclusions are predominantly $Al_2O_3 - MnO - MgO$ oxides. These oxide inclusions represent a potential risk to the properties of the material, as the melting point of these oxides is not reached during the WAAM and WLAM processes [176], making them likely to be transferred to the final components.

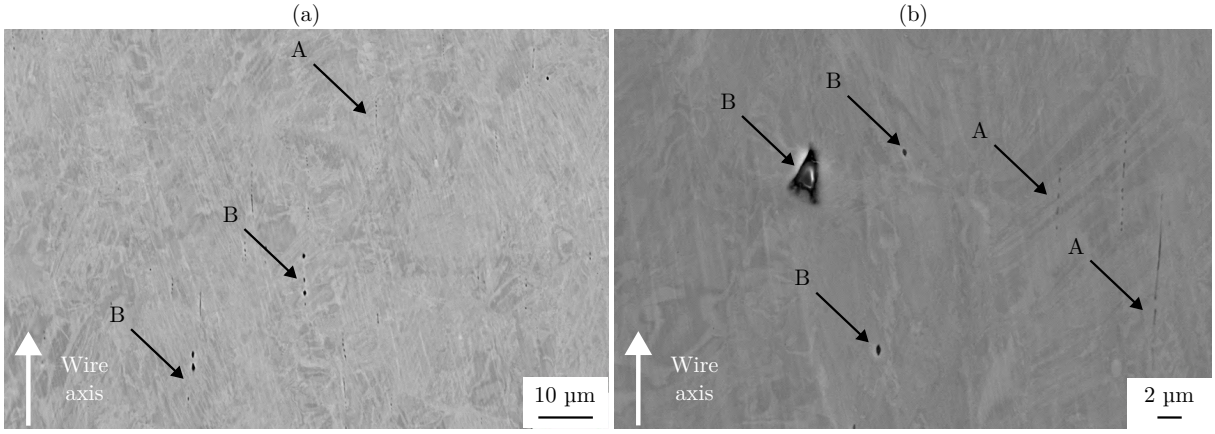

Figure 2.6. SEM micrographs obtained with secondary electron detector showing different inclusions within the austenite matrix: (a) low and (b) large magnifications. A: manganese sulfide (MnS) inclusions and B: oxide inclusions.

Table 2.2. Chemical compositions (at.%) obtained with EPMA of inclusions from families A and B compared to the chemical composition of the austenite γ-matrix.

Family A	S	Mn	Cu
γ-matrix	0.1	1.9	0.1
Inclusions	9.8	12.0	0.4
	7.8	10.0	2.6
	7.1	9.0	2.3

Family B	O	Mg	Al	Si	Ca	Ti	Mn
γ-matrix	0.7	-	-	0.9	-	-	1.9
Inclusions	33.2	0.4	14.3	2.5	3.4	0.6	3.4
	26.4	0.5	11.0	1.8	1.4	0.3	5.9
	54.7	2.9	25.8	0.3	-	0.3	10.8

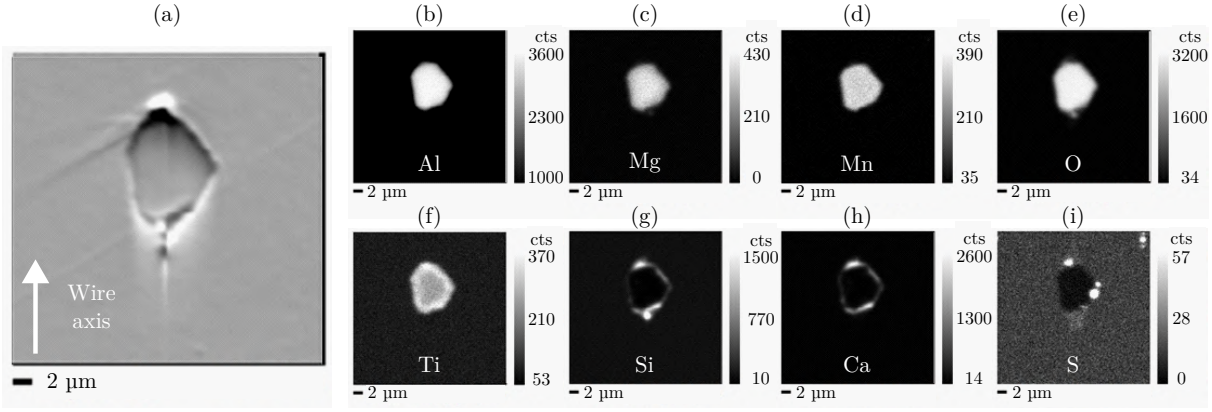

Figure 2.7. Chemical element map obtained with EPMA in a region with oxide inclusion. (a) SEM image of the oxide obtained with the secondary electron detector. Relative spatial distribution of (b) aluminum, (c) magnesium, (d) manganese, (e) oxygen, (f) titanium, (g) silicon, (h) calcium, and (i) sulfur in the analyzed inclusion.

2.3 Microstructure characterization

Multiscale microstructure characterization was required to get information at dendrite and grain scales as well as at the scale of crystal defects like dislocations.

2.3.1 Sample preparation

Several cross-sections of the WAAM and WLAM components were prepared in the transverse plane $(\underline{e_y}, \underline{e_z})$ and the longitudinal plane $(\underline{e_x}, \underline{e_z})$. Surfaces were mechanically polished using SiC papers with progressively finer grit sizes, starting from #P120 and ending at #P1200, followed by diamond solutions with particle sizes of 6, 3 and 1 µm for final polishing. Different finishing or etching procedures were applied depending on the intended characterization, except for hardness measurements, tensile tests, and porosity analysis, where the samples were left in the polished state. The following specific procedures were employed:

- chemical etching: Aqua Regia (a solution of 2 parts nitric acid and 1 part hydrochloric acid by volume) was used to reveal the shape of passes during optical micrograph;
- electrolytic etching: a 10 vol.% solution of oxalic acid diluted in water was used for 30 s at 7 V to observe the morphology of the ferrite in the components;
- fine polishing: an Oxide Polishing Suspension (OPS) solution was applied for 15 minutes to achieve a high-quality surface finish for SEM characterizations, particularly for EBSD analysis.

2.3.2 Optical microscopy

The manufactured specimens were visually characterized using two optical microscopes: the Evident Olympus BX-53 was used for dendrite analysis at the microstructural scale, and the Keyence VHX-X1 was used for observations at the scale of the deposited beads.

Primary Dendrite Arm Spacing (PDAS) and Secondary Dendrite Arm Spacing (SDAS) were measured on various transverse and longitudinal cuts of components manufactured using WAAM and WLAM processes. The measurements were performed using the intercept method, which involves drawing ten lines across at least three dendrites, calculating the spacing between dendrite arms along each line, and computing the weighted average of all measurements to determine the final PDAS or SDAS value. These PDAS and SDAS measurements were further used to estimate the cooling rate, $\dot{T}$, of different regions of the components during solidification. The estimation was based on empirical relationships established by Katayama and Matsunawa (Equations 2.2 and 2.3) [122] for 304L stainless steel processed by laser welding. This relationship was extrapolated to approximate cooling rates for 316L stainless steel manufactured using the WAAM and WLAM processes.

$$\text{PDAS} = 80 \cdot \dot{T}^{-0.33} \tag{2.2}$$

$$\text{SDAS} = 25 \cdot \dot{T}^{-0.28} \tag{2.3}$$

2.3.3 Scanning Electron Microscope (SEM)

The SEM characterizations of the specimens were conducted using a Zeiss Sigma 500 microscope equipped with secondary electron (SE), backscattered electron (BSE) detectors and energy dispersive spectroscopy (EDS), and electron backscatter diffraction (EBSD). SE and BSE analyses were performed at working distances ranging from 8 to 12 mm, magnifications between ×20 and ×20,000, voltages of 10 to 20 kV, and a diaphragm size of 60 µm.

For EDS, an accelerating voltage of 20 kV and a working distance of 8 mm were employed, with a diaphragm size of 120 µm to match the calibration library of chemical elements integrated into the system. Qualitative EDS analyses involved point measurements and mapping at a 1 µm pixel size with a counting time of 30 minutes. Moreover, quantitative mapping was carried out using a specific library for 316L stainless steel at a 1 µm pixel size with a counting time of 2 hours. The acquired EDS data were analyzed using Bruker Esprit software.

2.3.4 Electron Back-Scattered Diffraction (EBSD)

EBSD was performed for crystal orientation analysis with a voltage of 20 kV, a working distance of 20 to 30 mm, and pixel sizes varying from 50 nm for detailed dendrite observations to 5 µm for macroscopic-scale analyses (Figure 2.8a). The Kikuchi bands recorded by the EBSD camera (Figure 2.8b) were numerically corrected to enhance their detection (Figure 2.8c). Moreover, for macroscopic observations, EBSD maps covering areas of up to 15 cm^2 were obtained by stitching smaller maps using mosaic imaging. These smaller maps were captured at ×100 magnification with a 10% overlap, and in the most extensive cases, up to 700 maps were combined using the Esprit software for a total acquisition time of up to 48 hours.

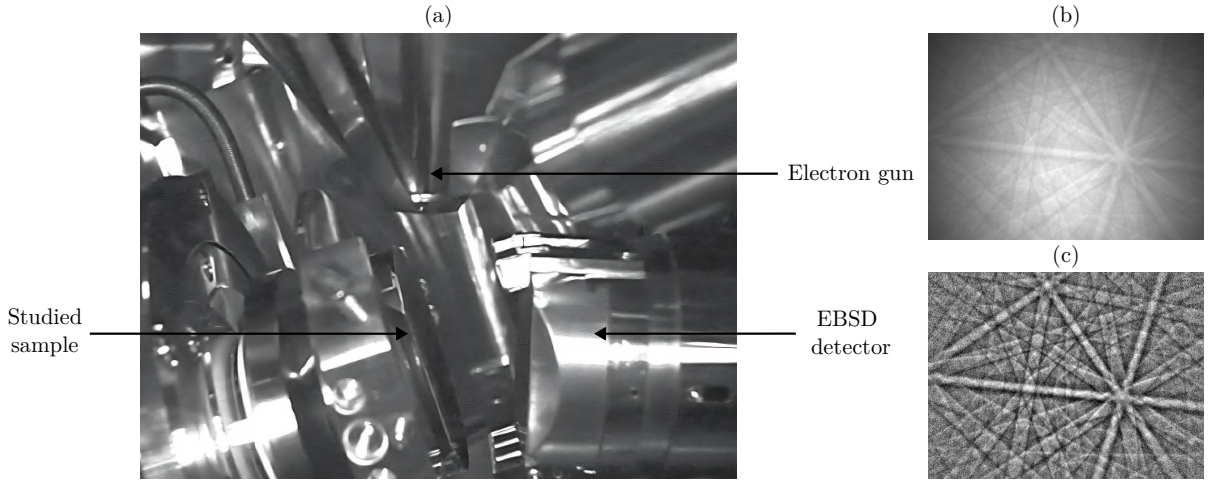

Figure 2.8. (a) Visualisation of the SEM chamber in its configuration for EBSD analysis. (b) Kikuchi bands as seen by the EBSD detector. (c) Kikuchi bands after numerical correction.

Next, EBSD data were analyzed using the MTEX toolbox developed in MATLAB. A single MATLAB script was implemented and applied uniformly across all EBSD analyses to ensure consistency. The analysis procedure included the following steps:

- Both FCC and BCC crystal structures, corresponding to austenite and ferrite phases, were selected.
- Orientation maps were plotted without orientation corrections along the deposition direction $\underline{e_x}$ and the manufacturing direction $\underline{e_z}$.
- The associated inverse pole figures for the $\underline{e_x}$ and $\underline{e_z}$ directions were plotted using identical scales to highlight textures in the crystal orientations.
- Noise was removed by excluding crystal orientation clusters smaller than 10 pixels.
- A grain misorientation threshold of 5° was applied, determined after evaluating thresholds of 5°, 10°, and 15° (Figure 2.9). In the literature review, we mentioned that one grain in WAAM and WLAM is defined as a group of dendrites with similar growth orientations due to the solidification process. We found that orientation thresholds of 10° and 15° produced single grains with strong orientation variations in the deposition direction $\underline{e_x}$ (Figures 2.9f, g), which were interpreted as a grouping of multiple grains instead of one grain. Oppositely, the 5° threshold creates grains comporting a group of dendrites with close orientation in both the deposition $\underline{e_x}$ and manufacturing $\underline{e_z}$ directions (Figures 2.9e, h).
- Twin boundaries were identified using a misorientation angle of 60° and a rotation along $\langle 111 \rangle$.
- Low-Angle Grain Boundaries (LAGBs) were defined as a misorientation threshold between 2° and 5°. The 2° value was chosen as it was the smallest value corresponding to forming consistent sub-grain boundary lines within the grains.
- The grain size was determined using the intercept method in the transverse $\underline{e_y}$ and deposition $\underline{e_x}$ directions. Due to the significant elongation of grains along the manufacturing direction $\underline{e_z}$, grain size was not measured in this orientation.
- The relative surface area occupied by grains was analyzed as a function of their aspect ratio, calculated as the ratio of the semi-major to the semi-minor axes of the equivalent ellipse of each grain.
- Grain Orientation Spread (GOS) was computed, corresponding to the average orientation deviation within each grain. Results were categorized into intervals defined as 0-1°, 1-2°, 2-5°, 5-15°, and $> 15°$.

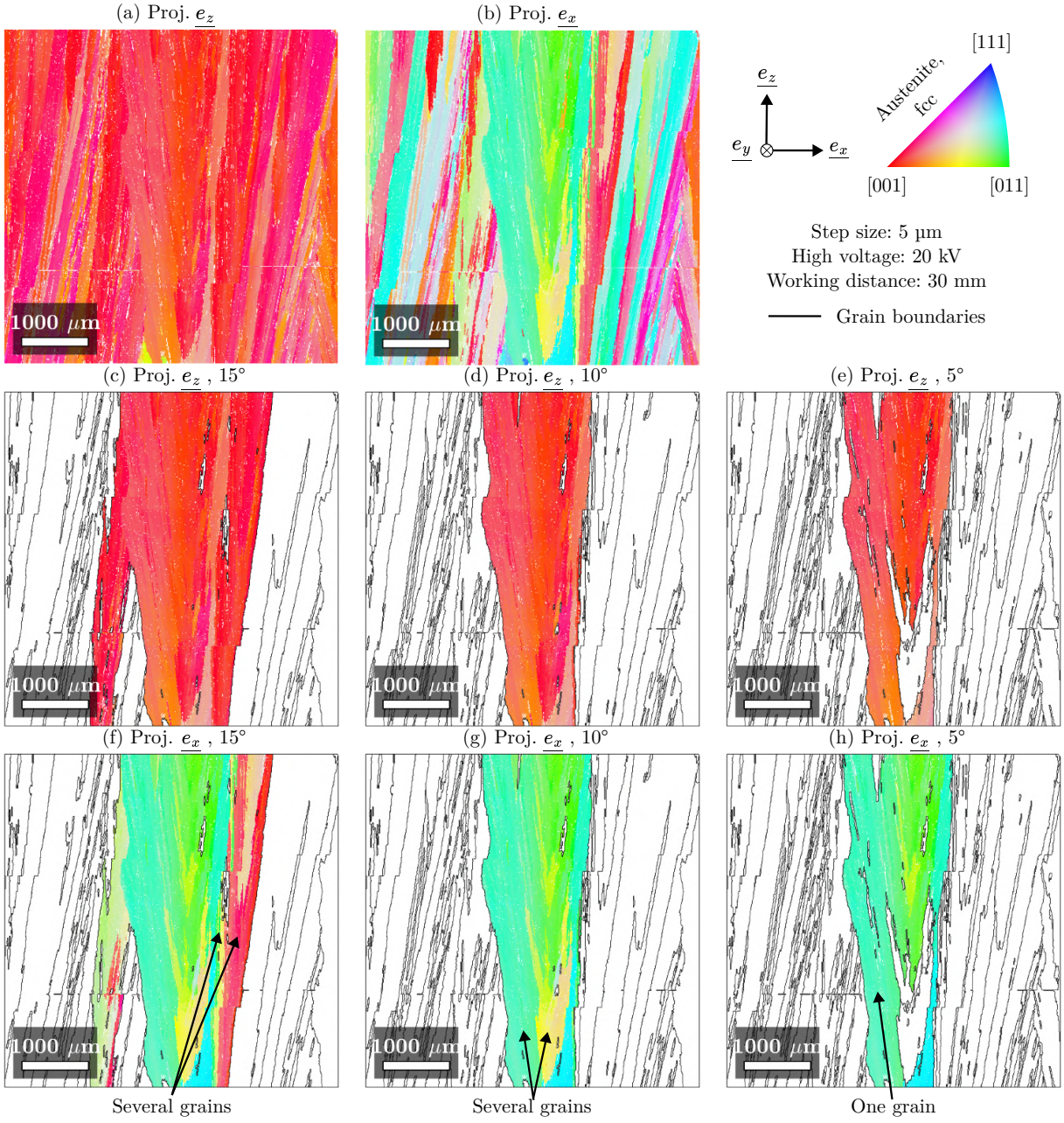

Figure 2.9. EBSD analysis of the longitudinal cut of a single-bead wall manufactured using WLAM: (a–b) orientation maps projected along the manufacturing $\underline{e_z}$ and deposition $\underline{e_x}$ directions, respectively; (c–e) grain boundary maps with 15, 10 and 5° misorientation criteria, with crystal orientations in the tallest grain projected along $\underline{e_z}$; (f–h) grain boundary maps with 15, 10 and 5° misorientation criteria, with crystal orientations in the tallest grain projected along $\underline{e_x}$.

2.3.5 Transmission Electron Microscopy (TEM)

Crystal defects (dislocations) were observed in as-manufactured state using TEM. The Tecnai F20-ST TEM was used with a tension of 200 kV. Thin sections were produced from 200 µm-thick disks extracted in the transverse direction $\underline{e_y}$ at the tenth layer of single-bead walls. The sections were polished mechanically and chemically thinned until a hole was observed in the center of the section. The area near the hole is only a few dozens nanometers thick and corresponds to the characterized area. Qualitatively viewing dislocations was achieved by observing close to the $\langle 001 \rangle$ zone axis of the austenite and ferrite phases. Moreover, EDS analysis was also achieved to estimate the local chemical composition of the ferrite and the austenite. The Brucker XFlash 6T/60 detector was used, with a counting time of 45 s per point. The data was analyzed using Esprit 2.2 software, and the chemical composition was estimated using the Cliff-Lorimer method with theoretical k-factors

2.3.6 Ferritoscope

The volume fraction of ferrite in the single-bead walls manufactured with WAAM and WLAM was analyzed using the Fischer FMP30 ferritescope after calibration on testing samples with a known ferrite content. Ten measurements per component were carried out to ensure the significance of the tests.

2.4 Heat treatments

To analyze the effect of temperature on the microstructure, heat treatments were performed using the Carbolite TZF 1500 furnace, which can reach a maximum temperature of 1400 °C. This study employed two treatment temperatures: 1100 and 1200 °C, each with a 30-minute holding time. Small sections of 20-layer single-bead walls manufactured using the WAAM and WLAM processes were characterized. The dimensions of the achieved sections were approximately $40 \times 10 \times 10$ mm^3 for WAAM and $20 \times 10 \times 3$ mm^3 for WLAM.

The components were placed into the preheated furnace, and the temperature rise was monitored using a K-type thermocouple positioned on the component. The 30-minute holding time began once the component reached the target temperature of 1100 or 1200 °C. During the holding, temperature stability was maintained within a tolerance of ±10 °C. At the end of the heat treatment, the components were rapidly cooled by quenching in a large volume of water.

2.5 Mechanical characterization

Mechanical characterizations were performed to assess the properties of the materials (yield stress, ultimate strength, elongation, hardness) induced by the microstructure, compared to materials elaborated with conventional processes.

2.5.1 Tensile testing

Tensile tests were conducted to evaluate the stress-strain behavior and the mechanical properties (yield stress, tensile strength and ultimate strain) of single-bead walls manufactured using the WAAM and WLAM processes.

Flat tensile specimens were designed based on the dimensional constraints of the manufactured single-bead walls. The walls were 40 mm high, while the width of the wall manufactured by WLAM was approximately 3 mm, with variations due to surface finish. Dogbone-shaped tensile specimens measuring $10 \times 40 \times 2$ mm^3 were machined, with an effective area being $10 \times 4 \times 2$ mm^3, as shown in Figure 2.10a. For each wall, three specimens were extracted along the manufacturing direction $\underline{e_z}$ from the bottom to the top of the wall, and three others were extracted along the deposition direction $\underline{e_x}$ from the middle of the wall in the $\underline{e_z}$-direction, as illustrated in Figure 2.10b. Additionally, each specimen was extracted from the center along the transverse direction $\underline{e_y}$. Specimens along the manufacturing direction are designated as H1 for WAAM and H2 for WLAM, while those along the longitudinal direction are labeled L1 for WAAM and L2 for WLAM.

Tensile tests were conducted at a constant strain rate of 10^{-3} s^{-1} on an Instron 5982 testing machine with a force capacity of up to 100 kN, coupled with an optical camera for retroactive control of the strain rate, as shown in Figure 2.11a. A white light is placed on top of the camera to avoid shadows and reflections on the surface being recorded. The elongation of the specimen was followed by image correlation using the VIC-2D software by controlling the displacement of sprayed black speckles on a painted white background at their surface (Figure 2.11b).

The ultimate engineering strain (US) was determined by measuring the length of the gauge area at the initial state (Figure 2.11b) and maximal elongation before failure (Figure 2.11c).

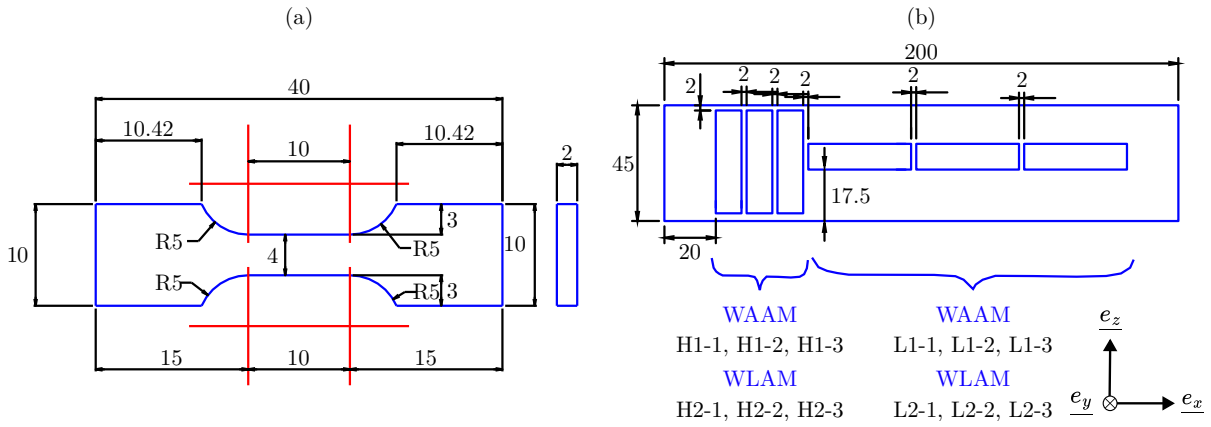

Figure 2.10. Samples for tensile tests on single-bead walls: (a) geometry of the tensile specimens, (b) schematization of extraction of the tensile specimens from single-bead walls manufactured by WAAM and WLAM.

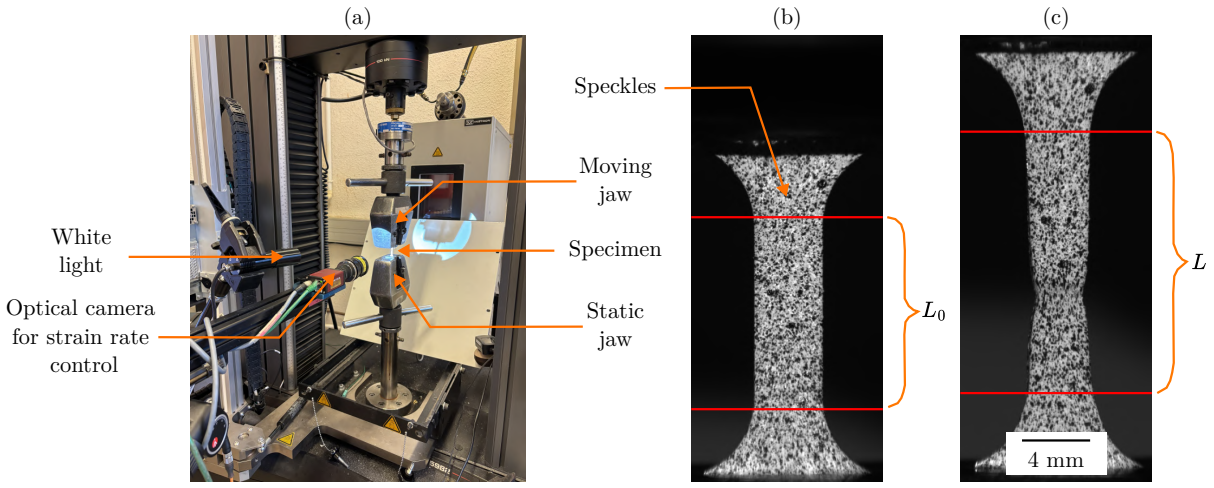

Figure 2.11. Tensile test on the sample for the single-bead wall: (a) experimental setup; (b) tensile specimen before the test; (c) tensile specimen at maximal elongation, just before failure.

The ultimate strain was then corrected using Equation 2.4, where L denotes the length of the gauge area before failure and L_0 its length at the initial state. The nominal strain ε_n was then recomputed adequately to agree with the measured ultimate strain. Next, the conventional yield stress σ_y was determined by considering the nominal stress associated with a strain of 0.2%. Finally, the tensile strength was determined by measuring the maximal nominal stress recorded during the test.

$$US = \frac{L - L_0}{L_0} \tag{2.4}$$

2.5.2 Hardness and micro-hardness measurements

Hardness measurements and microhardness profiles were performed using the Innovatest Falcon 500G Vickers hardness tester. A load of 10 kgf was applied for macrohardness measurements. Five measurements were taken on the same transverse cut for each sample to ensure repeatability, except for the single beads manufactured with WLAM. Four measurements were taken across two transverse cuts in this case due to dimensional constraints.

Vickers microhardness profiles were achieved with a 0.1 kgf load at the center of the transverse cuts, regarding the transverse direction $\underline{e_y}$ and oriented in the manufacturing direction $\underline{e_z}$. A step size of 0.2 mm was used, more than 2.5 times the diagonal of the indent, which was approximately 300 µm. Indents were positioned at least 2.5 times the diagonal distance from the edges of the transverse cuts to avoid edge effects. Finally, the microhardness profiles presented in this work were smoothed by calculating the sliding average for each point, using its two immediate neighbors.

Chapter 3

Processing conditions

Contents

Résumé en français du Chapitre 3 : paramètres des procédés

Une pièce complexe est constituée de parties fines, de parties épaisses, ainsi que d'angles et de jonctions. Notre objectif est d'établir des paramètres de fabrication pour les procédés WAAM et WLAM permettant la réalisation de murs monocordons (parties fines) et de blocs (parties épaisses) avec une bonne régularité en largeur et en hauteur. Pour cela, une étude paramétrique a été menée sur des monocordons, des murs de 20 passes et des blocs de 6×20 passes.

Les principaux paramètres influençant la géométrie des cordons aux WAAM et WLAM sont la puissance de la source d'énergie Q_{exp}, les vitesses de dépôt s et d'apport de fil v_w. Ces paramètres sont liés par des termes physiques tels que l'énergie linéique apportée E_l, proportionnelle à Q_{exp}/s, le volume de métal apporté par unité de longueur S, proportionnel à Q_{exp}/v_w, et le taux de dépôt d_{rate} dépendant de v_w. Le rapport entre E_l et S définit la densité volumique d'énergie E_v.

Des monocordons ont été réalisés en WLAM et WAAM en faisant varier ces paramètres. Les cordons irréguliers ou discontinus ont été identifiés, mettant en évidence l'impact de la densité volumique d'énergie sur la continuité des cordons (Figure 3.3). Pour le WAAM, une valeur trop basse entraîne un phénomène de "balling" (dépôt de billes métalliques à la surface du substrat). Pour le WLAM, elle provoque le phénomène de "stubbing", où le fil touche le fond de la zone fondue et ne peut plus être correctement apporté. Enfin pour le WLAM, une valeur trop élevée de E_v engendre le phénomène de "dripping", où le fil fond prématurément et n'atteint pas le bain de fusion. Une plage d'énergie volumique assurant des cordons réguliers avec un angle de mouillage inférieur à 90° a été déterminée (Figure 3.5).

Les cordons réguliers ont été mesurés afin d'étudier l'influence des paramètres sur leur géométrie (Figures 3.8 et 3.9). Une forte interdépendance de ces paramètres sur la géométrie des cordons a été observée. Pour le WAAM, la vitesse de dépôt a peu d'effet sur les rapports largeur/hauteur et de dilution en raison de la faible amplitude opératoire testée. Pour le WLAM, la vitesse de dépôt influe peu sur la dilution du cordon dans le substrat.

Des critères de sélection ont été établis en accord avec la littérature, cherchant à garantir l'absence de porosité tout en maximisant le taux de dépôt et la hauteur des cordons déposés. En pratique, le rapport largeur/hauteur doit être compris entre 2 et 4, et la dilution du cordon dans le substrat entre 10 et 35%. Trois jeux de paramètres par procédé ont été retenus (Tables 3.5 et 3.4). Malgré une géométrie régulière, certains cordons présentent des défauts microstructuraux tels que de la porosité intercouche (Figure A.2 pour les cordons obtenus par WLAM comportant une géométrie avec une faible dilution) et des hétérogénéités de taille de grains (Figure 3.12 pour les cordons obtenus par WLAM en appliquant une vitesse de fil élevée). Cependant, ces défauts sont obtenus pour des plages de paramètres en dehors des valeurs sélectionnées dans cette étude, et ne représentent donc pas un frein à la suite de la sélection.

Les conditions optimales ont ensuite été appliquées à la fabrication de murs monocordons. De nouveaux paramètres ont été calibrés : l'incrément de hauteur, la stratégie de dépôt et le temps de refroidissement interpasse.

L'incrément de hauteur a été ajusté pour le WLAM pour correspondre à la hauteur moyenne d'un cordon (Figure 3.17), tandis que pour le WAAM, il est défini automatiquement par la tension de l'arc.

Deux stratégies de dépôt ont été comparées : unidirectionnelle et bidirectionnelle (Figure 3.18). La stratégie unidirectionnelle entraîne un effondrement macroscopique à une extrémité du mur (à la fin des cordons déposés), lié à l'accumulation de chaleur dans cette zone. En revanche, la stratégie bidirectionnelle assure une meilleure régularité en hauteur et en largeur, due à une meilleure répartition de la chaleur dans la pièce.

Le temps de refroidissement interpasse a également été analysé (Figure 5.12). Un temps de refroidissement insuffisant augmente la largeur des cordons et réduit leur hauteur, causant des irrégularités de largeur et de hauteur dans la pièce finale. Nous avons finalement sélectionné un jeu de paramètres par procédé pour la réalisation de murs monocordons, en cherchant un compromis entre la rugosité de surface et le taux de dépôt. Pour le WAAM, des rugosités inférieures à 1 mm (jugées correctes) ont été mesurées pour toutes les conditions. Le jeu de paramètres sélectionné est celui possédant le plus fort taux de dépôt. Pour le WLAM, la rugosité est directement liée à la forme des cordons déposés. La paramétrie possédant le taux de dépôt intermédiaire a alors été sélectionné (Table 3.6).

Enfin, les paramètres sélectionnés ont été adaptés à la fabrication de blocs multipasses. De nouveaux paramètres ont été calibrés. La stratégie de dépôt alterne le sens de dépôt des cordons dans la direction transverse $\underline{e_y}$ et la direction de dépôt $\underline{e_x}$. L'incrément en largeur a été fixé à 70% de la largeur d'un cordon pour obtenir une surface de couche plane (Figure 3.25). Une augmentation de puissance de 20% a été nécessaire pour compenser le faible mouillage des cordons dans les blocs comparé aux murs. Enfin, une différence de hauteur a été observée entre le centre des couches et les extrémités, causant des problèmes de fabrication. Pour compenser cet effet, des passes additionnelles sont ajoutées afin de rattraper la hauteur des couches aux extrémités.

Des défauts ont toutefois été observés, notamment des porosités dans les blocs WLAM, bien que sans impact sur la microstructure de solidification. Leur élimination n'a pas été abordée dans cette étude.

3.1 Definition of a protocol for selecting process parameters

Based on the bibliographic review, process parameters were chosen according to a specific methodology. It consisted of using more and more complex geometries to understand how the process parameters impact the different component features. A complex component was considered to be composed of three simple regions:

- thin zones, where the component width is that of the bead;
- thick zones, where multiple beads are deposited within the same layer;
- angles or intersections linked to the geometrical features.

The processing of thin and thick walls have been widely studied in the literature. For instance, Dinovitzer *et al.* [70] and Abioye *et al.* [74] Xiong *et al.* [93] and Xu *et al.* [104] and Palmeira Belotti *et al.* [112] and Lee *et al.* [155] investigated the effect of processing parameters on, respectively, single beads, single-bead walls and tiles.

In this study, we first produced (i) simple single beads series along straight lines, followed by (ii) 20-layer single-bead walls and 100 mm-high walls and (iii) 20×6-layer thick tiles with several beads per layer. Optimal parameters for manufacturing were further selected using the characterization of the obtained

components.

(i) Single beads. The bibliographic review indicated that WAAM and WLAM involve numerous process parameters [56]. According to Dass and Moridi [52], the most critical are those that affect the geometry of a deposited single bead: the power of the heat source Q_{exp}, the wire feed speed v_w and the deposition speed s. Single beads were then achieved by varying these parameters.

A compromise between the manufacturing speed and the geometry of the components was looked for: an elevated wetting angle or lack of penetration is susceptible to leading to non-continuous beads or interlayer porosity. Conversely, a too elevated penetration can lead to intralayer porosity due to successive melts or affect the geometry of the component [52].

After the processing, the first selection involved a visual inspection of the single beads. Beads that exhibited discontinuities or irregularities (and corresponding processing conditions) were excluded from further analysis. The remaining beads were cut transversely, polished, chemically etched and observed under an optical microscope. A second visual inspection was conducted to eliminate beads with a wetting angle greater than 90°. Selected beads were subjected to further geometrical characterization. Width (w), height (h) and maximum depth into the substrate (p) were measured, as introduced in Figures 3.1a and b, for WAAM and WLAM, respectively.

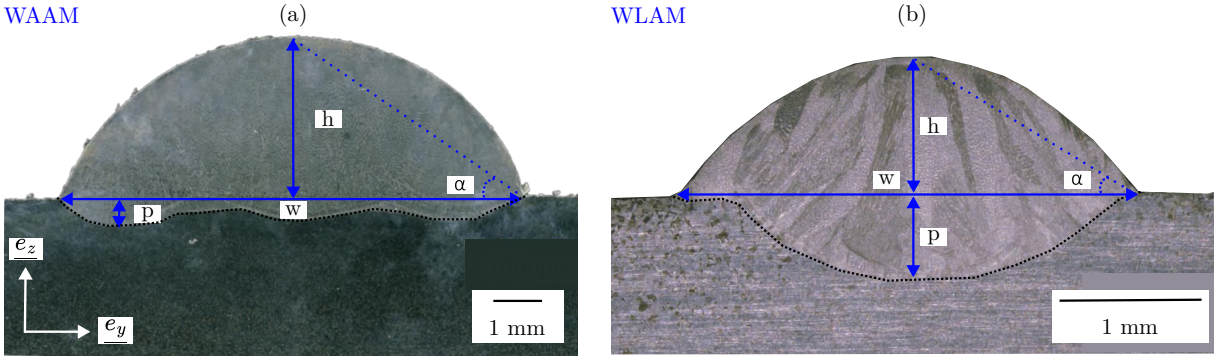

Figure 3.1. Geometrical characteristics of single beads achieved with (a) WAAM and (b) WLAM. "p" denotes the maximal penetration depth, "w" the width of the bead, "h" the maximal height and "α" the dilution angle.

Two selection criteria proposed by Dass and Moridi [52] were applied:

- the first concerns the geometrical ratio between the width and the height. The authors suggested that the angle α defined in Figure 3.1 and calculated according to Equation 3.1 has to be close to 30°. In practice, this is equivalent to having a shape factor, $\frac{w}{h}$, close to 3.5.

$$\alpha = \arctan\left(\frac{2h}{w}\right) \sim 30° \iff \frac{w}{h} \sim 3.5 \tag{3.1}$$

- the second criterion, the optimized dilution ratio, $d_{\text{Dass and Moridi}}$, defined by Equation 3.2, must be between 10% and 35%. In practice, we found that the shape of the remelted zone was very different in WAAM than in WLAM (Figure 3.1). To counter this difference, the average penetration of the bead into the substrate $< p >$ was determined instead of p by dividing the area of the remelted zone (measurement of the melted area under the substrate on transverse cross-sections) of the substrate by the width of the bead w. Similarly, the average height of the bead $< h >$ was determined by dividing the area of the deposited bead (without the remelted zone in the substrate) by the width of the bead w. The dilution ratio $d_{\text{This work}}$ is then defined by Equation 3.3 and referred to as d in

the following.

$$d_{\text{Dass and Moridi}} = \frac{p}{p+h} \in [10\%; 35\%] \tag{3.2}$$

$$d_{\text{This work}} = \frac{< p >}{< p > + < h >} \in [10\%; 35\%] \tag{3.3}$$

The selected parameters were further tested to guarantee the absence of microstructural defects, such as porosity, to ensure a certain grain size and morphology homogeneity. Three parameter sets per process are finally selected for WAAM and WLAM.

(ii) Single-bead walls. Additional process parameters are required when manufacturing single-bead walls, such as the deposition path, the height increment between the successive layers and the interlayer cooling time. Moreover, for the achieved walls, macroscopic regularity and surface roughness were assessed by calculating the average standard deviation of the width across transverse sections and profilometry surface measurements. A single parameter set associated with single-bead wall manufacturing was selected based on a compromise between minimizing macroscopic defects, reducing surface standard deviation and maximizing the deposition rate.

(iii) Multilayer tiles. The process parameters relevant to the manufacturing of tiles (deposition strategy and overlap between two beads in the same layer) were obtained by adapting those used for the single-bead. We checked that each successive bead overlapped and that the final component is of uniform height and width.

For the WAAM process, parameters $v_w = 2500$ mm/min, $s = 200$ mm/min, and $Q_{exp} = 2400$ W provided satisfactory results in an earlier study and were chosen as a reference in our study. To investigate the influence of each parameter, we varied the reference values by $\pm 25\%$ and $\pm 50\%$, generating an experimental matrix of 125 parameter sets. Due to practical constraints, not all beads could be manufactured, so the selection strategy was employed. Initially, the parameters were modified individually (for the first 12 beads). After, two or three parameters were varied at once. The objective was to maximize the observations to conclude on the influence of each parameter on the bead geometry. Ultimately, 24 single beads were fabricated using the WAAM process, with parameters varying within the intervals defined in Table 3.1.

For the WLAM process, we wanted to explore a large range of laser power, which can vary from 0 to 4000 W. Three specific power levels were then chosen: 1000 W (low power), 2400 W (for comparison with WAAM) and 3500 W (high power). The other parameters were chosen as follows. Before this work, the set of parameters A.($v_w = 1400$ mm/min, $s = 1000$ mm/min and $Q_{exp} = 2200$ W) was used in the same WLAM platform and produced satisfactory results. Additionally, Abkari *et al.* [109] used the parameters B.($v_w = 480$ mm/min, $s = 720$ mm/min and $Q_{exp} = 1000$ W) with a similar 316LSi wire with a diameter of 1.2 mm. The sets A. and B. were tested with slight adjustments:

- For the set A., we increased the power to 2400 W to align with our imposed powers, resulting in an initial set of parameters of A'. ($v_w = 1400$ mm/min, $s = 1000$ mm/min and $Q_{exp} = 2400$ W).
- For the set of parameters B. adapted from the literature, we rounded the values to B' ($v_w = 500$ mm/min, $s = 700$ mm/min and $Q_{exp} = 1000$ W).

From these two reference sets, the effect of wire feed speed and deposition rate was investigated by changing their values by $\pm$ 200 mm/min increments, initially modifying parameters individually and later simultaneously. This value was chosen as Akbari et Kovacevic [109] used variations steps of 120 mm/min and noticed significant differences in the geometry of the manufactured single beads.

Finally, for high laser power, the chosen reference set of parameters was C'. (v_w = 3000 mm/min, s = 1600 mm/min, and Q_{exp} = 3500 W). This parameter set was determined during the study once all the tests at 1000 and 2400 W had been carried out. The set of parameters C' was therefore established with an understanding of the influence of process parameters in WLAM on the geometry of the single beads. Once again, wire feed speed and deposition rate were varied by ± 200 mm/min increments, first individually and later simultaneously. In total, 40 single beads were produced using the WLAM process, with parameters varying within the intervals defined in Table 3.1.

The tested variation ranges for parameters have a larger amplitude for the WLAM process than for the WAAM process (×3.5 for Q_{exp}, ×7 for v_w and ×16 for s in the WLAM process, versus ×2 for Q_{exp}, ×3 for v_w and ×3 for s in the WAAM process). This difference is explained by the higher availability of the WLAM platform than the WAAM platform during this work. Moreover, the WLAM process was used with a higher deposition speed than the WAAM process, while the WAAM process was operated with the highest wire feed speed. Detailed process conditions applied for single beads manufactured using WAAM and WLAM processes are provided in Table A.1 of Appendix A.1.

Table 3.1. Variation range for the parameters for the manufacturing of single beads using WAAM and WLAM processes.

Investigated process parameters	WAAM	WLAM
Power of the heat source Q_{exp} (W)	1800-3600	1000-3500
Wire feed speed v_w (mm/min)	1250- 3750	500-3400
Deposition speed s (mm/min)	100- 300	100-1600

We also introduced physical relationships between the process parameters:

- the linear energy (Equation 3.4, *i.e.* the amount of energy applied per millimeter in the deposition direction. E_l is proportional to the ratio between the heat source power Q_{exp}, and the deposition speed s. The linear energy is then expressed in J/mm after conversion from mm/min to mm/s.

$$E_l = 60 \cdot \frac{Q_{exp}}{s} \tag{3.4}$$

- The second ratio, S (Equation 3.5), indicates the bead cross-section in the transverse direction, *i.e.* the amount of material deposited per unit of length in the deposition direction. This parameter is computed knowing that all the supplied wire is used to form the deposited bead. The volume of wire fed during a unit of time δt is determined by the wire cross-section, $\frac{\pi d_w^2}{4}$, where d_w is the wire diameter, and the wire feed rate v_w. Consequently, the area of the section of the bead above the substrate S is proportional to the ratio between the wire feed speed v_w and the deposition speed s. One can note that the actual total transverse surface of the single bead is greater than S, as the melt pool also consists of both the added surface on top of the substrate and the remelted part of the substrate. Still, this ratio allowed us to quantify the volume of supplied wire as a function of the deposition rate.

$$S = \frac{\pi \cdot d_w^2}{4} \cdot \frac{v_w}{s} \tag{3.5}$$

- The third ratio, E_v (Equation 3.6), approximates the applied volume energy in the deposited bead. This ratio is obtained by dividing E_l by S. However, E_v only approximates the actual experimental volume energy, as a part of E_l is used to melt the substrate or the previous layer under the deposited bead. E_v is helpful to highlight manufacturing trends because a too low applied volume energy is

susceptible to leading to a lack of melting of the deposited layer [177].

$$E_v = \frac{E_l}{S} = \frac{240}{\pi d_w^2} \cdot \frac{Q_{exp}}{v_w} \tag{3.6}$$

- Finally, the fourth ratio, d_{rate} (Equation 3.7), indicates the theoretical deposition rate during the manufacturing, where ρ is the density of the 316L steel. It should be noted, however, that this theoretical deposition rate is higher than the actual deposition rate, as it does not consider any interlayer breaks during the manufacturing process.

$$d_{\text{rate}} = \rho \cdot v_w \frac{\pi \cdot d_w^2}{4} \tag{3.7}$$

3.2 Processing conditions for single beads

3.2.1 Geometrical defects

Typical morphologies of single beads obtained with WAAM and WLAM are presented at the same scale in Figure 3.2. Beads deposited with WLAM (Figure 3.2b) are three to four times thinner than the ones obtained with the WAAM process (Figure 3.2a). In addition, the wire in the WLAM process remained solid until it reached the melt pool while it melted before reaching the melt pool in the WAAM process. It leads to two different typical shapes for the melt pool (Figure 3.1) but also influences the morphology of the resulting single beads depending on the applied volume energy.

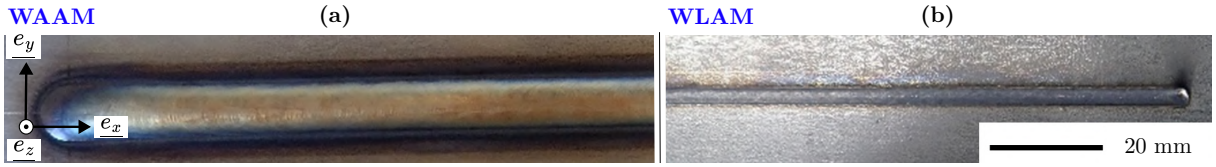

Figure 3.2. Morphologies of the regular single beads produced with (a) WAAM (parameters set 23) and (b) WLAM (parameters set 23) processes.

Figure 3.3 presents several single beads manufactured with WAAM and WLAM processes, using different volume energy densities. Several single beads, such as those in Figures 3.3e, f and g, were considered as correctly deposited and corresponded to the targeted shape criteria during the visual inspection.

However, single beads produced with a too low volume energy density for WAAM and WLAM and a too high volume energy density for WLAM presented irregular or discontinuous morphologies. For the WAAM process, three out of 24 beads were excluded due to their non-continuous profiles, and three were excluded due to irregular profiles. In contrast, for the WLAM process, only two out of 40 single beads exhibited irregular morphology. Moreover, no discontinuous beads were observed during the WLAM process under the tested parameter sets. To facilitate a comparison between WAAM and WLAM, two discontinuous single beads were produced by WLAM by increasing the distance between the deposition head and the substrate from 1 to 2 mm, modifying the energy distribution through a defocus of the laser [178]. The variations in parameter amplitudes then allowed us to explore the limits of both processes, producing both stable and unstable depositions.

For the WAAM process, the single bead processed with the lowest volume energy density (33.9 J/mm^3) shown in Figure 3.3a exhibited small, tear-like deposits along the deposition path, typical of balling. Another irregular bead was produced using the WAAM process with parameter set 4 (Table A.1), as shown in Figure 3.3c. The irregular bead was produced using a lower energy density of 40.7 J/mm^3, compared to 50.9 J/mm^3 for the regular beads. The irregular shape resulted from balling despite a higher applied volume energy. The liquid metal does not penetrate completely into the melt pool in the substrate, leading to poor wetting and an irregular morphology. This poor wetting is highlighted in Figures 3.4a and b presenting the obtained micrographs of transverse cross-sections of these irregular single beads manufactured with the WAAM and WLAM processes, respectively, showing an acute contact angle with the substrate.

For the WLAM process, defocusing the laser by 1 mm led to the discontinuous morphology shown in Figure3.3b. During this manufacturing, the laser spot size on the substrate increased due to the defocus, making wire penetration into the melt pool more difficult as the substrate is less melted due to the lower applied local energy density. The resulting bead morphology corresponds to stubbing, which occurs when the applied volume energy is insufficient during manufacturing [54]. Manufacturing had to be stopped due to the rapid unwinding of the wire, which accumulated around the deposition head.

The irregular shape of the WLAM bead in Figure 3.3d can also be attributed to stubbing, where the wire reached the bottom of the melt pool but could be melted, creating a continuous yet irregular bead. This bead was produced with an energy density of 71.0 J/mm^3, compared to 158 J/mm^3 for the regular bead shown in Figure 3.3f.

Finally, another discontinuous shape was observed after the WLAM processing (Figure 3.3h). This phenomenon, known as dripping, occurs when the wire melts before reaching the melt pool, causing droplets to fall onto the substrate surface [53]. As seen in the literature review, this phenomenon results from an excessively high applied volume energy density or a significant laser de-focus, as in this study, where the distance between the substrate and the deposition head was increased by 2 mm.

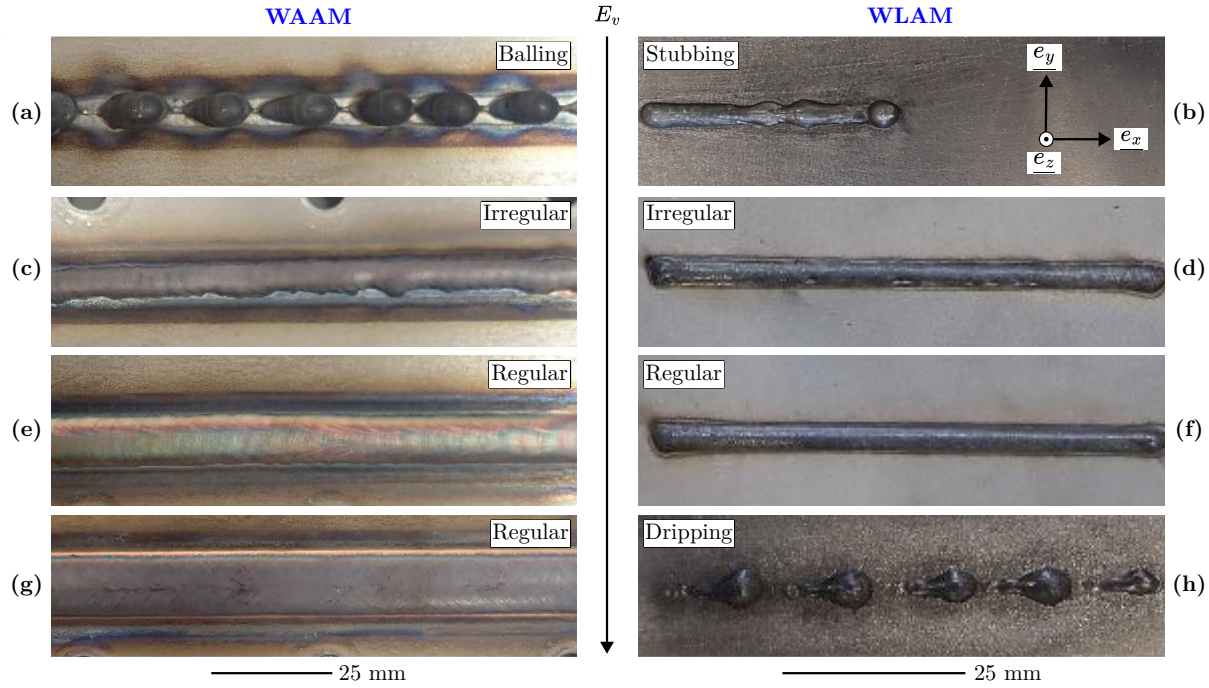

Figure 3.3. Different morphologies of single beads obtained by Wire Additive Manufacturing, depending on the applied volume energy density E_v. (a), (c), (e) and (g): WAAM; (b), (d), (f) and (h): WLAM. (a) and (b) non-continuous beads; (c) and (d) irregular beads; (e) and (f) correctly deposited beads. WAAM sets of parameters: (a) 5, (c) 4, (e) 1, (g) 24 (Table A.1). WLAM sets of parameters: (b) 9 with a defocus of 1 mm, (d) 17, (f) 9, (h) 9 with a defocus of 2 mm (Table A.1).

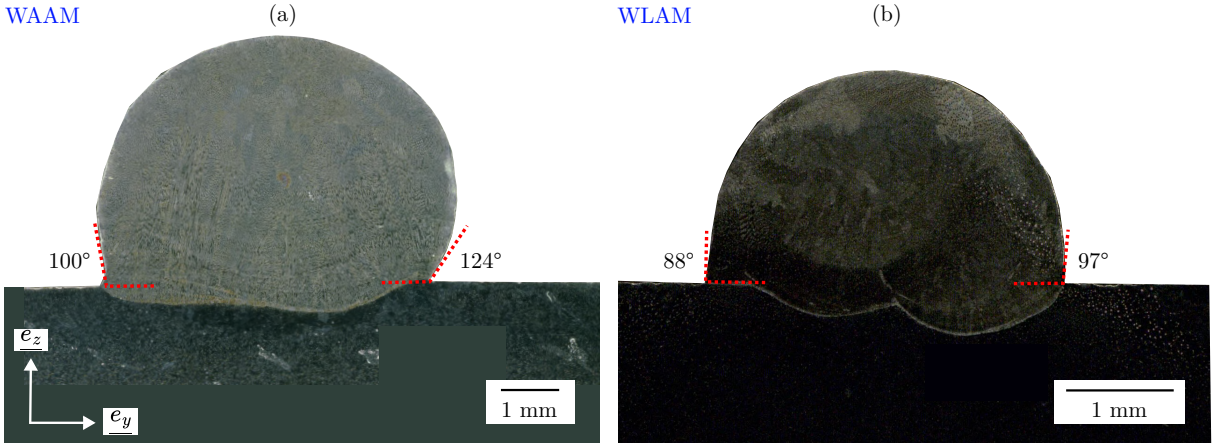

Figure 3.4. Macrographs of chemically etched transverse cross-sections of irregular single beads obtained with (a) WAAM and (b) WLAM processes, using sets of parameters 4 and 17 (Table A.1), respectively.

Figure 3.5 ranks the single beads manufactured using WAAM and WLAM processes based on applied linear energy and resulting area of the transverse section above the substrate S, as defined in Equations 3.4 and 3.5. Correctly deposited single beads are indicated in dark blue "+" for WAAM and cyan "·" for WLAM, while incorrect beads (discontinuous or irregular) are shown in red "×". As mentioned previously, no irregular bead was obtained using the WLAM process. The results revealed that the beads achieved with a low linear energy and a high area of the transverse section above the substrate consistently exhibited manufacturing defects. This supports the hypothesis that the volume energy density is a critical factor for bead geometrical regularity: if it is too low, it results in an irregular shape. However,

one bead obtained by WAAM was irregular even if regular beads were obtained using lower volume energy densities. This can be attributed to the influence of the deposition speed s, as this bead was produced at the lowest speed ($s = 100\ mm/min$). Yehorov *et al.* [76] mentioned that a too low deposition rate might result in an irregular morphology due to fluid dynamics within the melt pool.

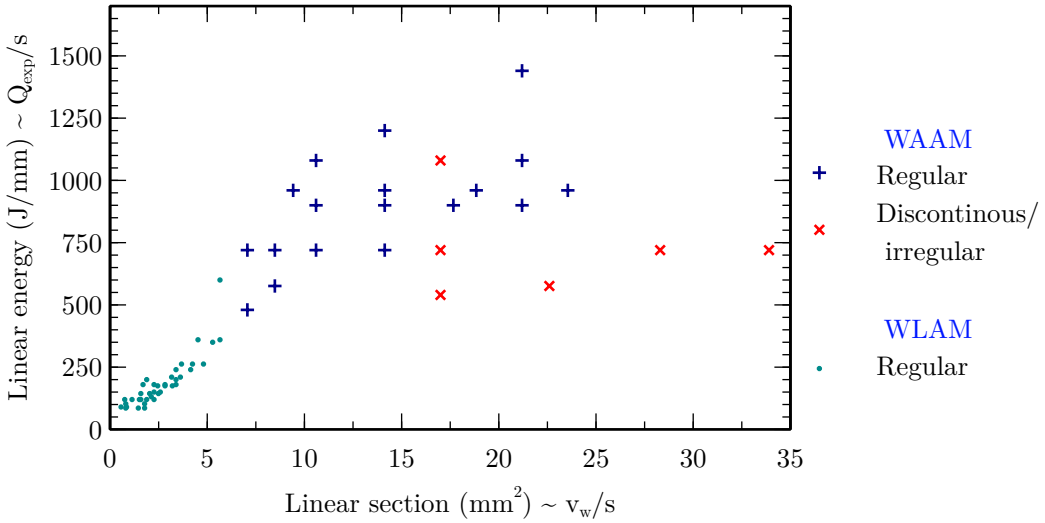

Figure 3.5. Applied linear energy E_l, and area of the transverse section above the substrate S of single-beads manufactured by WAAM and WLAM. Red crosses "×" depict the irregular/discontinuous single beads (obtained by WAAM), whereas dark blue "+" and cyan "·" represent the regular beads obtained by WAAM and WLAM, respectively.

3.2.2 Morphology of regular beads

Figures 3.6a and b present the evolution of the morphology of the single beads manufactured by WAAM and WLAM, respectively, as a function of the deposition speed s, and the wire feed speed v_w. One process parameter is being varied while the other is being kept constant. As expected from the literature review, for the WAAM process, increasing s leads to a reduction in both the height and width of the beads. However, for the WLAM process, increasing s reduces the height of the bead but does not significantly influence the width. Moreover, for both processes, increasing v_w results in taller single beads while their width remains constant. This contradicts the literature, where v_w is reported to increase the width of WAAM beads.

Figures 3.7a and b depict the influence of the applied linear energy E_l, and the cross-section area above the substrate S, on bead morphology for WAAM and WLAM, respectively. For the WAAM process, higher E_l results in a spreading of the bead, corresponding to an increase in width and a decrease of height. Additionally, higher E_l increases bead dilution into the substrate. For the WLAM process, increasing E_l affects the dilution of the bead into the substrate without significant variations in width or height. This difference arises from the nature of the heat source: increasing E_l broadens the arc in WAAM, whereas the laser in WLAM remains focused, such that the total energy is distributed similarly. For both processes, increasing S leads to a larger transverse cross-section above the substrate. However, differences in bead morphology arise. For WAAM, both the height and width of the beads increased, whereas, for WLAM, only the height increased, while the bead width remained constant. These variations are again attributed to the difference in energy sources, with the arc in WAAM spreading more than the focused laser in WLAM.

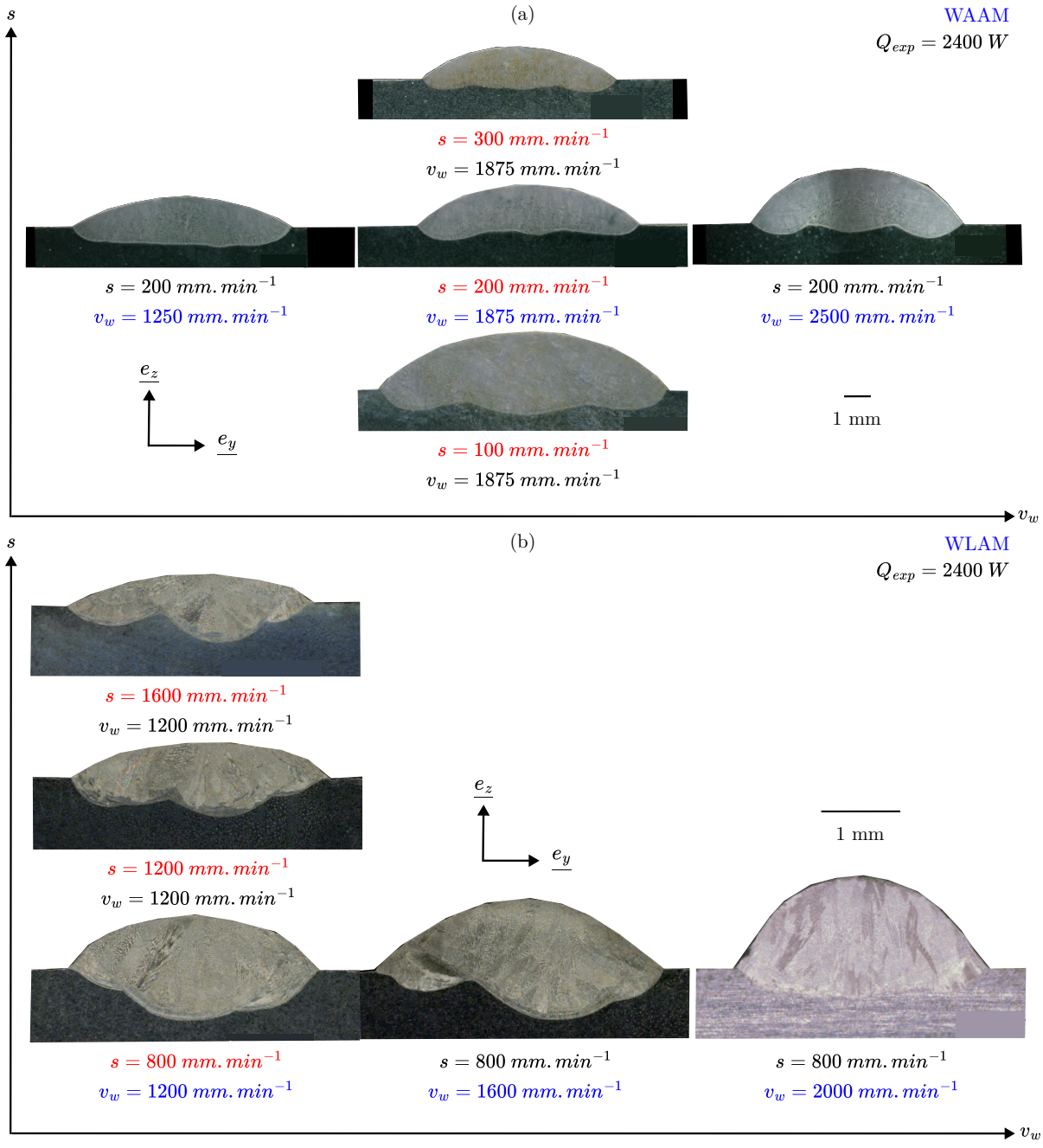

Figure 3.6. Morphology of single beads manufactured using (a) WAAM and (b) WLAM at a constant heat source power of 2400 W, as a function of deposition speed s and wire feed speed v_w.

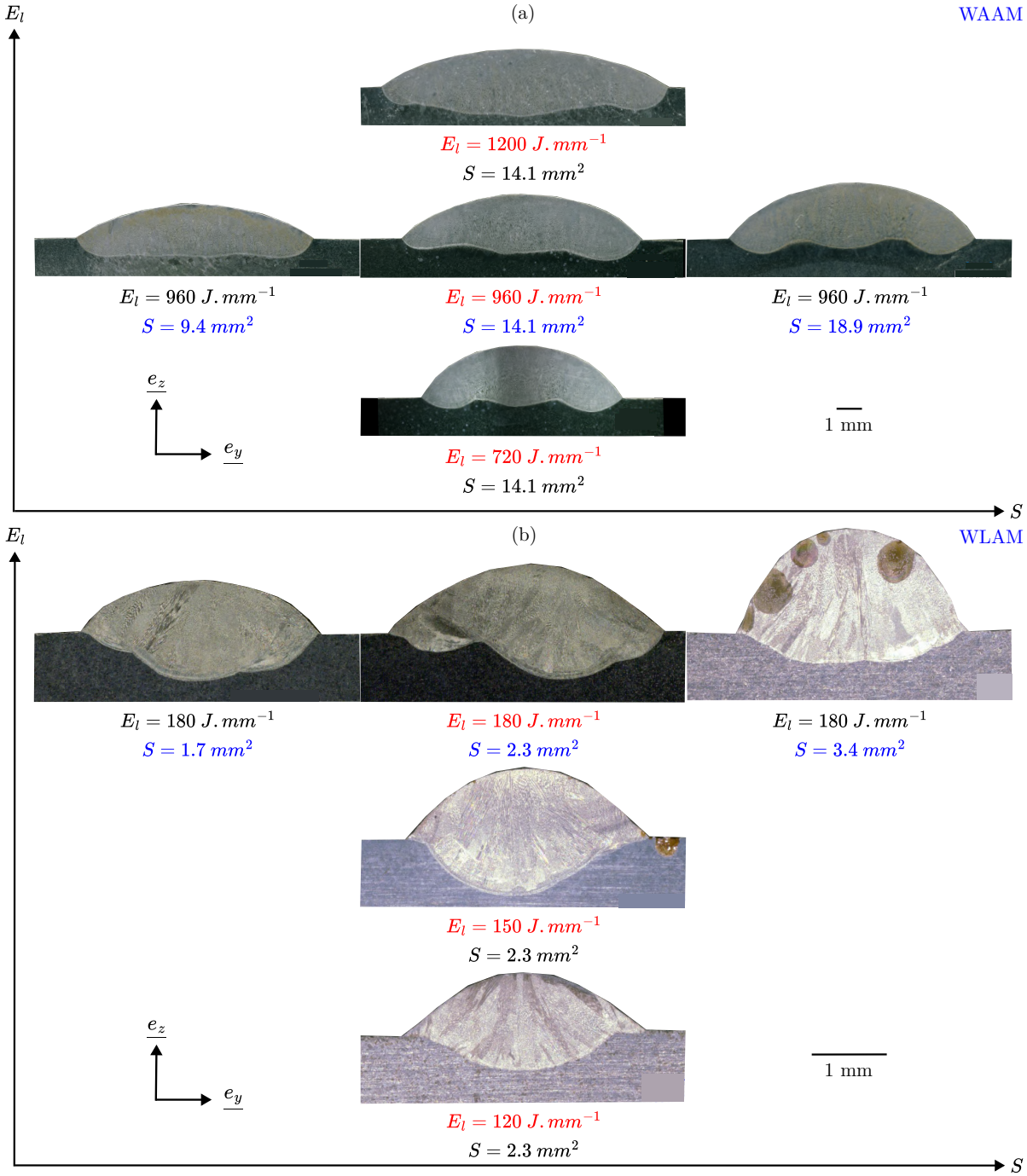

Figure 3.7. Morphology of single beads manufactured using (a) WAAM and (b) WLAM as a function of the applied linear energy E_l and the cross-section of the bead above the substrate S.

Next, we studied the influence of the process parameters (deposition speed s, wire feed speed v_w, power of the heat source Q_{exp}) on the shape factor w/h and the dilution ratio of the manufactured single beads with WAAM and WLAM processes (Figure 3.8). Each line depicts the evolution of the morphology with one parameter while keeping the two others constant. The continuous lines and dashed lines correspond to the WAAM and WLAM processes, respectively. Similarly, Figure 3.9 presents the evolution of the geometrical ratios as a function of the applied linear energy E_l, and the cross-section of the bead above the substrate S. Finally, Tables 3.2 and 3.3 summarize the evolution trends of the shape factor and dilution ratio with applied process parameters.

For the WAAM process, an increase in the applied power (Figures 3.8e and f for the shape factor and the dilution ratio, respectively) leads to an increase in both the width/height and the dilution ratios. This occurs because, with constant deposition speed and wire feed speed, higher power results in higher linear energy and then flatter beads, *i.e.* higher width/height ratios. The increased power also reduces the bead height while enhancing penetration into the substrate, thus raising the dilution ratio. The same trend can be observed for the linear energy in the WAAM process (Figure 3.9c and d). On the other hand, no clear trend was observed in the evolution of geometric ratios as a function of applied linear energy for the WLAM process. As mentioned earlier, this is due to a difference in the spatial distribution of the energy sources, as the laser remains focused while the arc spreads out.

We observed that for the WAAM process, the deposition speed only has a small impact on the geometrical ratios (Figure 3.8a and b). In contrast, for the WLAM process, an increase in deposition speed tends to raise both the width/height and dilution ratios.

Higher deposition speed with constant power and wire feed speed decrease the applied linear energy and the bead cross-section. We assumed that the negligible influence of the deposition speed in the WAAM process is explained by the fact that the linear energy and the cross-section are evolving similarly. In addition, the difference is also explained by the fact that the amplitude of s variations for the WAAM process is limited to just 200 mm/min, compared with over 1000 mm/min for WLAM.

Lastly, an increase in wire feed speed leads to a decrease of both ratios for both WAAM and WLAM processes (Figure 3.8c and d). As the wire feed speed increases, more metal is deposited for the same applied energy, resulting in a higher bead with a similar width and a lower width/height ratio. The lower dilution ratio can also be explained by the increased bead cross-section above the substrate, which reduces penetration into the substrate as the applied power remains constant.

These trends are summarized in Tables 3.2 and 3.3 and are consistent with those reported by Mohammed *et al.* [66] for the WLAM process. Our findings align with their study, except for the effect of laser power on the width/height ratio. They reported that after a certain point, an increase in the laser power decreases the width/height ratio, which is attributed to their extrapolation extending beyond the model validity range. In our case, we interpolate the results between the experimental points, which allows us to remain in the validity field of the model.

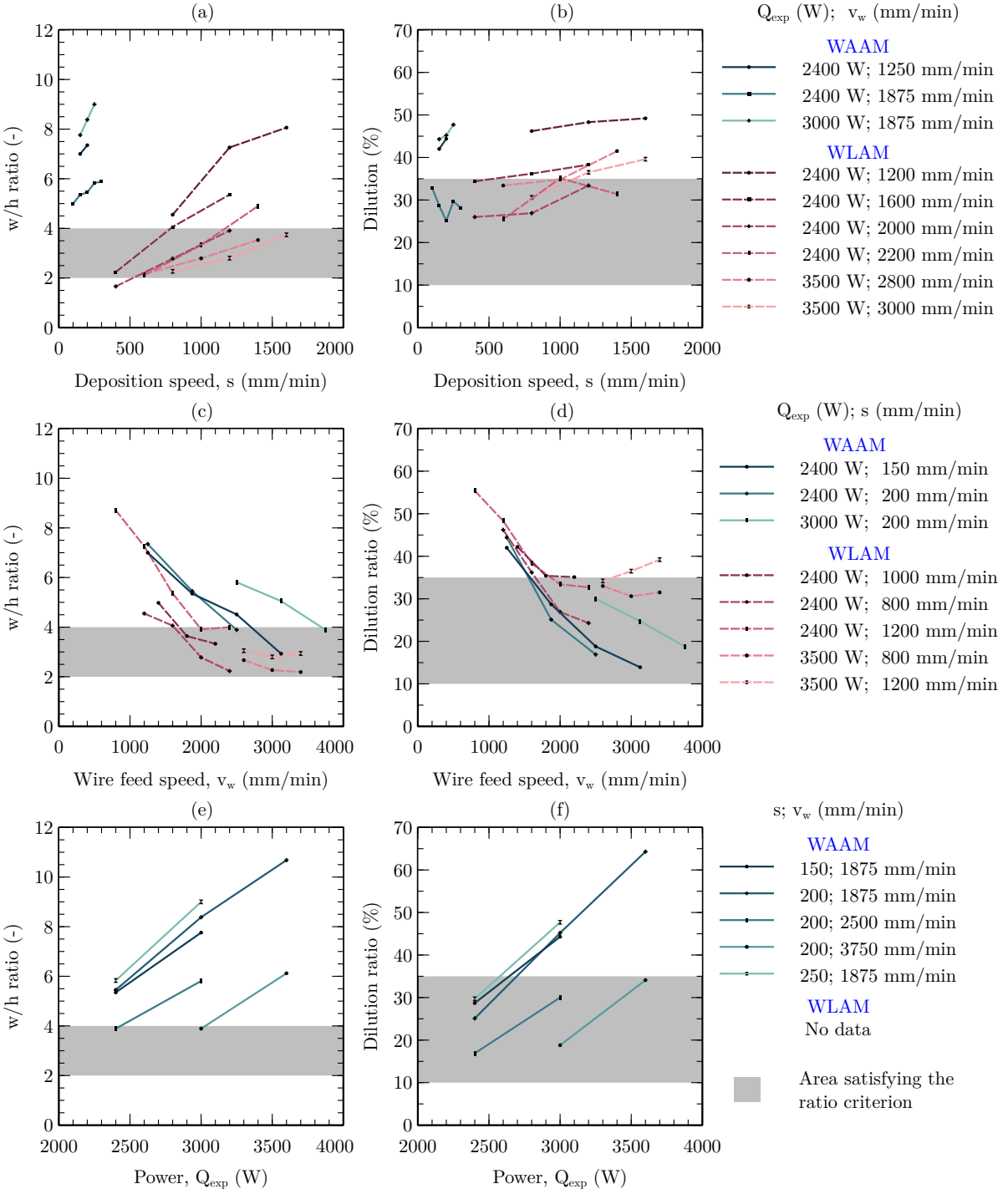

Figure 3.8. Effect of the process parameters (i.e. heat source power Q_{exp}, deposition speed s, and wire feed speed v_w) on the variations in (a), (c), (e) width/height ratio $\frac{w}{h}$ and (b), (d), (f) dilution ratio d, for WAAM (continuous lines) and WLAM (dashed lines). Each experimental measurement is represented by a black dot. The other process parameters are kept constant for each curve, as presented in the legend on the right. The grey areas correspond to the parameter intervals satisfying the defined geometric criteria.

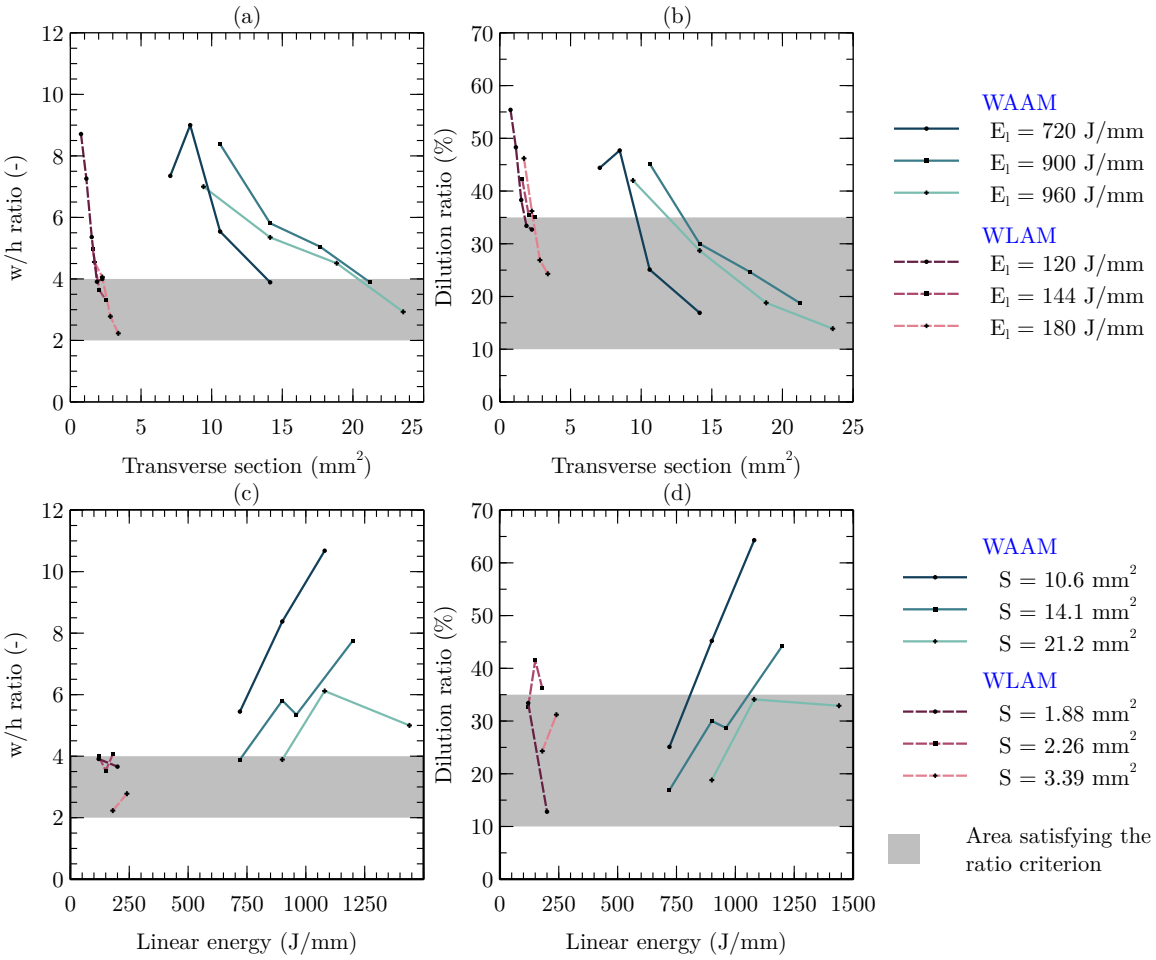

Figure 3.9. Effect of linear energy E_l and cross-section of the bead above the substrate S) to the variations in (a), (c) the width/height ratio $\frac{w}{h}$, and (b), (d), the dilution ratio d, for WAAM (continuous lines) and WLAM (dashed lines) processes. Each experimental measurement is represented by a black dot. The other process parameters are kept constant for each curve, as presented in the legend on the right. The grey areas correspond to the intervals satisfying the defined geometric criteria.

Table 3.2. Schematic illustration of the influence of the process parameters (Q_{exp}, s, v_w) on the geometric ratios ($\frac{w}{h}$ and d).

Ratio	Process	Power of the heat source Q_{exp} (W)	Deposition speed s (mm/min)	Wire feed speed v_w (mm/min)
w/h ratio	WAAM	↗	↗	↘
	WLAM	No data	↗	↘
Dilution ratio	WAAM	↗	⇝	↘
	WLAM	No data	⟶	↘

Table 3.3. Schematic illustration of the influence of the physical relationships (E_l and S) on the geometric ratios ($\frac{w}{h}$ and d).

Ratio	Process	Bead cross-section S (mm^2)	Linear energy E_l (J/mm)
w/h ratio	WAAM	↘	↗
	WLAM	↘	⇝
Dilution ratio	WAAM	↘	↗
	WLAM	↘	⇝

Figures 3.10a, b, and c illustrate the evolution of the width/height and the dilution ratios for beads produced using the WLAM process as a function of wire feed speed and deposition speed at a constant laser power of 1000 W, 2400 W, and 3500 W, respectively. At a laser power of 1000 W (Figure 3.10a), we observed that both the wire feed speed and the deposition speed significantly influence the width/height ratio. In contrast, the deposition speed tends to have less pronounced effect on the dilution ratio. The tested parameters presented width/height ratios ranging from 2 to 7, but the dilution ratios were restricted to a narrower range, from 5% to 25%. At a laser power of 2400 W (Figure 3.10b), both the deposition speed and the wire feed speed significantly influence the width/height ratio. However, the deposition speed has a less pronounced impact on the dilution ratio at this specific power. The tested parameters allowed us to achieve a wide range of bead morphologies, with the width/height ratio varying from 1 to 11 and the dilution ratio ranging from 10% to 60% across the manufactured beads. Finally, at a laser power of 3500 W (Figure 3.10c), we found that all the manufactured beads exhibited a width/height ratio between 2 and 4 and a dilution ratio between 30% and 40%. These smaller variations may result from the constant increment of 200 mm/min among the deposition and wire feed speeds, which becomes less significant for high values of s and v_w. The predominant parameter influencing the geometrical ratios at 3500 W is the deposition speed, while the wire feed speed plays a minor role.

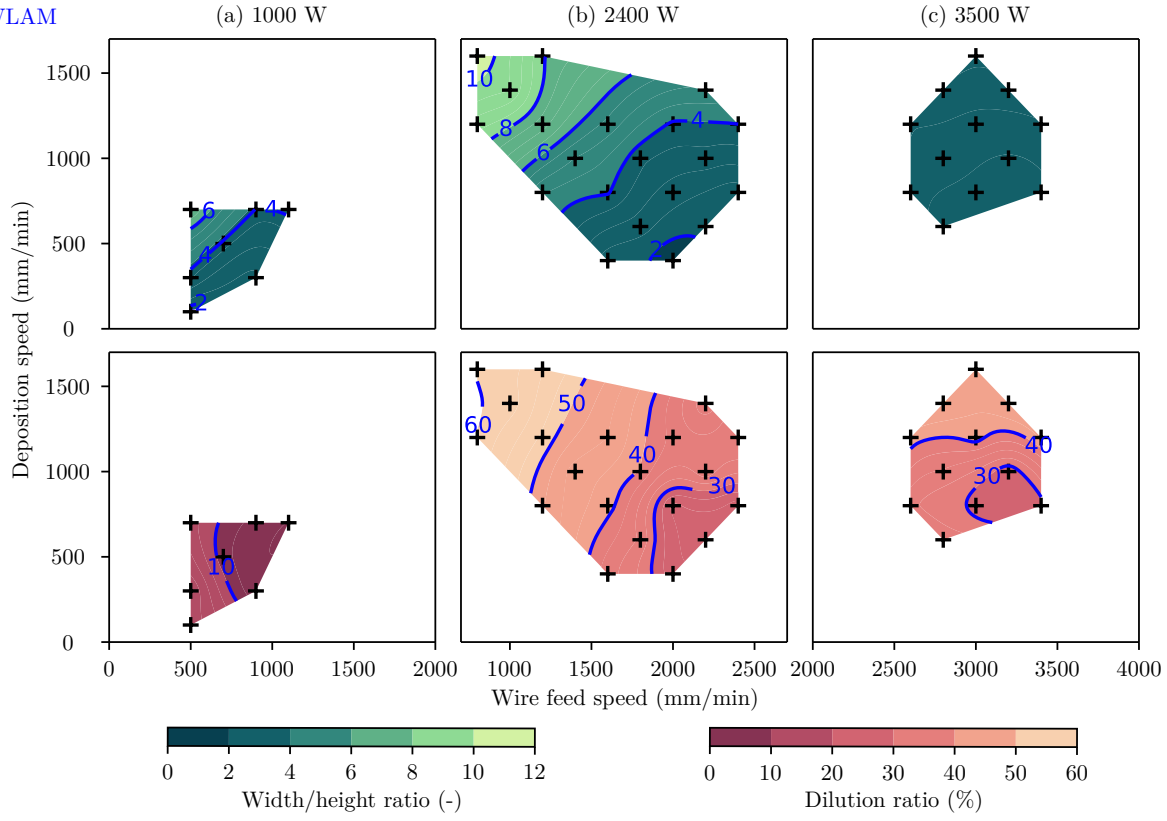

Figure 3.10. Width/height and dilution ratios among the manufactured single beads with WLAM process (dark crosses) with various power and wire feed speeds, at given laser powers of (a) 1000 W, (b) 2400 W and (c) 3500 W.

The same study was carried out on single beads manufactured with the WAAM process at a power of 2400 W. Figures 3.11 a and b present respectively the evolution of the width/height and the dilution ratios depending on the wire feed speed and the applied power. Unlike the WLAM process, we previously highlighted that the deposition speed only has a small influence on both the width/height and the dilution ratios, so we did not select this parameter to establish the process maps. It was observed that both the power and the wire feed speed influence the width/height and dilution ratios. As for the WLAM process, the tested parameters allowed us to cover many bead morphologies, as the width/height ratio varies from 4 to 11 and the dilution ratio from 20% to 60%.

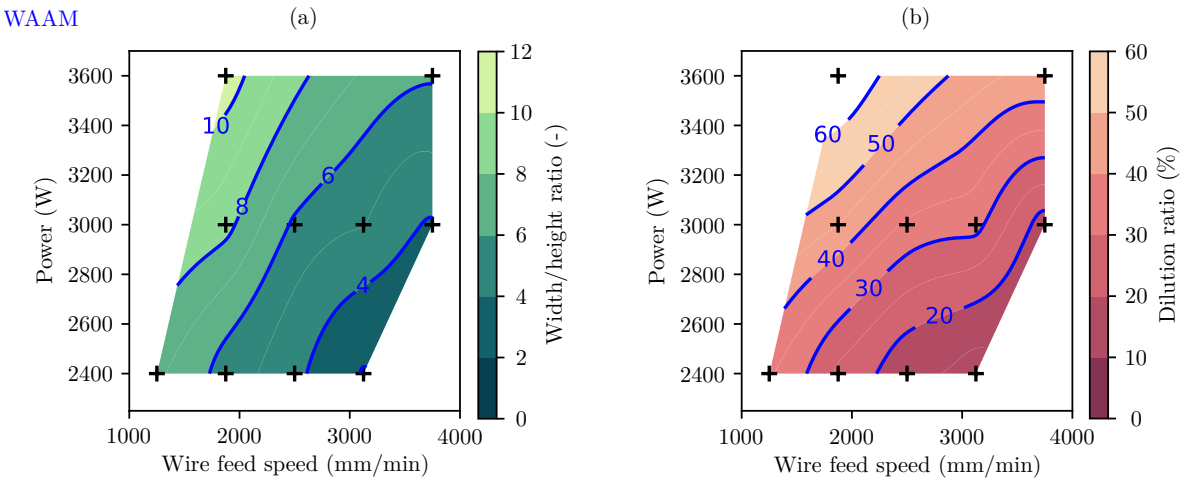

Figure 3.11. Evolution of (a) the width/height ratio and (b) the dilution ratio among the manufactured single beads with WAAM process (dark crosses) with various power and wire feed speeds.

3.2.3 Microstructural singularities

Despite a suitable geometry, microstructure defects such as porosity are susceptible to appear, strongly affecting the manufactured components properties [122]. Figure 3.12 presents the microstructure of a single bead manufactured with the WLAM process using the set of parameters 5 (Table A.1) on a transverse cross-section (a and b) and a longitudinal cross-section at the center of the bead (c and d). The EBSD maps are projected in the manufacturing direction ($\underline{e_z}$, a and c) and the deposition direction ($\underline{e_x}$, b and d).

As mentioned in the literature review, the typical microstructure of a single bead manufactured using the WAAM or WLAM process usually presents elongated grains oriented in the manufacturing direction. However, in the single bead manufactured by WLAM using the set of parameters 5 (Table A.1), a zone with fine equiaxed grains, with no apparent preferential orientation, was observed at the center of the bead. This particular microstructure was observed for single beads manufactured using high wire feed rate and was considered undesirable as grain size heterogeneities are susceptible to influence the material properties. It might result from the remelting of the microstructure. It was supposed to be the consequence of an incorrect calibration of the process, especially the alignment of the laser head.

In addition, porosity can be observed at the bottom of the melt pool of single beads manufactured with WLAM for some sets of parameters, as presented in Figure 3.13. This only concerns the single beads with a very low dilution in the substrate, where pores form due to insufficient dilution. However, an insufficient dilution is outside of the defined selection criterion for processing parameters ($d > 10\%$).

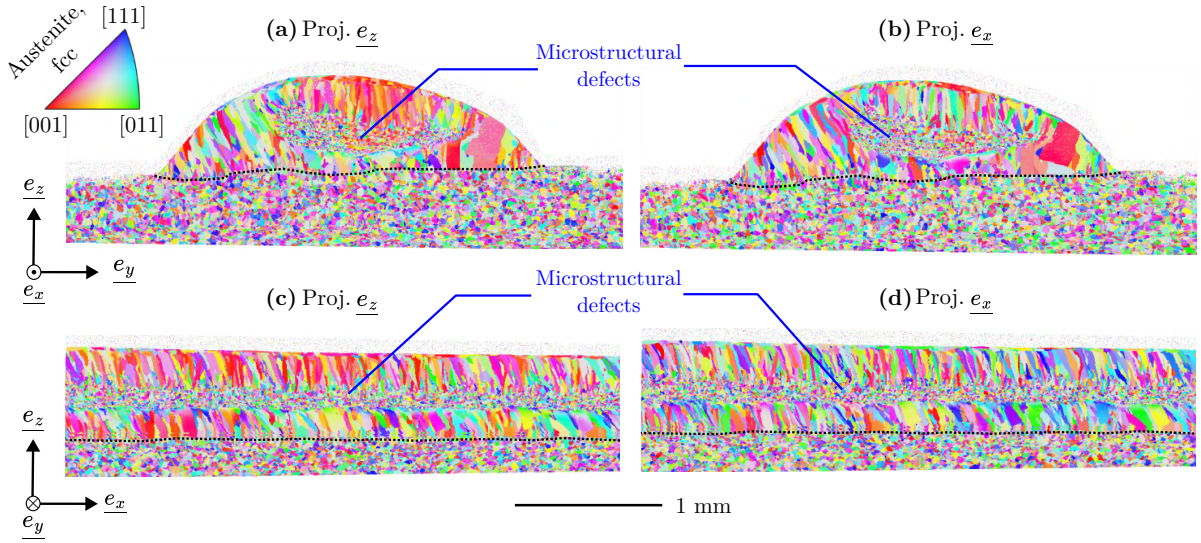

Figure 3.12. EBSD map of an incorrectly deposited single bead manufactured with WLAM process using the set of parameters 5 (Table A.1): (a) transverse cross-section, projected in the manufacturing direction $\underline{e_z}$; (b) transverse cross-section, projected in the deposition direction $\underline{e_x}$; (c) longitudinal cross-section, projected in the manufacturing direction (d) longitudinal cross-section, projected in the deposition direction.

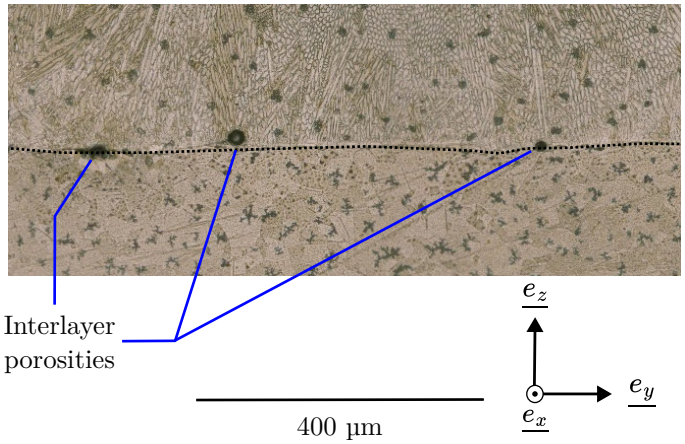

Figure 3.13. Micrography taken on an etched transverse cross-section of a single bead obtained by WLAM with the set of parameters 3 (Table A.1) where interlayer porosity can be observed.

3.2.4 Selection based on geometric criteria

Within the process parameter windows defined in Section 3.2.1, we aimed to identify three parameter sets for WAAM and WLAM that meet the following criteria: a dilution ratio between 10% and 35% and a width/height ratio within the range $\frac{w}{h} \in [2, 4]$ (Figures 3.14 and 3.15).

For WLAM, the cartographies are drawn for different wire feed speeds and deposition speeds at constant laser powers of 1000 W (Figure 3.14a), 2400 W (Figure 3.14b), and 3500 W (Figure 3.14c). The purple area on each map highlights the zones where both geometrical criteria are met, allowing us to select one set of parameters for each power level. Red or blue zones meet only one of the two conditions. For the 1000 W power, two parameter sets were within the acceptable dilution and width/height thresholds. We selected a deposition speed of 300 mm/min and a wire feed speed of 500 mm/min. The selected dilution value is at the lower limit of the acceptable threshold. However, reducing the wire feed speed further was not an option, as the WLAM deposition head manufacturer advises not to use wire supply speeds below this value. At 2400 W, four parameter sets were within the acceptable dilution and width/height thresholds. We chose a wire feed speed of 2000 mm/min and a deposition speed of 800 mm/min, as these values are centrally located within the acceptable zone. Finally, for the 3500 W power, six parameter sets met the acceptable criteria. We selected a wire feed speed of 2800 mm/min and a deposition speed of 1000 mm/min, aiming for a higher deposition speed than at 2400 W while keeping the wire speed sufficient to avoid potential manufacturing issues.

The selected parameters for manufacturing single beads with the WLAM process are summarized in Table 3.4.

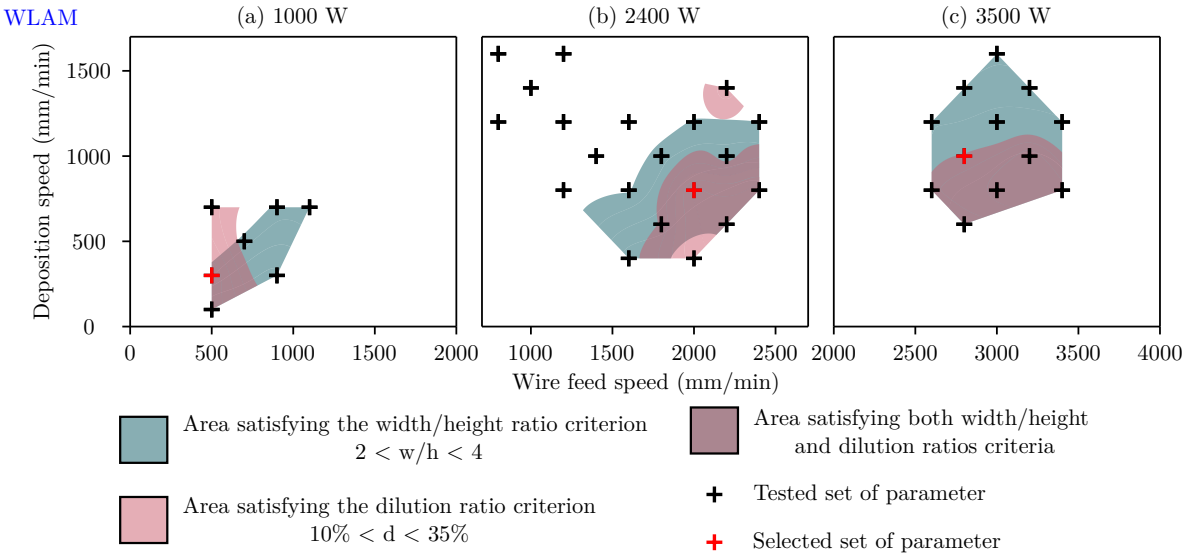

Figure 3.14. Areas satisfying the width/height and dilution ratios criteria for single beads among the tested parameters with the WLAM process, depending on the wire feed speed and the deposition speed, at a laser power of (a) 1000 W, (b) 2400 W and (c) 3500 W.

Similarly, Figure 3.15 displays the experimental parameter sets that satisfy the width/height and the dilution ratios criteria for single beads produced using the WAAM process based on their power and wire feed speed. We found that the width/height ratio criterion is the limiting factor as the corresponding processing zone is included in the zone satisfying the dilution criteria. It differs from the manufacturing made with the WLAM process, where several beads met the width/height ratio criterion without the

dilution criterion. The selected parameters for manufacturing single beads with the WAAM process were chosen in or near the zone satisfying both criteria and are listed in Table 3.5.

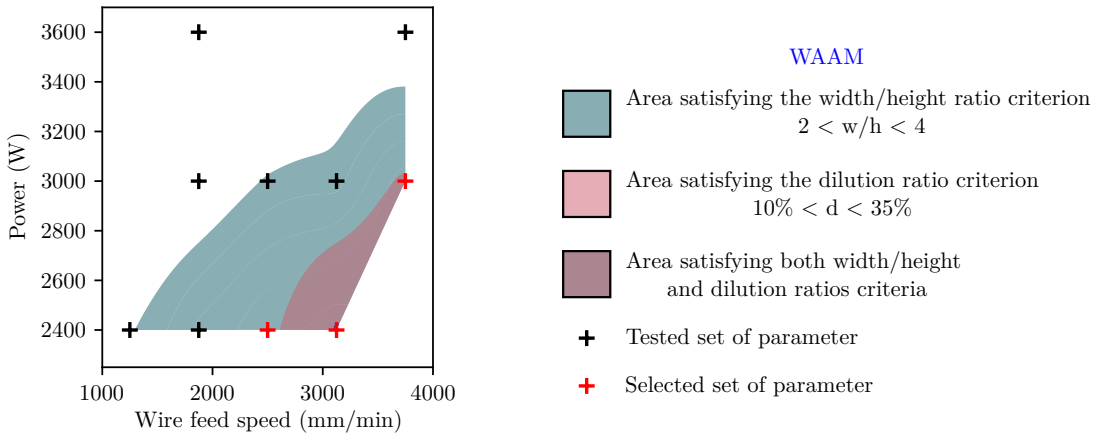

Figure 3.15. Areas satisfying the width/height and dilution ratios criteria for single beads among the tested parameters with the WAAM process, depending on the power and the wire feed speed.

Table 3.4. Selected sets of parameters for the manufacturing of single beads using the Wire Laser Additive Manufacturing process.

Set number	Power of the heat source Q_{exp} (W)	Deposition speed s (mm/min)	Wire feed speed v_w (mm/min)	Shape factor w/h (-)	Dilution ratio d (%)
Set 1	1000	300	500	3.66	12.8
Set 2	2400	800	2000	2.78	26.9
Set 3	3500	1000	2800	2.79	34.8

Table 3.5. Selected sets of parameters for the manufacturing of single beads using the Wire Arc Additive Manufacturing process.

Set number	Power of the heat source Q_{exp} (W)	Deposition speed s (mm/min)	Wire feed speed v_w (mm/min)	Shape factor w/h (-)	Dilution ratio d (%)
Set 1	2400	200	2500	3.89	16.9
Set 2	2400	150	3125	2.93	13.9
Set 3	3000	200	3750	3.89	18.8

The morphologies of the single beads manufactured with the selected sets of parameters (Tables 3.4 and 3.5) for WAAM and WLAM are presented in Figure 3.16. For the beads manufactured with WLAM, a very irregular melt pool was obtained for a laser power of 1000 W (Set 1), which could result from a misalignment of the laser or the effect of a too important focus. For the two other sets of parameters, symmetrical melt pools were obtained, reaching their maximum at their center, in agreement with the predominance of heat conduction physical phenomenon, compared to the single beads achieved by WAAM, which exhibited three local depth peaks due to fluid effects. As it was indicated in Table A.1, these selected sets of parameters are associated with deposition rates of 22.6, 28.3 and 33.9 g/min for WAAM, respectively, and 4.5, 18.1 and 25.3 g/min. Even if the deposition rates obtained for the single beads manufactured with the WLAM process are lower than those of the single beads, they remain comparable, especially at laser powers of 2400 and 3500 W.

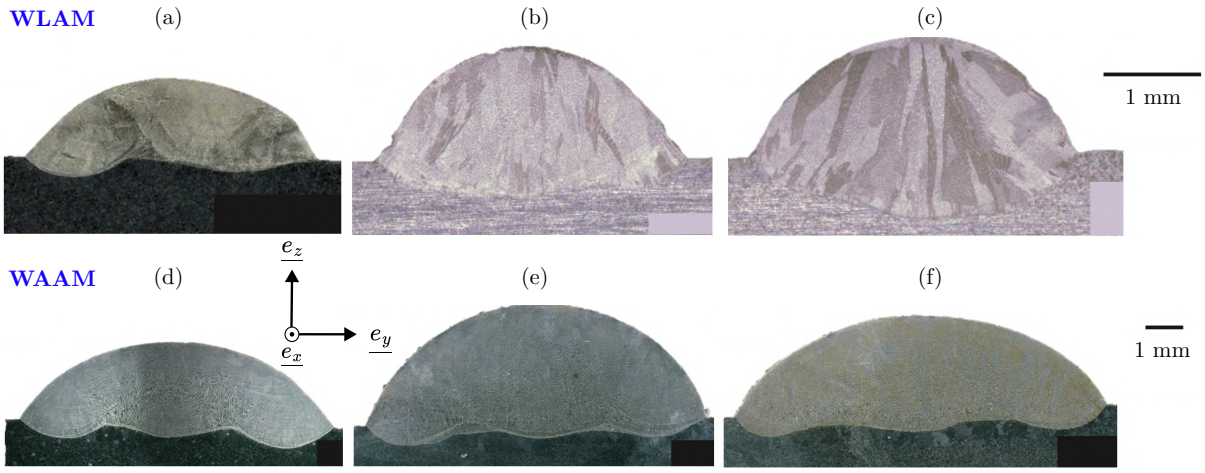

Figure 3.16. Single beads produced with selected processing parameters: (a), (b), and (c) WLAM process, corresponding to conditions 3, 23, and 35 in Table A.1; (d), (e) and (f) WAAM process, corresponding to conditions 1, 13, and 23 in Table A.1.

The study of the influence of the parameters on the geometry of single beads manufactured by WAAM and WLAM was further developed by setting up a statistical study presented in Appendix A.2. Empirical equations linking the geometric ratios (w/h and d) and the process parameters were established to enable the estimation of the bead morphology before manufacturing.

3.3 Processing conditions for single-bead walls

The selected sets of parameters in Tables 3.4 and 3.5 were applied to the manufacturing of single-bead walls up to 100 mm-high (approximating thin sections of complex components). New influent processing parameters (height increment, deposition strategy and interlayer cooling time) were calibrated to select one set of parameters for each process.

3.3.1 Geometry

The height increment between successive layers was the first parameter to be calibrated for manufacturing single-bead walls. Manual adjustment was unnecessary for WAAM as the used program automatically regulates the arc length to 15 mm (or sets its voltage to 12 V), then adjusts the deposition height.

For the WLAM process, we tested three different height increments for each set of parameters of ±0.1 mm around the average height of a single bead. At a laser power of 1000 W (Set 1, Table 3.4), the average height of a single bead was determined at 0.57 mm. We then considered three height increments of 0.5, 0.6 and 0.7 mm. Similarly, at a laser power of 2400 W (Set 2, Table 3.4), the average height of a single bead was determined at 0.81 mm. The three height increments were 0.7, 0.8 and 0.9 mm. Finally, at 3500 W (Set 3, Table 3.4), the average height of a single bead was determined at 0.88 mm. We then considered three height increments of 0.8, 0.9 and 1 mm.

Figure 3.17 shows single-bead walls produced with WLAM using height increments of 0.5 mm (Figure 3.17a) and 0.6 mm (Figure 3.17b), with the average height of a deposited bead being 0.57 mm. In the wall manufactured with a 0.5 mm height increment, an irregular profile emerged after a few layers. This was attributed to the decreasing distance between the deposition head and the previous layer as the number of layers increased, leading to irregular deposition due to defocusing, as described in Figure 3.3b and h. For each set of parameters, the closest height increment to the average height of a bead was selected, as it produced the most regular single-bead walls.

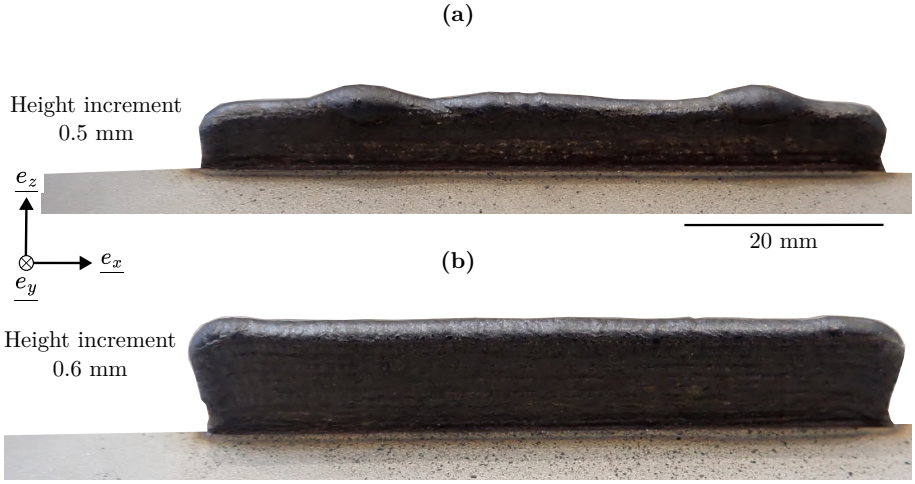

Figure 3.17. Single-bead walls manufactured by WLAM with parameter Set 1 (Table 3.4), with different height increments of (a) 0.5 mm and (b) 0.6 mm.

Figures 3.18a, b, and c present walls produced by WAAM using a one-way deposition strategy with parameter Sets 1, 2, and 3 (Table 3.5), respectively. To assess the impact of the deposition trajectory on the final geometry, another wall was produced with parameter set 3 (Table 3.5) with an alternating deposition strategy, where each layer was deposited in the opposite direction of the previous one (Figure 3.18d). As anticipated from the literature review, a significant collapse was observed in all three walls produced using the one-way deposition strategy. The wall in Figure 3.18c exhibited the most pronounced collapse, while the wall in Figure 3.18a showed the least. According to the literature, this height reduction occurs due to heat accumulation at the end of the walls when a one-way deposition strategy is used. The wall in Figure 3.18d, manufactured using an alternating deposition strategy, avoids heat accumulation by distributing it at the two extremities. Consequently, no significant height loss was observed with this deposition strategy. We also used this deposition strategy for the walls manufactured by WLAM, and no collapse was observed. Thus, all walls and blocks were manufactured with a two-way deposition strategy.

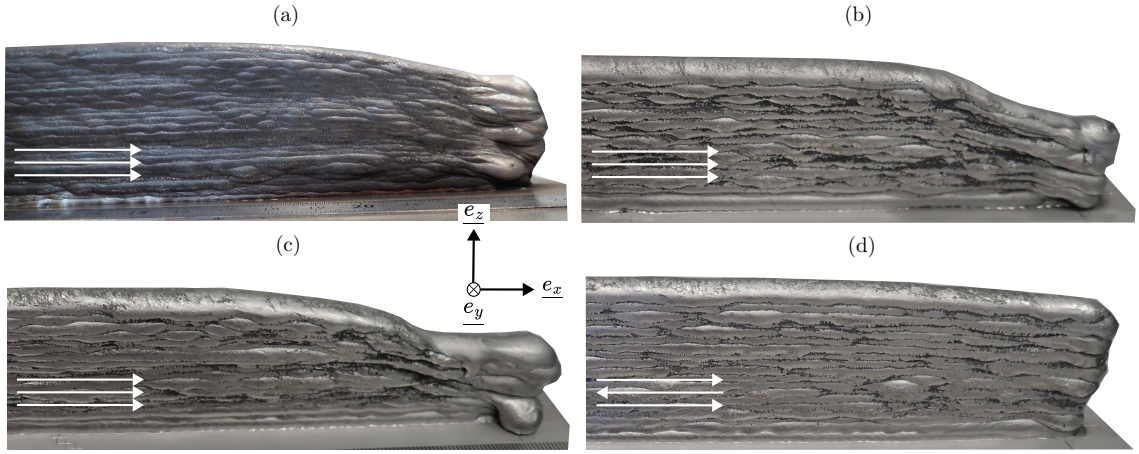

Figure 3.18. Single-bead walls obtained with WAAM using: (a), (b), and (c) one-way deposition strategy and parameters Sets 1, 2, and 3 (Table 3.5), respectively; (d) alternated deposition strategy and the parameter Set 3 (Table 3.5).

Additional parameter is the interlayer cooling time. The influence of the interlayer cooling time on the manufacturing of 20-layer single-bead walls was characterized by B.R. Ateba during his internship [179]. The profile of 20-layer single-bead walls manufactured by WLAM with the parameters Set 2 (Table 3.4) was compared when applying an interlayer cooling time of 20 s (Figure 3.19a) and 0 s (Figure 3.19b). It was found that the width of the wall manufactured with an interlayer cooling time of 20 s is nearly constant over its entire height. In contrast, a variation of 15% is observed when no interlayer cooling time is applied. The last layers are wider than the first one due to heat accumulation caused by insufficient cooling, resulting in a larger melt pool akin to an increase in power. In addition, we reported a variation of 10% on the height of the obtained walls for the same number of layers. It impacts the manufacturing as the height increment was calibrated on the average height of the first bead without taking the heat accumulation effect into account. The 20 s interlayer cooling time was selected at this step for the manufacturing of single-bead walls using the WLAM process. A similar study was achieved for the WAAM process, leading to selecting a 180 s interlayer cooling time.

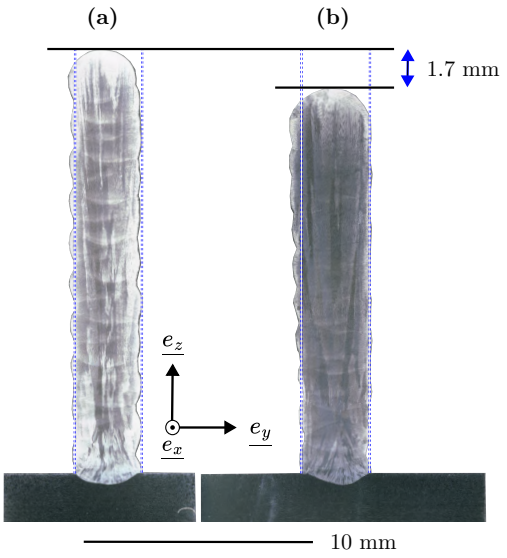

Figure 3.19. Etched transverse cross-section of 20-layer single-bead walls manufactured with WLAM process using the parameters Set 2 (Table 3.4) and interlayer cooling times of (a) 20 s and (b) 0 s.

3.3.2 Selection of processing parameters

In Section 3.2.1, three sets of parameters per process were selected for single-bead processing (Tables 3.4 and 3.5). This section aims to select a single set of parameters for further processing based on surface roughness measurements and deposition rates. A compromise is being sought between the deposition rate and the roughness of the manufactured components, considering that the WLAM process guarantees a better surface finish due to the smaller size of the deposits but a lower deposition rate than the WAAM process. A laser profilometer developed at CEA/LISN was employed to determine the surface state of several single-bead walls. The profilometer operates by laser triangulation and can measure surfaces of 40×150 mm^2 with an accuracy of around 5 µm.

The measurements were achieved in parts of the walls where no macroscopic collapse occurred (*i.e.* the left of the walls in Figure 3.18). This roughness was computed from 19 profiles measured using a laser profilometer. Among the walls (Figure 3.18), the one manufactured with Set 1 (Table 3.5) exhibited the lowest standard deviation at 0.27 mm, compared to 0.59 mm for the wall with Set 2 (Table 3.5), 0.62 mm for set 3 (Table 3.5), and 0.55 mm for the wall manufactured using set 3 (Table 3.5) with an alternating deposition strategy. We noted that the roughness of the wall manufactured with a one-way deposition strategy and set 3 is comparable to that of the wall manufactured using an alternated deposition strategy and set 3, indicating a low influence of the deposition strategy on the surface aspect of the walls. We then assumed that roughness measurements on (collapsed) walls made with a unidirectional deposition strategy could be extrapolated to (non-collapsed) walls made with a bidirectional deposition strategy. The wall manufactured with set 1 demonstrated the lowest surface roughness,, with a standard deviation in width representing only 3% of the total width. In contrast, walls manufactured with Sets 2 and 3 had higher standard deviations in width, accounting for 6% and 7% of their total widths, respectively. Moreover, the wall produced with Set 1 was produced with the highest applied volume energy of 50.9 J /mm^3, whereas the walls produced with Sets 2 and 3 had lower applied volume energies of 40.7 J/mm^3 and 42.4 J/mm^3, respectively. This suggests that the applied volume energy influences the surface roughness in the WAAM process.

However, knowing the dimensions of the manufactured components (approximately 10 mm in width and 40 mm in height), we considered a mean standard deviation of less than 1 mm satisfactory for this work, which is the case for all the walls manufactured with WAAM. Additionally, when evaluating deposition rates, the wall produced with Set 3 had the highest deposition rate at 33.9 g/min, compared to 22.6 g/min for the first set. Therefore, we selected Set 3 (Table 3.5) for WAAM manufacturing, as it provided a satisfactory surface state while maximizing the deposition rate.

20 mm-high single-bead walls were manufactured by WLAM (Figure 3.20) using the selected parameters for single beads (Table 3.4). Unlike the WAAM process, all three walls displayed a regular surface state along their deposition direction, as the surface roughness appears to be primarily influenced by the roundness of the deposited beads. For the WLAM process, we observed that the surface roughness was influenced by the number of deposited layers. The wall produced with Set 1 (Table 3.4), requiring 34 layers to reach the 20 mm height target, had the best surface finish, whereas the wall produced at 3500 W (Set 3, Table 3.4), requiring only 22 layers, had the worst. The roughness was not determined quantitatively for the single-bead walls manufactured by WLAM, as it was noticed that the roughness is directly linked to the shape of the beads and, therefore, their dimensions. However, in terms of deposition rate, Set 1 resulted in a lower rate of 4.5 g/min, while Set 2 (Table 3.4) achieved a rate more than four times higher at 18.1 g/min. Consequently, we selected Set 2 (Table 3.4) for WLAM, offering a reasonable compromise between surface roughness and deposition rate.

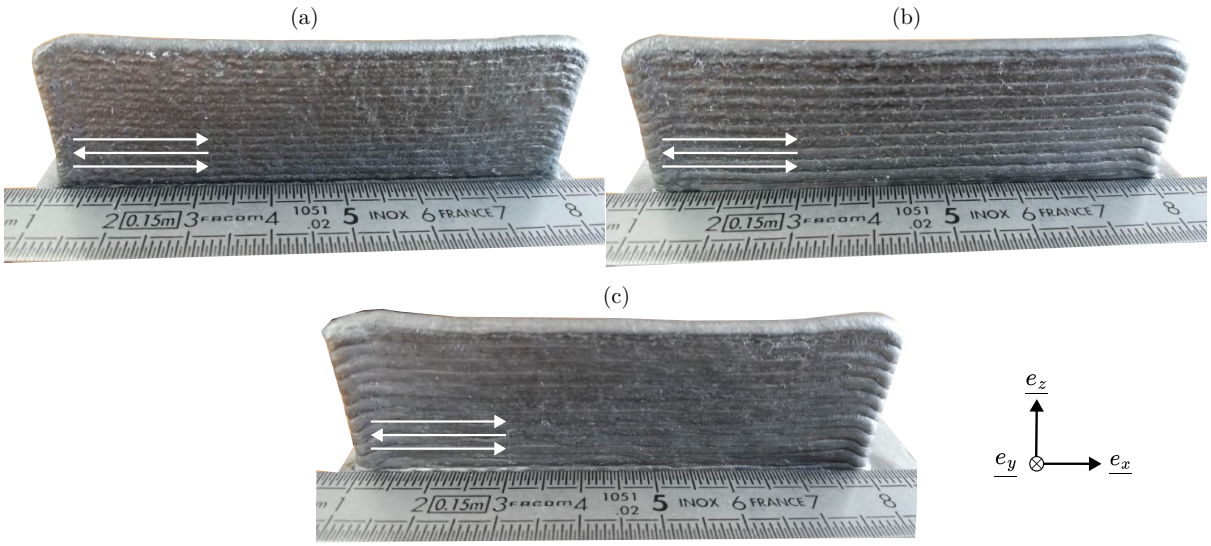

Figure 3.20. 20-layer single-bead walls manufactured with WLAM process using the sets of parameters presented in Table 3.4: (a) Set 1, (b) Set 2 and (c) Set 3 and "two-way" deposition strategy.

The selected process parameters for both WAAM and WLAM are summarized in Table 3.6.

Table 3.6. Sets of parameters after parametrical investigation, used for manufacturing the two selected single-bead walls with WAAM and WLAM processes.

Process parameters	**WAAM**	**WLAM**
Wire diameter, d_w $[mm]$	1.2	1.2
Wire feed rate, r_w $[mm/min]$	3750	2000
Deposition speed, s $[mm/min]$	200	800
Experimental heat source power, Q_{exp} $[W]$	3000	2400
Interlayer cooling time, t [s]	180	20
Layer height, δz $[mm]$	1.98	0.9
Argon flow rate, l $[L/min]$	30	15

Pictures of the walls manufactured with WAAM and WLAM using these parameters are presented in Figure 3.21. The wall obtained with WAAM (Figure 3.21a) reached the height of 40 mm with 20 layers, while 44 layers were required for the wall manufactured by WLAM (Figure 3.21b) to reach the same height. The wall produced by WLAM presents, however, the lower surface roughness. Moreover, both processes achieved a regular height of walls throughout the whole deposition, even if the WAAM wall tends to collapse slightly at the edges. This was not considered problematic, as the variation in height does not amplify as the number of deposited layers increases.

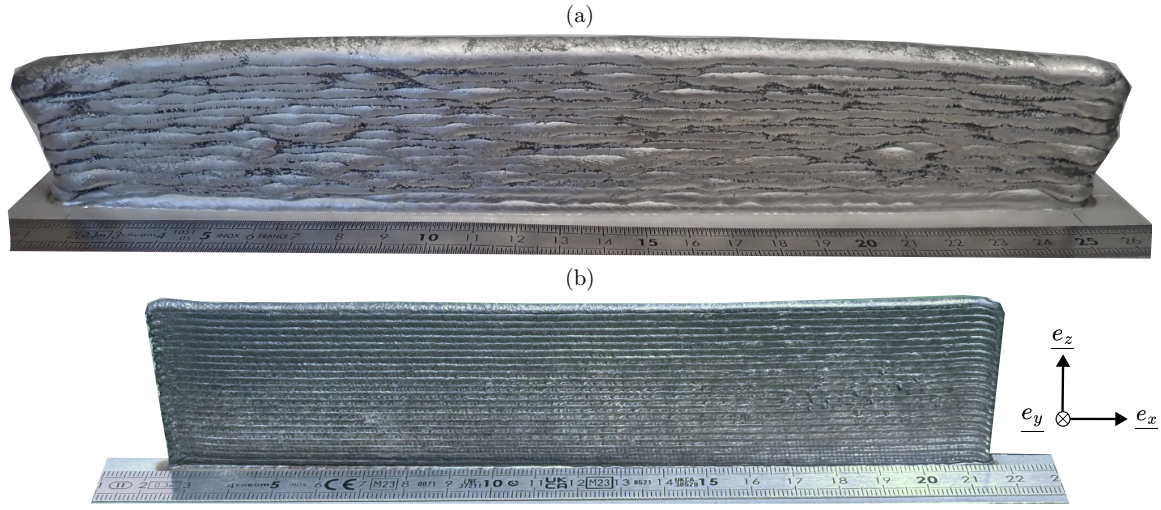

Figure 3.21. Processing of single-bead walls with the selected parameters (Table 3.6): (a) 20-layer wall produced with WAAM process; (b) 40-layer wall manufactured with WLAM process.

3.3.3 Manufacturing of a 100 mm-high wall

Now that we have selected parameters for the manufacturing of 20-layer single-bead walls, we want to adapt them to the production of higher walls, targeting a height of 100 mm. The first attempt was made using the WLAM process, using the experimental set of parameters outlined in Table 3.6. The manufacturing of a single-bead wall, shown in Figure 3.22, was stopped at a height of 60 mm due to deposition issues. As the number of deposited layers increased, the profile along the deposition direction became irregular. This irregularity was attributed to insufficient interlayer cooling time, as heat dissipation became more difficult with the accumulation of the number of layers, which caused the wall to be less high than expected. Indeed, a bead laid on a non-cooled wall will be wider and shorter as it will be manufactured with a higher effective linear energy. This further leads to a defocused laser since

the height increment becomes too high. We noticed previously for single beads that a defocus in the laser led to manufacturing issues, as it was presented in Figure 3.3.

Figure 3.22. Single-bead wall achieved with WLAM of height of 60 mm (instead of the targeted 100 mm) using an interlayer cooling time of 20 s. The wall manufacturing was stopped due to processing issues.

To address this issue, a second wall was manufactured using the WLAM process with an increased interlayer cooling time of 45 seconds. This wall, presented in Figure 3.23a, successfully reached the target height of 100 mm, requiring 112 layers. The wall presented a comparable surface state to the 20-layer single-bead wall made by WLAM with similar parameters (Set 2, Table 3.4), where the roughness is mainly determined by the size of the deposited layers. However, a defect is visible on the left side of the wall, where a failure to properly follow the laser extinction ramp caused a partial collapse. Despite this defect, the production was completed.

A similar wall was also produced using the WAAM process, consisting of 54 layers (Figure 3.23b). The surface roughness of the 100 mm-high wall is similar to that of the 20 mm wall shown in the previous Figure 3.21a. However, there is a slight irregularity in the wall height, with the edges being marginally lower than the central section. This collapse at the extremities is comparable to the one observed in the 20-layer single-bead walls achieved with a unidirectional deposition strategy, except in magnitude, which is less important due to a better heat distribution caused by the alternated deposition strategy.

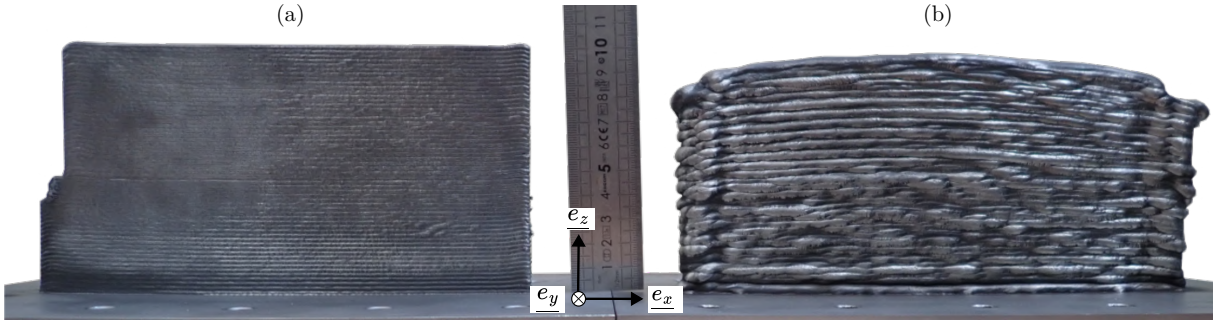

Figure 3.23. 100-mm high single bead walls produced with (a) WLAM process and (b) WAAM process. The two defects at the left of the wall manufactured by WLAM and at the right of the wall manufactured by WAAM are the consequence of production issues and are not linked to the choice of the processing parameters.

Thus, manufacturing process parameters allowing the production of thin components up to 100 mm in height were determined. The height increment, deposition strategy and interlayer cooling time significantly influence manufacturing. In the following Section 3.4, we will adjust the process parameters for manufacturing a thick component involving the juxtaposition of several beads per layer.

3.4 Processing conditions for multi-bead layer components

Now that processing conditions for the manufacturing of thin sections (single-bead walls) were determined, these parameters were transferred to the manufacturing of multilayer tiles, corresponding to thick zones of a complex component. Process parameters associated with tile manufacturing were also determined (overlap, deposition strategy).

3.4.1 Influence of the process parameters

To define the process parameters for multi-bead layered components, 20-layer high tile with six passes per layer was built following the trajectory illustrated in Figure 3.24. The manufacturing process employed an alternating deposition direction between layers, as explained previously. Specifically, the passes in layer n were deposited along $\underline{e_x}$ and $\underline{e_y}$, while the passes in layer n+1 were deposited along $-\underline{e_x}$ and $-\underline{e_z}$. This manufacturing strategy extends the approach used for fabricating thin components. Palmeira Belotti *et al.* [112] employed a similar deposition strategy in their WAAM process for manufacturing a 316LSi block. Their results showed that this approach produced a regular block along the deposition direction, even if height irregularities were present. Furthermore, Lee *et al.* [155] observed that an alternating deposition strategy can help reduce distortions and residual stresses within the components, compared to a unidirectional deposition strategy.

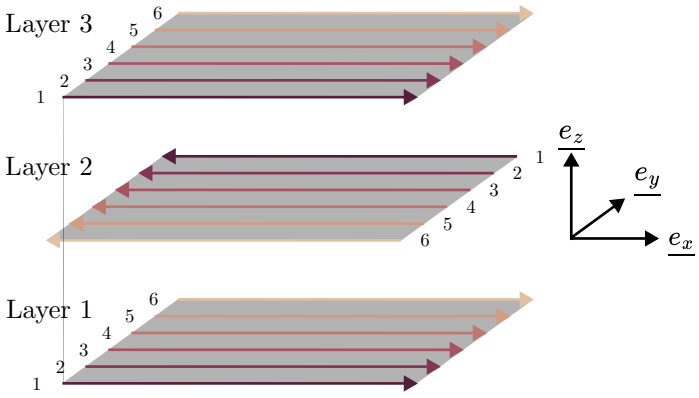

Figure 3.24. Schematic of the deposition sequence for tile manufacturing with WAAM and WLAM processes.

For the WLAM process, various inter-bead distances were tested for laser powers of 1000, 2400 and 3500 W using Sets 1, 2 and 3 (Table 3.4). Figure 3.25 illustrates the results of manufacturing a 12-bead layer using Set 1 (Table 3.4) and a laser power of 1000 W with different inter-bead distances. For a transverse overlap of nearly 60% (Figure 3.25a), metal accumulation occurred at the surface of the layer. In contrast, when applying a transverse overlap of 78%, holes were observed in the deposition profile due to a lack of covering (Figure 3.25c). The visually flattest layer was achieved with a transverse overlap of 68% (Figure 3.25b). Three overlaps were tested for Set 2 (Table 3.4): 61%, 67% and 79%, and for Set 3 (Table 3.4): 61%, 66%, and 78%. Similar results were observed, with the nearest value to a 70% overlap producing the visually flattest layer (*i.e.* 67% for 2400 W and 66% for 3500 W). These findings align with the observations of Shaikh *et al.* [38]. According to the literature, a flat surface over each layer of a block is achieved for overlap between two consecutive passes of approximately 70% of the bead width [38]. This guideline was successfully applied in the WAAM process, where a transverse overlap of 7 mm, corresponding to 67% of the bead width, resulted in a flat surface.

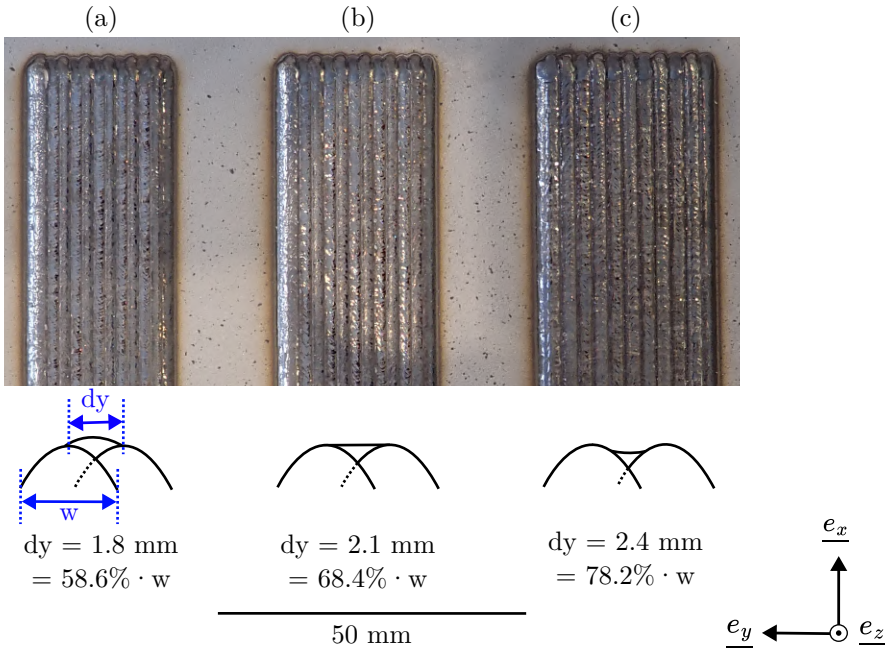

Figure 3.25. 12-bead layers manufactured by WLAM using set 1 (Table 3.4), with overlap distances of (a) 1.8 mm, (b) 2.1 mm and (c) 2.4 mm.

During the initial experimental tests with the WAAM process, the optimized parameters for thin walls led to issues when depositing six beads per layer. Specifically, there was insufficient wetting between the substrate and the beads, as well as between the beads themselves, as shown in Figure 3.26. In addition, depositing several beads in the same layer reduced the width/height ratio, making it more difficult for the beads to adhere to their neighbors.

Thus, the manufacturing power was increased to 3600 W, representing a 20% increase while maintaining the same deposition rate. This adjustment enhanced the wetting of the beads to the substrate by increasing the applied volume energy without altering the deposition rate. Experimental tests with the increased power demonstrated improved wetting of the beads. A similar result was observed for the WLAM process, thus the laser power was raised from 2400 to 2880 W.

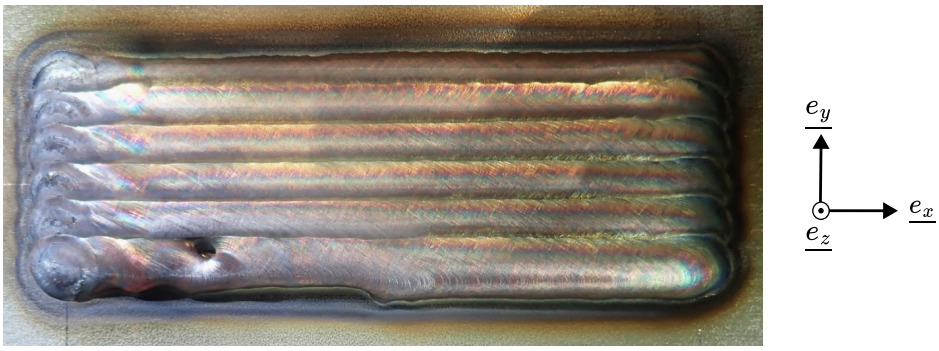

Figure 3.26. Layer of 6-beads achieved using WAAM process with set 3 (Table 3.5), and an overlap of 70%.

Finally, the presence of porosity was highlighted in the tile manufactured by WLAM, as presented in Appendix A.3. The tests aimed at adjusting the operating parameters to avoid the formation of this porosity were not carried out.

3.4.2 Geometric adjustment

During our initial attempt to manufacture the 6×20 tile (6 beads and 20 layers) using the WLAM process, we observed that edges of the tile lacked the expected height. Consequently, we had to stop the production of the tile shown in Figure 3.27 at the twelfth layer. This deviation led to an increase in the distance between the deposition head and the bead, resulting in manufacturing issues similar to those described in Figure 3.3h. This problem happened because one side of the beads at the layer extremities was not constrained by adjacent beads, allowing these beads to flatten, as schematized in Figure 3.27b. As more layers were added, this effect was amplified. To address this issue, we decided to add additional beads every four layers at the extremities, as shown in Figure 3.27c, to adjust the height. Similarly, six additional beads were added when necessary during the manufacturing of the 6×20 tile using the WAAM process, first at the tenth layer and then every fourth layer at the fourteenth and eighteenth layers.

The final 6×20 layer tiles manufactured using the WAAM and WLAM processes are presented in Figure 3.28. We achieved regular manufacturing regarding the height profile along the deposition direction and the transverse section. The component produced by WLAM (Figures 3.28a and d) reached a height of 26 mm after 20 layers, compared to 46 mm for the component manufactured by WAAM (Figures 3.28b and c). The block produced by WLAM exhibits a better surface roughness compared to the WAAM block. Additionally, the standard deviations of the width along the manufacturing direction and the height along the transverse direction were measured for the block achieved by WAAM to be 1.1 mm each, representing 2% of the width and the height, which is considered satisfactory. Despite a strong clamping, a significant deformation of the substrate (approximately 5 mm) was observed at the end of the WAAM process. A deflection of about 1 mm was also observed for the components manufactured with the WLAM process.

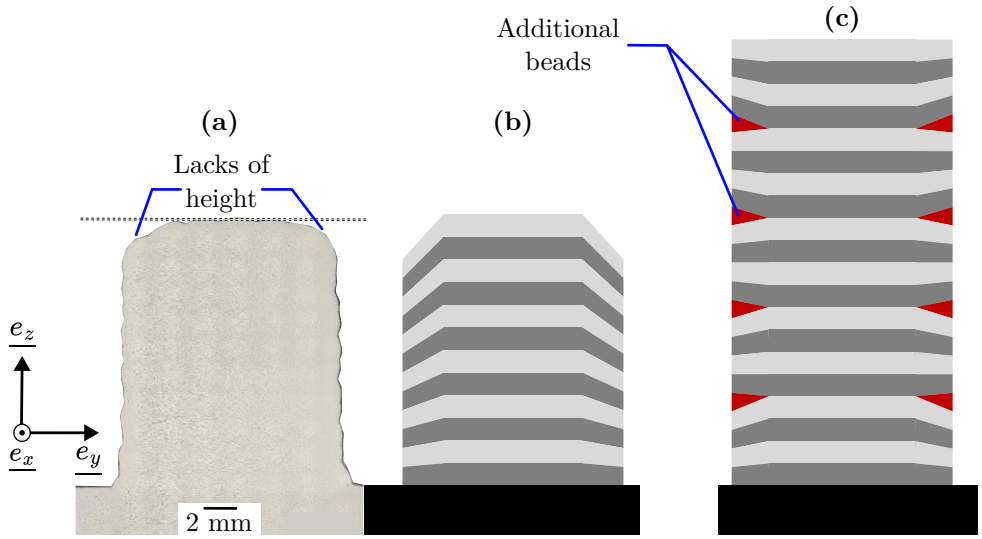

Figure 3.27. Height issues and height adjustments for a 6 × 12-bead tile manufactured with WLAM: (a) tile height without additional beads; (b) Schematic drawing of a 6 × 12-bead tile with WLAM without additional beads. The grey shades represent the successive layers deposited during the manufacturing. (c) Schematic drawing of a 6 × 20-layer tile, with additional beads added to balance the lack of height (red).

Figure 3.28. Tile manufactured using: (a) and (d) WLAM process; (b) and (c) WAAM process.

3.5 Conclusion to Chapter 3

In Chapter 3, we determined optimal manufacturing conditions to produce defect-free components with WAAM and WLAM processes. Single beads, single-bead walls, and multilayer tiles were achieved with a regular height and width.

The influence of the main process parameters (*i.e.* the deposition speed s, the wire feed speed v_w, and the power of the energy source Q_{exp}) on the morphology of the beads was studied. The process parameters were also linked to physical ratios, such as the linear energy density E_l, the volume energy density E_v, the surface of the bead cross-section S, and the deposition rate d_{rate}:

- The volume energy density impacts the continuity of the deposited beads, causing balling in WAAM if E_v is too low or stubbing and dripping in WLAM if E_v is too low or too high, respectively.
- A strong synergy was observed between the process parameters in both WAAM and WLAM. Targeted geometrical ratios were chosen, reaching a compromise between the absence of porosity and the maximization of the deposition rate. The width/height ratio has to be between 2 and 4, while the dilution of the single bead in the substrate has to be between 10 and 35%. Maps of the influence of the process parameters on the geometrical ratios were then drawn, allowing us to select three manufacturing conditions per process. The obtained maps can be reused or refined for future work to identify possible processing ranges before manufacturing.
- Empirical equations linking the geometrical selection criteria and the physical and process parameters were obtained, estimating the width/height and dilution ratios of a bead as long as remaining within the range tested in this work.

Next, the process conditions were chosen for the manufacturing of single-bead walls. New parameters influencing their geometry (height increment, deposition strategy, interlayer cooling time) were calibrated. One experimental condition was then selected for each process and further tested to manufacture 100 mm-high walls:

- The wall **height increment** was calibrated for the WLAM process by taking the closest value to the average height of a single bead. Too high or too low values resulted in irregularities in height, blocking the manufacturing. For the WAAM process, no calibration was required as the height increment is regulated by the tension of the electrical arc.
- For single-bead walls manufactured by WAAM with a one-way **deposition strategy**, a macroscopic collapse at one edge, attributed to local heat accumulation, limited the manufacturing. It was not observed using an alternated deposition strategy. We then established that the chosen deposition path must distribute the heat in the component as evenly as possible.
- The **interlayer cooling time** affects the final shape of the single-bead walls. An insufficient interlayer cooling time causes heat accumulation, resulting in variations in width and height. A thermal control of the manufacturing is required to ensure adequate cooling time between two layers.
- One set of parameters per process was selected by reaching a compromise between the surface roughness of the components and the deposition rate. For the WAAM process, all the single-bead walls had a satisfying surface roughness of less than 1 mm. Then, the set of parameters with the highest deposition rate was selected. For the WLAM process, we noted that the surface roughness is

mostly affected by the size of the deposited layers, creating bumps and valleys. Due to the relatively thin width of the single-bead walls, we selected the experimental condition manufactured at a laser power of 2400 W, to the detriment of the deposition rate.

Finally, we adapted the manufacturing conditions to produce multilayer components (6×20-layer tiles), reaching a satisfying geometrical homogeneity:

- The applied deposition path for the tiles manufacturing was inspired by the path applied for single-bead walls by alternating the deposition direction of the beads for each newly deposited layer and the order of deposition of the beads within the same layers.
- The **overlap between two adjacent beads** on the same layer was calibrated at 70% of the width of the bead, corresponding to the flattest profile in terms of height.
- Initial applied power resulted in insufficient wetting. To counter this effect, the power of the heat source was increased by 20% while keeping the other parameters constant.
- Height difference is created between the beads deposited at the edges of the layer and those located at the center, which caused manufacturing issues. To compensate for this effect, additional beads were added when necessary at the edges of the layers.
- Pores were observed within the tile manufactured by WLAM. This issue was not addressed in this work. We, however, noted that the presence of pores does not affect the shape of the grains, making it still satisfying for further characterization.

In the following chapters, we focused on characterizing the microstructure and the properties of the single beads, single-bead walls and tiles. In addition, they were also compared to finite element modeling results to provide a better understanding of the thermomechanical story experienced by the component during the manufacturing, at the scale of the whole component and more locally at the scale of the deposited bead.

This page was intentionally left blank.

Chapter 4

Microstructure and mechanical properties

Contents

Résumé en français du chapitre 4 : microstructure et propriétés mécaniques

La microstructure et les propriétés mécaniques des pièces en acier 316L fabriquées par WAAM et WLAM ont été étudiées pour différentes conditions de fabrication.

La composition chimique des murs (Tableau 4.1) s'est révélée être globalement similaire à celle du fil d'apport. Cependant, une augmentation significative du taux d'oxygène a été constatée (surtout pour le procédé WLAM (de 0 à 0,1 mass.%)). Cette augmentation est attribuée à un inertage insuffisant entraînant la contamination du métal fondu par l'air ambiant.

Les teneurs équivalentes en nickel et en chrome, à l'aide du diagramme de Schaeffler (Figure 4.1), indiquent la formation d'une microstructure majoritairement austénitique avec une fraction de ferrite comprise entre 5 et 10 vol.%.

L'étude préalable des monocordons a permis de mieux comprendre l'origine de la microstructure formées dans les pièces fabriquées par WAAM et WLAM. Deux zones aux microstructures distinctes ont été identifiées (Figure 4.2): (i) le cœur des cordons possédant une microstructure aux grains allongés, résultant d'une solidification colonnaire et épitaxiale (Figure 1.18), avec une texture cristallographique, et (ii) une "enveloppe" de grains équiaxes dans la coupe transverse, probablement formée au cours du refroidissement du métal par l'air ambiant ou bien au cours d'une transition colonnaire-équiaxe liée à la diminution de la vitesse de refroidissement à mesure que la solidification s'effectue. Lors du dépôt des cordons adjacents, nous avons supposé que l'enveloppe des cordons serait largement refondue. C'est donc la microstructure observée au cœur des cordons qui va servir de base à la microstructure des pièces fabriquées. Enfin, nous avons observé que chaque grain est constitué de plusieurs dendrites orientées dans la direction de fabrication $\underline{e_z}$ (Figure 4.5), entraînant la formation de sous-joints de grains et de désorientation intragranulaire (révélée par le critère GOS à partir des données EBSD).

La direction d'élongation des grains et la texture cristallographique sont étroitement liées à la forme des bains de fusion. Des différences de texture ont été observées entre les monocordons fabriqués par WAAM et WLAM, en raison de la géométrie distincte des bains : arrondie pour le WLAM et arrondie au centre mais aplatie aux extrémités pour le WAAM. La solidification colonnaire favorise les grains orientés selon $\langle 001 \rangle$ dans la direction du gradient thermique, privilégiant ainsi ces orientations. Enfin, nous avons observé que les grains obtenus par WLAM sont plus petits que ceux issus du WAAM (Figure 4.4).

L'analyse de la microstructure a indiqué une solidification de type FA, de par la présence de ferrite dite "vermiculaire" et "en lamelles" (Figure 4.6), typique pour l'acier 316L obtenu dans les conditions de solidification de la fabrication additive par dépôt de fil. La teneur en ferrite a été mesurée à 5-6% pour le WLAM et de 8-9% pour le WAAM, ce qui est cohérent avec les prédictions du diagramme de Schaeffler. Enfin les vitesses de refroidissement basées sur la mesure des espacements dendritiques ont été estimées à environ 100 °C/s pour le WAAM et dix fois plus à 1000 °C/s pour le WLAM.

L'étude des murs (Figures 4.11 et 4.12) a montré la présence de grains allongés sur plusieurs dizaines de passes, fortement texturés selon $\langle 001 \rangle_{\parallel \underline{e_z}}$ (où $\underline{e_z}$ est la direction de fabrication). Des dislocations sans organisation particulière ont été détectées dans l'austénite et dans la ferrite (Figure 4.24), indiquant un stockage d'énergie pouvant conduire a une évolution de la microstructure. Enfin, le mauvais inertage durant la fabrication a entraîné la formation d'inclusions sphériques d'environ 1 µm de diamètre (Figure 4.22), identifiées comme des oxydes complexes, avec des volumes totaux estimés

à 1,47% pour le WLAM et 0,47% pour le WAAM.

Des essais de traction (Figure 4.26) réalisés sur des éprouvettes prélevées dans les directions de fabrication $\underline{e_z}$ et de dépôt $\underline{e_x}$ ont été effectués et ont révélé une légère anisotropie des propriétés pour le mur fabriqué par WLAM, tandis que le mur fabriqué par WAAM présente des propriétés mécaniques similaires dans les deux directions. Cette anisotropie accrue induite par le WLAM est attribuée à des grains plus allongés et une texture cristallographique plus marquée (Figure 4.27). Le procédé WAAM apparaît ainsi plus adapté pour des applications où l'anisotropie est un critère limitant. Par ailleurs, des élongations à rupture (autour de 40%) et des résistances maximales à la traction comparables à celles du 316L obtenu par des procédés conventionnels ont été mesurées (Tableau 4.3).

Des duretés plus élevées pour les murs fabriqués par WLAM par rapport à ceux réalisés par WAAM ont été mesurées (Figure 4.25). En particulier, les premières couches déposées présentent les duretés les plus importantes (190 HV_{10} pour le WLAM et 182 HV_{10} pour le WAAM), supérieures à celles du 316L conventionnel (150 HV_{10}). Cette différence peut être expliquée par plusieurs facteurs : la présence de ferrite, l'écrouissage induit par des cycles de chauffage/refroidissement ou encore la présence de contraintes résiduelles.

L'étude des blocs fabriqués par WAAM et WLAM (Figures 4.29 et 4.30) a révélé une microstructure distincte de celle des murs, avec des grains plus petits et moins allongés. De plus, ces blocs présentent une dureté plus élevée et une taille de dendrites plus petite en comparaison aux murs. Plusieurs zones aux textures différentes ont été observées :

- Pour le bloc réalisé par WLAM, la zone centrale de fusion (CFZ, Center of Fusion Zone) et les extrémités des zones de fusion (SFZ, Side of Fusion Zone). La SFZ est majoritaire et est caractérisée par une texture crystallographique selon $\langle 011 \rangle_{\parallel \underline{e_z}}$ et une élongation des grains à 45° de la direction de fabrication $\underline{e_z}$, tandis que la CFZ présente une texture $\langle 001 \rangle_{\parallel \underline{e_z}}$ avec des grains orientés dans la direction de fabrication $\underline{e_z}$.
- Pour le bloc réalisé par WAAM, la zone refondue (OR, overlapped area) et la CFZ, dans des proportions équivalentes. L'OR se situe là où les bains de fusion ont une bordure plate. Les grains y présentent une texture selon $\langle 001 \rangle_{\parallel \underline{e_z}}$ et sont allongés dans la direction de fabrication $\underline{e_z}$. Dans la CFZ, associée à la partie arrondie du bain de fusion, une texture selon $\langle 011 \rangle_{\parallel \underline{e_z}}$ et une élongation des grains à 45° de la direction de fabrication $\underline{e_z}$ est observée.

L'effet des traitements thermiques sur la microstructure des murs monocordons a également été étudié. Des calculs réalisés à l'aide du logiciel Thermo-Calc indiquant les différentes phases formées à l'équilibre thermodynamique en fonction de la température (Figure 4.33) ont montré que la température de traitement thermique doit dépasser 1000 °C pour éviter la formation de la phase σ, néfaste aux propriétés du matériau. Deux traitements thermiques différents ont été alors réalisés (Figures 4.36 et 4.38) :

1. Un traitement à 1100 °C pendant 30 minutes, suivi d'une trempe à l'eau, a conduit à une faible modification de la taille et la morphologie des grains, mais a réduit la teneur en ferrite à 0,7 vol.% et la dureté à 160 $HV_{0,1}$ pour le mur réalisé par WLAM. Lorsque la présence de ferrite est un facteur limitant pour l'application des pièces, ce traitement thermique permet la réausténitisation de la microstructure sans influer sur la forme et l'orientation des grains.
2. Un second traitement à 1200 °C pendant 30 minutes, suivi d'une trempe à l'eau a conduit à une recristallisation partielle, notamment dans les zones où les grains sont les plus petits (au

pied et aux bordures des murs). La dureté a diminué à 150 $HV_{0,1}$, ce qui correspond à la valeur caractéristique du 316L obtenu à l'aide de procédés conventionnels, suggérant une diminution du taux de dislocations et la relaxation totale de l'énergie mécanique stockée dans le matériau. La forme de grains et la texture observées dans les murs sont donc peu susceptible d'évoluer sous l'effet de la température.

4.1 Chemical composition

To probe the effect of processing on chemical composition, the composition of single-bead walls produced by WAAM and WLAM using Set 3 (Table 3.5) and Set 2 (Table 3.4) was analyzed using ICP-AES and elementary analysis (Table 4.1). For the major alloying elements, the composition of the 316L single-bead walls is mainly consistent with that of the filler wire. However, a slightly reduced chromium content was observed in the walls compared to the wire: -0.2 wt.% for WAAM and -0.8 wt.% for WLAM. The oxygen content in the single-bead walls showed a significant increase compared to the filler wire, at 0.025 wt.% in WAAM and was five times higher in WLAM at 0.12 wt.%. This difference is attributed to contamination from ambient air despite the use of argon shielding near the melt pool to create an inert atmosphere. As noted by Deng *et al.* [180], such oxygen levels can lead to the formation of oxide inclusions within the metallic matrix. Additionally, increased concentrations of several minor alloying elements, including copper, cobalt and aluminum, were detected in the walls produced using the WLAM process, likely due to external contamination during manufacturing.

Table 4.1. Chemical compositions (wt. %) obtained by ICP-AES and elementary analysis of (a) the initial filler wire and single-bead walls obtained by (b) WAAM (Set 3, Table 3.5) and (c) WLAM (Set 2, Table 3.4).

wt.%	Cr	Ni	Mo	Mn	C	N	Si	Cu	Co	P	S	Al	O
(a) Wire	19.20	12.66	2.88	1.78	0.016	0.045	0.46	0.042	0.031	0.013	0.007	0.005	-
(b) WAAM	18.96	12.50	2.84	1.80	0.014	0.048	0.46	0.044	0.032	0.013	0.007	0.005	0.025
(c) WLAM	18.4	12.5	2.58	1.35	0.009	0.049	0.34	0.12	0.20	0.022	0.013	0.055	0.12

The equivalent content of chromium and nickel was calculated (Equations 4.1 and 4.2 [115]).

$$\text{wt.\%Cr}_{eq} = \text{wt.\%Cr} + \text{wt.\%Mo} + 1.5 \times \text{wt.\%Si} + 0.5 \times \text{wt.\%Nb} = \begin{cases} 22.5 \text{ (WAAM)} \\ 21.5 \text{ (WLAM)} \end{cases} \tag{4.1}$$

$$\text{wt.\%Ni}_{eq} = \text{wt.\%Ni} + 30 \times \text{wt.\%C} + 30 \times \text{wt.\%N} + 0.5 \times \text{wt.\%Mn} = \begin{cases} 15.3 \text{ (WAAM)} \\ 15.0 \text{ (WLAM)} \end{cases} \tag{4.2}$$

According to the Schaeffler diagram [115] (Figure 4.1a), which predicts the phase fractions in 316L steel manufactured under welding cooling conditions based on equivalent nickel wt.%Ni_{eq} and chromium wt.%Cr_{eq} contents, a predominant austenitic phase is expected for both WAAM and WLAM walls, with approximately 5 vol.% of ferrite phase. The Schaeffler diagram also indicates that the ferrite content may be slightly higher in the wall manufactured by WAAM than in the one made with WLAM.

Next, the $\frac{\text{wt.\%Cr}_{eq}}{\text{wt.\%Ni}_{eq}}$ ratio was used to predict the solidification mode, yielding values of 1.47 and 1.44 for the WAAM and WLAM single-bead walls, respectively. These ratios were plotted on a pseudo-binary diagram of the Fe-Cr-Ni alloy (Figure 4.1b) [97]. Values near the transition line from the austenite-ferrite (AF) to ferrite-austenite (FA) solidification mode (1.48) were observed, indicating that both solidification modes are plausible under these conditions.

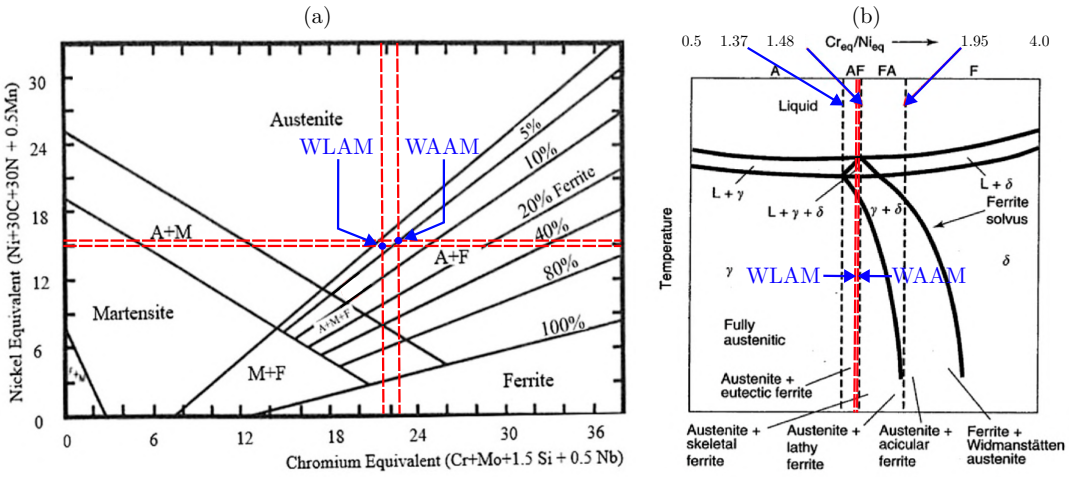

Figure 4.1. Analysis of expected phases in the manufactured 316L components with WAAM and WLAM using (a) the Schaeffler diagram [115] and (b) the Fe-Ni-Cr pseudo-binary diagram of 316L [97].

4.2 Single beads

4.2.1 Grain microstructure

Figure 4.2 shows EBSD orientation maps and associated inverse pole figures of transverse cross-sections of the single beads manufactured with WLAM using Set 2 (Table 3.4) and WAAM using Set 3 (Table 3.5). The crystal orientations are projected along the manufacturing direction $\underline{e_z}$ (Figures 4.2a and 4.2d) and the deposition direction $\underline{e_x}$ (Figures 4.2b and 4.2e), for WLAM and WAAM, respectively. Moreover, the inverse pole figures for WAAM and WLAM are presented in Figures 4.2c and 4.2f, respectively. The EBSD analyses of single beads fabricated with the other selected parameters (WLAM using Sets 1 and 3 (Table 3.4), and WAAM using Set 1 (Table 3.5)) are presented in Appendix B.1.

In addition, Figure 4.3 presents the grain morphology near the fusion line in a single bead produced with WLAM using Set 1. Orientation maps of the substrate and the bottom of the deposited bead were projected in the manufacturing direction $\underline{e_z}$ (Figure 4.3a) and the deposition direction $\underline{e_x}$ (Figure 4.3b), where the dotted line indicates the boundary between the melt pool and the substrate. The corresponding grain boundaries were identified (Figure 4.3c), distinguishing high-angle grain boundaries (HAGBs, dark lines), low-angle grain boundaries (LAGBs, cyan) and Σ3-twin boundaries (red).

The 316L substrate at the bottom of the maps shows equiaxed grains with a 50 µm average diameter and no visible texture. Each substrate grain contains Σ3-twin boundaries, which are characteristic of the microstructure of austenitic stainless steels obtained using conventional processing conditions [181].

Within the melt pool, elongated grains oriented along the manufacturing direction $\underline{e_z}$, with taller dimensions than the substrate grains, were observed. The columnar microstructure results from directional solidification along the thermal gradient, having a direction represented by the red arrow in Figure 4.3. Several grains at the fusion line were observed in both the melt pool and the substrate, indicating epitaxial growth in which the solidification follows the pre-existing crystal orientations. Colin *et al.* [98] reported that columnar solidification is typical in additive manufacturing processes due to the important thermal gradients. However, WLAM and WAAM additive manufacturing processes have the lowest thermal gradients among other additive manufacturing processes, which increases the probability of equiaxed

solidification under low dilution conditions. Nevertheless, equiaxed grains are not expected in this study as only the single beads with a sufficient dilution were selected (*cf.* Chapter 3).

Several crystal orientations are favored, notably in the two grains marked with a circled asterisk, having a $\langle 001 \rangle_{\parallel \underline{e_z}}$ orientation in the manufacturing direction $\underline{e_z}$ (Figure 4.3a). The predominance of the $\langle 001 \rangle_{\parallel \underline{e_z}}$ orientation results in crystal texture as the distance from the fusion line increases. In cubic crystals (such as fcc-austenite and bcc-ferrite), $\langle 001 \rangle$ is the preferential grain growth direction [182]. Grains with a $\langle 001 \rangle_{\parallel \underline{e_z}}$ orientation (aligned with the thermal gradient) will grow faster than those with other orientations. In contrast, the orientation map projected in the deposition direction $\underline{e_x}$ (Figure 4.3b) shows no preferred orientations in this direction. However, the tallest grains are oriented between $\langle 001 \rangle_{\parallel \underline{e_x}}$ and $\langle 011 \rangle_{\parallel \underline{e_x}}$, for geometrical reasons due to their orientation along $\langle 001 \rangle_{\parallel \underline{e_z}}$ in the manufacturing direction. Finally, unlike the substrate grains, the melt pool grains contain no $\Sigma 3$-twin boundaries (Figure 4.3c).

The direction of the epitaxial columnar solidification in the core region of the single beads, associated with elongated grains oriented perpendicularly to the fusion line, is represented by black arrows in Figure 4.2. A "skin effect" was also observed around the single beads, where equiaxed grains are reported, likely formed due to grain nucleation resulting from ambient air cooling or columnar-to-equiaxed transition due to a decrease in cooling rate as the solidification progresses. A similar effect was documented by Baumard [99] in the edges of 316L components produced by L-PBF.

Inverse pole figures revealed a general texture in the manufacturing direction $\underline{e_z}$, with a predominant orientation near $\langle 001 \rangle_{\parallel \underline{e_z}}$ (green and red asterisks, for WLAM and WAAM, respectively). This orientation is expected as it aligns with the preferential growth direction under the typical cooling conditions of WAAM and WLAM processes, where the thermal gradient, typically perpendicular to the fusion line, is roughly aligned with the manufacturing direction $\underline{e_z}$ [98]. However, a 15° misorientation relative to the $\langle 001 \rangle$ direction was observed for the single bead manufactured by WLAM, attributed to the curvature of the fusion line. The flatter fusion line at the sides of the bead manufactured by WAAM leads to a closer alignment of the thermal gradient with the manufacturing direction $\underline{e_z}$, but, as in WLAM, a similar 15° misorientation was noted in the center of the fusion zone due to the convex shape of the fusion boundary. Baumard [99] observed that in single beads manufactured with L-PBF, the convexity of the fusion line led to a $\langle 011 \rangle_{\parallel \underline{e_z}}$ texture and grains elongated diagonally, reflecting a 45° misorientation between the thermal gradient and the manufacturing direction.

In the deposition direction $\underline{e_x}$, a $\langle 113 \rangle_{\parallel \underline{e_x}}$ texture for WLAM (blue asterisk) and $\langle 111 \rangle_{\parallel \underline{e_x}}$ for WAAM (pink asterisk) were observed. These textures result from the three-dimensional nature of the thermal gradient, which has components along both the manufacturing $\underline{e_z}$ and deposition $\underline{e_x}$ directions. The textures correspond to a 15° misorientation with respect to the deposition direction for WLAM and 45° for WAAM, indicating a thermal gradient predominantly oriented in the manufacturing direction $\underline{e_z}$ in WLAM, but not in WAAM. Debroy *et al.* [3] noted that melt pool elongation in the deposition direction $\underline{e_x}$ correlates with the deposition speed s; a faster deposition speed, as in WLAM, leads to a solidification mainly oriented parallelly to the manufacturing direction $\underline{e_z}$, while slower deposition speeds in WAAM lead to inclined solidification (*cf.* Figure 1.18).

Similar microstructures were observed in single beads manufactured by WLAM using Sets 1 and 3 (Table 3.4) and by WAAM using Set 1 (Table 3.5), as shown in Appendix B.1. Beads produced at the lowest powers (Set 1 for WLAM and WAAM) presented a more pronounced texture in the manufacturing direction, likely due to the reduced convexity of the melt pool.

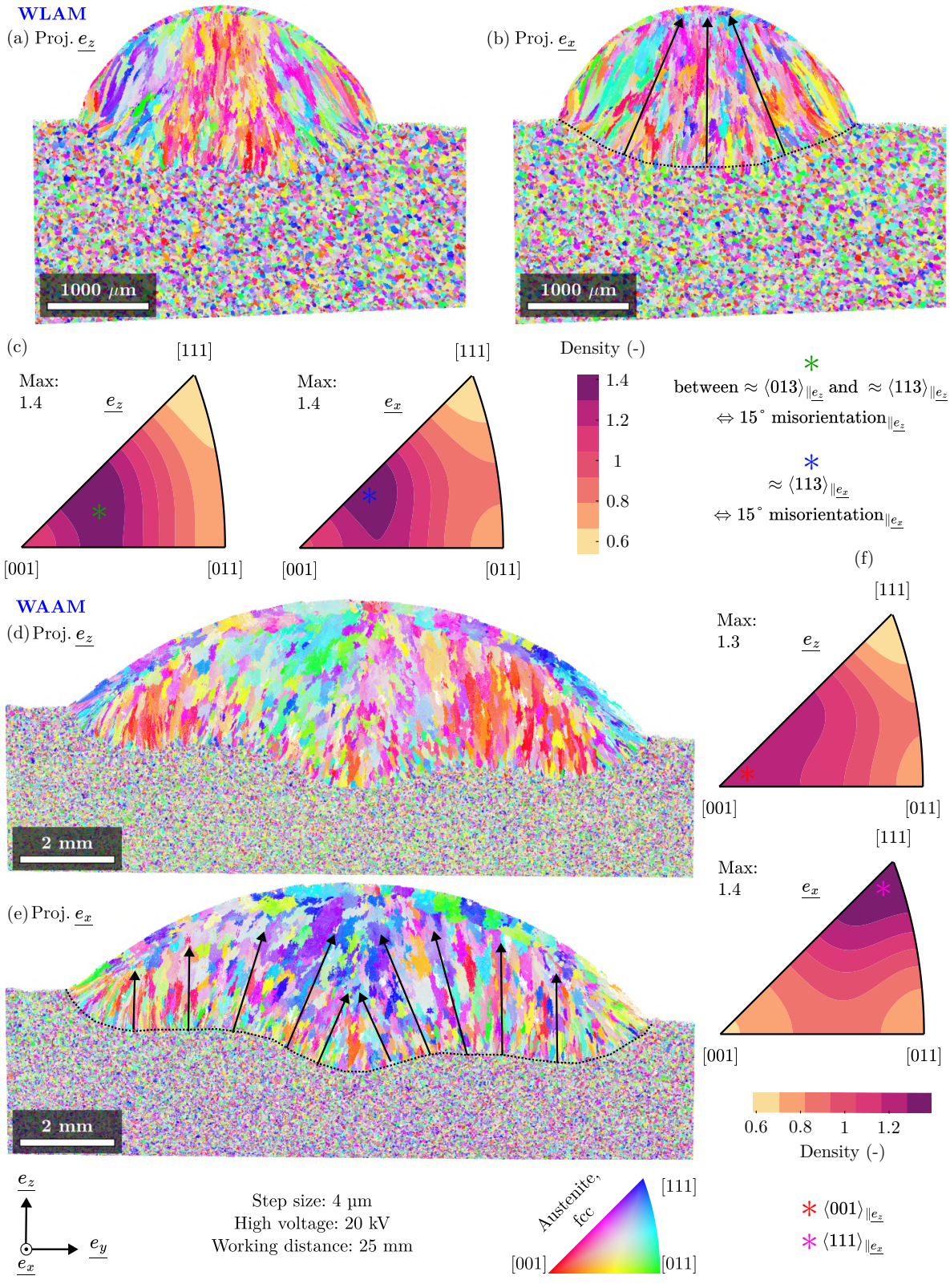

Figure 4.2. EBSD orientation maps and associated inverse pole figures of transverse cross-sections of single beads manufactured with WLAM using Set 2 (Table 3.4) and WAAM using Set 3 (Table 3.5): (a) WLAM single bead, projected along the manufacturing direction $\underline{e_z}$; (b) WLAM single bead, projected along the deposition direction $\underline{e_x}$; (c) associated inverse pole figures; (d) WAAM single bead, projected along the manufacturing direction $\underline{e_z}$; (e) WAAM single bead, projected along the deposition direction $\underline{e_x}$; (f) associated inverse pole figures. The black arrows indicate the local trend of the direction of elongation of the grains, and the different asterisks are the predominant textures.

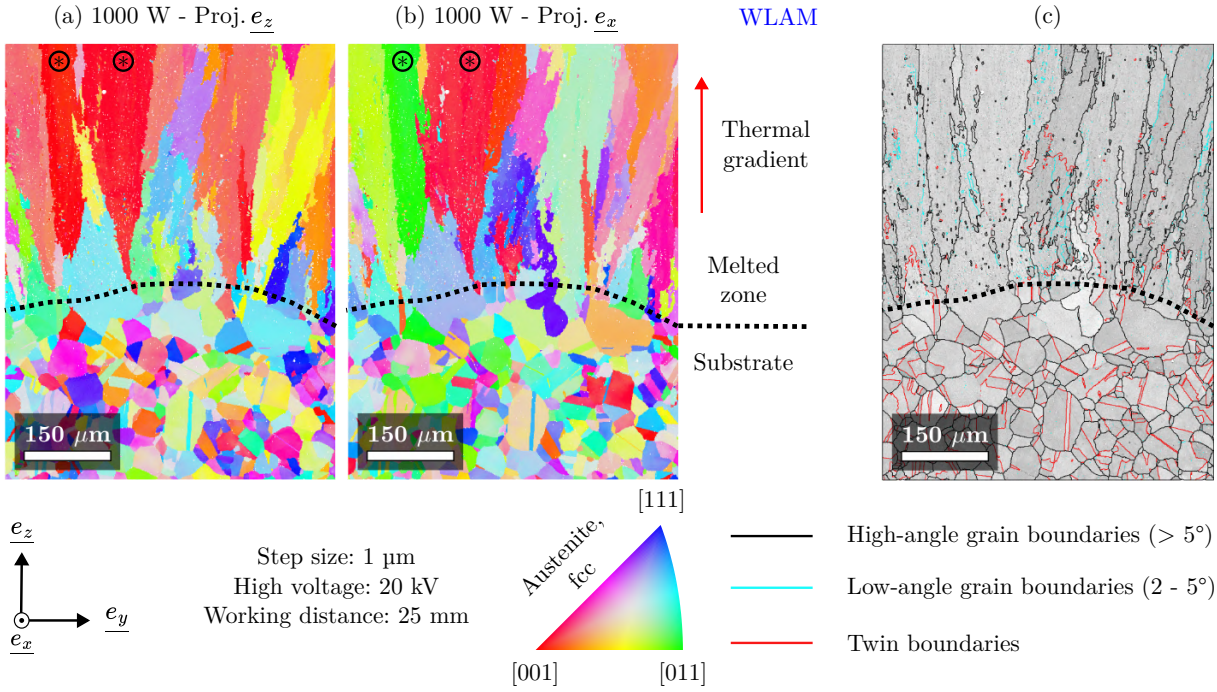

Figure 4.3. EBSD orientation maps of a transverse cross-section at the fusion line of a single bead produced by WLAM using Set 1 (Table 3.4): (a) orientation map projected along the manufacturing direction $\underline{e_z}$; (b) orientation map projected along the deposition direction $\underline{e_x}$; (c) index quality map showing high-angle (black) and low-angle (cyan) grain boundaries, along with Σ3-twin boundaries (red). Grains with their easy-growth direction aligned with the thermal gradient are marked with a circled asterisk.

Figures 4.4a and b show orientation maps of the microstructure in the center of single beads produced by WLAM and WAAM, respectively, at a finer scale than the macrographs in Figure 4.2. The maps were projected along the manufacturing direction $\underline{e_z}$ and overlaid with HAGBs and LAGBs. Smaller grains were observed in the single bead manufactured by WLAM. Moreover, a difference in the grain morphology was noted: elongated grains for WLAM versus equiaxed-like grains for WAAM. These equiaxed grains for WAAM could be formed due to the larger bead size and slower solidification rate as compared to WLAM. Baumard [99] also observed equiaxed-like grains in the center of 316L L-PBF single beads, noting, however, that these grains were columnar in the deposition direction. It might also be the case for our beads manufactured by WAAM, where the grains could have an elongated shape aligned with the deposition and manufacturing directions, appearing like equiaxed grains on the cross-sections.

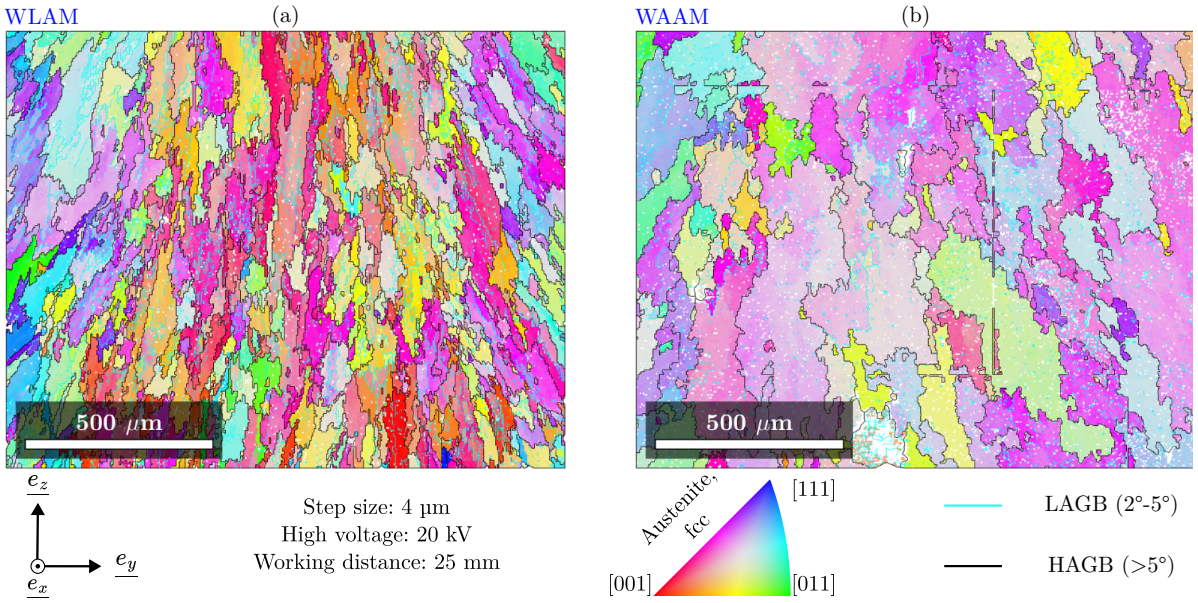

Figure 4.4. EBSD orientation maps of transverse cross-sections of the single beads manufactured with (a) WLAM using Set 2 (Table 3.4) and (b) WAAM using Set 3 (Table 3.5), projected in the manufacturing direction $\underline{e_z}$. The cyan lines represent the low-angle grain boundaries (LAGBs) and the black lines the high-angle grain boundaries (HAGBs).

Figures 4.5a and 4.5c illustrate the HAGBs (black), LAGBs (cyan) and Σ3-twins (red) for single beads produced by WLAM and WAAM, respectively. Notable differences were observed between the melt pool and the substrate:

- the substrate is constituted of numerous HAGBs, indicating relatively small grains and numerous Σ3-twins and few LAGBs, typical of a recrystallized state;
- to the opposite, the deposited metal is constituted of few HAGBs, indicating relatively coarse grains, no Σ3-twins and numerous LAGBs.

These differences highlight that the metal deposition by WAAM and WLAM allows for reaching a microstructure different from that of the forged and recrystallized substrate. The numerous LAGBs in the melt pool also reflect that each grain consists of multiple dendrites growing in similar directions, as shown in Chapter 1. In addition, the grain size in the transverse direction $\underline{e_y}$ was estimated using the intercept method (Table 4.2) to be of 27 µm for WLAM (using Set 2 (Table 3.4)) and of 52 µm for WAAM (using Set 3 (Table 3.5). No apparent influence of the process parameters on the grain size was observed in both processes.

Figures 4.5b and 4.5d present grain orientation spread (GOS) maps for single beads manufactured with WLAM and WAAM, respectively. The presence of several dendrites within each grain causes slight intragranular misorientations, resulting in GOS values between 1° and 5°. The intragranular misorientation in these grains remained low, as each dendrite maintains a similar orientation throughout the whole solidification. Smaller grains without intragranular misorientation were observed near the fusion line. The presence of smaller grains than in the rest of the single beads, caused by the initiation of the epitaxial solidification, is assumed to limit intragranular misorientations as these grains can comprise fewer dendrites than the taller grains located far from the fusion line.

Substrate grains situated far from the deposited bead showed no internal disorientation (GOS between 0° and 1°), while those close to the deposited bead exhibited higher internal disorientation (GOS between

1° and 2°). It was assumed that the increased GOS value in these grains is the consequence of thermal strains, indicating that this region of the substrate corresponds to the heat-affected zone. In addition, grain boundaries and GOS maps for single beads produced by WLAM using Sets 1 and 3 (Table 3.4) and by WAAM using Set 1 (Table 3.5) are presented in Appendix B.1. Single beads produced at the lowest power levels exhibited more elongated grains and reduced GOS values. This observation agrees with the observed more pronounced $\langle 001 \rangle_{\parallel \underline{e_z}}$ texture at lower powers, as the grains are more aligned in the manufacturing direction $\underline{e_z}$ and appear bigger on the achieved cross-sections.

Hardness measurements were carried out for samples produced with various process conditions of WLAM and WAAM (Table 4.2). The hardness seems to be slightly higher in single beads achieved by WLAM than in those achieved by WAAM (174 HV_{10} vs. 162 HV_{10}). Comparatively, the 316L substrate showed a lower hardness of 150 HV_{10}. Additionally, no significant impact from the process parameters on hardness was observed.

Compared to the conventionally manufactured 316L substrate, the increased hardness induced by both processes may be due to the presence of ferrite in the single beads or strain hardening associated with rapid cooling rates. This last hypothesis could explain the higher hardness in beads achieved by WLAM compared to those achieved by WAAM, as faster solidification might induce higher residual stress and dislocation densities [132]. This point will be discussed in more detail in Section 4.3. Conversely, the increase in hardness is unlikely to result from Hall-Petch strengthening (grain size) since the grains in the single beads are larger than those in the substrate, nor due to the composition of the solid solution, as both substrate and single beads were manufactured using 316L steel with similar chemical compositions.

Table 4.2. Average grain size along the transverse direction $\underline{e_y}$ and hardness of single beads produced by WAAM and WLAM. The grain size was determined using the intercept method, averaging five line measurements, and hardness was calculated as the average of five measurements taken with a 10 kgf load.

Process	Reference (Tables 3.4 and 3.5)	Grain size along $\underline{e_y}$(µm)	Hardness (HV_{10})
WLAM	Set 1	26	167
	Set 2	27	174
	Set 3	25	172
WAAM	Set 1	45	159
	Set 3	52	162

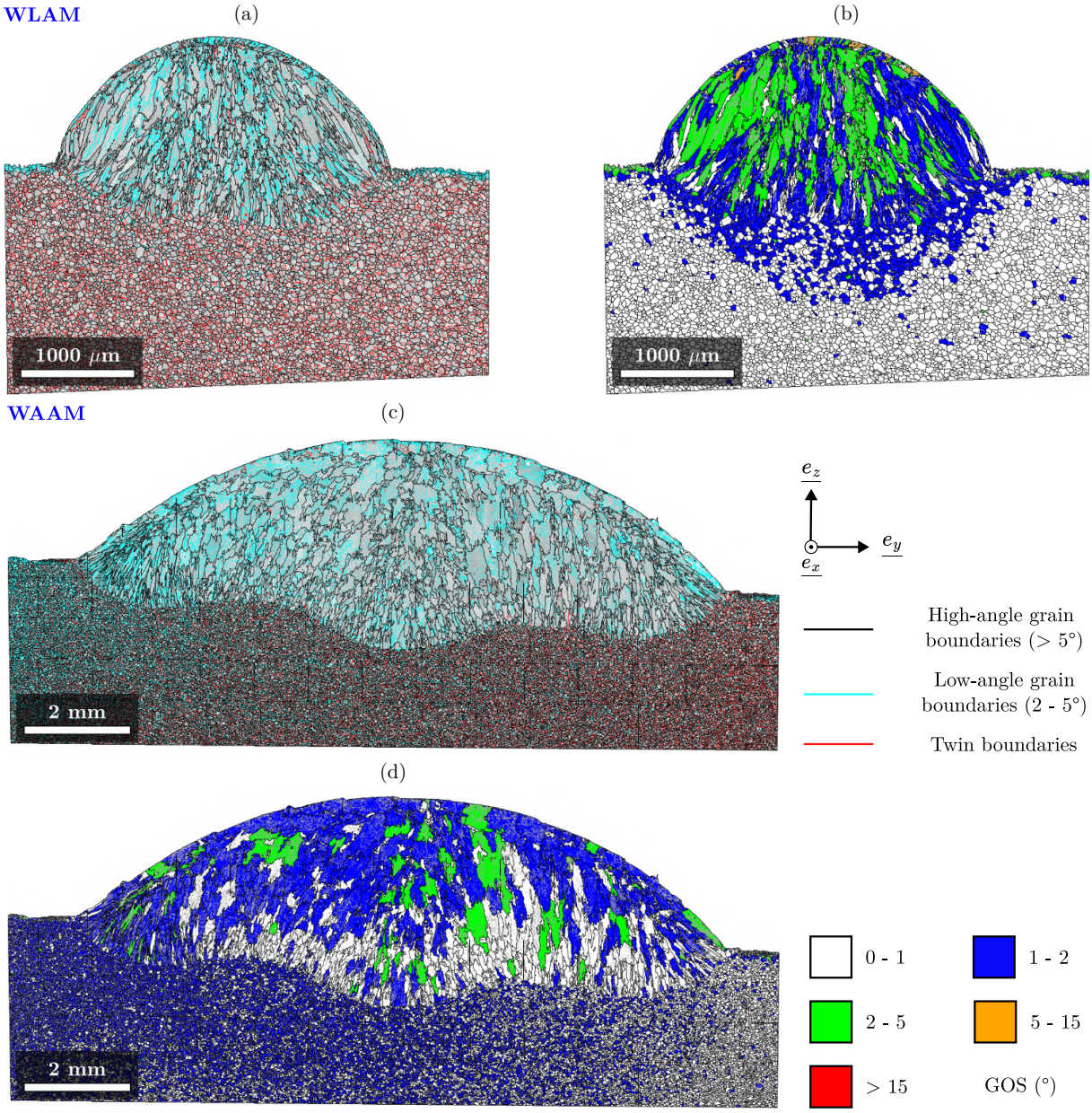

Figure 4.5. Grain boundary (GB) and grain orientation spread (GOS) maps from EBSD of transverse cross-sections of single beads manufactured using WLAM and WAAM: (a) GB map of a single bead produced with WLAM; (b) GOS analysis of the WLAM-manufactured bead; (c) GB map of a single bead produced with WAAM; (d) GOS analysis of the WAAM-manufactured bead.
In GB maps (a) and (c), high-angle grain boundaries (HAGBs) are depicted in black, low-angle grain boundaries (LAGBs) in cyan, and Σ3-twin boundaries in red.
In GOS maps (b) and (d), HAGBs are represented by black lines, while LAGBs are depicted in grey.

4.2.2 Austenite-ferrite dendrite structure

Dendrites elongated in the manufacturing direction $\underline{e_z}$ were observed on transverse cross-sections of single beads produced by WAAM and WLAM (Figures 4.6a and b, respectively). Dendrites after WAAM are coarser than those after WLAM.

The precise geometry of the dendrites could not be completely revealed in transverse cross-sections, making it difficult to measure the primary dendrite spacings. To address this, we used secondary dendrite arm spacing (SDAS) as a representative measure of dendrite size in single beads. The SDAS was estimated at 6 ± 1 µm for WAAM and approximately 3 ± 1 µm for WLAM, suggesting faster solidification in WLAM as dendrite size correlates with the cooling rate at solidification [122]. Cooling rates were estimated at 10^2 °C/s for WAAM and 10^3 °C/s for WLAM. Furthermore, no significant SDAS variation was observed across positions within the deposited single beads, suggesting that the cooling rate variations between the bead edges (start of solidification) and center (end of solidification) are insufficient to alter the microstructure significantly.

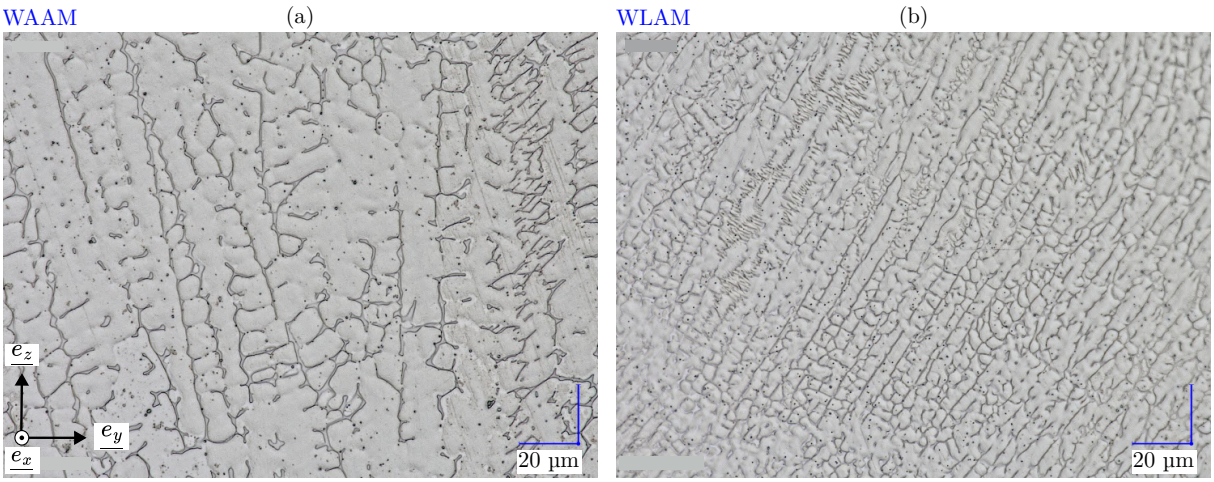

Figure 4.6. Optical micrographs after electrolytic etching in a transverse cross-section of single beads produced by (a) WAAM and (b) WLAM processes.

For WAAM, the two phases were identified by EBSD as face-centered cubic (fcc) crystals, corresponding to austenite (cyan), and body-centered cubic (bcc) crystals, corresponding to δ-ferrite (dark blue) (Figure 4.7). For WLAM, the small dimensions of ferrite areas did not allow for analyzing it confidently. Differently from the single beads, the 316L substrate is fully austenitic.

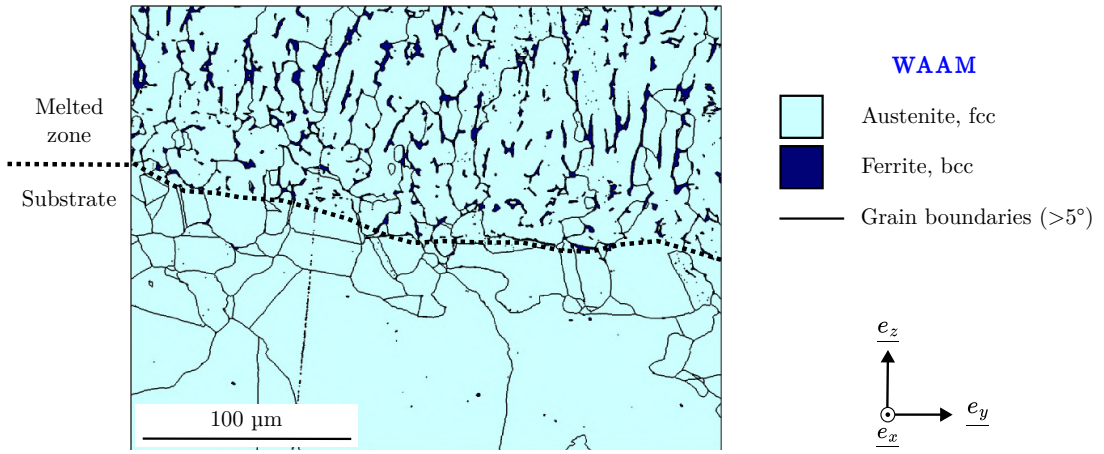

Figure 4.7. EBSD phase map of a transverse cross-section at the fusion line of a single bead produced by WAAM using Set 3 (Table 3.5). Austenite is depicted in cyan, ferrite in blue and grain boundaries in black. $\underline{e_z}$ indicates the manufacturing direction, and $\underline{e_x}$ the deposition direction. EBSD settings: high voltage = 20 kV, step size = 500 nm.

Local chemical composition of single beads manufactured by WAAM was analyzed using EDS. Figure 4.8a shows an SEM image acquired with the secondary electron detector, showing the austenite-ferrite microstructure on a transverse cross-section. Quantitative chromium and nickel content maps were generated on this surface with a 1 µm^2 pixel step size (Figures 4.8b and 4.8c, respectively). As expected, the δ-ferrite phase is enriched in chromium relative to the γ-austenite phase, while the δ-ferrite is depleted in nickel [183, 184]. The measured weight percentages should be interpreted cautiously due to the interaction volume of the electron beam with the sample during EDS measurements, around 1 µm^3, which is larger than the width of ferrite regions.

Similar observations were made for single beads manufactured by WLAM (Figure 4.9). Figure 4.9a shows an SEM image captured with the backscattered electron detector, presenting the austenite-ferrite microstructure in a transverse cross-section, with the manufacturing direction oriented from right to left. Figures 4.9b, 4.9c, 4.9d and 4.9e present the relative distribution of chromium, molybdenum, nickel and manganese, respectively. As in the single bead produced by WAAM, the ferrite phase in WLAM contains higher levels of chromium, molybdenum and lower levels of nickel than the austenite. Additionally, the EDS analysis indicates that the spherical inclusions are manganese-rich, consistent with their identification as manganese oxide inclusions, as it will be discussed in the next Section 4.3. More accurate chemical quantification of chromium and nickel content in the austenite and ferrite phases, using TEM-EDS, will be provided in Section 4.5.

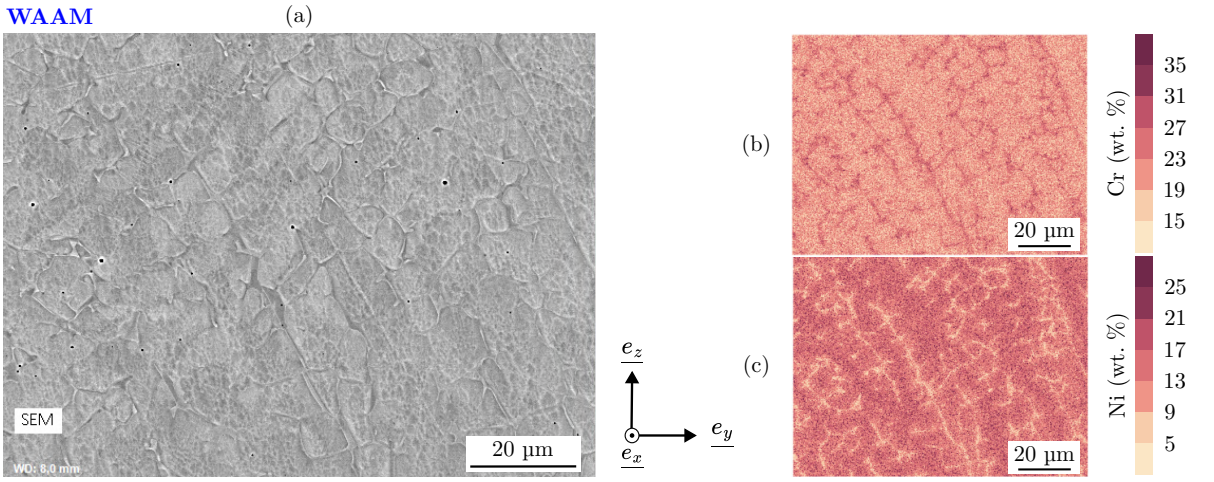

Figure 4.8. EDS quantitative chemical analysis of a transverse cross-section of a single bead manufactured by WAAM using Set 3 (Table 3.5): (a) SEM image obtained with secondary electron detector; (b) chromium content estimation (wt.%); (c) nickel content estimation (wt.%).
EDS settings: high voltage = 20 kV, working distance = 8 mm, pixel size = 1 µm^2.

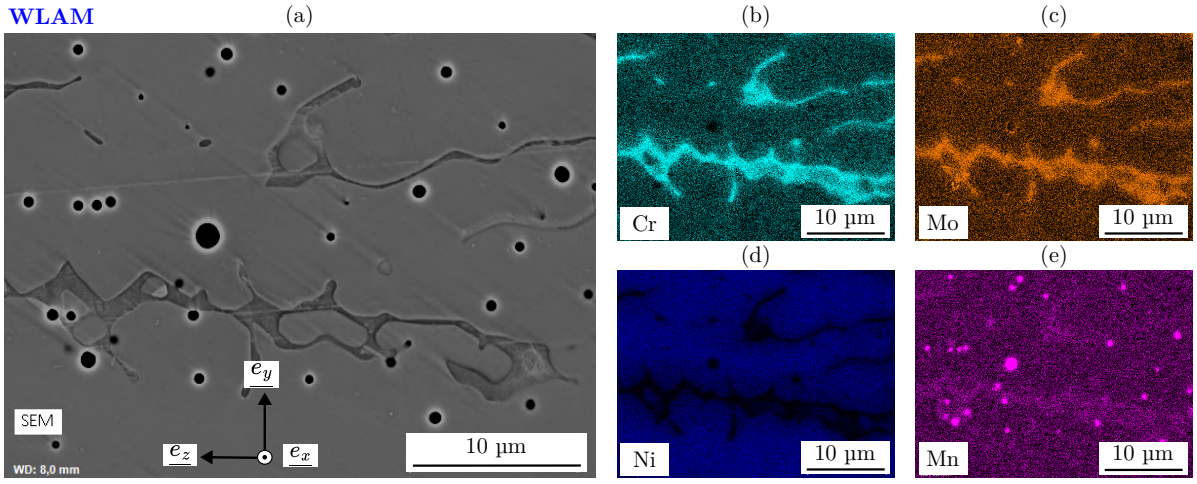

Figure 4.9. EDS qualitative chemical analysis of a transverse cross-section of a single bead manufactured with WLAM using Set 2 (Table 3.4): (a) SEM image obtained with backscattered electron detector; relative distribution of (b) chromium, (c) molybdenum, (d) nickel, (e) manganese.
EDS settings: high voltage = 20 kV, working distance = 8 mm, pixel size = 1 µm^2.
Note that in these images, the manufacturing direction is from the right to the left of the image.

As discussed in Section 4.1, the chemical composition of the 316L components did not provide a definitive indication of the solidification mode. With a Cr_{eq}/Ni_{eq} ratio close to 1.5, the solidification could potentially follow either the AF mode, where austenite is the primary phase, or the FA mode, where ferrite precipitates first. In the AF solidification mode, δ-ferrite is formed in interdendritic regions, while in the FA mode, it manifests as vermicular or lathy ferrite in the core of the dendrites [185, 118]. Both processes revealed the presence of vermicular and lathy δ-ferrite, indicating an FA solidification mode. Under WAAM and WLAM cooling conditions and FA solidification, some ferrite in the core of the dendrites does not transform into austenite, as the austenite formation gradually depletes nickel and increases the chromium content of the ferrite, stabilizing a significant ferrite fraction within the austenite in the final microstructure. Similar ferrite morphologies were observed in studies by Lee *et al.* [90] for 316L components manufactured by CMT-WAAM with a Cr*eq*/Ni*eq* ratio of 1.75 and by Li *et al.* [139] for 308L components manufactured by WLAM with a Cr*eq*/Ni*eq* ratio of 1.89, both in FA solidification mode.

4.3 Single-bead walls

4.3.1 Grain microstructure

Transverse $\left(\underline{e_y}, \underline{e_z}\right)$ cross-section

Figure 4.10 presents macrographs of etched transverse cross-sections of single-bead walls. Walls in Figures 4.10a, b and c were fabricated by WLAM using Sets 1, 2 and 3 (Table 3.4), respectively. Figures 4.10d and e present the single-bead walls manufactured by WAAM using Sets 1 and 3 (Table 3.5), respectively. Lastly, Figure 4.10f shows a WAAM wall manufactured with a welding device using Set 3. Walls in Figures 4.10b and e were produced using the selected parameters at the end of the parametrical study for single beads (*cf.* Chapter 3).

The electrolytic etching highlighted the successive fusion lines and grains across the walls. Each single-bead wall exhibited elongated grains, up to 10 mm long, oriented along the manufacturing direction $\underline{e_z}$, going through multiple deposited layers. This grain structure results from epitaxial solidification, where each new layer solidifies from bottom to top, continuing the grain orientation of the preceding layer. These observations align with those of Chen *et al.* [186], who observed similar elongated grains extending through multiple layers in 316L single-bead walls manufactured by CMT-WAAM.

Due to the similar microstructure of the walls manufactured with the different processing conditions, only the wall manufactured by WLAM using Set 2 (Table 3.4) and the wall manufactured by WAAM using Set 3 (Table 3.5) are analyzed in this chapter.

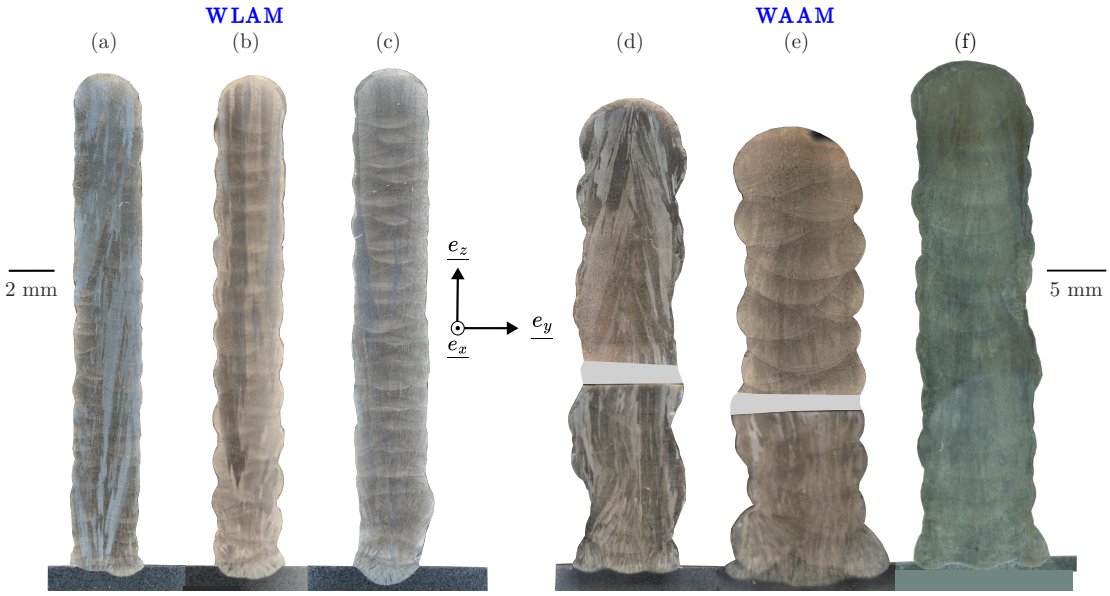

Figure 4.10. Transverse cross-sections of single-bead walls manufactured via WLAM and WAAM under varying process conditions after polishing and electrolytic etching: (a), (b) and (c) WLAM using Sets 1, 2 and 3 (Table 3.4), respectively; (d) and (e) WAAM using Sets 1 and 3 (Table 3.5), respectively; (f) WAAM using Set 3, manufactured with a welding device.

EBSD analyses of transverse cross-sections are displayed in Figures 4.11, 4.12, 4.13 and 4.14 for the walls processed with WLAM using Set 2 (Table 3.4) and WAAM using Set 3 (Table 3.5).

Figure 4.11 presents the EBSD maps of a transverse cross-section from the single-bead wall produced by WLAM. Grain orientation maps are projected in the manufacturing direction ($\underline{e_z}$, Figure 4.11a) and in the deposition direction ($\underline{e_x}$, Figure 4.11b). Figure 4.11c illustrates the grain boundary map, with black lines representing HAGBs and cyan lines indicating LAGBs. Additionally, Figure 4.11d shows the orientation spread within each grain (GOS map), and Figure 4.11e displays the inverse pole figures associated with the orientation maps. Similarly, Figure 4.12 presents the EBSD analysis for the transverse cross-section of the single-bead wall produced by WAAM, divided into two sections due to its large size.

Furthermore, orientation maps are shown in Figure 4.13 at the same scale for the single-bead walls manufactured with WLAM and WAAM, near the fifteenth and the fourth deposited layers. These maps are projected along the manufacturing direction $\underline{e_z}$ and overlaid with HAGBs and LAGBs. Figure 4.13e provides a schematic of the solidification and the predominant texture.

Finally, Figures 4.14a and b show the aspect ratios of grains as a function of their relative area in the transverse cross-sections of the single-bead walls for WLAM and WAAM, respectively. The associated grain aspect ratio maps are presented in Appendix B.2.

Similarly to the single beads, the microstructure consists of two distinct regions: a core region and a skin region. WAAM and WLAM single-bead walls displayed elongated grains oriented in the manufacturing direction $\underline{e_z}$, reaching lengths up to 10 mm. As noted in Section 4.2, this elongation is the consequence of the epitaxial solidification, combined with a unidirectional thermal gradient along $\underline{e_z}$ throughout the entire process [186]. The grains in WLAM components are notably more elongated: 60% of the area corresponds to grains with an aspect ratio above ten (Figure 4.14). At the same time, in WAAM, only 22% of the surface has grains of this ratio. The remaining area in WAAM is mainly occupied by grains with an aspect ratio of around five.

Next, the grain size was measured in the transverse direction $\underline{e_y}$ using the intercept method on the boundary maps[1]. Profiles taken every millimeter along the walls indicate similar grain sizes for the first five millimeters of each wall (62 µm and 61 µm in WLAM and WAAM, respectively). Figures 4.13c and d illustrate comparable microstructures near the fourth layer for both walls. However, at the tops of the walls (last five millimeters), the grain size in WLAM is nearly double than that in WAAM (130 µm versus 73 µm). This difference was noted in Figure 4.13, where the grains in the fifteenth layer of the single-bead walls are larger in WLAM than in WAAM. However, this could again be a local artifact due to the fewer grains in WLAM. The difference may also result from the grains in WAAM growing in directions other than along $\underline{e_z}$, limiting the epitaxial growth along the thermal gradient for the columnar grains.

A "skin effect" is observed around the walls, with small equiaxed grains with varied orientations. While the skin was observed at the top of the single beads (*cf.* Section 4.2), it disappeared on the top of the beads between each layer during the stacking of beads due to remelting of their upper part. Similar conclusions were mentioned by Baumard [99] in studies on 316L single-bead components elaborated with the L-PBF process, where the partial remelting of the beads led to the disappearance of grains at their upper parts, resulting in the epitaxial growth of the columnar grains in the bead cores only.

A strong $\langle 001 \rangle_{\parallel \underline{e_z}}$ texture was observed in the manufacturing direction $\underline{e_z}$, marked by a preferential crystal alignment with the thermal gradient (green asterisk in the inverse pole figures). Similar grain elongation and $\langle 001 \rangle_{\parallel \underline{e_z}}$ texture were reported in 316L single-bead walls by Engel [107] for the L-PBF process and by

[1]The grain size along the manufacturing direction $\underline{e_z}$ was not measured due to the excessive elongation of the grains.

Pan *et al.* [187] for WAAM, indicating this microstructure is typical of single-bead components made using additive manufacturing processes. For the single beads, we reported that the thermal gradient was not precisely aligned with the manufacturing direction due to the rounded shape of the fusion lines. It does not affect the grain growth in the single-bead walls, as grains are highly elongated in the manufacturing direction $\underline{e_z}$ and cross through several beads. It is assumed that this is related to the cumulative effect of the phenomenon of growth competition for grains depending on their orientation.

In the wall produced by WLAM, almost all grains aligned along the $\langle 001 \rangle_{\parallel \underline{e_z}}$ direction after the tenth layer. For WAAM, this orientation also becomes dominant after the fifth layer. However, equiaxed-like grains with various orientations are observed in the upper section, such as those oriented along $\langle 011 \rangle_{\parallel \underline{e_z}}$ in Figure 4.13b. These grains may be formed due to the larger melt pool and the lower thermal gradients in WAAM compared to WLAM, allowing grain growth in directions not aligned with the thermal gradient. As a result, the density of the $\langle 001 \rangle_{\parallel \underline{e_z}}$ texture in the inverse pole figures was reported to be lower in the single-bead wall manufactured using WAAM than WLAM (Figures 4.11e and 4.12e).

Additionally, a $\langle 001 \rangle_{\parallel \underline{e_x}}$ texture is noted in the single-bead wall produced by WLAM. In contrast, in WAAM, the inverse pole figures show a distribution between the $\langle 001 \rangle_{\parallel \underline{e_x}}$ and $\langle 011 \rangle_{\parallel \underline{e_x}}$ orientations, with no dominant crystal texture along $\underline{e_x}$. This difference could be due to the smaller number of grains visible in the WLAM transverse cross-section compared to WAAM, suggesting that the texture along $\underline{e_x}$ may be a local artifact. Additional cross-sections from different locations within the wall could provide further insights into this observation.

Finally, the GOS maps revealed internal misorientations exceeding 1° per grain, reflecting that a grain consists of multiple similarly oriented dendrites growing in the same general direction. A smaller fraction of the grains showed higher GOS values, between 2 and 5°. The GOS values for WLAM and WAAM single-bead walls are comparable with those observed in the single beads (*cf.* Section 4.2), suggesting that the crystal orientations between dendrites belonging to a single grain remain stable throughout the solidification.

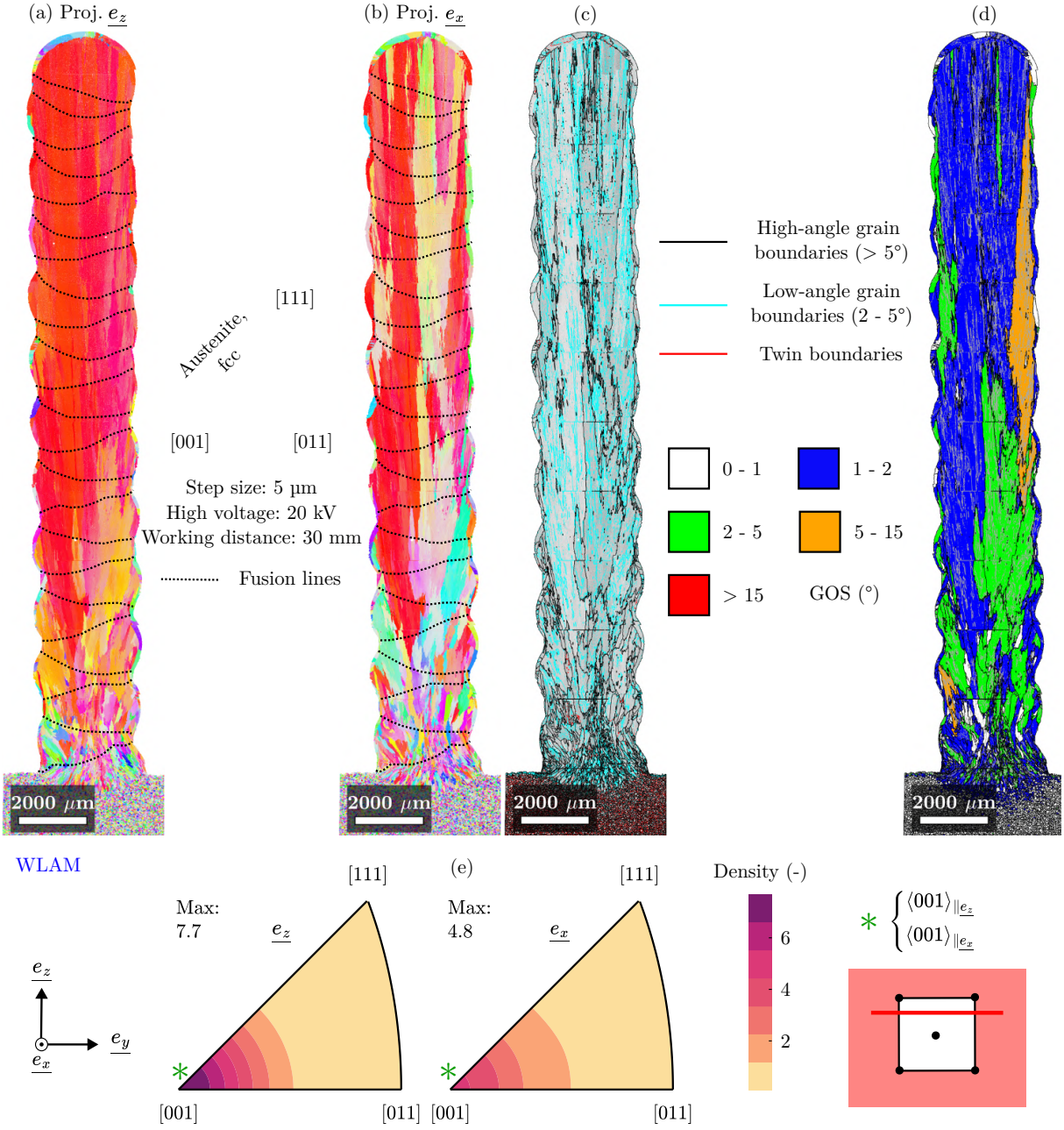

Figure 4.11. EBSD analysis of a transverse cross-section of a single-bead wall produced by WLAM using Set 2 (Table 3.4): (a) orientation map projected along the manufacturing direction e_z; (b) orientation map projected along the deposition direction e_x; (c) grain boundary (GB) map, where black lines represent high-angle grain boundaries (HAGB) and cyan lines indicate low-angle grain boundaries (LAGB); (d) grain orientation spread (GOS) map, with HAGB in black and LAGB in grey; (e) associated inverse pole figures. The asterisks mark the predominating texture.

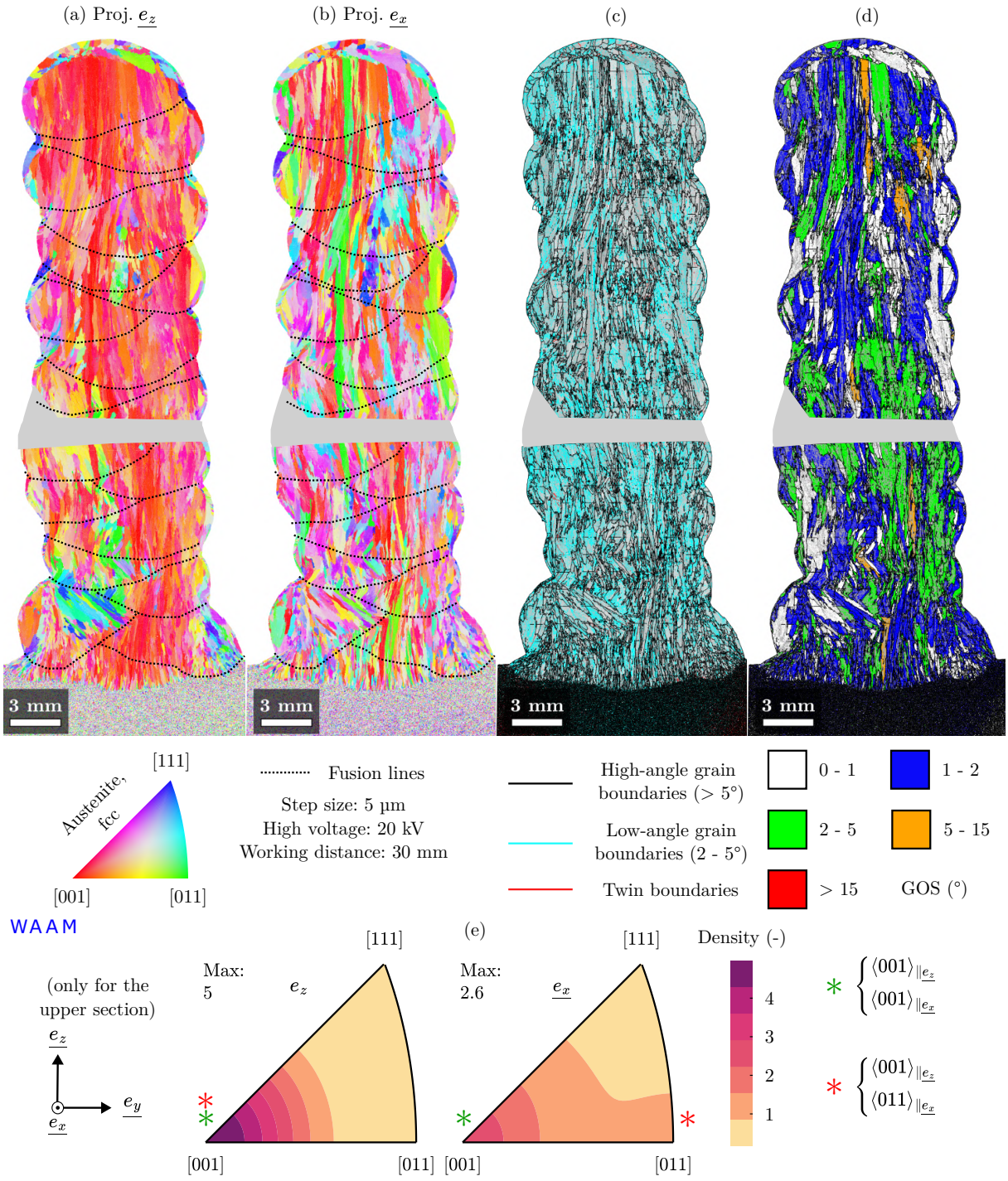

Figure 4.12. EBSD analysis of a transverse cross-section of a single-bead wall produced by WAAM using Set 3 (Table 3.5): (a) orientation map projected along the manufacturing direction e_z; (b) orientation map projected along the deposition direction e_x; (c) grain boundary (GB) map, where black lines represent high-angle grain boundaries (HAGB) and cyan lines indicate low-angle grain boundaries (LAGB); (d) grain orientation spread (GOS) map, with HAGB in black and LAGB in grey; (e) associated inverse pole figures. The asterisks mark the predominating textures.

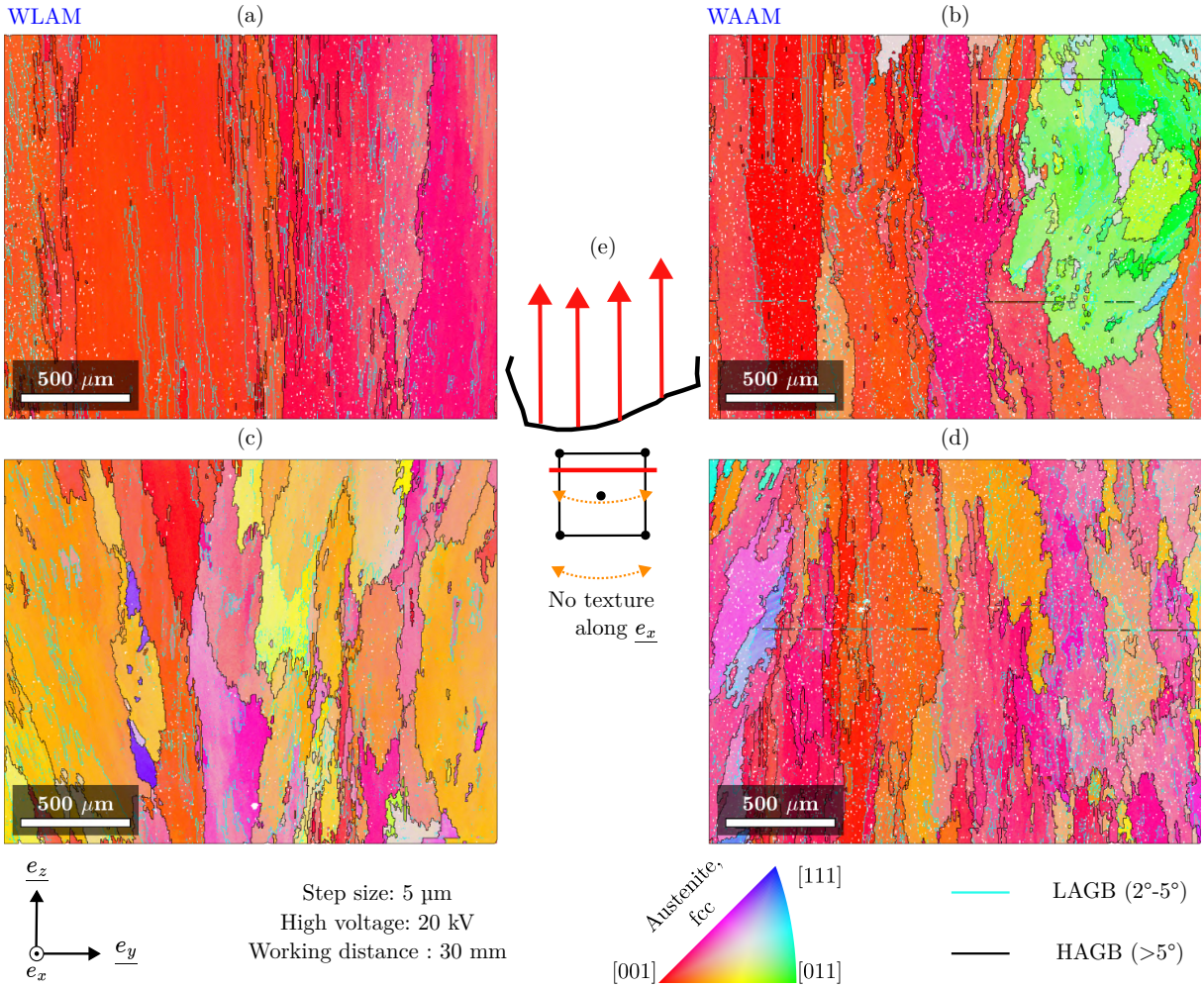

Figure 4.13. EBSD orientation maps of transverse cross-sections from single-bead walls manufactured with WLAM using Set 2 (Table 3.4) and WAAM using Set 3 (Table 3.5), projected along the manufacturing direction $\underline{e_z}$: (a) WLAM single-bead wall near the fifteenth deposited layer; (b) WAAM single-bead wall near the fifteenth deposited layer; (c) WLAM single-bead wall near the fourth deposited layer; (d) WAAM single-bead wall near the fourth deposited layer; (e) schematic illustration of the predominant solidification direction and crystal orientation. Cyan lines indicate LAGBs and black lines represent HAGBs.

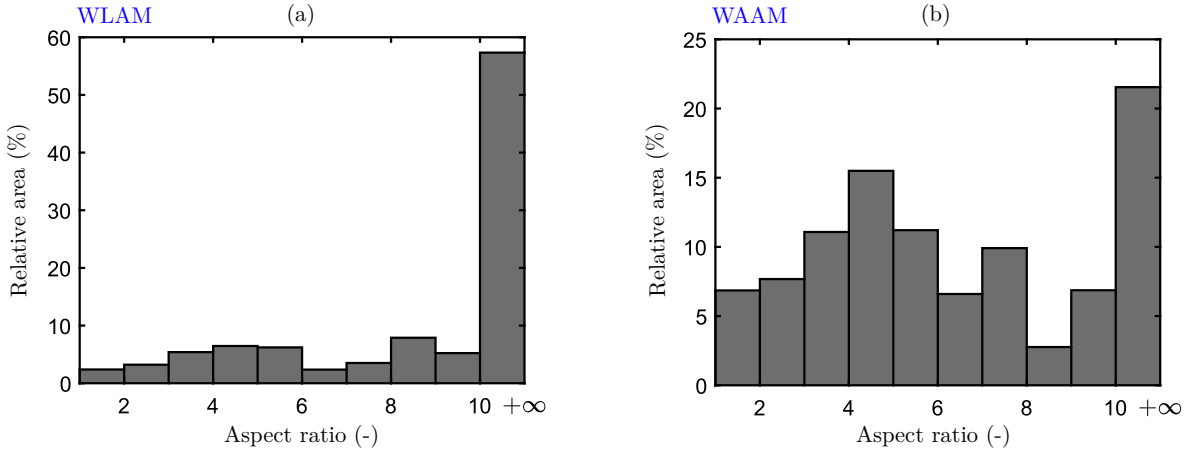

Figure 4.14. Relative surface area (%) occupied by grains as a function of their aspect ratio on transverse cross-sections of single-bead walls obtained by (a) WLAM and (b) WAAM.

Longitudinal $(\underline{e_x}, \underline{e_z})$ cross-section

Additional EBSD analyses were performed on longitudinal cross-sections of the single-bead walls (Figure 4.15). These cross-sections were prepared from the center of the walls. Figures 4.15a and 4.15b show the orientation maps of the entire wall manufactured by WLAM, projected along the manufacturing direction $\underline{e_z}$, and the deposition direction $\underline{e_x}$, respectively. Figure 4.15c presents the associated inverse pole figures. Similarly, Figures 4.15d and 4.15e show the orientation maps of the longitudinal cross-section of the WAAM wall along $\underline{e_z}$ and $\underline{e_x}$. Figure 4.15f presents the associated inverse pole figures for the upper part of the component (above the section[2]).

EBSD orientation maps were compared at the same scale for the longitudinal cross-sections of the single-bead walls manufactured using WLAM and WAAM, taken at both the top (Figures 4.16a and 4.16b) and bottom (Figures 4.16c and 4.16d) of the components. These maps are projected along the manufacturing direction $\underline{e_z}$ and overlaid with high-angle grain boundaries. The black arrows indicate the direction of the deposition of the successive layers. Finally, Figures 4.17a and 4.17b present the aspect ratios of grains as a function of their relative area in the longitudinal cross-sections of the single-bead walls for WLAM and WAAM, respectively. The histogram for the wall manufactured by WAAM is obtained only for the upper part of the global map.

The longitudinal $(\underline{e_x}, \underline{e_z})$ cross-sections of the single-bead walls produced using WLAM and WAAM exhibited elongated grains oriented in the manufacturing direction $\underline{e_z}$, across almost the entire component height. In the first layers, we observed a slight influence of the deposition direction on the grain elongation, alternating between right and left (Figures 4.16c and 4.16d). This alternating effect disappears after the third layer due to the phenomenon of growth competition for grains depending on their orientation, resulting in no visible "zig-zags" within the microstructure despite the alternating deposition strategy. It suggests that the thermal gradient is more closely aligned with the manufacturing direction $\underline{e_z}$ than with the deposition direction $\underline{e_x}$. In addition, we observed a slight deviation from $\underline{e_z}$ of the direction of elongation of the grains for WLAM, but not for WAAM. The faster solidification speed and the smaller size of the melt pool in WLAM compared to that in WAAM resulted in a more significant deviation of the grain elongation direction from the deposition direction at the top of the first deposited bead in the longitudinal cross-section. Even though the deposition direction does not affect the direction of solidification after the third layer, the epitaxial growth forces the grain to keep the initial orientation, which results in the observed deviation of the microstructure with $\underline{e_z}$. Engel [107] observed similar results in longitudinal cross-sections of 316L single-bead walls created using the L-PBF process, where elongated grains grew in the manufacturing direction without being affected by the alternating deposition strategy. Engel also noted that the grain elongation direction is slightly misaligned with the manufacturing direction based on the orientation of the initial deposition layer. Similarly, Palmeira Belotti *et al.* [112] reported that the deposition strategy does not significantly affect the elongation of the grains in the longitudinal direction for 316L components produced via WAAM, although they analyzed multi-layer components.

The grain elongation is slightly less pronounced in the components produced by WAAM than those manufactured by WLAM. The analysis of the surface occupied by the grains depending on their aspect ratios (Figure 4.17) showed that for both processes, most of the surface of the wall is occupied by grains with an aspect ratio above ten (75% in WLAM and 60% in WAAM). The less pronounced elongation in WAAM is likely due to the larger dimensions of the melt pool for this process, consistent with the previous observations in the transverse cross-sections, even though fewer equiaxed-like grains are observed in the longitudinal cross-section, possibly because it was taken from the center of the melt pool, where

[2]The WAAM wall was cut into two parts for characterization due to its dimensions.

the thermal gradient is the most aligned with the manufacturing direction.

The analysis of the longitudinal cross-section in the last deposited layer (Figures 4.16a and 4.16b) revealed two and three distinct solidification zones for the single-bead walls manufactured by WLAM and WAAM, respectively.

Equiaxed grains without specific texture were observed at the top of the walls (Zone A). Combined with the observations in the transverse cross-sections (Figures 4.11 and 4.12), it confirms that the edges of the WAAM and WLAM single-bead walls are likely isotropic in terms of grain structure. Below Zone A, the wall produced by WLAM directly exhibited Zone C, *i.e.* elongated grains. However, in the single-bead wall produced by WAAM, an intermediate zone was observed (Zone B), with elongated grains in the deposition direction $\underline{e_x}$. These grains were associated with the previously observed "equiaxed-like" grains in the transverse cross-section of the WAAM wall and corresponded to solidification dendrites growing in directions other than the manufacturing direction $\underline{e_z}$. According to Debroy *et al.* [3], the thermal gradient is directed along the deposition direction at the rear of the fusion line in additive manufacturing processes with low deposition speeds, such as WAAM. Zone B did not appear in the WLAM wall due to the higher deposition speed in this process. Zones A and B are only observed for the last layer at the top of the component manufactured by WAAM, as the upper part of the previous layers was remelted, leaving elongated grains from Zone C through epitaxial growth. In WAAM, however, we assumed that some grains from Zone B (directed along $\underline{e_x}$) were not fully remelted, creating initiation sites for the solidification of grains with orientations differing from those aligned with $\underline{e_z}$, explaining the equiaxed-like grains observed in the transverse cross-section.

As for the transverse cross-sections, a strong $\langle 001 \rangle_{\parallel \underline{e_z}}$ texture (green asterisk) was observed in the longitudinal cross-sections of WLAM and WAAM single-bead walls, even in the first layers. The inverse pole figures estimated the density of this texture at 9.2 for WLAM and 9.9 for WAAM along $\underline{e_z}$. Additional less pronounced textures were noted in the orientation maps projected along $\underline{e_x}$. The inverse pole figures indicated a predominance of $\langle 001 \rangle_{\parallel \underline{e_x}}$ for WAAM (green asterisk) and both $\langle 001 \rangle_{\parallel \underline{e_x}}$ and $\langle 011 \rangle_{\parallel \underline{e_x}}$ textures for WLAM in the deposition direction (green and red asterisks, respectively).

Grain size in the deposition direction $\underline{e_x}$ was measured using the intercept method for WAAM and WLAM walls. Five profiles measuring 15,000 µm for WAAM and 10,000 µm for WLAM were taken within the longitudinal cross-section. The grain sizes along $\underline{e_x}$ were estimated to be 89 ± 1 µm for WAAM and 63 ± 1 µm for WLAM. These results differ from the determined grain sizes in the transverse cross-sections, suggesting variability in grain size between manufacturing and deposition directions. Additionally, we observed in Figures 4.16a and 4.16b that the grains, on average, are larger in WLAM than in WAAM.

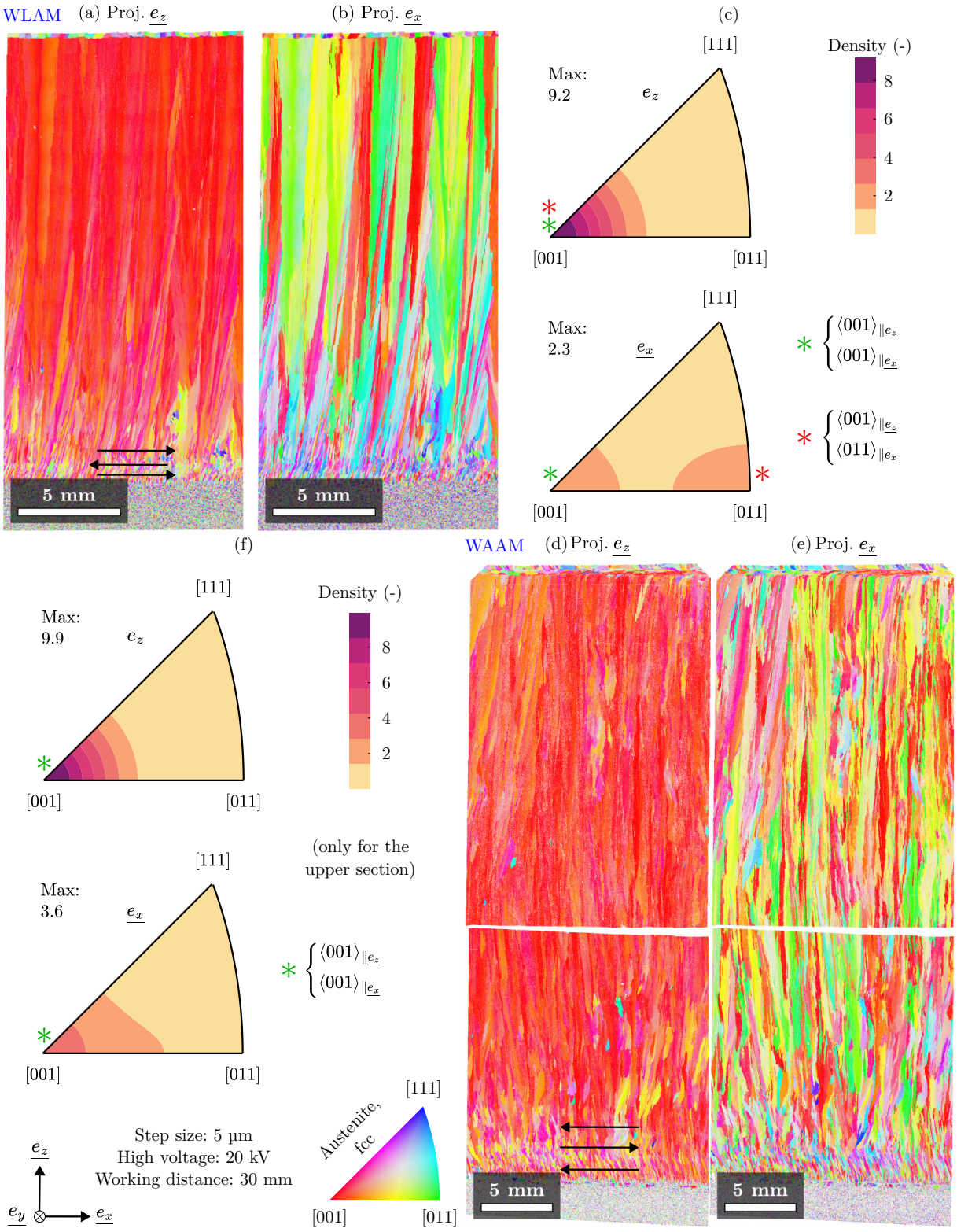

Figure 4.15. EBSD orientation maps and inverse pole figures of the longitudinal cross-section of single-bead walls manufactured by WLAM using Set 2 (Table 3.4) and WAAM using Set 3 (Table 3.5): (a) and (b) orientation maps of the WLAM-manufactured specimen, projected along the manufacturing $\underline{e_z}$ and deposition $\underline{e_x}$ directions, respectively; (c) inverse pole figures associated with the WLAM specimen; (d) and (e) orientation maps of the WAAM-manufactured specimen, projected along the $\underline{e_z}$ and $\underline{e_x}$ directions, respectively; (f) inverse pole figures associated with the WAAM specimen. The asterisks mark the predominating textures. The black arrows indicate the direction of deposition of the three first layers.

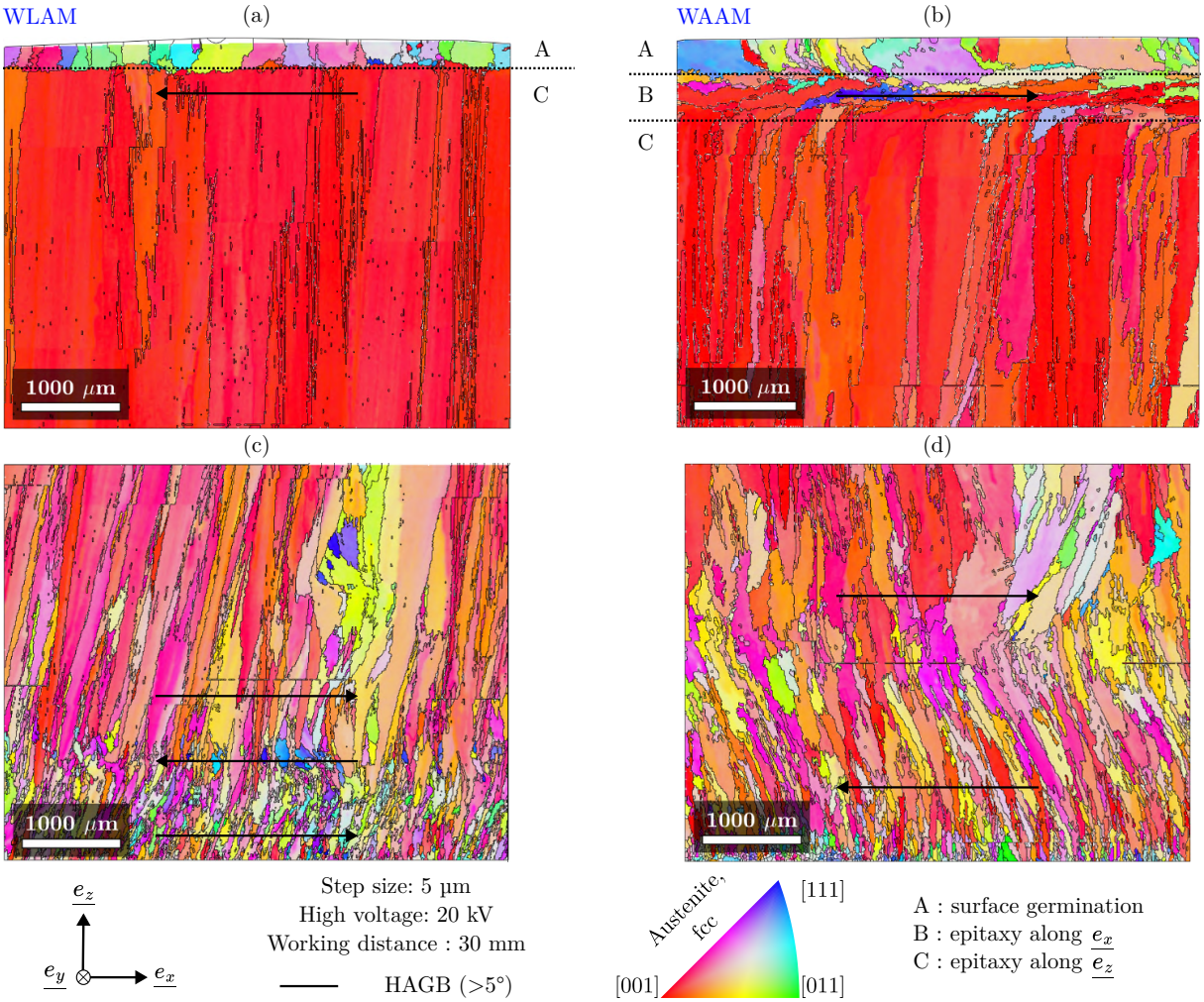

Figure 4.16. EBSD orientation maps of longitudinal cross-sections from single-bead walls manufactured with WLAM using Set 2 (Table 3.4) and WAAM using Set 3 (Table 3.5), projected along the manufacturing direction e_z: (a) WLAM, at the top of the wall; (b) WAAM, at the top of the wall; (c) WLAM, at the bottom of the wall; (d) WAAM, at the bottom of the wall. The black lines represent the HAGB, and the arrows indicate the local deposition direction.

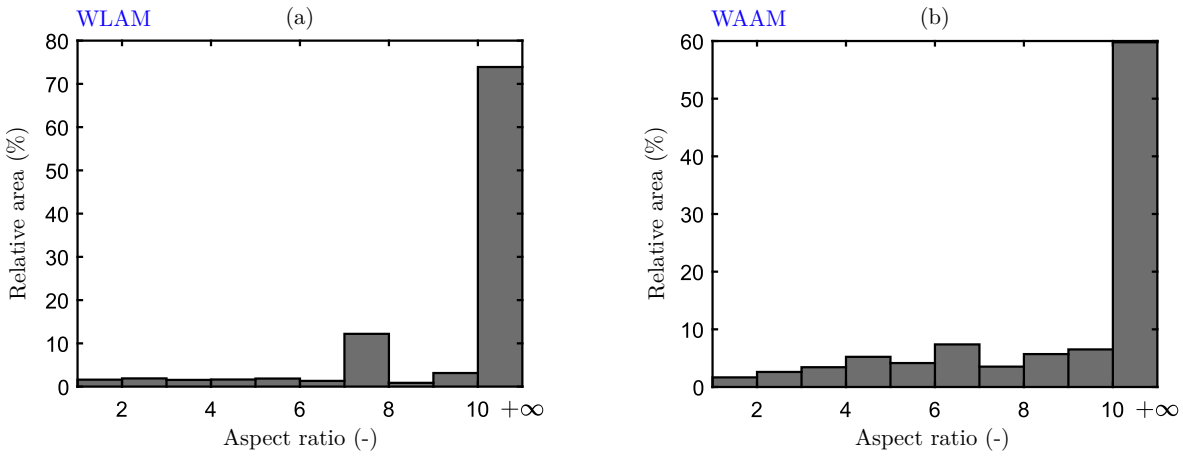

Figure 4.17. Relative surface area (%) occupied by grains as a function of their aspect ratio on longitudinal cross-sections of single-bead walls obtained by (a) WLAM and (b) WAAM.

4.3.2 Dendrite structure

Figures 4.19a and b present optical micrographs after chemical etching of the tenth layer of single-bead walls produced by WAAM with Set 3 (Table 3.5) and WLAM with Set 2 (Table 3.4), respectively. The dendrites grow in the manufacturing direction (upwards in the images) and appear larger for WAAM than for WLAM, reflecting the lower cooling rate in WAAM. In addition, while the WAAM wall dendrites display both primary and secondary arms, those in the wall manufactured with WLAM show mainly primary arms, distinct from the dendrite morphology observed for the WLAM single beads in Section 4.2.

In single beads, the δ-ferrite morphology was identified as vermicular and lathy, characteristic of a FA solidification mode. The single-bead wall manufactured with WAAM in Figure 4.19a shows a similar microstructure corresponding to FA solidification. However, in the single-bead wall manufactured by WLAM (Figure 4.19b), the δ-ferrite morphology differs from that observed in the single bead made with WLAM, predominantly taking the shape of straight lines oriented in the manufacturing direction. This morphology can arise from two solidification mechanisms, as noted by Suutala [119]:

- vermicular ferrite (associated with FA solidification), associated with fast solidification and no SDAS formation;
- interdendritic ferrite (linked to AF solidification), forming as straight lines between the dendrites [105].

As discussed in Section 4.2, both FA and AF solidification modes are possible in our case due to the $\frac{\mathrm{Cr}_{eq}}{\mathrm{Ni}_{eq}}$ ratio of the 316L wire near the threshold between the solidification modes. Elmer *et al.* [185] also noted that a higher cooling rate could result in a shift from FA to AF solidification for compositions with a $\frac{\mathrm{Cr}_{eq}}{\mathrm{Ni}_{eq}}$ ratio close to both solidification domains. Given the higher cooling rates in WLAM, the hypothesis that the WAAM single-bead wall solidified in FA mode while the WLAM wall solidified in AF mode is possible. However, a solidification according to the FA mode and no SDAS is also plausible, especially since FA solidification was reported for the single beads.

Primary dendrite spacings[3] were measured using the intercept method, with lines perpendicular to the primary axis of dendrites. The PDAS was measured at 7.1 ± 0.5 µm for WLAM and nearly double that for WAAM, at 16.5 ± 0.5 µm. These values align with the analysis of Goland *et al.* [114], who reported PDAS values of 11-14 µm for WAAM and 5-9 µm for WLAM components. Next, we investigated whether the ferrite maintained a consistent morphology throughout the entire single-bead wall produced by WLAM. As previously noted in Section 4.2, the dendrite size in the single bead manufactured with WLAM did not significantly vary across the bead. However, in the tenth layer of the single-bead wall manufactured by WLAM, the primary dendrite arm spacing (PDAS) increased from 4.1 ± 0.5 µm at the bottom of the bead to 7.1 ± 0.5 µm at the top. Moreover, the PDAS continued to increase at the top of each subsequent layer, reaching 8.3 ± 0.5 µm at the seventeenth layer. These variations are a result of a decrease of the cooling rate due to the heat accumulation in the manufactured component [122] and likely influence dendrite morphology, as a slower cooling rate can allow the formation of secondary dendrite arms.

In addition, phase analysis was conducted using EBSD on transverse, longitudinal and top cross-sections of single-bead walls to observe dendrite structure (Figures 4.18a and 4.18b). The EBSD analyses were performed on one grain of austenite oriented along the $\langle 100 \rangle$ direction in both the manufacturing $\underline{e_z}$ and deposition $\underline{e_x}$ directions, in the tenth layer of single-bead walls achieved by WAAM and WLAM, to ensure consistent dendrite solidification orientation across all maps (aligned along $\underline{e_z}$).

[3] PDAS measurements were reported previously to be challenging due to the difficulty of identifying the primary arms of the dendrites; thus, SDAS was used to estimate dendrite size. However, in the case of WLAM, secondary arms are non-existent, making it necessary to measure PDAS to compare the dendrites in the single-bead walls.

The pseudo-3D maps illustrated the solidification morphology, with dendrites growing along $\underline{e_z}$. The ferrite morphology in the transverse and longitudinal cross-sections is similar, mainly exhibiting primary dendrite arms in the WLAM process, whereas, in WAAM, secondary dendrite arms were also observed. The top sections revealed cross-sections of the dendrites, where ferrite surrounds the austenite dendrites.

The average dendrite cross-section was estimated using the intercept method by counting intersections along ten 80 µm-long lines: five along the deposition direction $\underline{e_x}$ on both the top and longitudinal cross-sections and five along the transverse direction $\underline{e_y}$ on both the top and transverse cross-sections. Measurement uncertainties were estimated by assuming that one intersection with ferrite per line was missed on average.

In the transverse direction $\underline{e_y}$, the dendrite size was estimated to be of 6.9 ± 0.7 µm for WLAM and 13 ± 2 µm for WAAM. In the deposition direction $\underline{e_x}$, the estimated dendrite sizes were 6.5 ± 0.7 µm for WLAM and 11 ± 2 µm for WAAM. These values are comparable to those observed using an optical microscope. Then, the average dendrite cross-section is approximately 45 ± 6 µm^2 for WLAM and 140 ± 40 µm^2 for WAAM, assuming rectangular cross-sections. The dendrite size is similar in both the transverse and deposition directions, with WAAM producing dendrites of nearly twice larger than those in WLAM.

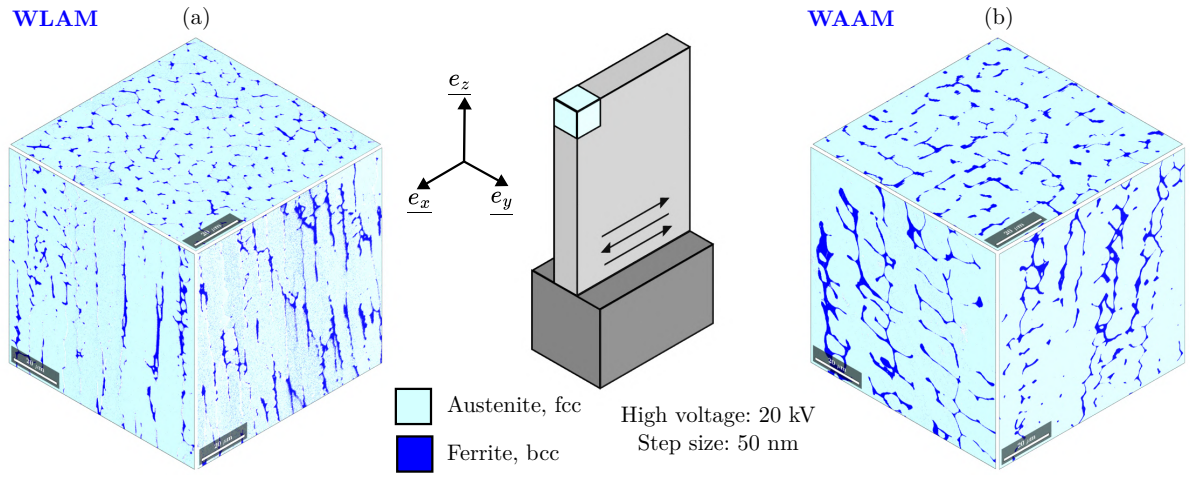

Figure 4.18. Pseudo-3D EBSD phase maps of 316L single-bead walls produced by (a) WLAM and (b) WAAM processes. The austenite phase is shown in cyan, while the ferrite phase is depicted in blue. The transverse, longitudinal, and top cross-sections were not obtained from the same grain. However, an austenite grain aligned along the ⟨100⟩ direction in both the manufacturing $\underline{e_z}$ and deposition $\underline{e_x}$ directions was selected for each map.

Figure 4.20 shows an optical micrograph of the twelfth layer of the single-bead wall produced by WLAM, taken after electrolytic etching. In the lower part of the micrograph, dendrites mainly consisted of primary arms, similar to those observed in Figure 4.19b. In the upper part of the image — with lower cooling rates — dendrites with both primary and secondary arms appeared. Additionally, the morphology of ferrite regions can be identified as vermicular and lathy, indicating FA solidification mode, as observed previously in the single bead. Furthermore, continuity was noted at the boundary between the zone where the dendrites are only constituted of primary arms and that where dendrites exhibited PDAS and SDAS. It suggests that the entire component solidified via the FA mode, as a transition from AF to FA mode would have resulted in a mismatch in the ferrite alignment, given that ferrite resulting from FA mode forms within dendrite cores, while AF-mode ferrite appears between the dendrites.

We concluded that the ferrite in Figure 4.19b adopts a vermicular morphology without secondary arms,

aligning with the work of Abioye *et al.* [73], who observed similar microstructures in 308LSi single-bead walls produced using WLAM. With a $\frac{Cr_{eq}}{Ni_{eq}}$ ratio of 1.77, their component solidified in FA mode and presented dendrites with only primary arms at the bottom of the beads and both primary and secondary arms at their top.

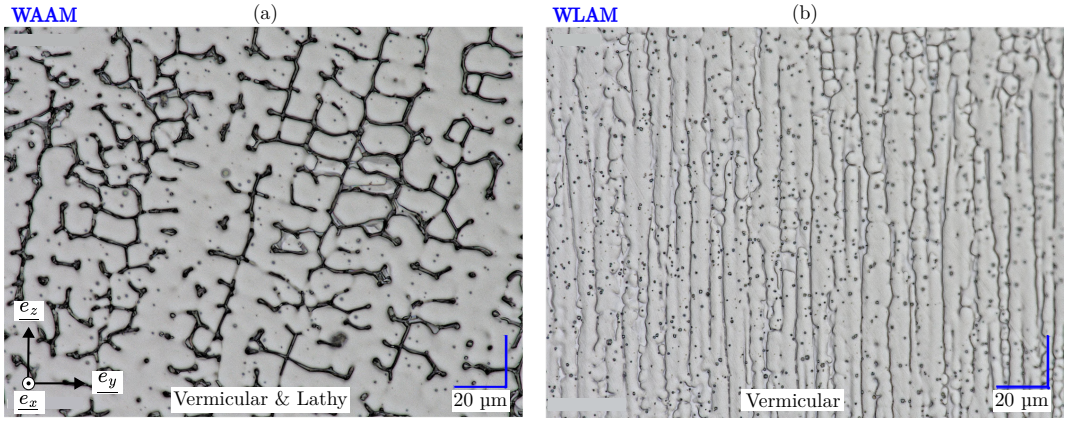

Figure 4.19. Optical micrographs after electrolytic etching of ferrite in a transverse cross-section of the tenth layer of a single-bead wall produced by (a) WAAM using Set 3 (Table 3.5) and (b) WLAM using Set 2 (Table 3.4).

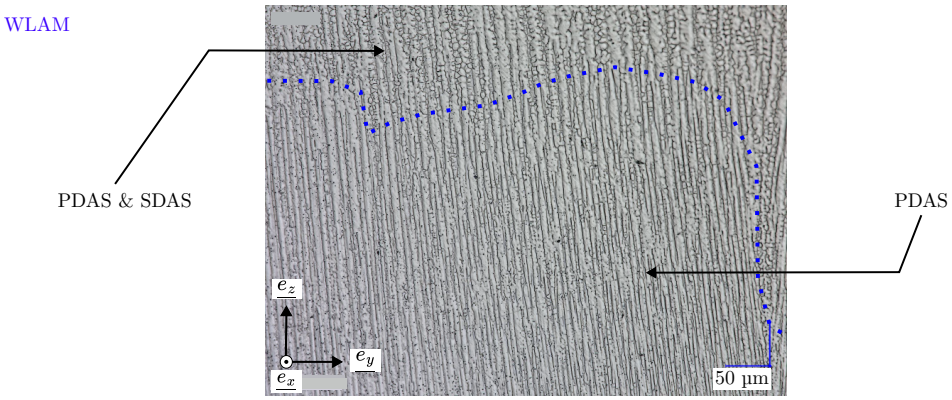

Figure 4.20. Optical micrograph after electrolytic etching of ferrite in a transverse cross-section of the tenth layer of a single-bead wall produced by WLAM using Set 2 (Table 3.4).

A ferritoscope was used to analyze the ferrite phase within the austenitic matrix of the 316L single-bead walls produced by WAAM and WLAM. The ferrite fraction was estimated to be of 5-6 vol.% for WLAM and 8-9 vol.% for WAAM. As discussed in Section 4.1, the Schaeffer diagram predicted approximately 5 vol.% of ferrite for the composition of the 316L stainless steel under typical welding conditions. However, the single-bead wall manufactured by WAAM exhibited nearly double this amount, likely due to the different cooling conditions in WAAM and GTAW welding. De Sonis [188] reported a lower ferrite content of 5.8 vol.% in 316L multilayer components produced by WAAM, but our 316L wire has a higher chromium content (19.2 wt.% versus 18.4 wt.%), promoting ferrite stability.

Several studies reported a higher ferrite content in WLAM components than that in WAAM [15, 114]. For instance, Goland *et al.* [114] found ferrite contents of 7 vol.% for WLAM and 4 vol.% for WAAM in 316L multilayer components. Their wire had a lower chromium content (18.15 wt.%) than ours (19.2 wt.%), which can explain the different ferrite fractions between WAAM components. However, it does not justify why they reported higher ferrite rates after WLAM than after WAAM, while we observed the opposite.

Finally, the presence of zones with only primary dendrite arms may explain the lower measured ferrite content in our component manufactured by WLAM compared to the one produced by WAAM, contrary to the findings of Elmer *et al.* [15]. In their study, the solidification microstructure of components produced by WLAM contained numerous secondary arms, increasing the final ferrite content. This difference is due to variations in cooling rates caused by the geometry and therefore the heat accumulation in the manufactured components: while Elmer *et al.* [15] studied multi-layer components, our analysis focused on single-bead walls.

Ferrite orientation maps were analyzed within austenite grains with a $\langle 001 \rangle$ orientation relative to the manufacturing and deposition directions. These orientation maps are displayed in Figure 4.21, with the main maps depicting ferrite orientations and the inserts showing austenite orientations. In the manufacturing direction $\underline{e_z}$ (Figure 4.21a for WAAM and Figure 4.21b for WLAM), ferrite consistently aligned with the $\langle 001 \rangle$ direction of the austenite, for both processes. This alignment matches the findings of Inoue *et al.* [189], who reported that both ferrite and austenite tend to align their $\langle 100 \rangle$ direction with the thermal gradient imposed by the heat source, close to $\underline{e_z}$ in the single-bead walls. In the deposition direction $\underline{e_x}$, ferrite in the WAAM component was oriented close to $\langle 100 \rangle_{\parallel \underline{e_x}}$ within an austenite grain oriented along $\langle 100 \rangle_{\parallel \underline{e_x}}$ (Figure 4.21c). This orientation relationship indicates only a slight misorientation between ferrite and austenite, aligning with the findings of Chen *et al.* [127] for GMAW-fabricated 316L components. In contrast, the ferrite in the WLAM component displayed an orientation close to $\langle 011 \rangle$ in the deposition direction, resulting in a 45° misorientation relative to the austenite crystal (Figure 4.21d). Zhai *et al.* [190] reported a similar orientation relationship in 304L stainless steel produced via L-PBF. Our observations showed a similar 45° misorientation on the top cross-section, while the longitudinal cross-section showed a 0° misorientation between ferrite and austenite, as for WAAM. This variation suggests that, in WLAM, ferrite locally adopts distinct orientations relative to the austenite without maintaining a consistent orientation relationship across the entire component. Inoue *et al.* [191] noted that multiple ferrite orientations could coexist within a single austenite grain, independently of the austenite solidification process. The authors reported that no orientation relationship governs vermicular ferrite and austenite solidification under additive manufacturing cooling conditions.

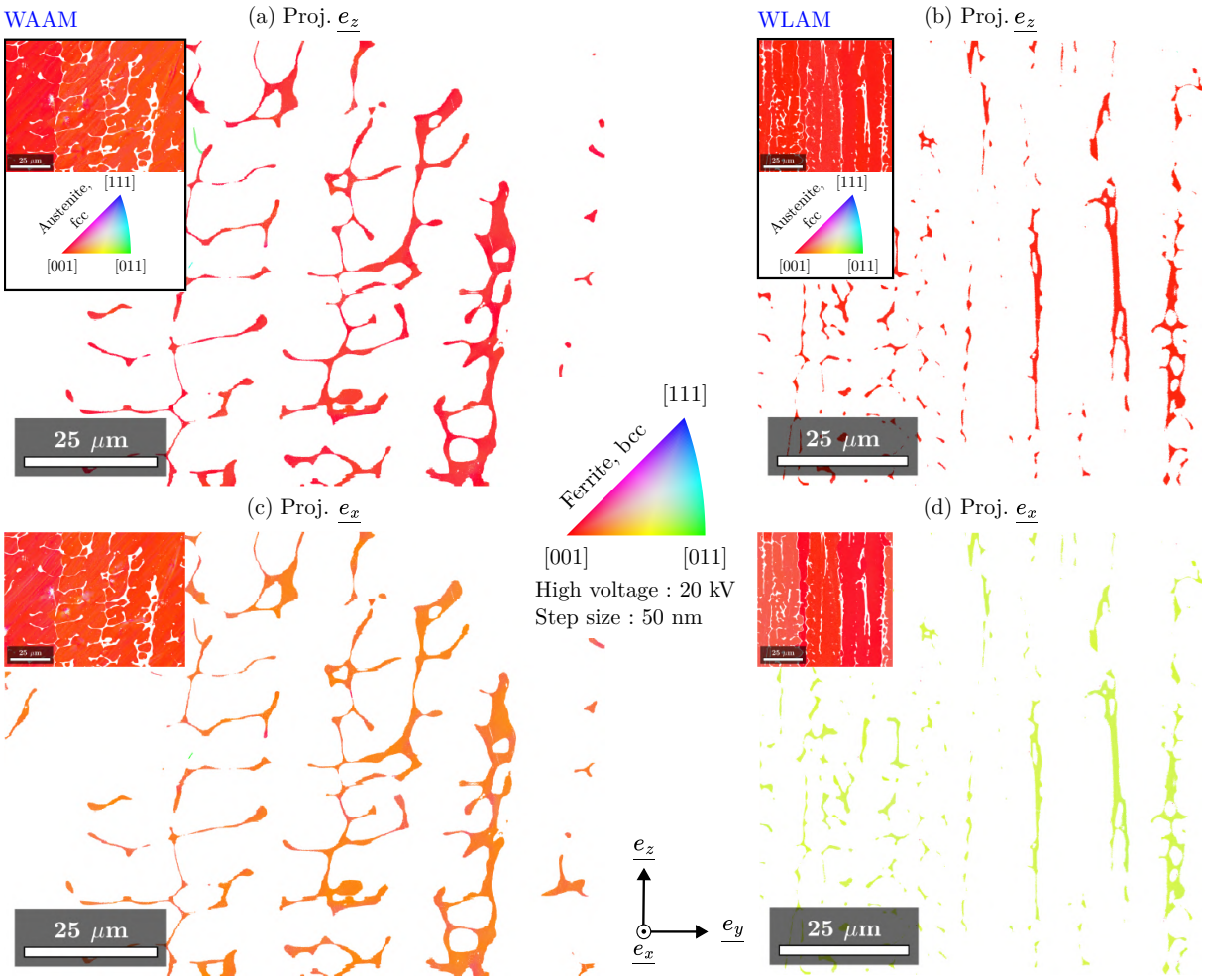

Figure 4.21. EBSD orientation maps of ferrite within an austenite grain aligned along the ⟨100⟩ direction, analyzed in both the manufacturing $\underline{e_z}$ and deposition $\underline{e_x}$ directions from transverse cross-sections of single-bead walls produced by WAAM and WLAM: (a) WAAM, projected in the manufacturing direction $\underline{e_z}$; (b) WLAM, projected in the manufacturing direction $\underline{e_z}$; (c) WAAM, projected in the deposition direction $\underline{e_x}$; (d) WLAM, projected in the deposition direction $\underline{e_x}$. The top-left insets show orientation maps for austenite.

Finally, no σ phase was detected in the single-bead walls produced by either WAAM or WLAM. It suggests that the cooling conditions in both processes were sufficient to limit the heat accumulation in the components, preventing σ phase formation. However, this conclusion should be interpreted cautiously, as studies reporting σ phase in as-built components were based on multi-layer components, while our study focused on single-bead walls. Multi-layer components experience significant thermal cycling, which could promote σ-phase formation [192].

4.3.3 Inclusions

We previously noted that Al_2O_3-MnO-MgO oxides were present in the initial wire. The inclusions in single-bead walls manufactured using WAAM and WLAM were observed through optical microscopy on non-etched, polished transverse cross-sections (Figures 4.22a and b, for WAAM and WLAM, respectively). Numerous round-shaped inclusions, likely oxides, were visible in the metallic matrix, particularly in the wall manufactured by WLAM (Figure 4.22b), suggesting that the inert gas shielding was significantly less effective during WLAM manufacturing compared to WAAM.

High-resolution optical micrographs were analyzed to quantify the global volume of these inclusions. A threshold was applied to the binary black-and-white image to distinguish inclusions (dark regions). The estimated volume fraction of inclusions was 0.47 vol.% for WAAM and three times higher at 1.47 vol.% for WLAM. Also, the WAAM single-bead wall characterized using ICP-AES was produced with a semi-manual welding device instead of the WAAM platform. This wall exhibited a two-times lower inclusion volume fraction of 0.20 vol.% than with the WAAM platform, indicating a better control of the inert atmosphere.

These findings highlight the need to improve the inert gas shielding in WAAM and WLAM platforms to minimize oxygen contamination and reduce the inclusion volume in the manufactured components.

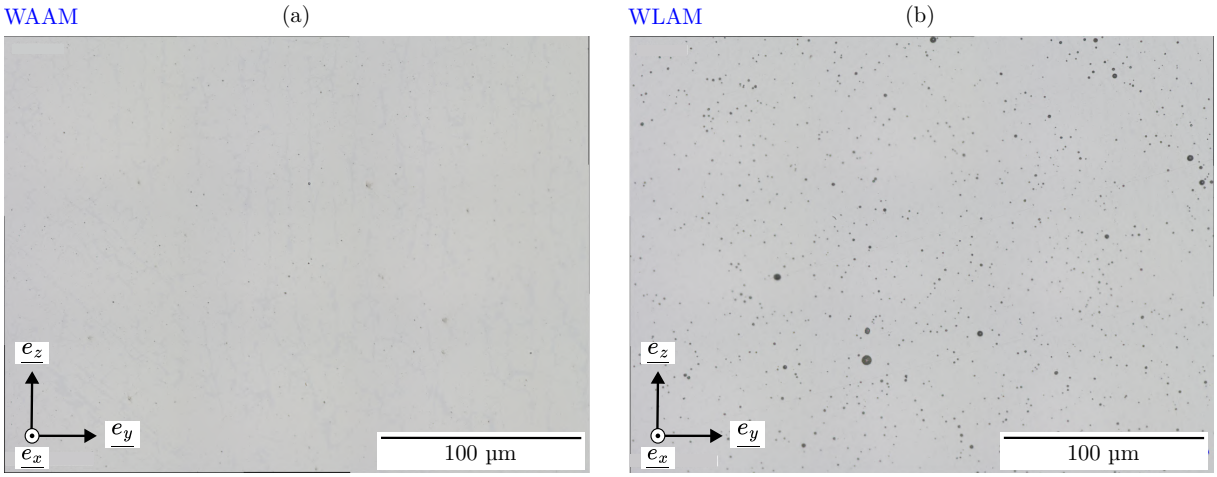

Figure 4.22. Optical micrographs of the polished surface of the transverse cross-section of a single-bead wall manufactured with (a) WAAM and (b) WLAM (observation without chemical etching).

Finally, the chemical composition of the oxides in WAAM and WLAM single-bead walls was obtained qualitatively using SEM-EDS. A close-up micrograph of the inclusions in WLAM (Figure 4.23) indicates that these inclusions have the specific shape of oxides [173]. Moreover, EDS measurements indicated a higher content of manganese, aluminum, silicon and oxygen in the inclusions than in the matrix, consolidating the assumption that, as in the filler wire, these inclusions are a complex mix of $Al_2O_3 - MnO - SiO_2$ oxides. We were not able to get the precise chemical composition of the oxides with SEM-EDS due to the small size of the oxides (less than 1 µm in diameter). Further characterizations can be achieved using WDS-EPMA measurements, as for the filler wire.

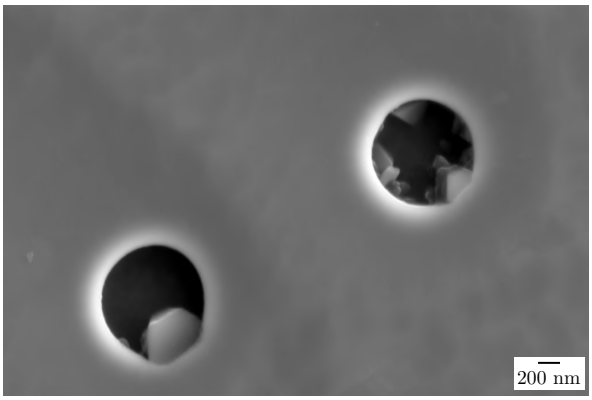

Figure 4.23. Close-up micrograph of two oxide inclusions obtained with SEM and secondary electron detector in a single-bead wall achieved by WLAM.

4.3.4 Crystal defects

Bright-field TEM images were acquired near the ⟨001⟩ zone axis in both the austenite and ferrite of WAAM and WLAM single-bead walls (Figure 4.24), focusing on regions near the tenth deposited layer, where the $\langle 001 \rangle_{\parallel \underline{e_z}}$ crystal orientation has become predominant. Figure 4.24a is focused on the austenite of the WLAM wall, Figure 4.24b the austenite of the WAAM wall, Figure 4.24c the ferrite of WLAM and Figure 4.24d on the ferrite in WAAM.

Dislocations were observed in both phases, with a qualitatively significant density, as expected due to the manufacturing conditions. The thermal cycling during successive layer deposition and the rapid cooling rates induced plastic strain hardening and residual stress accumulation in various layers [132]. Numerical analyses, presented in Chapter 5, showed that residual stresses persist throughout the component, with varying intensities, due to the combined effects of strain hardening during multiple cooling cycles and recovery.

No particular organization of dislocations (such as cells) was observed. It contrasts with the L-PBF process, where dislocations within the austenite matrix are often organized into cellular structures [132]. Similar disorganized dislocations were noted by De Sonis [116], who observed bright-field TEM images of 316L tiles manufactured using the GMAW-WAAM process. However, he reported that the dislocation density was higher, potentially due to:

- the use of the GMAW process instead of GTAW, where the higher deposition rate may lead to a greater deformation rate;
- the characterization of tiles rather than single-bead walls, as the increased number of deposited beads could lead to more pronounced thermal strain hardening;
- localized factors, which may not fully represent the overall material or could vary based on the acquisition conditions relative to the zone axis;
- a difference in the thickness of the thin foils used to observe the dislocations.

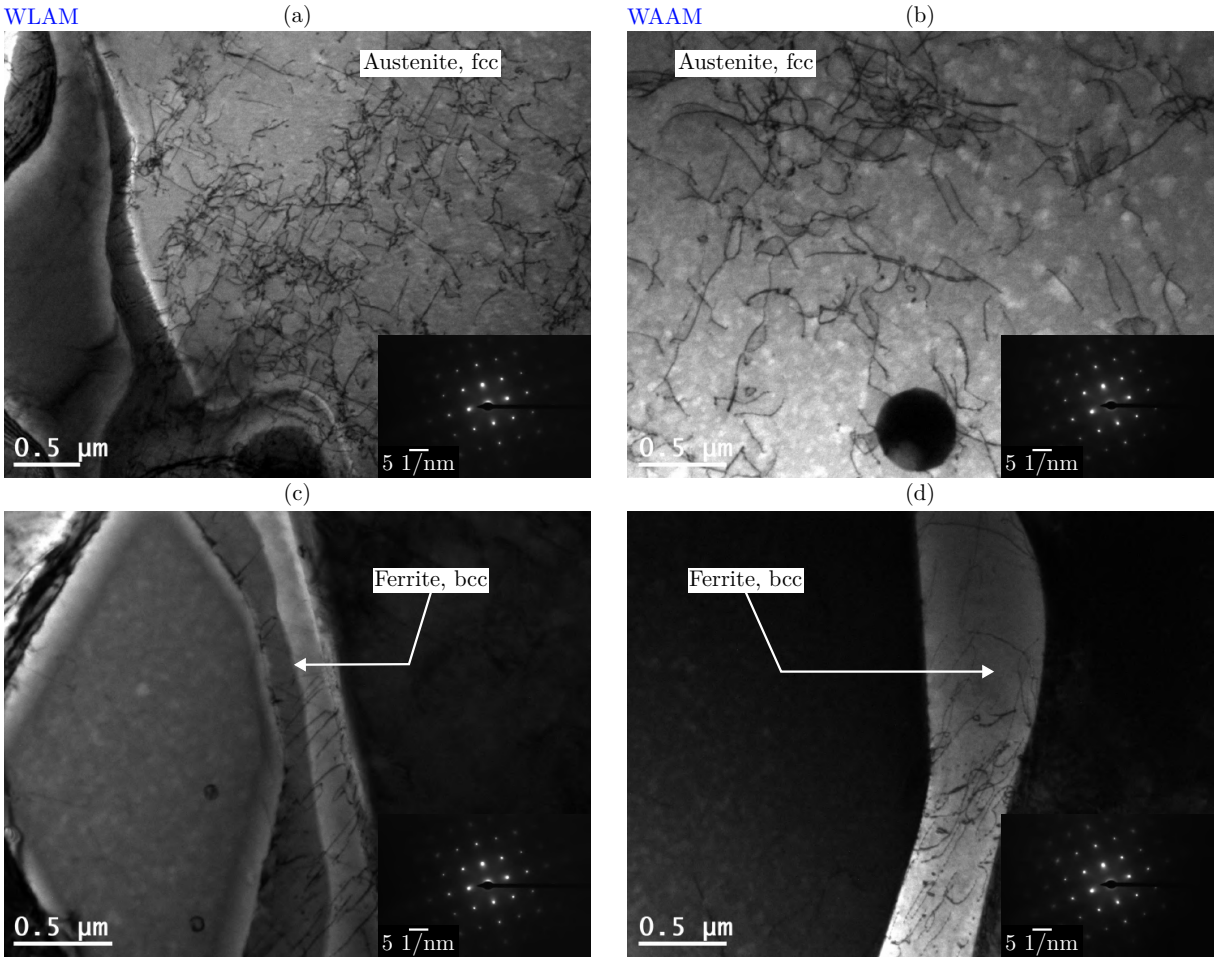

Figure 4.24. TEM analysis of the single-bead walls manufactured with WAAM and WLAM and associated crystalline diffraction patterns near the ⟨001⟩ zone axis: (a) and (b) bright-field images of the austenitic phase in the WLAM and WAAM specimens, respectively; (c) and (d) bright-field images of the ferritic phase in the WLAM and WAAM specimens, respectively. High voltage setting: 200 kV

4.3.5 Mechanical properties

Hardness

Microhardness profiles along the manufacturing direction were acquired for WLAM and WAAM walls using a 0.1 kgf load (Figures 4.25a and b) for the walls produced under different process conditions: WLAM using Sets 1, 2 and 3 (Table 3.4), and WAAM using Sets 1 and 3 (Table 3.5). The process parameters had little effect on the hardness, as all the walls exhibited similar profiles. However, hardness values were slightly higher in WLAM components compared to WAAM ones. Additionally, hardness values decreased from the bottom to the top of the walls:

- 220 $HV_{0.1}$ (bottom) to 185 $HV_{0.1}$ (top) for WLAM;
- 205 $HV_{0.1}$ (bottom) to 180 $HV_{0.1}$ (top) for WAAM.

The macrohardness was also measured using a 10 kgf load at the top and bottom of walls produced with WLAM using Set 2 (Table 3.4) and WAAM using Set 3 (Table 3.5) to compare the values with those determined for single beads in Section 4.2. The macrohardness was reported to be higher in the wall produced by WLAM than in that produced by WAAM and decreased from the bottom to the top of the single-bead walls:

- bottom - 190 HV_{10} (WLAM) and 182 HV_{10} (WAAM) (higher than the hardness values of 174 HV_{10} (WLAM) and 162 HV_{10} (WAAM) for single beads);
- top - 153 HV_{10} (WLAM) and 157 HV_{10} (WAAM) (lower than the hardness values for single beads).

Xu *et al.* [104] and Chen *et al.* [127] observed similar microhardness profiles in 316L single-bead walls fabricated by WLAM (from 210 $HV_{0.3}$ at the bottom to 189 $HV_{0.3}$ at the top) and WAAM (from 202 $HV_{0.5}$ at the bottom to 180 $HV_{0.5}$ at the top). Moreover, it was also observed that single-bead walls made by WLAM are harder than those made by WAAM.

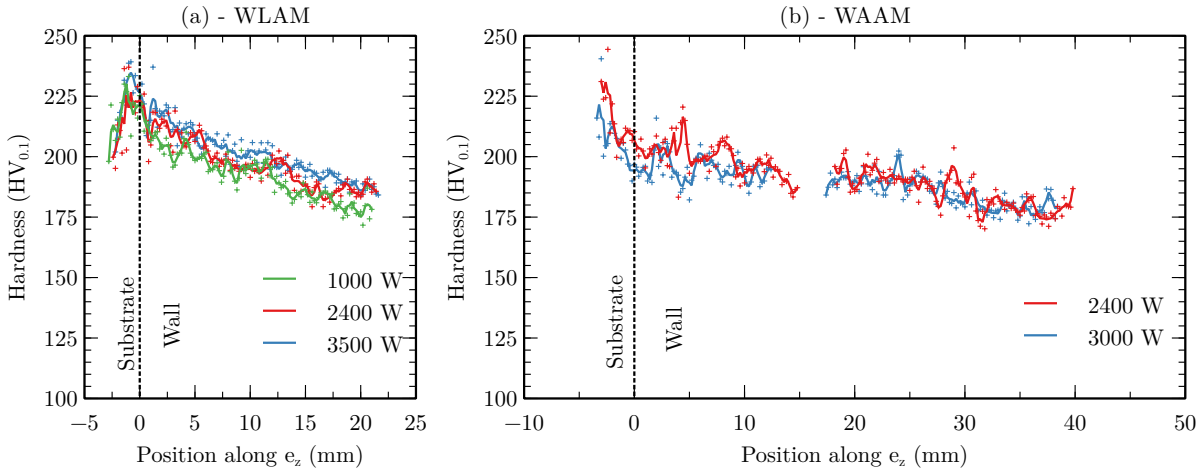

Figure 4.25. Hardness profiles along the manufacturing direction $\underline{e_z}$ from transverse cross-sections of single-bead walls produced by (a) WLAM and (b) WAAM under varying process conditions (Sets 1, 2 and 3 (Table 3.4) for WLAM; Sets 1 and 3 (Table 3.5) for WAAM). Hardness measurements were performed with a 0.1 kgf load. The lines are obtained by plotting the moving average around the five closest values. The WAAM curves are divided into two parts, as the sample was cut in two to enable analysis.

The variations of the hardness in the 316L single-bead walls manufactured with WLAM and WAAM can be attributed to multiple factors:

1. Differences in chemical composition; however, variations in the composition of the solid solution are not considered to occur, as the same wire was used for all components.
2. The ferrite content in the austenitic matrix, as ferrite is harder than austenite [181]. However, no significant variations in the ferrite fraction were observed between the top and bottom of the walls. Additionally, while the walls manufactured by WAAM contain more ferrite than those manufactured with WLAM, the hardness is higher in the walls manufactured by WLAM, suggesting that the ferrite fraction alone can not explain the variations in hardness.
3. The variations in the grain and dendrite sizes, related to Hall-Petch strengthening, as mentioned by Le *et al.* [65]. If the grain size were the only dominant factor, the first deposited layer of the walls would have the same hardness as a single bead, as the deposition conditions were identical, which was not the case. However, the last deposited layer of the wall shows lower hardness compared to single beads, which is likely due to the larger grain and dendrites that form at the top of the wall, resulting from epitaxial growth due to unidirectional thermal gradients and lower cooling rates due to the increasing difficulty to dissipate the heat in the components.
4. The effect of strain hardening: plastic strain is formed due to mechanical blockages during the deposition and is accumulated during the successive heating and cooling cycles, despite some recovery [103, 137]. Higher plastic strains are expected at the bottom of the wall because the substrate limits the shrinkage of the first layers and because this area endures all the heating/cooling cycles. In contrast, the top layers endure a smaller amount of thermal cycles and are free to deform. The plastic strain is associated with dislocation density and increased hardness. It justifies why the first layer of the single-bead walls is harder than the single beads with equivalent microstructure. Finally, the faster cooling rate in WLAM enhances strain hardening compared to WAAM, resulting in higher hardness in WLAM components. Bertsch *et al.* [132] noted that components manufactured with faster cooling rates (as in L-PBF) showed a higher dislocation density than those experiencing lower cooling rates (as in DED processes).
5. Residual stresses induced by the boundary conditions and the geometry. As for strain hardening, higher residual stresses are expected at the bottom of the wall than at the top.

To conclude, increased hardness in components achieved by WAAM and WLAM compared to 316L manufactured using conventional processes would be mainly due to the strain hardening and is susceptible to increase if the number of deposited layers increases.

Tensile tests

The mechanical properties of 316L stainless steel components produced using WAAM (Set 3 - Table 3.5) and WLAM (Set 2 - Table 3.4) were examined through tensile testing. Flat specimens with dimensions of $10 \times 40 \times 2$ mm^3 were machined from each component in the manufacturing and deposition directions. Each test was performed at room temperature under a constant strain rate of 10^{-3} s^{-1}.

Figures 4.26 a and b show the resulting engineering stress-strain curves for WLAM and WAAM, respectively. Two tensile tests were conducted in the manufacturing direction for WLAM (WLAM-V sample) and in the deposition direction for WAAM (WAAM-L sample). For WLAM-L and WAAM-V samples, three tests were performed[4]. Table 4.3 summarizes the obtained mechanical properties (yield strength, tensile strength, and ultimate strain before fracture), measured from the stress-strain curves. Additionally, Figure 4.27 provides orientation and grain boundary maps for the grains within the tensile specimens. Figures 4.27a, b and c show maps for the WLAM specimen in the manufacturing direction (WLAM-V), Figures 4.27d, e and f for the WAAM specimen in the manufacturing direction (WAAM-V), Figures 4.27g, h, and i for the WLAM specimen in the longitudinal direction (WLAM-L), and Figures 4.27j, k, and l for the WAAM specimen in the longitudinal direction (WAAM-L).

The mechanical behaviors of the single-bead walls manufactured with WLAM and WAAM have notable differences. The WLAM specimen exhibited some anisotropy, with a tensile strength 64 MPa higher in the manufacturing direction than in the deposition direction (586 MPa versus 522 MPa) and a yield stress 39 MPa higher (416 MPa versus 377 MPa). In contrast, tensile specimens manufactured by WAAM displayed similar mechanical properties in both manufacturing and deposition directions (538 MPa versus 531 MPa) and yield stress (374 MPa versus 382 MPa). The measured mechanical properties are consistent with the observations of Elmer *et al.* [15], who reported yield stresses between 320 and 410 MPa and tensile strengths between 550 and 610 MPa in 304L components manufactured with both WLAM and WAAM processes.

The observed anisotropy for WLAM wall is attributed to the grain elongation and texture in the WLAM specimens (*cf.* Figures 4.27a, b, c for the manufacturing direction and g, h, i for the deposition direction). It differs from the findings of Xu *et al.* [104], who observed higher tensile strength in the deposition direction for 316L single-bead walls manufactured with WLAM. However, they reported a less columnar microstructure than ours.

Similar results to our findings were observed by Palmeira Belotti *et al.* [84], who reported higher tensile strength in the manufacturing direction, $\underline{e_z}$, than in the deposition direction $\underline{e_x}$, for 316L components manufactured by WAAM, with a microstructure constituted of elongated and textured grains, similar to our WLAM wall. We then assumed that the dislocation slip may be restricted by the small size of the elongated grains in the deposition direction, where the numerous grain boundaries limit the appearance of striction within the tensile test, resulting in higher tensile strength than in the manufacturing direction.

In contrast, the grains in WAAM tensile specimens were more equiaxed than WLAM ones (*cf.* Figures 4.27d, e, f for the manufacturing direction $\underline{e_z}$, and j, k, l for the deposition direction $\underline{e_x}$), contributing to a more isotropic mechanical response. These results diverge from the observations of Laghi *et al.* [131] and Long *et al.* [77], who reported higher tensile strengths in the deposition direction for 316L components manufactured by WAAM. More tensile testing is needed to confirm/infirm the isotropy in WAAM, as the microstructure of our WAAM tensile specimens may not fully represent the entire wall, given that the

[4]Each condition was initially tested three times. However, one test for WLAM-V sample and one for WAAM-L sample were excluded as necking occurred outside the gauge area.

single-bead wall manufactured by WAAM showed elongated grains along the manufacturing direction, suggesting potential anisotropy (*cf.* Section 4.3).

In the deposition direction $\underline{e_x}$, the tensile strength is 16 MPa higher in WAAM than in WLAM, contrary to observations by Elmer *et al.* [15], who reported a higher tensile strength for WLAM compared to WAAM. This discrepancy may result from the lower average grain size in the WAAM tensile specimens than in the WLAM tensile specimens due to numerous equiaxed grains, enhancing the tensile strength through Hall-Petch effect. For the longitudinal cross-sections, WAAM processing resulted in larger grain and dendrite sizes and a higher ferrite content than WLAM, which may explain the observed differences.

Next, measured tensile strengths are lower than those obtained for powder-based additive manufacturing processes. Suryawanshi *et al.* [193] measured tensile strength of 622 MPa and yield stress of 512 MPa in 316L components manufactured using L-PBF, attributed to the finer grain size, dendritic structure, and the higher thermal strain hardening [132]. Additionally, the strong texture in the components contributes to anisotropy of mechanical properties, governed by the Schmid factor related to the grain orientation [194]. Palmeira Belotti *et al.* [84] noted that tensile testing at 45° in WAAM components relative to the manufacturing direction results in different mechanical properties than in both the manufacturing and deposition directions.

Finally, both WLAM and WAAM specimens showed ultimate strains around 40% across all the tested conditions, comparable with the typical elongation range of 40–45% for conventional rolled 316L steel [195]. We also noted higher ultimate strain for WAAM samples due to the fewer oxide inclusions content (*cf.* Section 4.3.3), as oxide inclusions in WLAM and WAAM can serve as initiation sites for fracture [116].

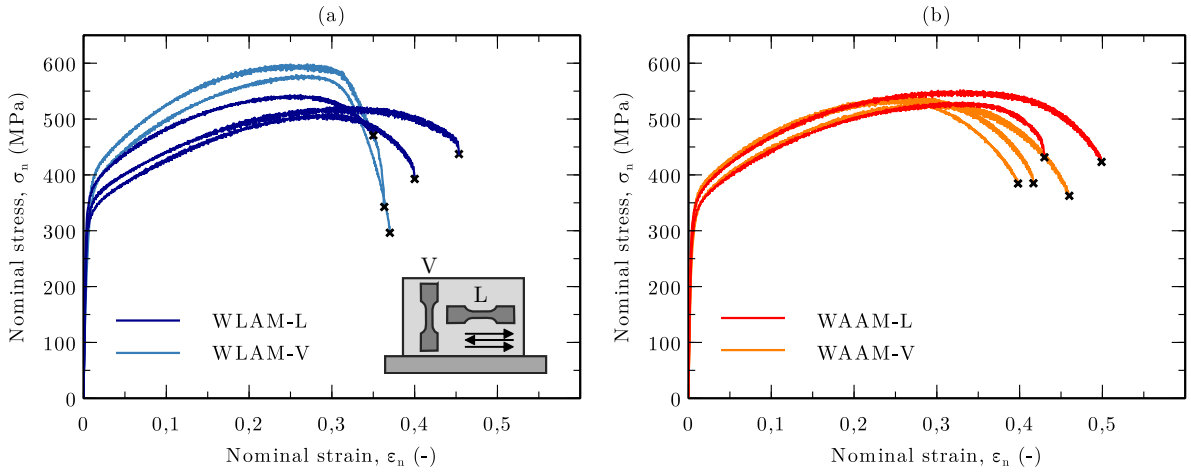

Figure 4.26. Engineering tensile curves for samples machined from single-bead walls produced by (a) WLAM and (b) WAAM, tested along the manufacturing direction $\underline{e_z}$ (WLAM-V, WAAM-V), and deposition direction $\underline{e_x}$ (WLAM-L, WAAM-L). Tests were conducted at room temperature with a constant strain rate of 10^{-3} s^{-1}, using flat tensile specimens with dimensions of $10 \times 40 \times 2$ mm^3 and a gauge area of $10 \times 5 \times 2$ mm^3.

Table 4.3. Mechanical properties (yield stress, tensile strength, and ultimate strain) of 316L single-bead walls manufactured by WLAM using Set 2 (Table 3.4) and WAAM using Set 3 (Table 3.5).

Process	Tensile Direction	Yield Stress (MPa)	Tensile strength (MPa)	Ultimate strain (-)
WLAM	Deposition direction $\underline{e_x}$	377 ± 5	522 ± 5	0.40 ± 0.01
	Manufacturing direction, $\underline{e_z}$	416 ± 5	586 ± 5	0.37 ± 0.01
WAAM	Deposition direction $\underline{e_x}$	374 ± 5	538 ± 5	0.47 ± 0.01
	Manufacturing direction $\underline{e_z}$	382 ± 5	531 ± 5	0.43 ± 0.01

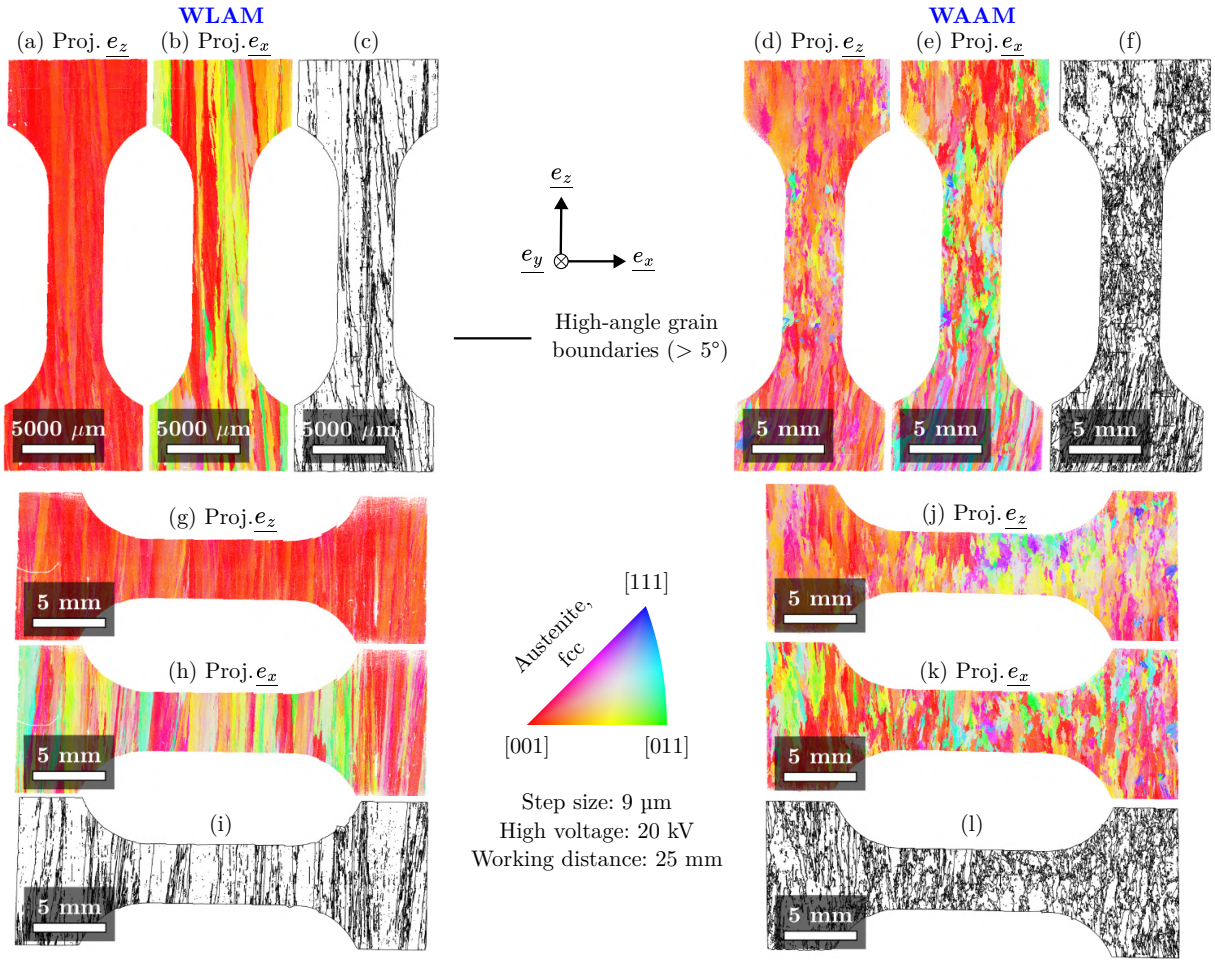

Figure 4.27. EBSD orientation maps and grain boundary maps of transverse cross-sections from tensile test specimens: (a) and (b) orientation maps of the WLAM specimen along the manufacturing direction ($\underline{e_z}$, WLAM-V), projected along $\underline{e_z}$ and $\underline{e_x}$, respectively; (c) grain boundary map associated with the WLAM-V specimen; (d) and (e) orientation maps of the WAAM specimen along the manufacturing direction ($\underline{e_z}$, WAAM-V), projected along $\underline{e_z}$ and $\underline{e_x}$, respectively; (f) grain boundary map associated with the WAAM-V specimen; (g) and (h) orientation maps of the WLAM specimen along the deposition direction ($\underline{e_x}$, WLAM-L), projected along $\underline{e_z}$ and $\underline{e_x}$, respectively; (i) grain boundary map associated with the WLAM-L specimen; (j) and (k) orientation maps of the WAAM specimen along the deposition direction ($\underline{e_x}$, WAAM-L), projected along $\underline{e_z}$ and $\underline{e_x}$, respectively; (l) grain boundary map associated with the WAAM-L specimen.
High-angle grain boundaries (HAGB, $> 5°$) are depicted in black on all GB maps.

The fracture surfaces resulting from the tensile tests performed at room temperature were then analyzed using SEM (Figure 4.28). Figure 4.28a shows the fracture surface of the sample machined from WAAM single-bead wall after tensile testing in the deposition direction $\underline{e_x}$, while Figure 4.28b displays the fracture surface of the sample machined from WLAM wall in the same direction. Additionally, Figure 4.28c provides a close-up of the fracture surface of the sample machined from a single-bead wall manufactured with WLAM.

The fractographies of WLAM and WAAM specimens exhibit circle-like dimples typical of transgranular ductile fracture. This fracture behavior was expected, as necking occurred during the tensile tests, which is also consistent with the usual mechanical response of 316L stainless steel at room temperature [131]. Notably, no differences were observed in the fracture profiles between the specimens tested in the manufacturing $\underline{e_z}$ and the deposition $\underline{e_x}$ directions.

Finally, Figure 4.28c highlights unbroken oxide inclusions at the bottom of the dimples in both WAAM and WLAM samples, indicating that these oxide-metal interfaces act as microvoid initiation sites leading to failure. Similar results were reported by de Sonis [116] for 316L components manufactured by WAAM, where they reported that the average dimple size in the WAAM fracture surfaces obtained by impact toughness tests was 2.9 µm, which is consistent with the dimple sizes observed in our fractographies.

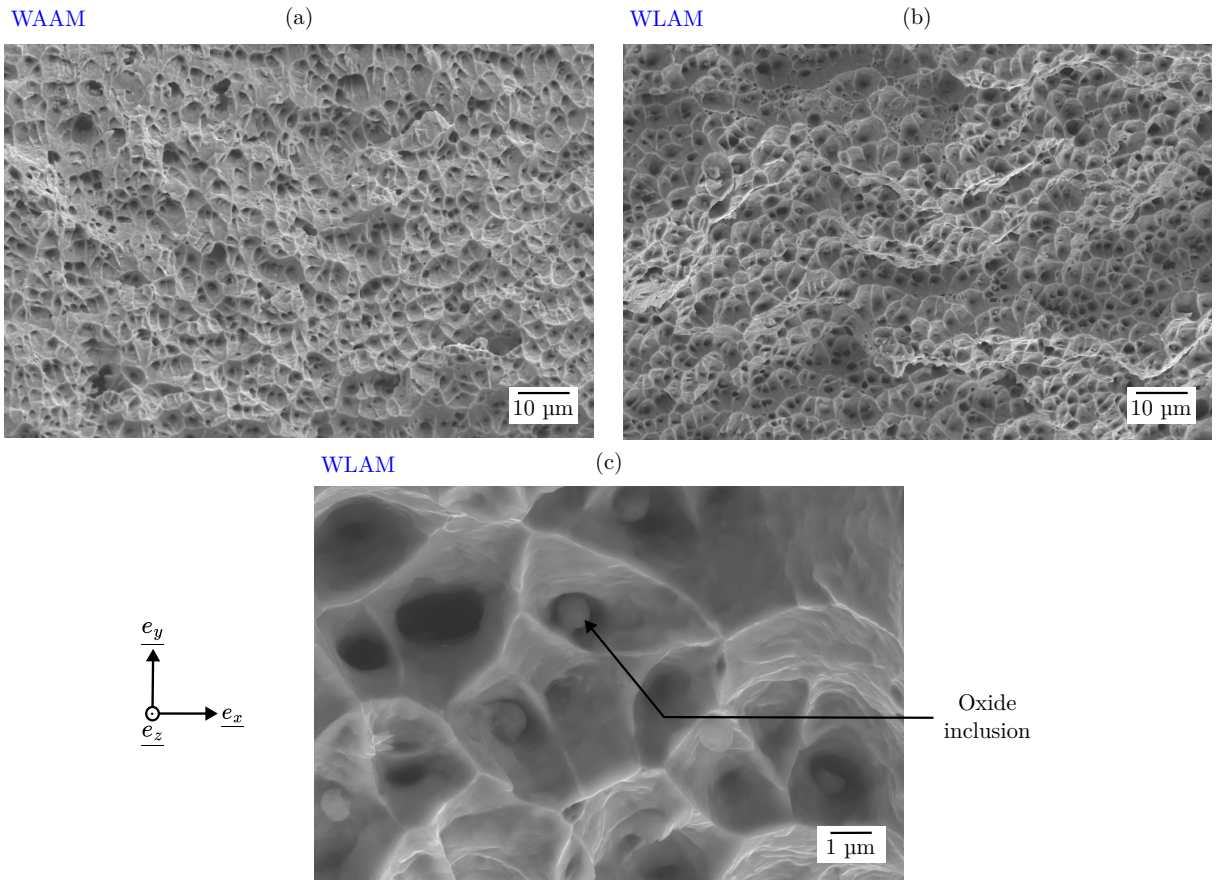

Figure 4.28. Fractographies at room temperature of the single-bead wall of 316L steel manufactured with (a) WAAM and (b) WLAM, after tensile tests in the manufacturing direction $\underline{e_z}$. (c) Oxide inclusions in dimples in the sample obtained by WLAM. SEM settings: secondary electron detector, high voltage = 15 kV, working distance = 10 mm.

4.4 Tiles

4.4.1 Grain structure

The grain microstructures of the 6×20-layer tiles manufactured by WLAM and WAAM were analyzed on transverse cross-sections using orientation maps obtained by EBSD (Figures 4.29 and 4.30, respectively). The dimensions of the tile manufactured by WLAM allowed the characterization of the entire transverse cross-section ($\underline{e_z} - \underline{e_y}$). However, the larger size of the tile manufactured with WAAM required sectioning it into six parts to carry out EBSD analysis. Only two sections were characterized: the upper middle and upper right[5].

Orientation maps were projected in the manufacturing direction $\underline{e_z}$ (Figures 4.29a for WLAM and 4.30a for WAAM), and in the deposition direction $\underline{e_x}$ (Figures 4.29b and 4.30b). In addition, the associated inverse pole figures were obtained for the full WLAM section (Figure 4.29c) and separately for the upper-middle and upper-right sections of the WAAM tile (Figures 4.30c and d, respectively). Moreover, the black arrows on the maps indicate the deposition order of successive beads in the same layer, dotted lines denote fusion boundaries between adjacent beads, and the colored asterisks indicate the main textures.

In addition, Figure 4.31 shows the orientation maps projected in the manufacturing direction $\underline{e_z}$, at the scale of the deposited beads in both WLAM and WAAM tiles. This figure also includes a schematic drawing of the solidification direction and the grain orientations across the characterized zones for beads positioned in the middle (Figures 4.31a for WLAM and 4.31c for WAAM) and at the right edge (Figures 4.31b for WLAM and 4.31d for WAAM) of the seventeenth deposited layer of the WLAM and WAAM tiles.

Finally, Table 4.4 provides a comparative analysis of hardness measurements taken with a 10 kgf load at different positions in the single beads, single-bead walls (bottom and top), and tiles (bottom-right, bottom-middle, top-right, top-middle) manufactured by the WAAM and WLAM processes.

Compared to the single-bead walls, the grains in the tiles are less elongated and not consistently aligned with the manufacturing direction (*cf.* the grain aspect ratio maps presented in Appendix B.3). During the manufacturing of multilayer components, the thermal gradient is not consistently oriented in the manufacturing direction due to the influence of previously deposited beads in each layer, limiting the grain elongation across multiple beads. Furthermore, the microstructure in the tile manufactured with WLAM differed from that achieved by WAAM.

In the WLAM tile (Figure 4.29c), two primary textures were identified:

$$A.(*) \begin{cases} \langle 001 \rangle_{\parallel \underline{e_z}} \\ \langle 001 \rangle_{\parallel \underline{e_x}} \end{cases} \text{ and } B.(*) \begin{cases} \langle 011 \rangle_{\parallel \underline{e_z}} \\ \langle 001 \rangle_{\parallel \underline{e_x}} \end{cases}$$

Several zones were defined based on these textures. Texture A appeared at the edges of the tile (Edge Region, ER) and at the center of the deposited beads in the middle section of the tiles (Center of Fusion Zone, CFZ). Texture B is found at the sides of the deposited beads in the middle of the tile (Side of Fusion Zone, SFZ) and the central part of the beads at the tile edges (also labeled SFZ). For the single bead located in the tile center (Figure 4.31a), the $\langle 001 \rangle_{\parallel \underline{e_z}}$ texture is visible in the CFZ, with elongated grains indicating solidification along the $\underline{e_z}$ direction. In the SFZ, the $\langle 011 \rangle_{\parallel \underline{e_z}}$ texture is caused by

[5]The middle-bottom and right-bottom sections were also analyzed but not processed due to their similarity to the upper sections.

the elongated grains growing at a 45° angle to $\underline{e_z}$, influenced by the rounded shape of the melt pool and the dendritic solidification perpendicular to the fusion line. Similar textures have been observed by Dépinoy *et al.* [196] in 316L tiles manufactured with L-PBF, where rounded melt pools produced a strong $\langle 001 \rangle_{\parallel \underline{e_z}}$ texture in bead centers (CFZ) and a $\langle 011 \rangle_{\parallel \underline{e_z}}$ texture in bead sides (SFZ). However, the L-PBF microstructure showed a stronger texture than WLAM, which we attributed to larger melt pool dimensions and lower thermal gradients in WLAM, allowing more dendritic deviation and crystal orientation variety.

At the edges of the WLAM tile (Figure 4.31b), the shape of the melt pools is flatter, similar to those in WLAM single-bead walls, with elongated grains extending through multiple layers at a 45° angle to the $\underline{e_z}$ direction. The ER region presents elongated grains in the manufacturing direction, textured with $\langle 001 \rangle_{\parallel \underline{e_z}}$, also observed in L-PBF components with flatter bead morphologies, as reported by Ishimoto *et al.* [197].

In the tile manufactured by WAAM, the same $\langle 001 \rangle_{\parallel \underline{e_z}}$ and $\langle 011 \rangle_{\parallel \underline{e_z}}$ textures were observed (Figure 4.30), but with an inverse distribution in the component as compared to the WLAM tile. The $\langle 001 \rangle_{\parallel \underline{e_z}}$ texture was observed at the sides of the beads, attributed to the flat fusion boundary in this zone (overlapping region, OR), where beads are remelted by the adjacent beads within the same layer. Moreover, the $\langle 011 \rangle_{\parallel \underline{e_z}}$ texture appeared in the bead centers (CFZ), where the fusion boundary follows a rounded shape. These two similar zones (OR and CFZ) were observed by Monier [28] in 316L CMT-WAAM tiles. This unique bead shape in WAAM-manufactured tiles, resulting from the larger dimensions of the beads, creates microstructural differences between WAAM and L-PBF or WLAM components.

Distinct microstructures were also observed at the WAAM tile edges. The edge overlapping region (ORE) presented similar elongated grains as in the OR, though slightly deviated to the right at a 20° angle. Palmeira Belotti [112] reported a similar grain deviation in 316L WAAM components, where a 30° deviation was attributed to the rotation of the thermal gradient at the component edges. Finally, the ER region appeared to result from surface nucleation during solidification.

In the deposition direction $\underline{e_x}$, the textures of WLAM and WAAM tiles are different. In the WLAM tile, a strong $\langle 001 \rangle_{\parallel \underline{e_x}}$ texture is present, similar to that in 316L L-PBF tiles, as reported by Ishimoto *et al.* [197], indicating a thermal gradient within the transverse plane with a limited deviation in the deposition direction. Oppositely, in the CFZ of the WAAM tile, a $\langle 112 \rangle_{\parallel \underline{e_x}}$ texture appears, suggesting a thermal gradient with components in both the manufacturing $\underline{e_z}$ and deposition $\underline{e_x}$ directions, consistent with the rear melt pool solidification previously observed for WAAM longitudinal cross-sections [3].

Finally, hardness in the centers of the tiles is higher compared to single-bead walls, with a value comprised between 218 to 205 HV_{10} for WLAM and 197 to 195 HV_{10} for WAAM, from the bottom to the top. No significant variation was observed between the right and middle sections of the tiles. The increased hardness likely results from a higher strain hardening rather than the grain size variation, as the grain dimensions in CFZ and ER regions differ, yet hardness remains unaffected. Goland *et al.* [114] reported comparable hardnesses in 316L WAAM and WLAM tiles (182 $HV_{0.5}$ for WAAM and 196 $HV_{0.5}$ for WLAM), consistent with our findings.

Table 4.4. Determined hardnesses with a 10 kgf load in the different manufactured components (single beads, single-bead walls, and multilayer tiles) with WLAM and WAAM processes.

(HV_{10})		WLAM	WAAM
Single bead		174	162
Wall	Bottom	190	182
	Top	153	157
Tile	Right-bottom	205	190
	Right-top	207	182
	Middle-bottom	218	197
	Middle-top	205	195

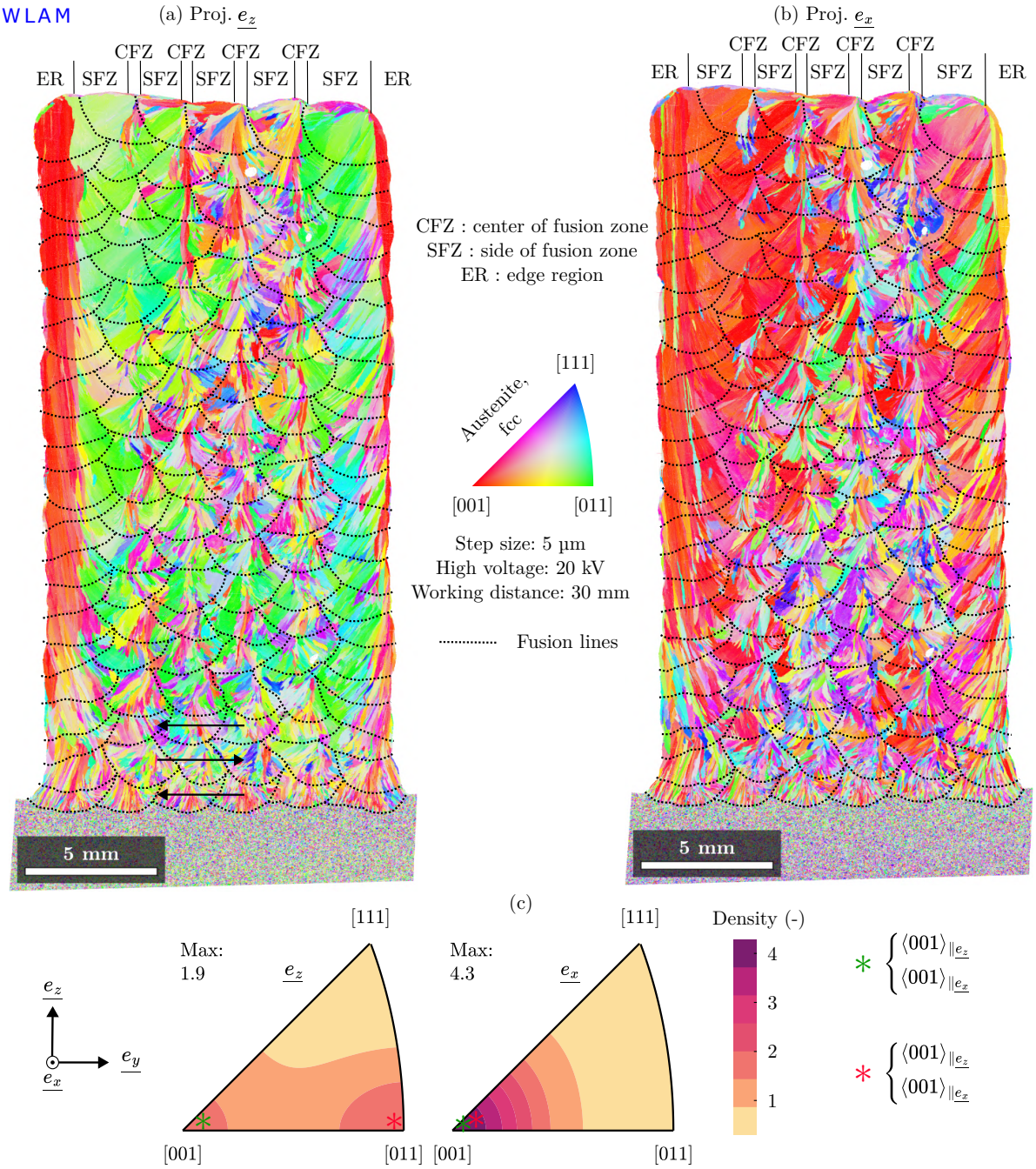

Figure 4.29. EBSD analysis of the transverse cross-section of a tile manufactured with the WLAM process: (a) and (b) orientation maps, projected respectively in the manufacturing direction, $\underline{e}_z$, and the deposition direction $\underline{e}_x$; (c) associated inverse pole figures. The black arrows depict the order of deposition of the successive beads in the same layer, and the asterisks indicate the main textures.

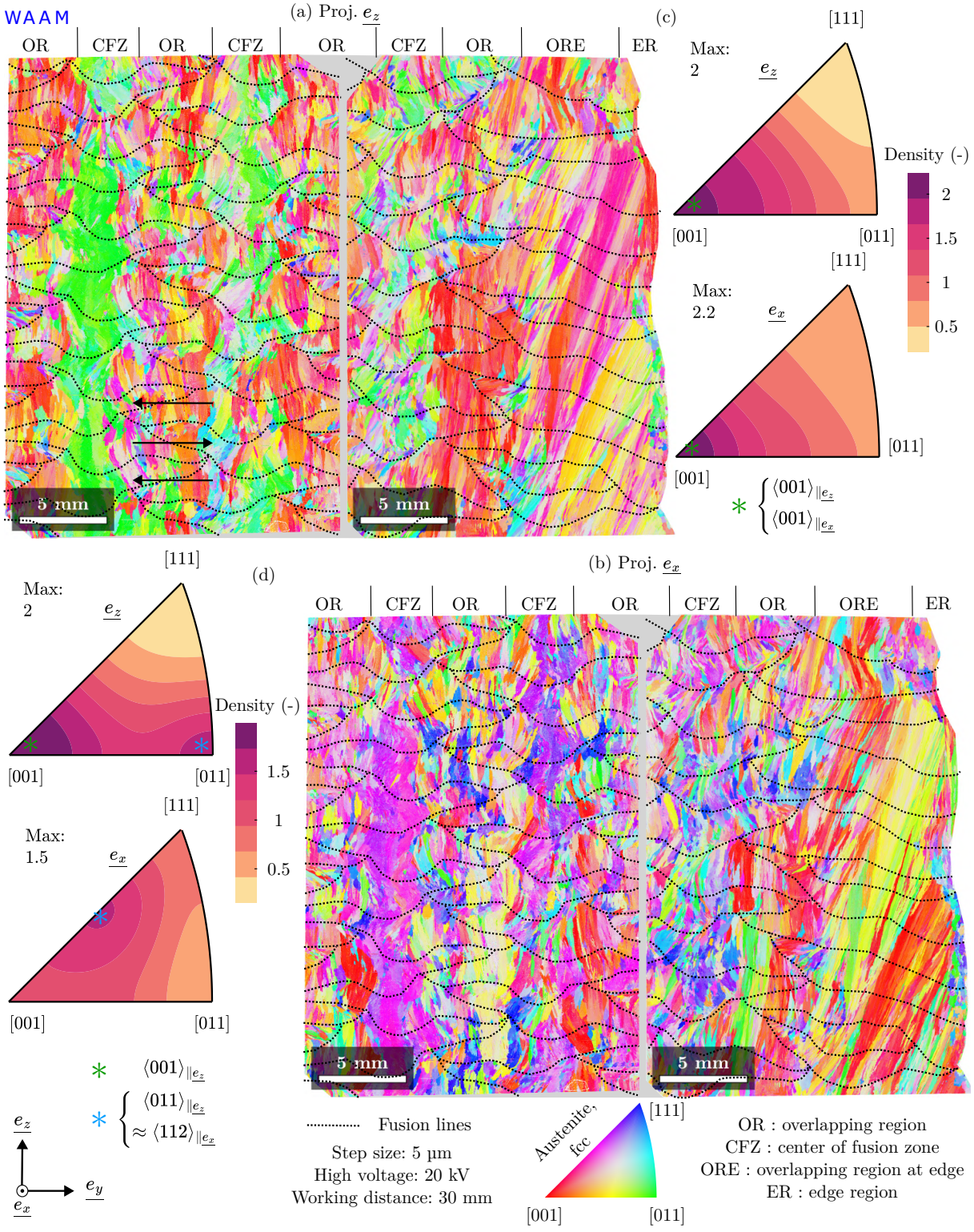

Figure 4.30. EBSD analysis of the transverse cross-section of a tile manufactured with the WAAM process: (a) and (b) orientation maps, projected respectively in the manufacturing direction $\underline{e_z}$, and the deposition direction $\underline{e_x}$. The left part of the map corresponds to the upper middle part of the transverse cross-section of the tile. The right part of the map corresponds to the upper right part of the transverse cross-section of the tile; (c) inverse pole figures associated with the right part of the maps; (d) inverse pole figures associated with the left part of the maps. The black arrows depict the order of deposition of the successive beads in the same layer, and the asterisks indicate the main textures.

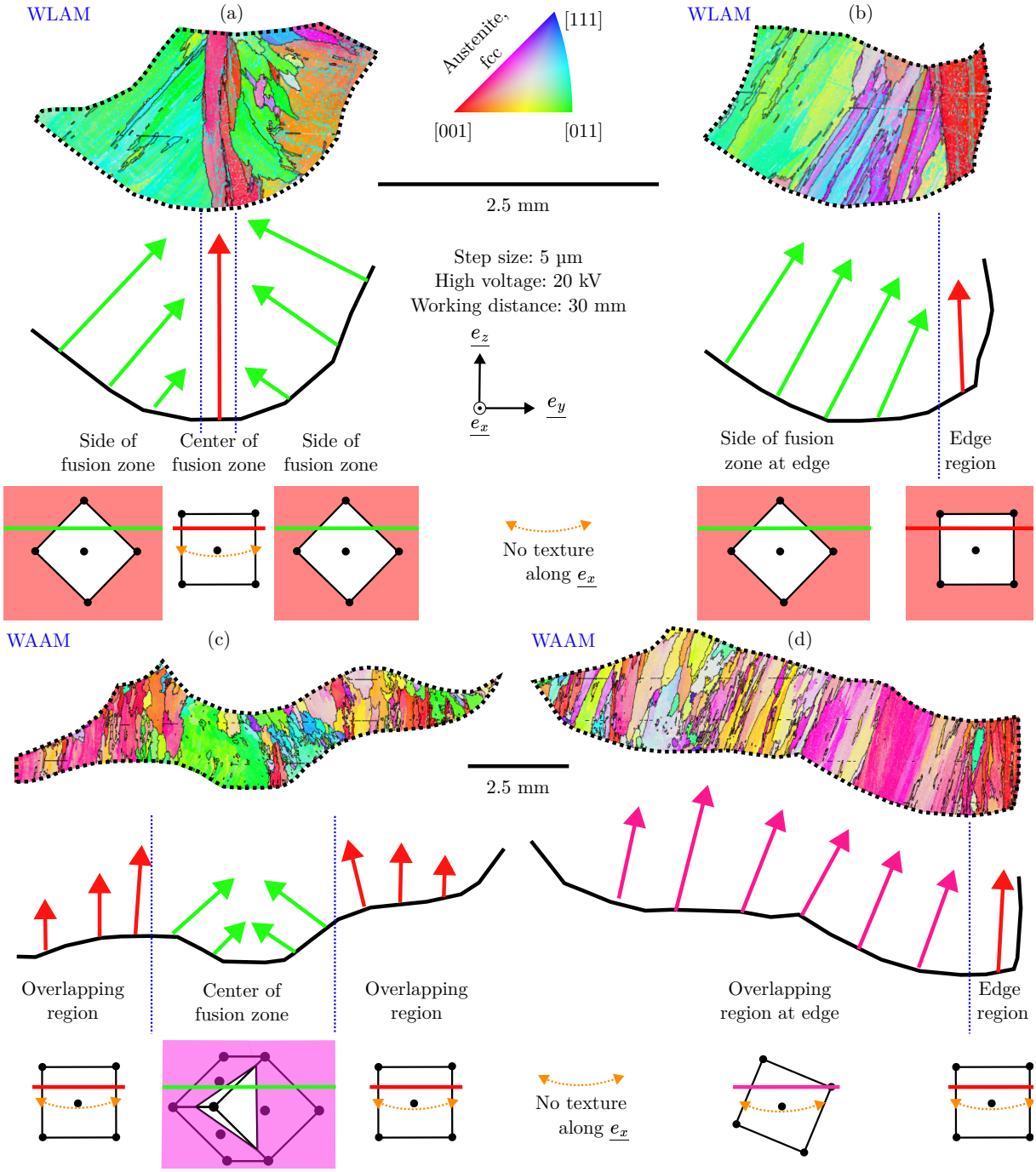

Figure 4.31. EBSD orientation maps and schematic representation of the solidification for the seventeenth deposited layer of tiles manufactured by WLAM and WAAM, located at the center and edges of the component. The maps are projected along the manufacturing direction $\underline{e_z}$: (a) close-up of a single bead in the center of the tile manufactured with WLAM; (b) close-up of a single bead at the edge of the tile manufactured with WLAM; (c) close-up of a single bead in the center of the tile manufactured with WAAM; (d) close-up of a single bead at the edge of the tile manufactured with WAAM.

4.4.2 Dendrite structure

In the tile manufactured by WAAM, dendrite morphology is similar to that of the WAAM single-bead wall (Figure 4.19), showing bands of ferrite situated between both the primary and secondary dendrite arms, indicating FA solidification mode.

Figures 4.32a and b show optical micrographs taken after electrolytic etching of a transverse cross-section of the tile built by WLAM near the edge and the center of the tenth deposited layer, respectively. In the single-bead wall produced by WLAM, we previously observed in Figure 4.19 that the ferrite phase was only located between primary dendrite arms near fusion lines but was present in both primary and secondary dendrite arm spacings (PDAS and SDAS) at the center of the deposited bead. In the WLAM tile (Figure 4.32), vermicular and lathy ferrite was consistently observed throughout the component, appearing between primary and secondary dendrite arms. In addition, the primary dendrite arm spacing (PDAS) was estimated using the intercept method. In the tenth layer of the WLAM-manufactured tile, the PDAS was measured to be of 5.6 ± 0.5 µm near the edges and 1.5 times smaller, of 3.8 ± 0.5 µm, in the tile center. These values are lower than the PDAS observed in the single-bead wall achieved by WLAM (7.1 ± 0.5 µm). This difference is attributed to the higher cooling rates in the WLAM tile, where the heat dissipates more efficiently into the solidified neighboring metallic beads rather than ambient air. These findings align with observations made by Akbari and Kovacevic [109], who reported that tiles manufactured with WLAM experience higher cooling rates than thin walls, resulting in lower PDAS (4 ± 0.5 µm versus 5.5 ± 0.5 µm).

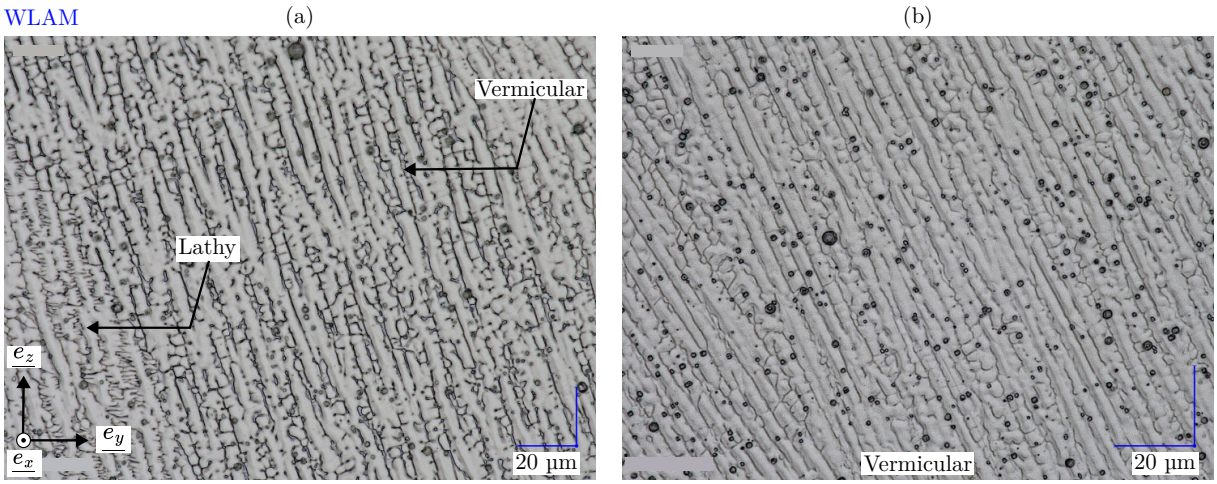

Figure 4.32. Optical micrographs after electrolytic etching in a transverse cross-section of the tenth layer of the tile produced by WLAM. (a) Right part and (b) Middle part.

4.5 Effect of heat treatment on single-bead walls

To identify heat treatment conditions to avoid the formation of σ-phase, we first analyzed the chemical composition of austenite and ferrite using STEM/EDS in single-bead walls manufactured by WAAM and WLAM (Table 4.5).

After both WAAM and WLAM processes, the nickel content in austenite was approximately twice than that of ferrite. Conversely, ferrite displayed higher concentrations of chromium and molybdenum. However, WLAM ferrite contained about 3 wt.% less chromium and 2 wt.% more molybdenum than WAAM ferrite.

Table 4.5. Chemical composition (wt.%) determined by STEM-EDS of the austenite and ferrite in 316L single-bead walls manufactured with WAAM and WLAM processes.

(wt. %)	Phase	Fe	Ni	Cr	Mn	Mo	Si
WAAM	Austenite	64.4	12.0	19.3	2.1	1.9	0.4
	Ferrite	61.6	6.0	27.5	1.8	2.3	0.9
WLAM	Austenite	66.0	11.1	18.9	1.5	2.4	0.2
	Ferrite	63.4	6.1	24.6	1.3	4.3	0.3

Using the measured phase composition, simulations using Thermo-Calc software with the TCFE9 database were conducted to determine the equilibrium volume fractions of various phases (Figure 4.33). A calculation based on the global chemical composition of the WAAM and WLAM components, obtained through ICP-AES, was also performed (Figure 4.33c). Continuous lines represent the volume fractions of the different phases for WAAM, while dotted lines represent the volume fractions of the different phases for WLAM.

At equilibrium, simulations indicated that the σ-phase may form up to 900 °C in WAAM and 950 °C in WLAM austenite and up to 900 °C in WAAM and 1000 °C in WLAM ferrite. Literature suggests that the σ-phase can precipitate at the austenite grain boundaries [96], though it most often forms in ferrite [198]. Laves phase, π-phase (labeled as PI in Figure 4.33), Cr_2N phase (labeled as HCP), and $M_{23}C_6$ carbides, are expected to coexist with the σ-phase. For example, 2-3% of austenite at equilibrium could transform into Laves phase if the temperature is below 750 °C for a sufficient time. Taking into account their low fraction, these phases were excluded from our analysis. Py-Renaudie's thesis work [96] discusses Laves phase precipitation in aged welded structures made from 316L steel.

Below 1000 °C, approximately 30-40% of the ferrite could transform into σ-phase in WAAM and WLAM components. Additionally, above 1200 °C, up to 10% of austenite could transform into ferrite at equilibrium. Finally, between 600 °C and 800 °C, up to 60% of ferrite may transform into austenite.

Therefore, to avoid σ-phase formation, the heat treatment temperatures should exceed 1000 °C. Thus, we selected temperatures of 1100 and 1200 °C. A 30-minute holding time was chosen, as de Sonis [116] demonstrated complete recrystallization of CMT-WAAM 316L tiles at 1200 °C after 30 minutes. Furthermore, a 30-minute hold at 1100 °C is expected to dissolve ferrite as this phase is not stable at this temperature, without causing recrystallization, as observed by Monier [28]. The heat treatment was followed by a quenching to avoid ferrite re-formation.

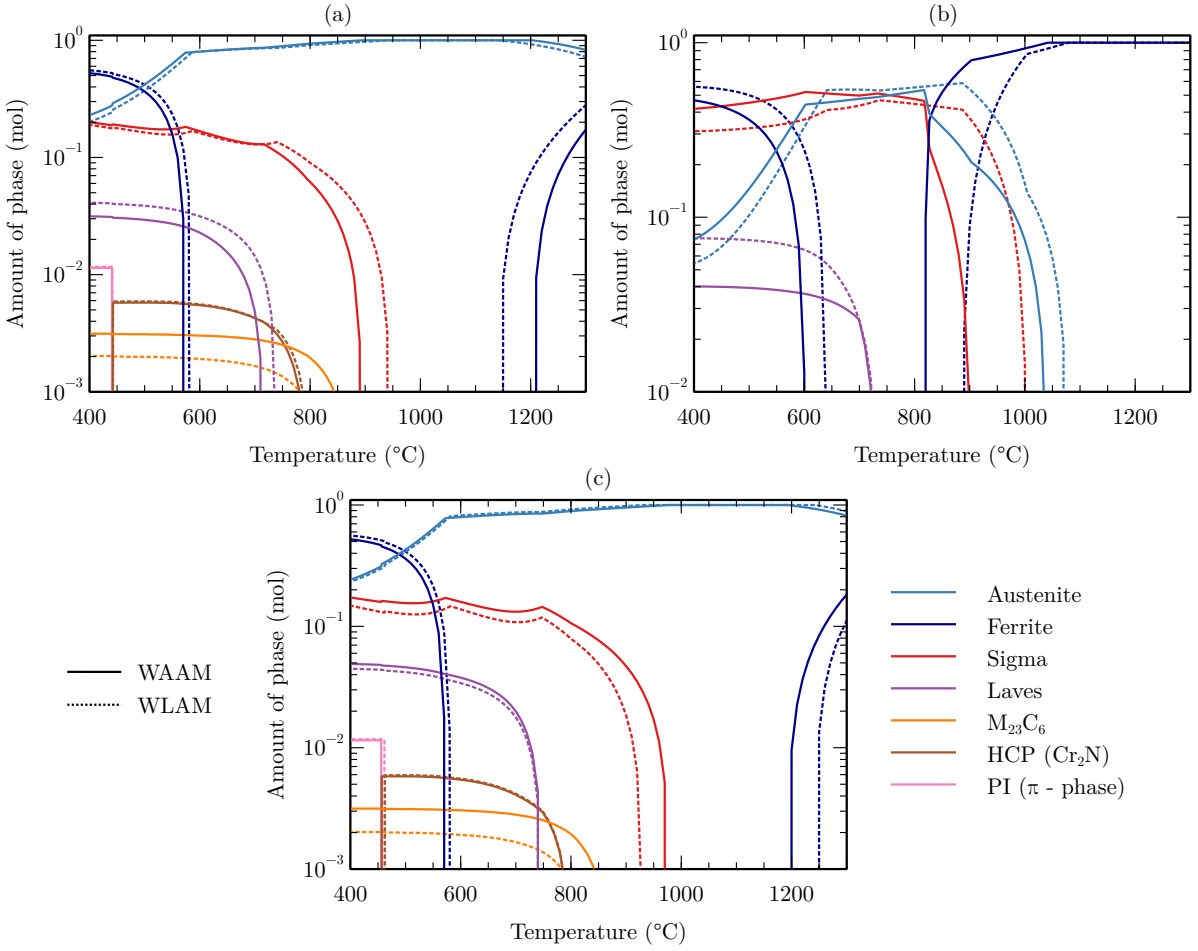

Figure 4.33. Phase fractions at equilibrium in WLAM and WAAM single-bead walls (Thermo-Calc software with TCFe9 database) using the determined chemical compositions of (a) the austenite, (b) the ferrite with STEM-EDS (Table 4.5) and (c) the nominal composition of the 316L stainless steel determined using inductively coupled plasma spectroscopy.

4.5.1 Dendrite microstructure

Figures 4.34a and b compare the dendrite microstructure in the single-bead wall produced using the WLAM process, shown respectively in as-built state and after a 30-minute heat treatment at 1100 °C, followed by quenching. The optical micrographs were taken from transverse cross-sections near the tenth deposited layer, at the middle of the single-bead walls, after electrolytic etching with oxalic acid.

The heat treatment led to the transformation of ferrite into the austenite phase, with only a minimal amount of ferrite remaining in the heat-treated component. This ferrite takes a globular form (Figure 4.34b). Ferritescope measurements indicated a ferrite content of 0.7 vol.% in the heat-treated state, significantly reducing from the as-built ferrite content of 5-6 vol.%. Similarly, after a 30-minute heat treatment at 1200 °C, no ferrite was observed in the single-bead walls achieved by WAAM and WLAM. Monier [28] observed a similar decrease of the ferrite fraction in a 316L tile manufactured using WAAM, following a 1-hour heat treatment at 1050 °C, although some areas retained up to 4.5 vol.% of residual globular ferrite. Moreover, no chemical heterogeneity was found in the austenite using SEM-EDS.

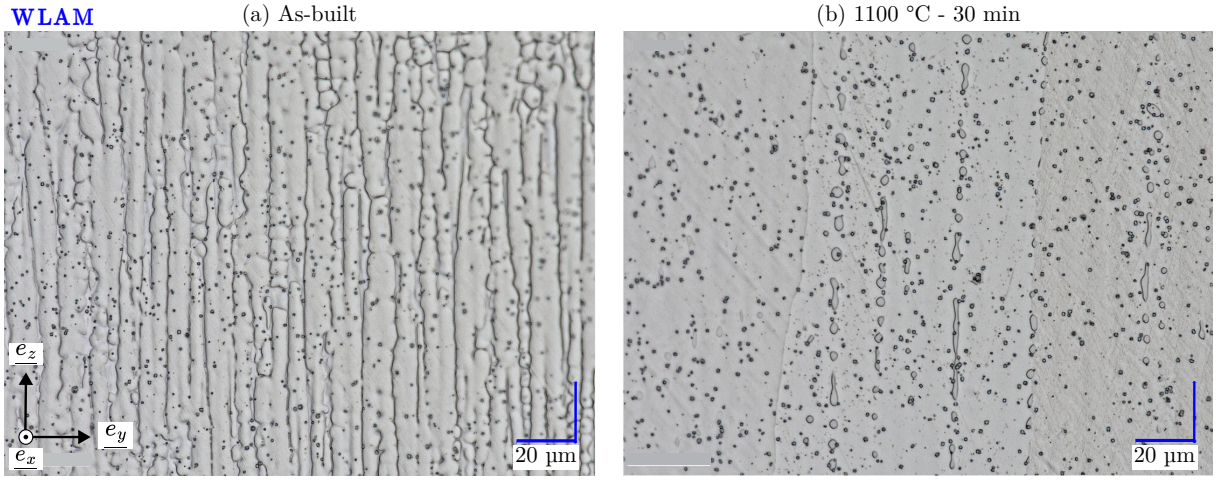

Figure 4.34. Optical micrographs after electrolytic etching in a transverse cross-section of the tenth layer of the single-bead wall manufactured with WLAM (a) before and (b) after heat treatments at 1100 °C for 30 min.

4.5.2 Grain microstructure

Figures 4.35a and b present the microhardness profiles along the manufacturing direction $\underline{e}_z$ of single-bead walls made using WLAM and WAAM, respectively, for each heat treatment condition (1100 °C - 30 min and 1200 °C - 30 min for WLAM; 1200 °C - 30 min for WAAM[6]). Figure 4.36 shows the EBSD orientation maps obtained from the transverse cross-section of a single-bead wall manufactured with WLAM after heat treatments at 1100 °C for 30 minutes (Figures 4.36a and b) and at 1200 °C for 30 minutes (Figures 4.36c and d). The orientation maps are projected along the manufacturing direction $\underline{e}_z$ in Figures 4.36a and c and along the deposition direction $\underline{e}_x$ in Figures 4.36b and d. These orientation maps were used to generate grain boundary (GB) and Grain Orientation Spread (GOS) maps for the wall produced with WLAM (Figure 4.37). HAGBs are shown in black, LAGBs in cyan, and Σ3-twin boundaries in red. The GB maps for the WLAM components after heat treatment at 1100 °C for 30 minutes and at 1200 °C for 30 minutes are shown in Figures 4.37a and c, respectively, while the GOS maps for these treatments are presented in Figures 4.37b and d.

[6]The EBSD analysis of the single-bead wall achieved made with WAAM treated at 1100 °C - 30 min was not achieved to optimize the analysis time.

A similar EBSD analysis was conducted on a single-bead wall manufactured with WAAM after heat treatment at 1200 °C for 30 minutes (Figure 4.38). Orientation maps projected along $\underline{e_z}$ and $\underline{e_x}$ are shown in Figures 4.38a and b, respectively. The corresponding GB and GOS maps are presented in Figures 4.38c and d.

Lastly, EBSD orientation maps were obtained at the same scale for single-bead walls made with WAAM and WLAM after a 30-minute heat treatment at 1200 °C, showing regions near the fifteenth deposited bead (Figures 4.39a and b for WLAM and WAAM, respectively) and near the third deposited bead (Figures 4.39c and d for WLAM and WAAM, respectively).

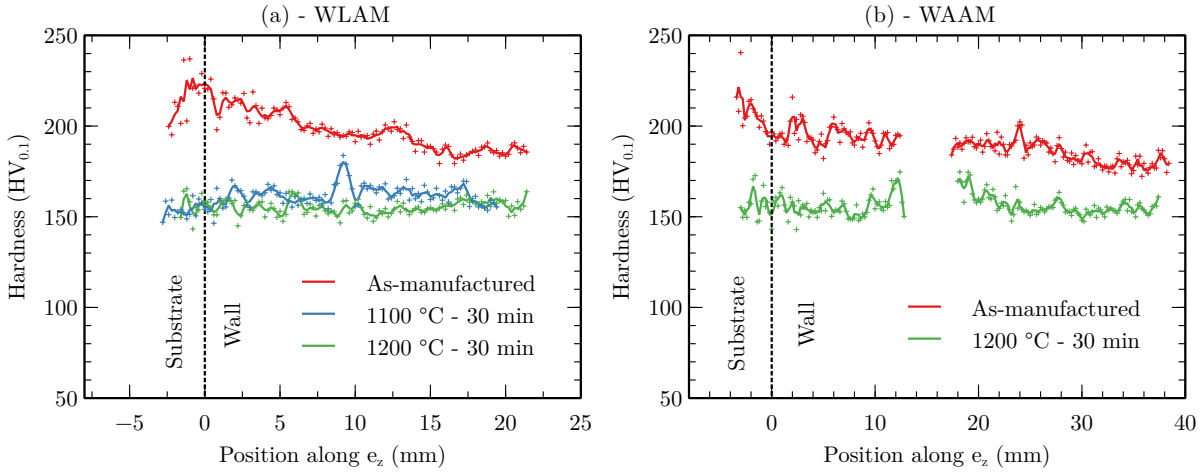

Figure 4.35. Hardness profiles along the manufacturing direction $\underline{e_z}$, achieved on a transverse cross-section of single-bead walls manufactured by WLAM and WAAM, in their as-built state, and after heat treatments at 1100 °C for 30 min and 1200 °C for 30 min.

The heat treatment carried out at 1100 °C for 30 minutes applied to the WLAM single-bead wall did not result in significant microstructure variation at the grain scale. Figures 4.36a and b show a similar microstructure to the as-built state, with elongated grains in the manufacturing direction and a texture along $\langle 001 \rangle_{\parallel \underline{e_z}}$. Monier [28] observed similar results for a WAAM tile heat-treated at 1050 °C for 1 hour, concluding that the ferrite dissolution did not affect the grain microstructure for these treatment conditions. Additionally, the microhardness profile decreased from approximately 200 $HV_{0.1}$ in the as-built state to 160 $HV_{0.1}$ in the heat-treated component. This reduction in hardness is likely due to a combination of dislocation recovery and a lower ferrite content.

In contrast, the heat treatment at 1200 °C for 30 minutes resulted in partial recrystallization in the WLAM single-bead wall. Complete recrystallization was observed in the first ten deposited layers, with equiaxed grains with no specific orientation, no visible GOS or LAGB, and multiple Σ3 twin boundaries, all characteristic of recrystallized grains. However, beyond the tenth layer, the recrystallization was limited to the edges of the walls, with the main microstructure still comprising elongated, textured grains, as in the as-built state.

This partial recrystallization may have multiple origins:

- smaller grain size at the bottom of the walls, promoting easier nucleation of new grains;
- higher thermal strain hardening at the bottom of the wall compared to the top part, thus more driving forces for recrystallization;
- insufficient conditions of the heat treatment for full recrystallization.

The hardness decreased to 150 $HV_{0.1}$ for both processes, which aligns with the hardness of conventionally manufactured 316L steel. Achieving this hardness suggests that most of the stored dislocation energy has been consumed. A longer heat treatment may lead to grain coarsening of the already recrystallized areas, potentially resulting in full recrystallization but with a notably larger grain size.

The single-bead wall manufactured using the WAAM process, analyzed after a 1200 °C - 30 minutes heat treatment, presented similar results. Complete recrystallization was observed only in the first five layers, with no visible recrystallization in subsequent layers. The hardness similarly dropped to 150 $HV_{0.1}$, comparable to conventional stainless steel.

Several authors such as de Sonis [116] and Goland [114] obtained fully recrystallized WAAM and WLAM tiles with a 1200 °C heat treatment for 30 minutes and 2 hours, respectively. However, their studies used multilayer tiles, which differ microstructurally from single-bead walls. Wang *et al.* [141] observed only partial recrystallization in a component treated at 1200 °C for 1 hour, agreeing with our results.

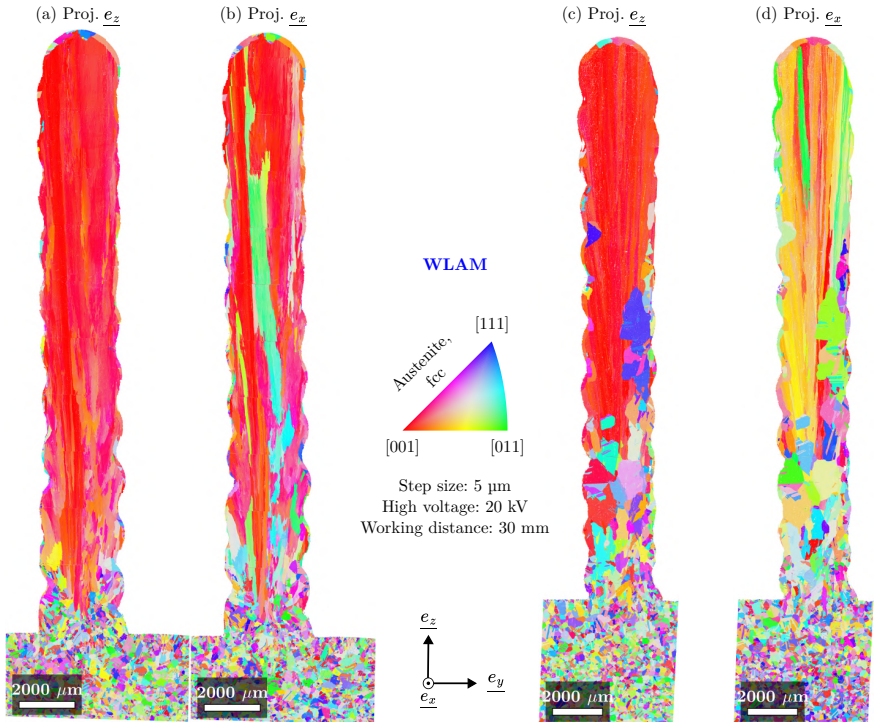

Figure 4.36. Orientation maps obtained by EBSD of the transverse cross-section of a single-bead wall manufactured with WLAM after heat treatments at (a) and (b) 1100 °C for 30 mins and (c) and (d) 1200 °C for 30 min. (a) and (c) Projection in the manufacturing direction $\underline{e_z}$ (b) and (d) Projection in the deposition direction $\underline{e_x}$.

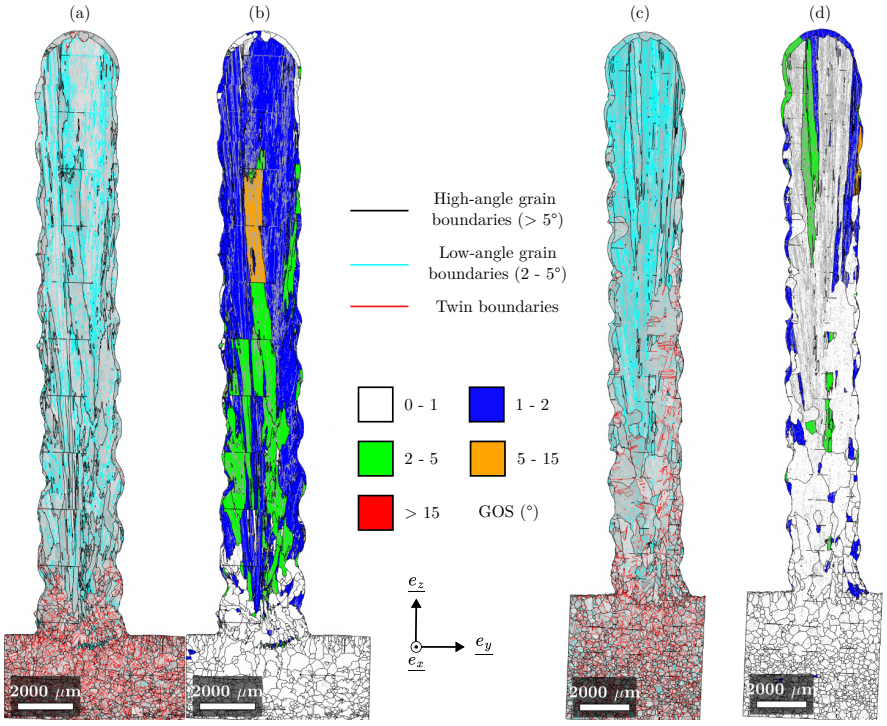

Figure 4.37. Grain boundaries maps and GOS maps of the single-bead wall manufactured with WLAM, after heat treatments at (a) and (b) 1100 °C and (c) and (d) 1200 °C for 30 min. (a) and (c) Grain boundary maps. The black lines correspond to HAGB, the cyan lines to LAGB, and the red lines to Σ3-twins. (b) and (d) GOS maps. The black lines represent the HAGBs, and the grey lines the LAGBs.

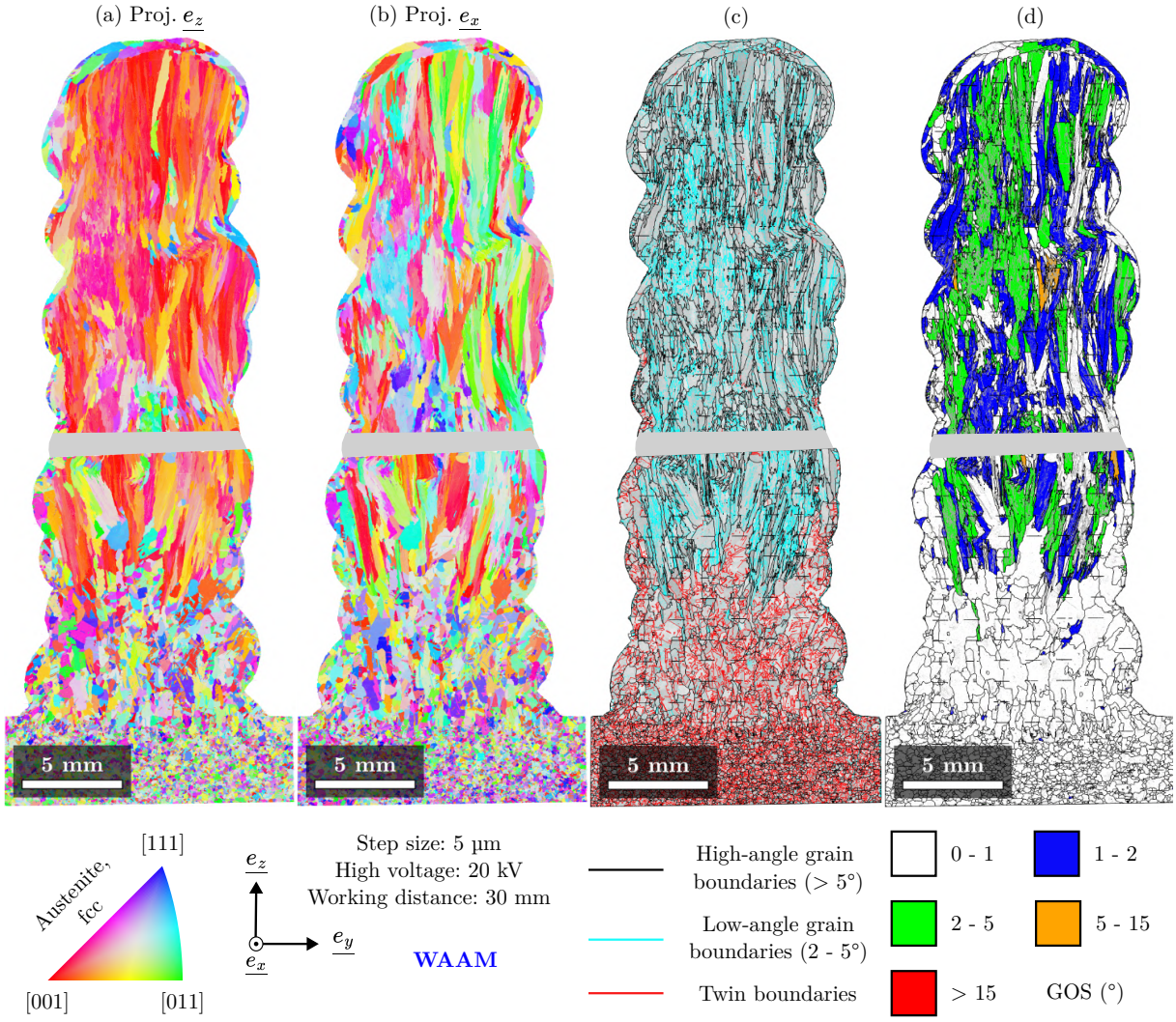

Figure 4.38. EBSD analysis of the transverse cross-section of a single-bead wall manufactured with WAAM after heat treatment at 1200 °C for 30 min. (a) and (b) Orientation maps, projected in the manufacturing direction $\underline{e_z}$, and the deposition direction $\underline{e_x}$, respectively. (c) Grain boundary map. The black lines correspond to HAGBs, the cyan lines to LAGBs, and the red lines to Σ3-twins. (d) GOS map. The black lines represent the HAGBs, and the grey lines the LAGBs

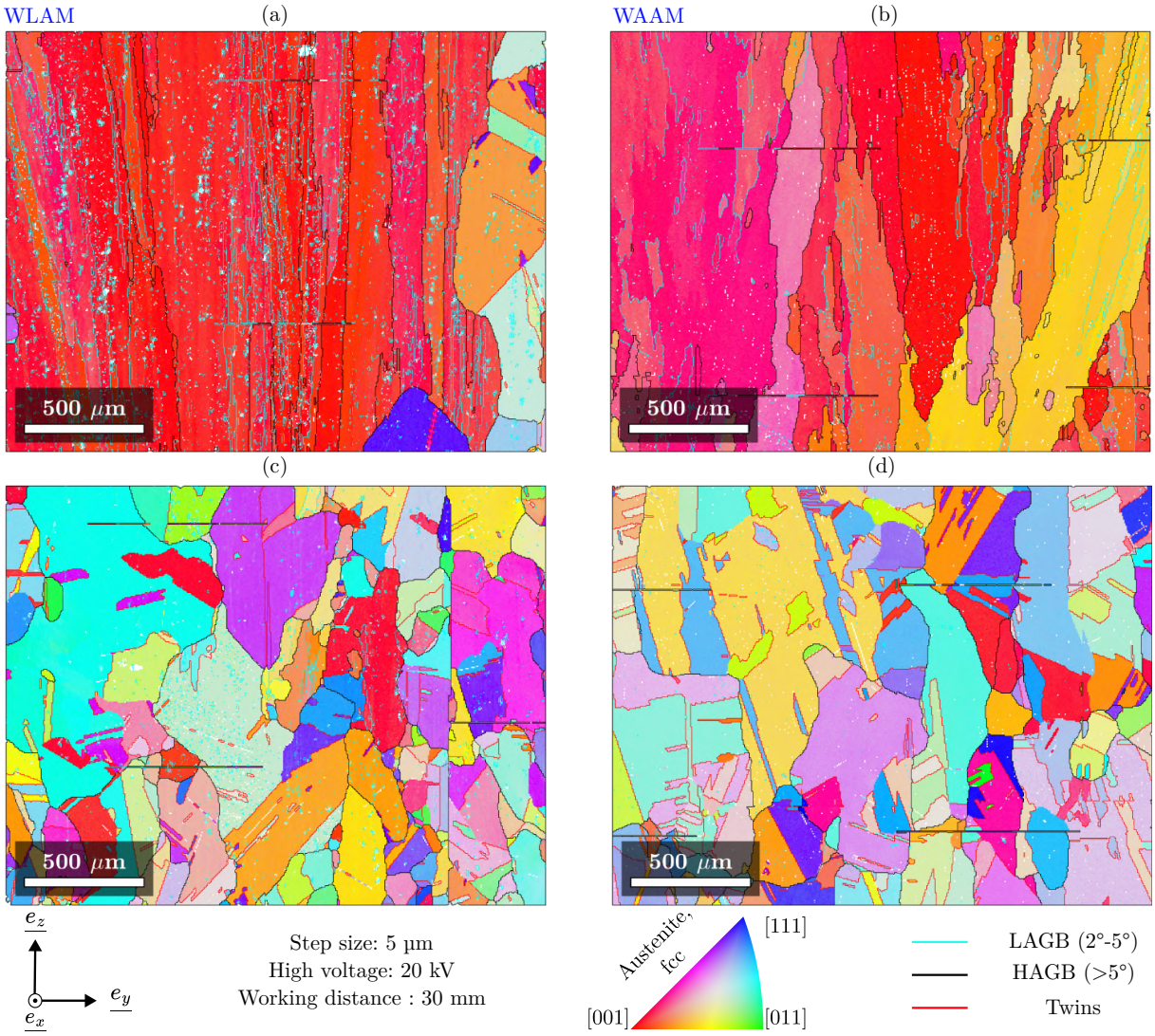

Figure 4.39. Orientation maps obtained by EBSD of the transverse cross-section of single-bead walls manufactured by WLAM and WAAM processes after heat treatments at 1200 °C for 30 min. The maps are projected in the manufacturing direction $\underline{e_z}$: (a) WLAM single-bead wall, near the fifteenth deposited layer; (b) WAAM single-bead wall, near the fifteenth deposited layer; (c) WLAM single-bead wall, near the third deposited layer; (d) WAAM single-bead wall, near the third deposited layer. The cyan lines represent the LAGBs, and the black lines represent the HAGBs

4.6 Conclusion to Chapter 4

We characterized the microstructure and mechanical properties of 316L components produced by WAAM and WLAM processes. First, single beads were analyzed to better understand the origin of the microstructure in more complex components:

- Two distinct microstructural regions were observed : (i) elongated grains in the core formed by epitaxial dendritic solidification and (ii) a "skin" of equiaxed grains. The core region, which is less likely to remelt during the deposition of neighboring layers, will determine the microstructure of multi-layer components.
- The direction of elongation of the grains and the crystallographic texture were linked to the shape of the melt pool. Therefore, different textures were observed for WAAM and WLAM (due to the different shapes of the melt pools): rounded for WLAM and rounded in the middle, flat at the edges for WAAM. In addition, smaller and more elongated grains were observed after WLAM compared to WAAM.
- One grain comprises several dendrites growing in the manufacturing direction with similar orientations, creating low-angle grain boundaries (LAGBs) and grain orientation spread (GOS).
- Finally, the single beads solidified according to a ferrite-austenite (FA) mode typical for 316L steel manufactured with wire additive manufacturing processes. The solidification cooling rates were estimated at 10^2 °C/s for WAAM and ten times higher at 10^3 °C/s for WLAM. In addition, the ferrite content was measured at 5-6 vol.% in WLAM and 8-9 vol.% in WAAM.

The microstructure of single beads was observed to evolve during the manufacturing of more complex components due to the deposition of neighbor layers. Next, the microstructure and the mechanical properties of single-bead walls achieved by WAAM and WLAM were analyzed:

- elongated grains throughout dozens of layers, oriented in the manufacturing direction $\underline{e_z}$, were observed for both processes, with a strong $\langle 001 \rangle_{\parallel \underline{e_z}}$ texture. In addition, dislocations with no particular organization were detected within the austenite and the ferrite, indicating the presence of stored energy for potential microstructural evolution;
- tensile tests were conducted in manufacturing $\underline{e_z}$ and deposition $\underline{e_x}$ directions, showing anisotropy for the single-bead wall manufactured by WLAM. The WAAM specimen displayed similar mechanical properties in both directions, making this process more adapted if anisotropy is a limiting factor in the applications of the component. In addition, compared to conventionally rolled 316L steel, the components manufactured by WAAM and WLAM exhibited similar ultimate strains (around 40%) and tensile strengths;
- higher hardness values were measured for WLAM than for WAAM, with the first layers exhibiting the greatest hardness (190 HV_{10} for WLAM and 182 HV_{10} for WAAM). These values are higher than the hardness of conventional rolled 316L steel (150 HV_{10}), caused by the presence of ferrite, greater hardening and residual stresses.

Next, we observed that the microstructure of tiles was different from that of single-bead walls, with smaller and less elongated grains. In addition, higher hardness values and lower dendrite spacings were measured for tiles than for single-bead walls. Different regions associated with specific microstructures were also defined:

- For the WLAM tile, the center of the fusion zone (CFZ) and the side of the fusion zone (SFZ) exhibited different textures and directions of grain elongation, with the SFZ representing most of the components. In this area, the $\langle 011 \rangle_{\parallel \underline{e_z}}$ texture associated with elongated grains growing at a 45° angle to the manufacturing direction $\underline{e_z}$, is predominant.
- For the WAAM tile, the overlapped region (OR) and the center of the fusion zone (CFZ) are the two main regions in equivalent proportions. The OR has a predominant $\langle 001 \rangle_{\parallel \underline{e_z}}$ texture whereas the CFZ has a $\langle 011 \rangle_{\parallel \underline{e_z}}$ predominant texture.

In addition, no σ phase was observed within the manufactured components. Finally, the effect of processing heat treatments on the microstructure of single-bead walls manufactured by WAAM and WLAM was studied:

- Thermo-Calc computations of the equilibrium volume fraction of 316L phases in WAAM and WLAM components indicated that the heat treatment temperature should exceed 1000 °C to avoid σ phase formation.
- The first treatment conducted at 1100 °C for 30 mins, followed by a quench, did not result in significant variation of the grain shape. However, it reduced the ferrite content to 0.7 vol.% and hardness to 160 $HV_{0.1}$ for WLAM. If the presence of ferrite is a limiting factor in the applications of an industrial component, this heat treatment allows the component to be re-austenitized.
- The second heat treatment conducted at 1200 °C for 30 mins resulted in partial recrystallization at the bottom and the edges of the single-bead walls, where the smallest grains were observed. In addition, their hardness decreased to 150 $HV_{0.1}$, corresponding to the value of 316L steel in its conventional state, suggesting that most of the stored dislocation energy has been released.

Chapter 5

Finite element modeling

Contents

Résumé en français du Chapitre 5 : simulation numérique

Un modèle thermomécanique de la fabrication de pièces en acier 316L par WAAM et WLAM a été développé à l'aide du logiciel Cast3M, basé sur la méthode des éléments finis. Ce modèle intègre une procédure d'ajout progressif d'éléments au maillage pour représenter l'apport de matière. La séquence de fabrication, incluant la stratégie de dépôt, les durées d'allumage et d'extinction de la source d'énergie, les temps de refroidissement interpasse et les déplacements de la tête de fabrication, est définie en fonction des paramètres expérimentaux (Figure 5.4). La géométrie étudiée est celle d'un mur de 20 passes déposé sur un substrat, en reprenant la géométrie des essais expérimentaux (Figure 5.5).

Les propriétés du matériau sont dépendantes de la température et sont renseignées de la température ambiante jusqu'à la fusion (Figure 5.1). Afin de compenser l'absence de modélisation des effets fluides dans le bain de fusion, nous avons majoré la valeur de la conductivité thermique dans le métal liquide. Le modèle prend en compte des hypothèses thermiques et mécaniques non linéaires. La thermique inclut la conduction dans la pièce, le refroidissement par convection, le pompage thermique de la table d'essai et le rayonnement. La source de chaleur est modélisée par une distribution gaussienne isotrope, avec un rayon de Gauss adaptable dans la direction de fabrication pour reproduire la pénétration du bain. La mécanique repose sur un comportement quasi-statique élastoplastique, intégrant soit une loi d'écrouissage isotrope, soit une loi d'écrouissage cinématique, afin d'encadrer les déformations et les contraintes dans la pièce.

La calibration thermique a été réalisée à partir de données expérimentales, à la fois à l'échelle du mur (mesures thermocouples) et à celle du cordon (pénétration, largeur, hauteur), garantissant un bon apport d'énergie et une distribution thermique réaliste. Les taux de rendement obtenus, de 90% pour le WAAM et 46% pour le WLAM, sont cohérents avec les valeurs de la littérature. La validation mécanique repose sur la comparaison des déformations du substrat (Figure 5.13), modélisées numériquement après débridage et mesurées expérimentalement par profilométrie laser.

L'analyse thermique révèle des zones d'accumulation de chaleur en lien avec les irrégularités géométriques observées avec une stratégie de dépôt unidirectionnelle (Figure 5.12). Le modèle mécanique identifie également des zones aux déplacements plus importants (Figure 5.14).

L'analyse des contraintes résiduelles pour une pièce fabriquée par WAAM met en évidence des zones atteignant 400 MPa avec une loi d'écrouissage isotrope, notamment aux extrémités des cordons et au sommet de la pièce (Figure 5.15).

Malgré les limitations dues à l'absence de modélisation des effets fluides, nous avons appliqué de manière qualitative le modèle à l'échelle du cordon.

Les temps de refroidissement interpasse ont été optimisés pour éviter l'accumulation de chaleur tout en maximisant le taux de dépôt. Un temps de refroidissement interpasse constant entraîne une accumulation progressive de chaleur, tandis qu'un temps variable ajusté selon le nombre de cordons permet de maintenir la température sous 200 °C (Figure 5.20).

Le modèle montre, en accord avec les observations expérimentales, que le WLAM conduit à des vitesses de refroidissement supérieures à celles du WAAM, avec une réduction progressive de cette vitesse au fur et à mesure de la fabrication (Table 5.3). Cependant, le modèle sous-estime la vitesse de refroidissement en raison d'une représentation imparfaite de la taille et de la morphologie des cordons et de la zone fondue. Les tendances sont cependant reproduites (Figure 5.21) : la vitesse de refroidissement chute significativement au cours des cinq premières passes, en raison de la dissipation thermique permise par le substrat. Au-delà, un temps de refroidissement interpasse variable assure une vitesse de refroidissement stable d'environ 550 °C/s avec le nombre de passes, conduisant à un espacement dendritique primaire de 10 µm. En revanche, des temps de refroidissement constants de 0 et 20 s conduisent à une diminution respective de la vitesse de refroidissement de 400 °C/s et 200 °C/s entre la cinquième et la vingtième passe.

Enfin, la précipitation de phases indésirables telles que les carbures et la phase sigma peut être contrôlée en limitant le temps passé dans la plage de température 500-900 °C. Pour le WAAM, ce temps cumulé augmente avec la réduction du temps de refroidissement interpasse, soulignant l'importance de son contrôle pour préserver les propriétés du matériau (Figure 5.22). Au WLAM, ce problème semble écarté du fait de la plus faible énergie injectée dans la géométrie et des plus forts gradients thermiques.

5.1 Implementation of the modeling

A thermomechanical finite element model was implemented using Cast3M [199]. A transient thermal analysis is first applied to the geometry to estimate the evolution of the thermal field during manufacturing. This thermal loading is used in a second step to estimate the evolution of stresses and strains during manufacturing, based on a quasi-static elastoplastic mechanical model.

5.1.1 Parameters for 316L stainless steel

The temperature dependency of the physical parameters of 316L steel was considered in the modeling. For that sake, we used the parameters of 316L steel experimentally determined by Depradeux [200], represented by black crosses in Figure 5.1. The evolution of the thermal conductivity λ (Figure 5.1a), the density ρ (Figure 5.1b), the heat capacity c (Figure 5.1c), the Young modulus E (Figure 5.1d), the linear thermal expansion α (Figure 5.1e) and the yield strength σ_y (Figure 5.1f) is reported for temperatures going from room temperature to metal melting temperature zone (above 1450 °C, represented by the blue dotted area). Linear evolution relationships have been used in the numerical model to determine the physical parameters associated with temperatures between two experimental measurements. For temperatures outside the range covered by the experimental data, the evolution of the physical parameters was considered constant and equal to their value at the closest bound of their definition interval. One can notice that the value of the thermal conductivity λ (Figure 5.1a) evolves linearly in the temperature range where the metal is solid, then increases suddenly above the melting temperature. The value of λ in the melted zone was artificially increased to compensate for the fact that the developed model does not account for fluid phenomena in the molten metal, such as the Marangoni effect, even though they are predominant in the heat exchanges at the liquid state in the 316L steel [52].

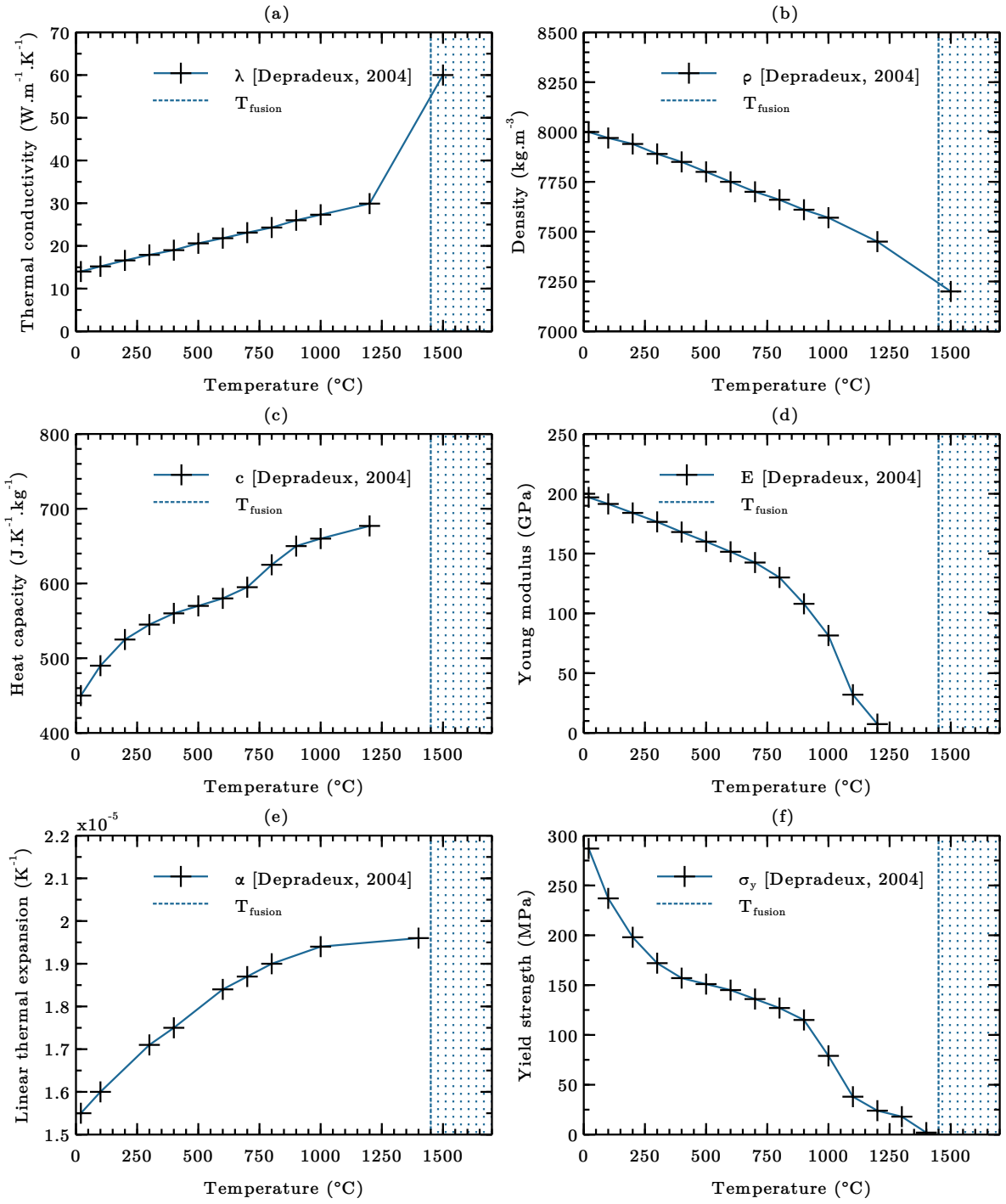

Figure 5.1. Material parameters for the AISI 316L stainless steel as a function of temperature: (a) thermal conductivity λ; (b) density ρ; (c) heat capacity c; (d) Young modulus E; (e) linear thermal expansion α; (f) yield strength σ_y. The experimental data (black crosses) were taken from Depradeux [200]. The blue dotted area corresponds to the domain in which the metal is liquid.

Some temperature-independent parameters were also used, as presented in Table 5.1. The values of the liquidus temperature T_m, the room temperature T_0, the Poisson's ratio ν, and the mass enthalpy of fusion H_{mass} were also taken from the work of Depradeux [200].

Moreover, hardening of the 316L steel was considered in the finite element model, based on isotropic and kinematic assumptions, as it will be presented in Section 5.1.2. The modeling of kinematic hardening uses experimental values of the hardening modulus of 316L steel as a function of the temperature determined by Depradeux *et al.* [200] (Figure 5.2a). Finally, to model the isotropic hardening, we applied stress-plastic strain curves as a function of the temperature, reported by Depradeux [200] (Figure 5.2b).

Table 5.1. Temperature-independent parameters for the AISI 316L stainless steel [200].

Physical parameter	Value
T_m [°C]	1450
T_0 [°C]	20
ν [−]	0.3
$H_{\text{mass.}}$ [$J.kg^{-1}$]	2.5 10^5

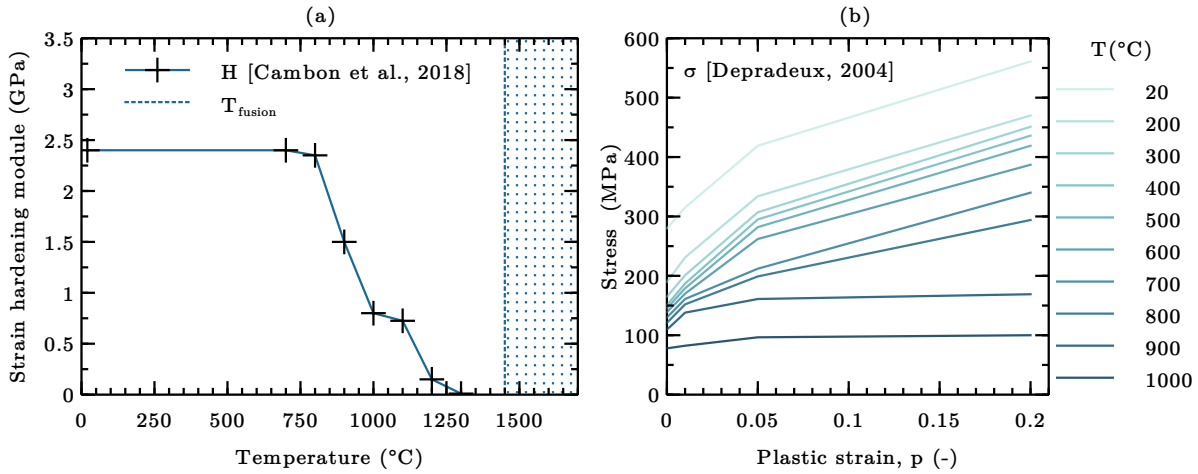

Figure 5.2. (a) Hardening modulus as a function of temperature. Experimental data (black crosses) was taken from Cambon et al. [158]. The blue dotted area corresponds to the domain in which the metal is liquid. (b) Stress-plastic strain curves as a function of temperature, based on experimental values determined by Depradeux [200].

5.1.2 Constitutive equations

Thermal modeling

The transient thermal analysis considers conduction, convection, radiation and heat transfer from the substrate to the welding table (illustrated by red marks and comments in Figure 5.5b). The set of thermal equations involved in the modeling is given in Equations 5.1 to 5.4. The heat equation governs the temperature of the component (Equation 5.1). Thermal conduction is modeled according to Fourier's law (Equation 5.2). Conditions of heat exchange are applied at the boundaries of the mesh. Convection with the ambient air is defined at the boundary $\partial\Omega_R^e$, according to Newton's law (Equation 5.3), with a convective exchange coefficient H_1. The heat losses from the component into the welding table at the boundary $\partial\Omega_T^e$ are also modeled using Newton's law, with an equivalent convective exchange coefficient H_2. Finally, thermal radiation cooling is also considered at the boundary $\partial\Omega_R^e$, defined physically by Stephan-Boltzmann's law (Equation 5.4). This equation is linearized with an equivalent "convective exchange coefficient" equal to $H_R\left(T^3\right)$. One can note that the temperature-dependency of the thermophysical parameters of 316L stainless steel and the consideration of thermal radiation make the thermal

problem non-linear.

$$\rho(T) \cdot c(T) \cdot \frac{\partial T}{\partial t} + div\left(\underline{q}\right) = s^{Q}\left(\underline{x}, \underline{x}^{s}\right) \text{ on } \Omega^{e} \tag{5.1}$$

$$\underline{q} = -\lambda(T) \cdot \underline{grad}(T) \text{ on } \Omega^{e} \tag{5.2}$$

$$\underline{q} \cdot \underline{n} = H\left(T - T_0\right) \text{ where } \begin{cases} H = H_1 & \text{on } \partial\Omega_R^e \\ H = H_2 & \text{on } \partial\Omega_T^e \end{cases} \tag{5.3}$$

$$\underline{q} \cdot \underline{n} = \epsilon\sigma_B\left(T^4 - T_0^4\right) = H_R\left(T^3\right)\left(T_0 - T\right) \text{on } \partial\Omega_R^e \tag{5.4}$$

The next step is to model the heat source (electrical arc or laser). The thermal power used in the modeling corresponds to experimental conditions, *i.e.* $\eta_{\text{source}} \times Q_{exp}$, where Q_{exp} denotes the thermal power supplied by manufacturing process, and η_{source}, its efficiency. The values of efficiency for WAAM and WLAM processes were found based on temperature measurements and represent the amount of power lost due to energy transfer using an electrical arc or a laser. It will be discussed in Section 5.1.4. It was found that a part of the "numerical" power is lost as it is introduced outside the limits of the mesh due to its discretization. Figure 5.3 presents the Gauss volume distribution of the applied power at a given arbitrary time step while manufacturing a single bead with WAAM. The part of the volume distribution surrounded in blue is injected outside the numerical geometry (in grey) and is not considered for the thermal resolution. To ensure that the mesh still receives a power corresponding to $\eta_{\text{source}} \cdot Q_{exp}$ on average, we determined a "heat source numerical correction coefficient" η_{num}, set up at 78.5 and 79.7% for WAAM and WLAM, respectively. Thus, the total introduced power in the mesh is $Q_{exp} \cdot \frac{\eta_{\text{source}}}{\eta_{\text{num}}}$.

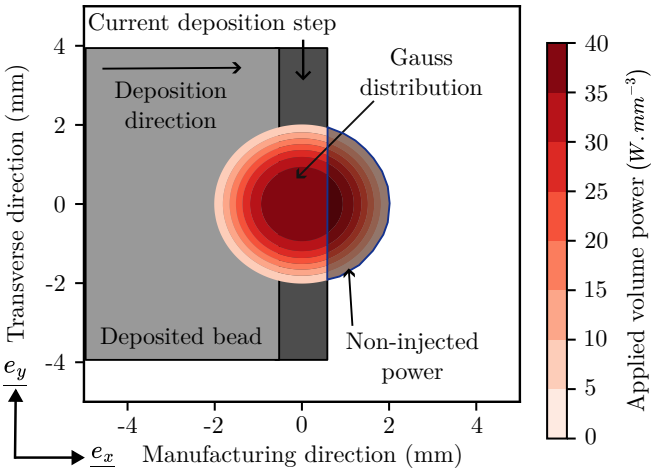

Figure 5.3. Gauss volume distribution for the applied power during the deposition of a single bead with WAAM process. The numerical geometry corresponding to the single bead is depicted in grey. The part of the volume power not injected into the mesh is surrounded by blue.

Next, we assumed that the total power of the heat source is distributed in two ways in the model: **(i)** the power required to bring the wire to its melting temperature T_{fus} and **(ii)** the remaining power as a volume Gaussian distribution (Equation 5.5):

$$\underbrace{Q_{exp} \cdot \frac{\eta_{\text{source}}}{\eta_{\text{num}}}}_{\text{total power}} = \underbrace{Q_{\text{heat}} + Q_{\text{melt}}}_{\substack{\text{Applied to} \\ \text{the wire}}} + \underbrace{Q_{\text{comp}}}_{\substack{\text{Applied to} \\ \text{the volume}}} \tag{5.5}$$

- **(i)** First, the required power to bring the wire to its melting temperature is expressed by computing the required energy to heat the wire from room temperature to melting temperature (Equation 5.6), based on the volumetric heat capacity $\rho(T) \times c(T)$, and the required energy to melt the wire (change of state, Equation 5.7), based on the latent heat of fusion of the material, H_{mass}.

$$Q_{\text{heat}} = \frac{\pi \cdot {d_w}^2}{4} \cdot v_w \cdot \int_{T_0}^{T_{fus}} \rho(T) \cdot c(T) dT \tag{5.6}$$

$$Q_{\text{melt}} = \rho(T_{fus}) \cdot H_{mass} \cdot \frac{\pi \cdot {d_w}^2}{4} \cdot v_w \tag{5.7}$$

- **(ii)** The remaining thermal power, Q_{comp} (Equation 5.8), is distributed in the mesh volume according to the Gaussian function (Equation 5.9), where $\underline{x_s}$ denotes the center position, moving according to loading conditions. The values of the Gauss radii R_0 and Z_0 were calibrated using the observed dimensions of the melt pool (Table 5.2). Finally, the s_0 coefficient ensures that the integration of $s^Q\left(\underline{x}, \underline{x}^s\right)$ on the whole half-space under the z_s coordinate of $\underline{x_s}$ equals the total Gaussian power Q_{comp} (Equation 5.10).

$$Q_{\text{comp}} = Q_{exp} \cdot \frac{\eta_{\text{Source}}}{\eta_{\text{Num}}} - \rho(T_{fus}) \cdot H_{mass} \cdot \frac{\pi \cdot {d_w}^2}{4} \cdot v_w - \frac{\pi \cdot {d_w}^2}{4} \cdot v_w \cdot \int_{T_0}^{T_{fus}} \rho(T) \cdot c(T) dT \tag{5.8}$$

$$s^Q\left(\underline{x}, \underline{x}^s\right) = s_0 \cdot exp\left(-2\left[\left(\frac{x - x_s}{R_0}\right)^2 + \left(\frac{y - y_s}{R_0}\right)^2 + \left(\frac{z - z_s}{Z_0}\right)^2\right]\right) \tag{5.9}$$

$$\text{with: } s_0 = \frac{Q_{\text{comp}}}{Z_0 \cdot {R_0}^2}\sqrt{\frac{2^5}{\pi^3}}, \quad \text{such as: } \iiint_{z<z_s} s^Q\left(\underline{x}, \underline{x}^s\right) dV = Q_{\text{comp}} \tag{5.10}$$

This distribution between Q_{heat}, Q_{melt} and Q_{comp} is justified experimentally by the fact that the wire is already liquid when touching the molten pool. However, the actual temperature of the wire can be underestimated, as temperatures over 2700 °C can be found in the wire under the electrical arc in the WAAM process [163].

Mechanical modeling

In the continuity of the thermal modeling, a quasi-static non-linear elastoplastic mechanical model was applied to the geometry, considering the substrate clamping and contact with the table, as shown by blue marks and comments in Figure 5.5a. In addition, the framework of small displacement and small strain using an implicit solver was considered.

Equations 5.11 to 5.14 present the local mechanical formulation of the problem. First, the static equilibrium equation involves no body force (Equation 5.11). The used constitutive equation is expressed in Equation 5.12, taking into account the plastic strain $\underline{\underline{\varepsilon}}^p$ and the thermal expansion $\underline{\underline{\varepsilon}}^{th}$. In addition, the Hook tensor $\underline{\underline{\underline{\underline{\mathcal{C}}}}}^e(T)$ is temperature-dependent as the Young's modulus is. The strain induced by the thermal expansion at a given time is computed using Equation 5.13 by considering that the reference temperature for which the thermal strain is zero is the room temperature T_0.

$$div\left(\underline{\underline{\sigma}}\right) = \underline{0} \text{ on } \Omega^e \tag{5.11}$$

$$\underline{\underline{\sigma}} = \underline{\underline{\underline{\underline{\mathcal{C}}}}}^e(T) : \left(\underline{\underline{\varepsilon}} - \underline{\underline{\varepsilon}}^p - \underline{\underline{\varepsilon}}^{th}\right) \text{ on } \Omega^e \tag{5.12}$$

$$\underline{\underline{\varepsilon}}^{th} = \underline{\underline{\alpha}}(T)\,(T - T_0) \text{ on } \Omega^e \tag{5.13}$$

Two hardening laws were modeled and compared to describe the elastoplastic behavior of the material:

- **Isotropic hardening**. In this case, the plasticity criterion is expressed by Equation 5.14, where $\mathcal{J}_2$ refers to the second invariant of the stress tensor, and $R(p)$ a function introduced to model the isotropic hardening. The evolution of the parameter $R(p)$ is defined by the hardening curves presented in Figure 5.2b.

$$f(\underline{\underline{\sigma}}, R) = \mathcal{J}_2\left(\underline{\underline{\sigma}}\right) - \sigma_y - R(p) \text{ on } \Omega^e \tag{5.14}$$

- **Kinematic hardening**. In this case, the plasticity criterion is expressed by Equation 5.15, where $H(T)$ refers to the kinematic strain hardening modulus presented in Figure 5.2a.

$$f(\underline{\underline{\sigma}} - \underline{\underline{X}}) = \mathcal{J}_2\left(\underline{\underline{\sigma}} - \underline{\underline{X}}\right) - \sigma_y \text{ on } \Omega^e, \text{ where } \underline{\underline{X}} = \frac{2}{3}H(T)\ \underline{\underline{\varepsilon}}^p \tag{5.15}$$

Temperature annealing was considered by setting the hardening variables p or $\underline{\underline{X}}$ to zero when the temperature exceeds 1000 °C. Moreover, the mechanical behavior is assumed to be purely thermo-elastic above this temperature.

Finally, displacement boundary conditions are prescribed on the supporting substrate. Contact conditions with the table are applied on the bottom surface of the substrate ($U_z \geq 0$). The screws that clamp the substrate on the table are modeled by an elastic stiffness $\underline{\underline{\underline{\underline{K^s}}}}$ defined at nodes located at the same points as they were on the upper surface of the substrate. The value of $\underline{\underline{\underline{\underline{K^s}}}}$ is computed using the diameter of the screws and the Young's modulus of 316L stainless steel at room temperature, considering that the screws experience purely elastic strain. $\underline{\underline{\underline{\underline{K^s}}}}$ acts on the U_z component of displacement on these nodes, whereas their U_x and U_y components are set to zero. However, no pre-stress is applied to take into account the initial tightening of the screws. The only external loading applied to the system is temperature variations.

5.1.3 Finite element discretization

Thermal modeling

The thermal equations were discretized in space using the classical finite element method [201], with non-linearities due to the evolving geometry and the temperature dependencies of the finite element matrices. The time and temperature-dependent differential equation was solved using the first-order Euler implicit algorithm. The convergence criterion is based on the temperature, whose relative variation between two iterations must be less than 10^{-4}: this criterion allowed us to reach the accuracy of the solution within a few degrees Celsius. The overall simulations of the WAAM and WLAM processes then involved about 20 000 time-steps and approximatively 100 000 finite elements at maximum. The computing times were around 10^5 s for both processes with a 14-core, 128 GB RAM configuration.

Mechanical modeling

The static equilibrium equation was discretized using a classical finite element method. Boundary conditions on displacements are prescribed by introducing Lagrange multipliers. The temperature changes were applied step by step to describe the temperature evolution in the component during manufacturing. The time discretization is the same as for the thermal analysis. At each time step, the mechanical equilibrium (Equation 5.11) is solved according to a fixed-point algorithm with a convergence criterion equal to 10^{-4} with respect to the internal forces induced by thermal expansion.

Definition of the deposition sequence

The addition of material was modeled by incrementally adding blocks of finite elements to the mesh at various time steps, enabling it to evolve from an initial substrate to the final component shape. At the same time, the deposition sequence experienced by the geometry was defined by determining the on/off sequences and the movements of the heat source and the wire. The *SOUDAGE* procedure of Cast3M allowed us to determine this deposition sequence by inputting the provided experimental data, *i.e.* the deposition speed, the wire feed speed, the power of the heat source, the deposition path, the interlayer cooling times and the width of a deposited single bead. This last parameter is required since our model cannot estimate it. The width can be measured only after experimental manufacturing, which limits our model to be used only *a posteriori* to manufacturing. However, one can estimate the width of beads by considering the measured and interpolated values obtained based on the WAAM and WLAM process parameters, as shown in Chapter 3.

In this study, we modeled the manufacturing using the following sequences:

- **holding time** of 0.5 s at the beginning of each bead deposition, where the power is applied without displacement of the heat source, as achieved experimentally to initiate the melt pool;
- metal beads **deposition sequences** where the deposition head is moving, and the power is set on;
- **waiting sequences** at the end of each bead deposition where neither power nor displacements are modeled, corresponding to the experimental interlayer cooling times;
- **deposition head movements** between each deposition where no power is applied, corresponding to the $\underline{e_z}$-increments to achieve the successive layers.

Figure 5.4a and b defines, respectively, the displacement of the deposition head along its trajectory and the on/off sequences for the power and the wire supply associated with the deposition sequence of the first ten layers of a 200 mm-long single-bead wall manufactured with WAAM process.

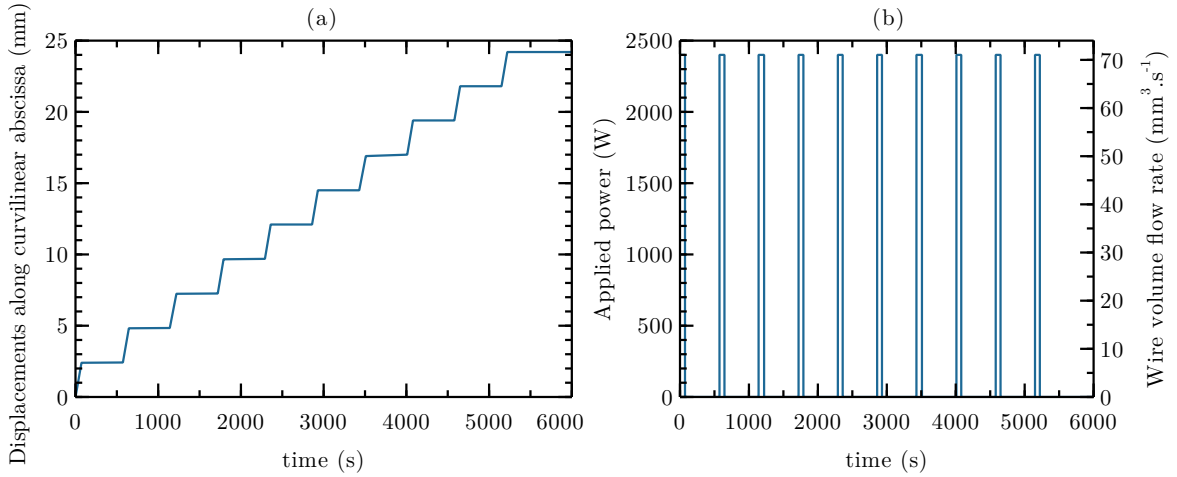

Figure 5.4. Deposition sequence of the first ten layers of a 200 mm-long single-bead wall manufactured by WAAM. (a) Displacement of the deposition head along its trajectory (curvilinear abscissa) and (b) applied power and wire volume flow as a function of time.

Definition of the geometry

The final geometry of the manufactured components was meshed using three-dimensional cubic linear finite elements. The deposited wall and the substrate are modeled, as presented in Figure 5.5a for the WAAM process, to fit with the experimental manufacturing, presented in Figure 5.5b. Moreover, the numerical beads are modeled as rectangles to facilitate the global conformity of the mesh, with a height equivalent to the experimental mean height of the beads. However, it is worth noting that rectangular-shape modeling does not affect thermal and mechanical prediction compared to arc-shape modeling, as reported by Prajadhiama *et al.* [150]. Two different mesh sizes were applied in our study: a fine mesh at and near the deposit and a coarser mesh elsewhere. This approach is usable for small components as the number of introduced finite elements remains reasonable, as for simulations of the WAAM process.

The location of the thermocouples point is also considered, as shown in red in Figure 5.5a. Moreover, several hanging nodes are left when using the non-conform interface between the fine and coarse mesh zones. These nodes are treated by applying linear relationships between the unknowns (thermal or mechanical fields) of the fine and coarse meshes. Further detail is given in Appendix C.1. For the WLAM process, the selected mesh sizes are based on the transposition of the geometrical dimensions of WAAM to the geometrical dimensions of WLAM. Assuming that the single beads manufactured by WLAM are four times smaller than those manufactured by WAAM, the mesh size and the computing time in WLAM were one quarter of those determined for WAAM. Table 5.2 presents the final chosen mesh sizes.

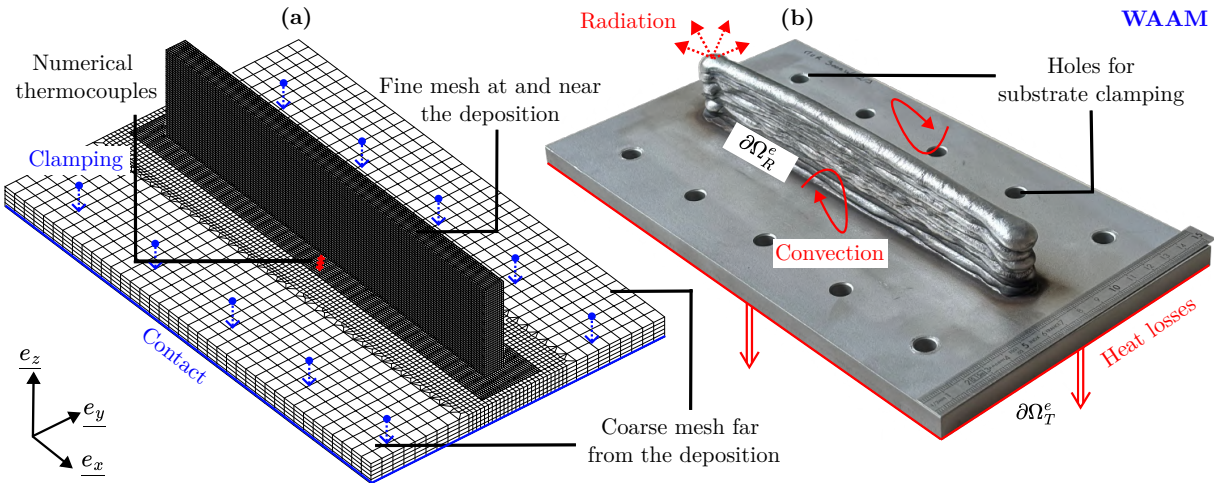

Figure 5.5. Example of a wall built by WAAM: (a) simplified geometry with mesh used for modeling, (b) as-built geometry (the considered thermal and mechanical hypotheses are represented in red and blue, respectively).

Next, the *WAAM* procedure of Cast3M was used to create the evolving mesh associated with the manufacturing. Figure 5.6a presents the evolving geometry, where the different added blocks are depicted in distinct colors. The final geometry is indicated by blue outlines. The size of the added blocks, specified in Table 5.2, was calibrated using a convergence study to minimize thermal discontinuities along the deposited beads. The trajectory of the deposition head forms a continuous path, represented with red and green lines in Figures 5.6a and b. The red lines represent the movements of the deposition head with power and wire supply while the green lines indicate the displacement of the deposition head from one layer to another. The energy conservation equation for the nodal fields was satisfied by ensuring their adaptation to the new mesh at each element addition sequence (Appendix C.2).

Computing time can become a limiting factor in the simulation of wire additive manufacturing, as the number of elements can significantly increase, particularly for large components or for modeling WLAM with finer mesh size. A fine mesh is necessary only near the manufacturing zone due to the high thermal gradients caused by the movement of the energy source. An evolving re-meshing procedure was thus introduced for the WLAM process to create an adaptive mesh based on the position of the energy source. As shown in Figure 5.6b, a fine mesh zone moves along the wall length, following the movements of the energy source, where coarser meshes corresponding to the previous weld bead are already implemented. The fine mesh maintains a chosen radial distance from the center of the energy distribution. The re-meshing procedure was used to simulate manufacturings with the WLAM process, as the thin dimensions of the components produced using this process would require a consequent number of finite elements.

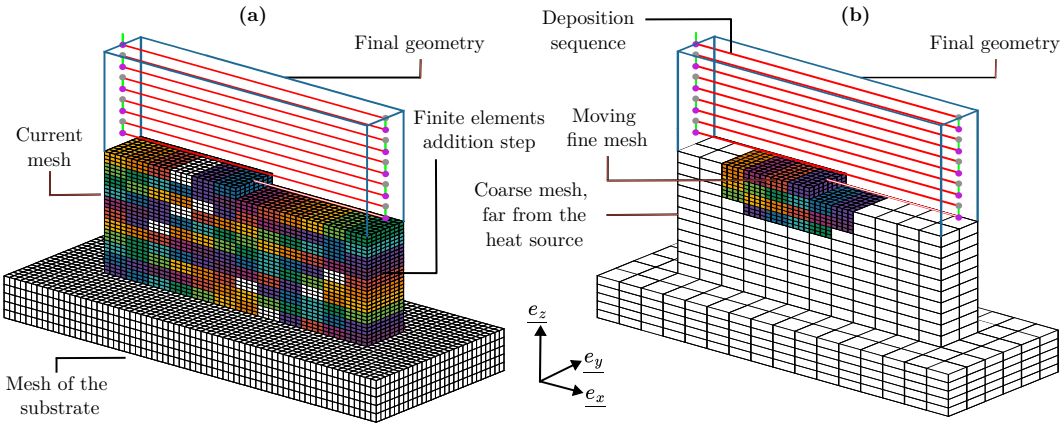

Figure 5.6. Finite element meshes used for modeling WAAM and WLAM processing of 316L stainless steel walls: (a) Finite element addition procedure. Each color block represents elements added during successive discretization steps to achieve the final geometry (outlined in blue). The required deposition sequence is represented by a continuous path of red and green lines and grey and purple dots. Red lines indicate deposition sequences, while green lines indicate adjusting movements. Purple dots represent interlayer waiting sequences and grey dots initiation sequences. (b) Remeshing procedure. The fine mesh near the heat source is replaced by a coarser mesh (shown in white) at 10 mm from the center of the heat source.

Table 5.2. Simulation parameters used for FEM modeling of 316L walls manufactured using WAAM and WLAM.

Parameter	**WAAM**	**WLAM**
Fine mesh size, $\boldsymbol{e_1}$ $[\boldsymbol{mm}]$	1	0.25
Coarse mesh size, $\boldsymbol{e_2}$ $[\boldsymbol{mm}]$	6	6
Material addition step size $\boldsymbol{e_3}$ $[\boldsymbol{mm}]$	2	2
Computing time step, $\boldsymbol{\delta t}$ $[\boldsymbol{ms}]$	71.7	17.9
Gauss radius in the $\underline{e_x}$ and $\underline{e_y}$ direction, $\boldsymbol{R_0}$ $[\boldsymbol{mm}]$	5	1.5
Gauss radius in the $\underline{e_z}$ direction, $\boldsymbol{Z_0}$ $[\boldsymbol{mm}]$	0.5	0.5
Heat source numerical correction, $\boldsymbol{\eta_{num.}}$ $[-]$	0.785	0.797
Heat source efficiency, $\boldsymbol{\eta_{source}}$ $[-]$	0.90	0.46
Emissivity, $\boldsymbol{\epsilon}$ $[-]$	0.40	0.40
Mass enthalpy of change of state, $\boldsymbol{H}_{\text{mass.}}$ $[\boldsymbol{J.kg^{-1}}]$	2.5×10^5	2.5×10^5
Convective exchange coefficient with the air, $\boldsymbol{H_1}$ $[\boldsymbol{W.m^{-2}.K^{-1}}]$	10	10
Convective exchange coefficient with the table, $\boldsymbol{H_2}$ $[\boldsymbol{W.m^{-2}.K^{-1}}]$	300	300
Room reference temperature, $\boldsymbol{T_0}$ [°C]	20	20
Liquidus temperature point, $\boldsymbol{T_{fus}}$ [°C]	1450	1450

5.1.4 Model calibration

A convergence study was achieved to calibrate the mesh sizes, finite element addition steps, and computing times used in the numerical model (Figure 5.7).

Figure 5.7a presents the maximum temperature reached along the deposition direction on the substrate surface, 2 mm from the deposited single bead, using the WAAM process with different material addition steps of 1 mm, 2 mm, 4 mm, and 6 mm. The mesh size in the deposited area (fine mesh) and the computing time step were maintained constant at 1 mm and 47.8 ms, respectively. The maximum temperature along the $\underline{e_x}$ profile decreased as the material addition step decreased, given that a more significant part of the power distribution is lost outside of the mesh. As mentioned in Section 5.1.2, this effect was later compensated by introducing a "numerical efficiency" coefficient η_{num}. The thermal profiles associated with the 4 mm and 6 mm material addition steps were irregular. The material addition step e_3 of 2 mm was selected due to its regular thermal distribution along the deposition direction, avoiding an unnecessary increase in computing time associated with a 1 mm step.

Figure 5.7b displays the maximum temperature reached along the deposition direction on the substrate surface, 2 mm from the deposited single bead, using different mesh sizes in the finely meshed area (0.5 mm, 1 mm, and 2 mm). The material addition step was maintained at 2 mm, and the computing time step at 47.8 ms. Similar thermal profiles were obtained with mesh sizes of 0.5 mm and 1 mm, while a decrease in temperature was observed with the 2 mm mesh size. Therefore, a mesh size e_1 of 1 mm was selected for the finely meshed zone.

For the coarse mesh zone, no differences in thermal profiles were observed with mesh sizes of 2 mm, 4 mm, 6 mm, and 8 mm. Additionally, a coarse mesh did not significantly reduce computing time, as most finite elements were in the finely meshed zone. Hence, a mesh size e_2 of 6 mm was selected for the coarse zone for geometrical reasons.

Figure 5.7c illustrates the maximum temperature reached along the deposition direction on the substrate surface, 2 mm from the deposited single bead, with different computing time steps δt of 47.8 ms, 95.6 ms, 71.7 ms, and 191.2 ms. The material addition step was maintained at 2 mm, and the mesh size in the fine zone was kept at 1 mm. The maximum reached temperature was similar across all computing time steps, but the profiles were irregular for the computing time steps of 191.2 ms and 95.6 ms. Therefore, a computing time step of 71.8 ms was selected.

Finally, Figure 5.7d presents the time-evolution of the temperature on the substrate surface at a point located 2 mm from the deposition in the middle of the substrate along the deposition direction, depending on whether an increase in computing time steps following a geometric sequence with a ratio of 2 was applied during the cooling sequences. Only a slight difference (< 20 °C) was observed in the temperature at the end of cooling, which justifies our choice to lower the computing time during the cooling sequence by progressively increasing the time step.

The selected values of $e1$, e_2 and e_3 in the numerical model are summarized in Table 5.2.

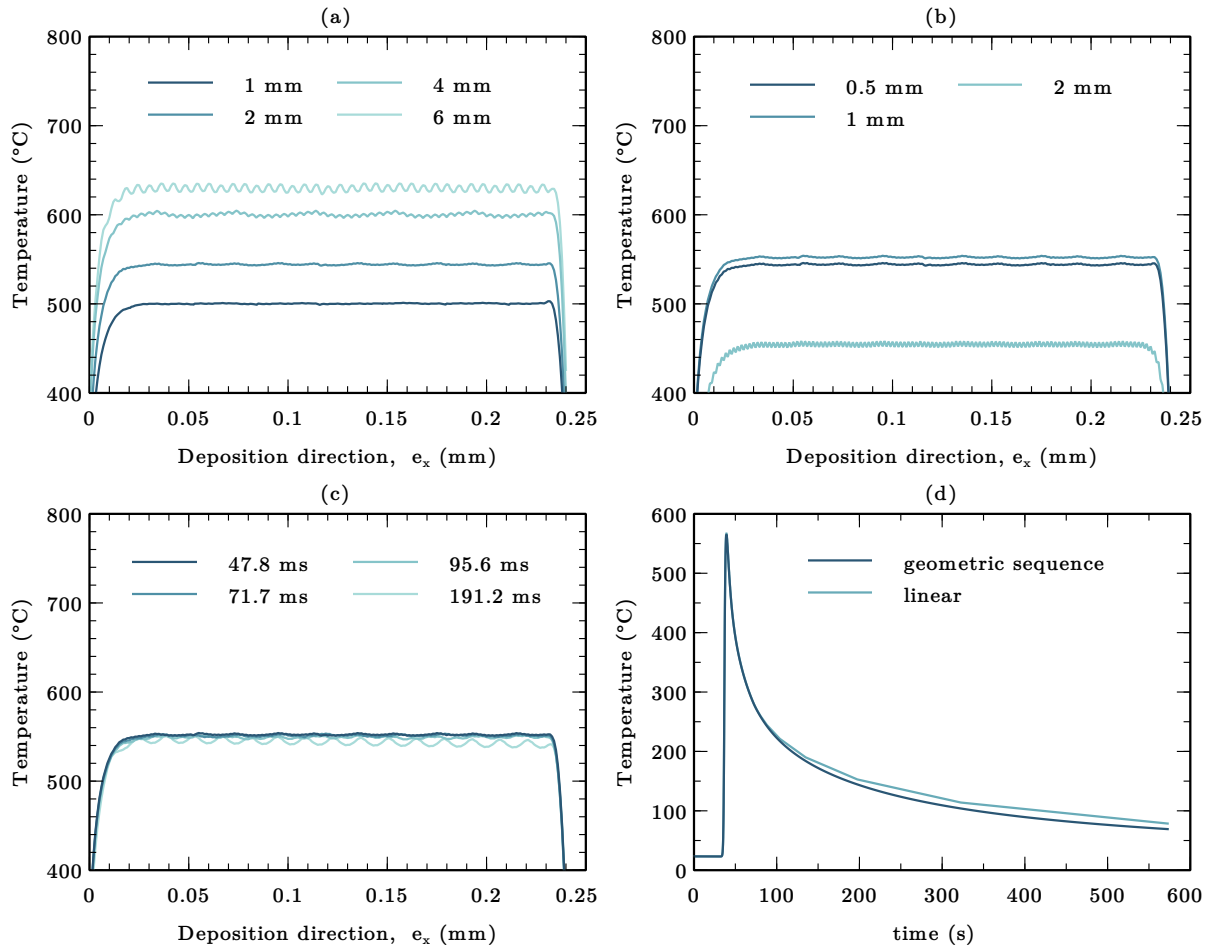

Figure 5.7. Maximum temperature reached along the deposition direction at 2 mm from the deposit on the substrate surface, for (a) different material addition step sizes e_3, (b) different mesh sizes in the fine mesh area e_1 and (c) different time steps δt. (d) Evolution of the temperature as a function of time at a numerical thermocouple located at 2 mm from the deposit in the middle of the substrate along the deposition direction, depending on whether the cooling times are progressively increased during the cooling sequences.

The numerical parameters left for calibration of the numerical thermal field are the exchange coefficients with ambient air and testing table, the efficiencies of the heat sources and their spatial distribution based on their Gauss radii in both the deposition direction and the manufacturing direction.

The exchange coefficients with the air and the work table H_1 and H_2 and the heat source efficiencies η_{source} of the thermal supply were calibrated based on experimental data obtained from the thermocouple measurements. The two obtained convection coefficients H_1 and H_2, presented in Table 5.2, have the same values for the WAAM and the WLAM model. The value of $H_1 = 10\ W.m^{-2}.K^{-1}$ is within the usual range of values for natural convective heat exchange in ambient air [202].

The efficiency coefficients, η_{source}, were set at 90% for WAAM and 46% for WLAM, which is in the usual range of experimental efficiency values for such processes:

- Collings *et al.* [203] estimated the arc efficiency (ratio of the power applied to the component to the total arc energy) in GTAW welding of stainless steel to be in the range from 77 to 90%.
- Tadamalle *et al.* [204] reported that the coupling efficiency (*i.e.* the ratio between the power going in the component and the output power from the laser source) in laser welding of 316L stainless steel with a Nd:YAG laser is within the range 38 to 55%.

Figure 5.8 compares the experimental temperature, measured at the surface of the substrate at 4 mm from the border of the deposited metal, with the computed temperature for the first, the tenth, and the twentieth layer, after cooling under 100 °C, for the WAAM process (Figure 5.8a) and the WLAM process (Figure 5.8b). These experimental data were used as a reference for calibrating the numerical thermal parameters H_1, H_2, and η_{source}. A satisfying correspondence was found between numerical and experimental results with the calibrated parameters given in Table 5.2 for both manufacturing processes. However, some limitations can be found. The cooling rate was slightly overestimated after depositing the first layer in the WAAM process (see the curve tail), whereas it was underestimated for the WLAM process. Moreover, the model underestimates the temperature of the twentieth layer in both cases. Nevertheless, we concluded that the model can predict the temperature of the component during manufacturing with relatively good accuracy for both WAAM and WLAM processes.

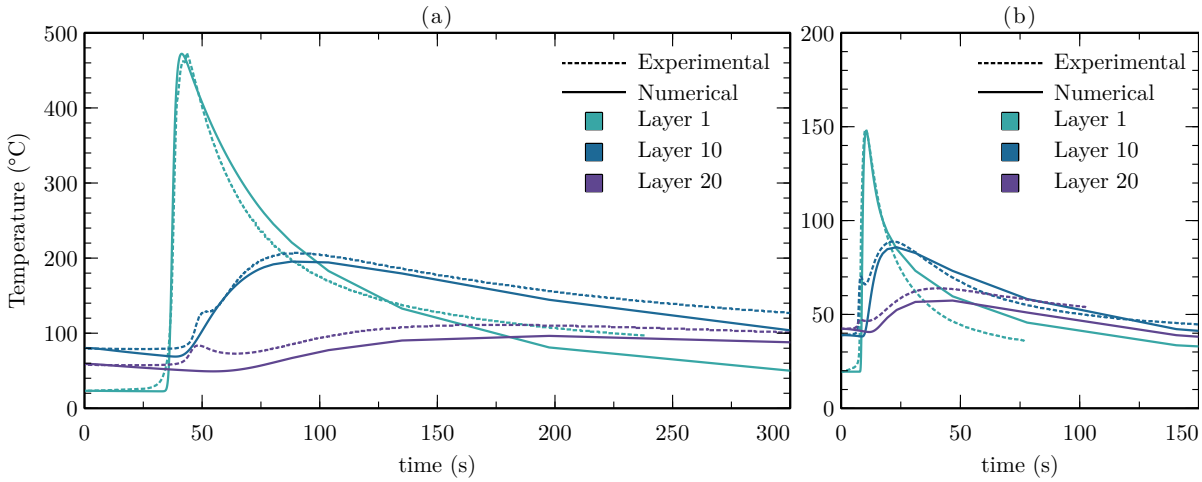

Figure 5.8. Time-evolution of temperature during the deposition of the 1^{st}, the 10^{th} and the 20^{th} bead of single-beads manufactured by (a) WAAM and (b) WLAM. Numerical results and temperature measurements made with a K-type thermocouple placed at the surface of the substrate and 4 mm far from the deposit were compared. Note that the y-axis is different between the two graphs, while the x-axis remains the same.

Finally, the Gauss radius in the deposition direction R_0 and in the manufacturing direction Z_0 were calibrated based on comparisons of the measured mean penetration of the fusion zone of a single bead achieved with the optimal parameter sets determined in Chapter 3 (Figure 5.9a and b, for WAAM and WLAM, respectively). R_0 was considered equal to half of the width of a bead so that power is distributed across the entire width of the bead. The values of Z_0, presented in Table 5.2, were selected to minimize the depth of the numerical fusion zone while ensuring the complete melt of the finite elements in the single beads. It is worth noting that the geometric shape and the depth of the numerical fusion zone still do not match the experimental ones since fluid effects, predominant in the experimental melt pool [163], were not considered. The selected Gauss radii for WAAM and WLAM are presented in Table 5.2.

Figures 5.10a and 5.10b present respectively the temperature during the deposition of a single-bead wall with WLAAM and WAAM. The melted zone is visible in the thermal field ($T > 1450\,°\text{C}$), and the component is cooled quickly behind it. The isotherm at $T = 1450\,°\text{C}$ was extracted in the middle of the deposition of each layer, and the obtained surface was re-meshed, as presented in Figure 5.10c. The remeshing of the fusion boundary was achieved with the *@ISOSURF* procedure of Cast3M with a triangular mesh.

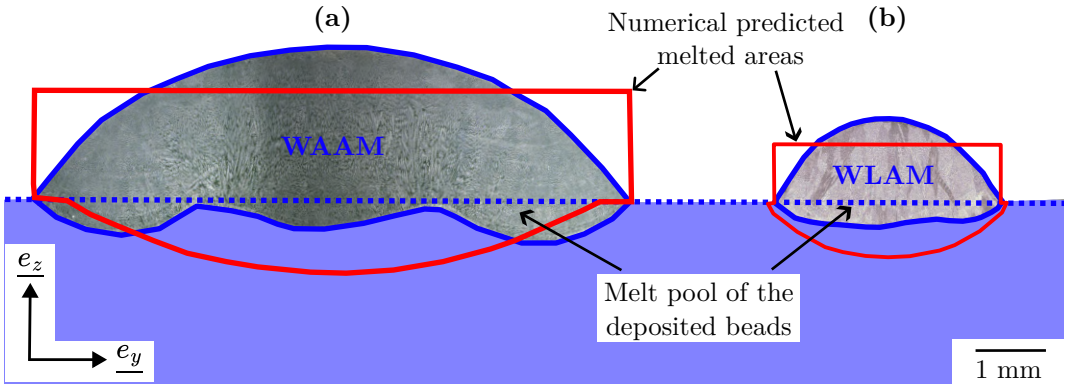

Figure 5.9. Comparison of the shape of the experimental (blue outlines) and numerical fusion zone (red outlines) for the selected set of parameters during (a) WAAM and (b) WLAM single bead manufacturing.

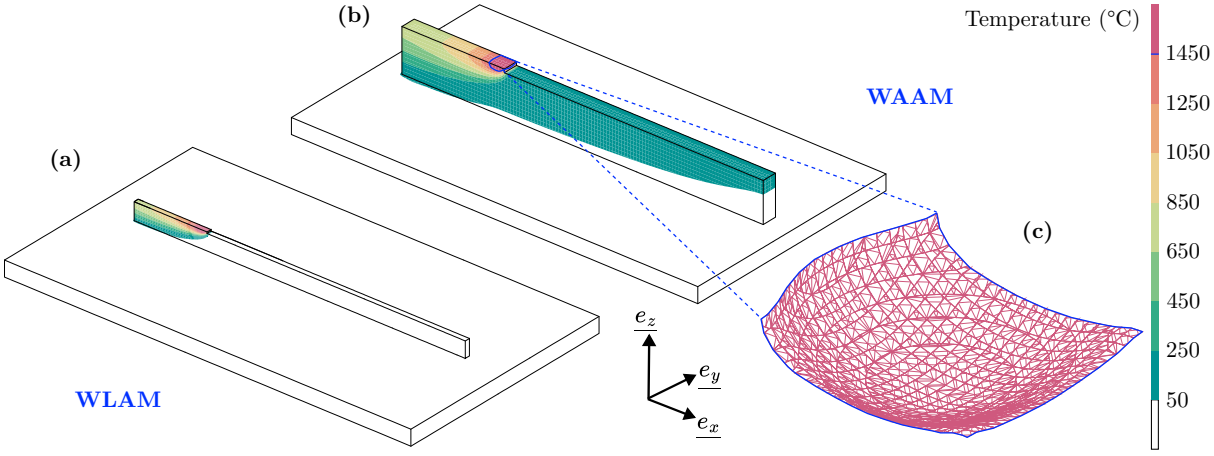

Figure 5.10. Contour plots of the thermal fields during manufacturing of a specimen achieved by (a) WLAM and (b) WAAM. (c) Illustration of the meshing of the melting isotherm for the WAAM process.

5.2 Thermal modeling at the component scale

5.2.1 Thermal field

To determine the accuracy of the thermal model at the macroscopic scale, calculated and measured thermal fields obtained with thermal cameras in the specimens during their manufacturing by both WAAM and WLAM processes were compared in Figure 5.11. The walls measured 200 mm long for WAAM and 100 mm for WLAM. Experimental thermal fields at the end of the deposition of the fourteenth bead form elongated ellipses of isotherm behind the melt zone (Figures 5.11a and 5.11c). These zones, corresponding to red regions, were not accurately measured, particularly for WAAM where the fusion zone is not visible, due to the considered uniform thermal emissivity assumption despite the difference of emissivity between liquid and solid 316L [202]. Finally, both processes exhibit high thermal gradients, especially in the manufacturing direction (the $\underline{e_z}$ axis), characteristic for additive manufacturing processes, potentially leading to anisotropic properties in the produced components [205].

Figures 5.11b and 5.11d present the thermal fields estimated by the model for equivalent conditions. Good agreement between the numerical and experimental thermal fields is obtained, with minor differences around the melt zone, which appears smaller according to the model. The agreement can be improved by modifying the energy distribution and using a Goldak heat source [206], which will calibrate the dimensions of the melt pool. However, this study maintains model simplicity and avoids additional calibration to ensure transferability across different manufacturing conditions or processes.

The average thermal gradient and cooling rate between 1450 and 800 °C were estimated based on the numerically predicted thermal fields in Figure 5.11. We measured the distance between the isotherms along the deposition direction ($\underline{e_x}$) at the top of the fourteenth layer. For the WLAM process, the thermal gradient was estimated at 9 °C/mm, while for the WAAM process, it was 16 °C/mm. The thermal gradient is nearly twice as large for WAAM compared to WLAM due to the four times higher deposition speed, which enables the heat to dissipate more effectively throughout the metallic component. The cooling rate was estimated at 114 °C/s for the WLAM process, compared to 54 °C/s for the WAAM process and, thus, approximately two times higher for WLAM than for WAAM, attributed to the finer scale of the components and the lower amount of energy introduced.

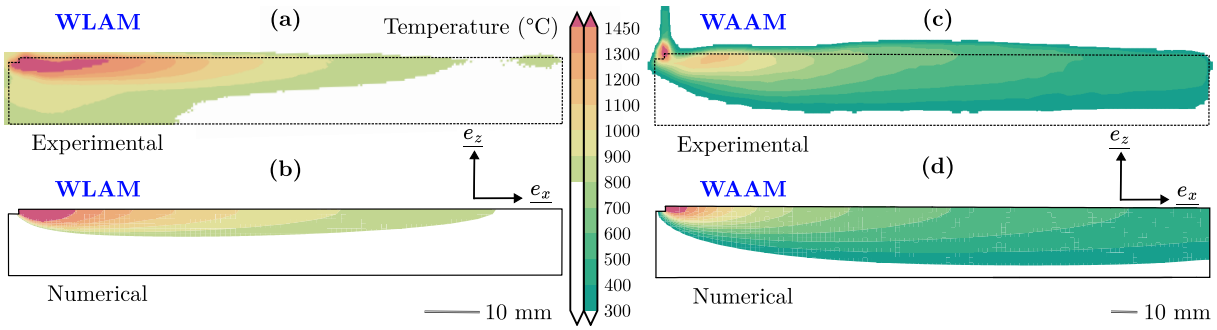

Figure 5.11. Comparison of temperature fields on specimens measured by thermal cameras and obtained from the numerical model: (a) Experimental temperature field for WLAM specimen; (b) numerical temperature field for WLAM specimen; (c) experimental temperature field for WAAM specimen; (d) numerical temperature field for WAAM specimen. Temperature fields are shown at the end of the deposition of the fourteenth layer of a 100 mm-long wall for WLAM and a 200 mm-long wall for WAAM.

5.2.2 Heat accumulation

Next, we used the numerical model to predict thermal features leading to defects in the built components. Two specimens were thus achieved using WAAM under identical manufacturing conditions, differing only in the deposition strategy. One wall was produced using a unidirectional deposition strategy, while the second used a bidirectional deposition strategy. The average temperature at each point during the manufacturing process was estimated using the thermal numerical model to assess potential heat accumulation (Figure 5.12), which could lead to macroscopic deformations in the components [155]. Indeed, heat accumulation increases the local energy, enlarging the melt pool and causing irregularities in the height and width of the wall [90]. Only temperatures exceeding 500 °C were considered for computing the average to minimize the influence of colder areas far from the deposition zone. The average then corresponds to the "average temperature" observed near the fusion zone when the component is hot. This approach is reasonable as potential deformations occur at high temperatures, as indicated by Depradeux's measurement of Young's modulus of 316L steel, decreasing from 197 GPa at room temperature to 7 GPa at 1200 °C [200]. The numerical predictions of the average temperature distribution for points exceeding 500 °C are presented in Figures 5.12a and 5.12b for the unidirectional and bidirectional deposition strategies, respectively. These sections are located transversely at the center of the walls, corresponding to the peak temperatures predicted by the Gaussian heat source model. It is worth noting that the predicted average temperatures are overestimated because the numerical model did not consider fluid flow effects, which are critical for the fusion zone geometry [162].

In the case of the wall produced using a unidirectional deposition strategy (Figure 5.12a), one can observe that the average temperature in a significant part of the walls is approximately 700 °C. However, a zone exceeding 1000 °C is observed at the end of the deposited beads, indicating significant heat accumulation. In contrast, the wall fabricated with the bidirectional deposition strategy exhibits a more uniform temperature distribution. Experimental observations (Figures 5.12c and 5.12d) show significant wall collapse at the end of the beads in the unidirectional strategy, whereas the bidirectional strategy results in more consistent wall height. The experimental macroscopic collapse correlates with the substantial numerical heat accumulation in the unidirectional deposition strategy.

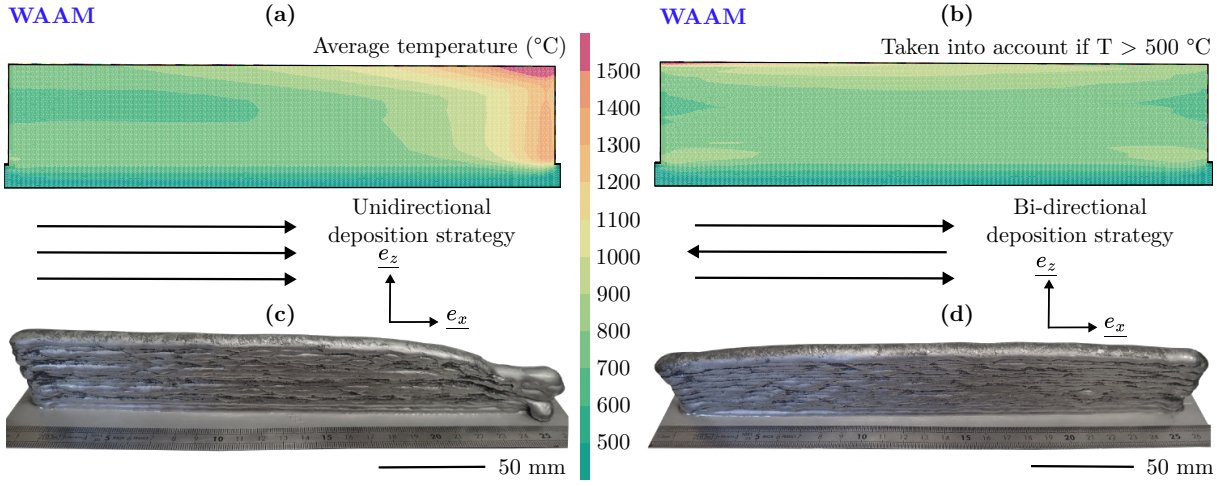

Figure 5.12. Analysis of average temperatures for unidirectional and bidirectional deposition strategies and corresponding specimens produced by WAAM: Numerical prediction of the average temperature distribution for points exceeding 500 °C using (a) a unidirectional deposition strategy and (b) a bi-directional deposition strategy; (c) wall produced with a unidirectional deposition strategy; (d) wall produced with a bi-directional deposition strategy.

5.3 Mechanical modeling at the component scale

5.3.1 Substrate deflection

We are now interested in studying the strains using the mechanical model for the manufacturing conditions presented previously, leading to macroscopic deformations when using the unidirectional deposition strategy. Figure 5.13 presents the experimental and numerical displacements in the $\underline{e_z}$ direction observed at the end of the deposition process, following the cooling and unclamping of the WAAM specimen. Figures 5.13a and 5.13b compare the experimentally measured Z-displacements obtained through laser profilometry with the numerically predicted displacements in the $\underline{e_z}$ direction along profiles on the $\underline{e_x}$ and $\underline{e_y}$ axes, respectively, as illustrated in the Figure 5.13c, representing the final numerical displacements in the substrate and the WAAM component. The numerical predictions show a good fit with the experimental data, with a maximum deflection of 2 mm. This deflection is mainly attributed to the shrinkage of the deposit during cooling, which pulls on the substrate surface. Along the $\underline{e_x}$ axis, which corresponds to the deposition direction, the minimum deflection occurs near the middle of the substrate. However, the displacements are not symmetrical due to the unidirectional deposition strategy. Along the $\underline{e_y}$ axis, which is transverse to the deposition direction, the maximum deflection is observed at the center of the substrate, where the wall is deposited. The computational time required for the mechanical modeling of this geometry was approximately seven days.

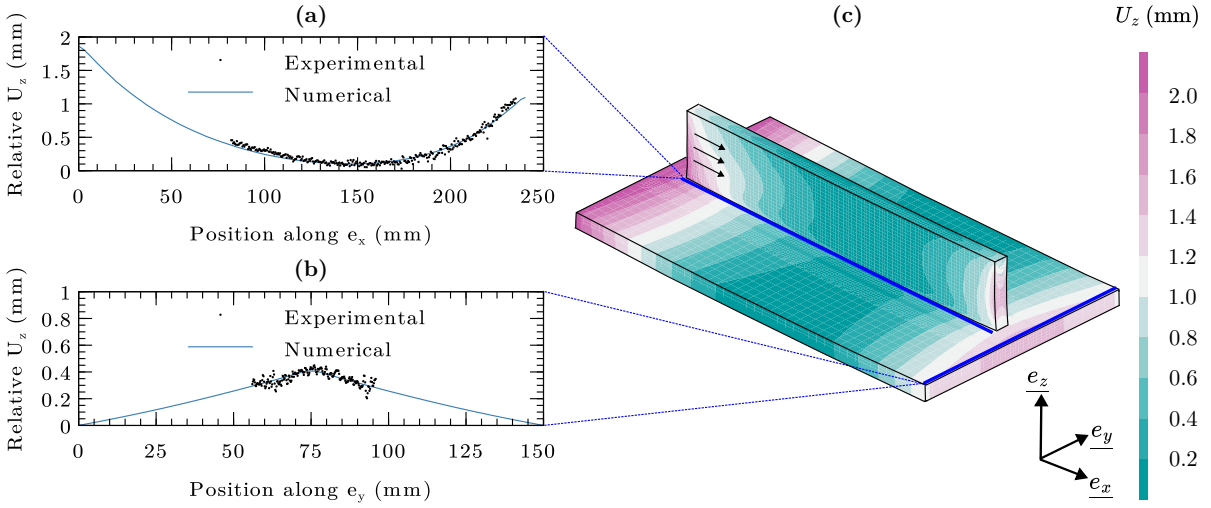

Figure 5.13. Comparison of the experimental and numerical displacements in the $\underline{e_z}$ direction at the end of the deposition after cooling and unclamping the WAAM specimen: (a) experimental laser profilometry and numerical $\underline{e_z}$-displacement evolution along the $\underline{e_x}$ axis near the manufacturing area; (b) experimental laser profilometry and numerical $\underline{e_z}$-displacements evolution along the $\underline{e_y}$ axis at the extremity of the substrate; (c) numerical estimation of the $\underline{e_z}$-displacements after complete cooling and unclamping of the component.

5.3.2 Total displacements

The numerical estimation of the total displacements after unclamping was computed along the manufacturing direction ($\underline{e_z}$ axis) for the two walls manufactured by WAAM with bidirectional (Figure 5.14a) and unidirectional deposition strategies (Figure 5.14b). The mechanical model predicts a displacement of about 1.8 mm at the end of the deposited beads in the wall manufactured with unidirectional deposition strategy (Figure 5.14b) in qualitative agreement with experimental observation (Figure 5.12c). In contrast, the wall manufactured with a bidirectional deposition strategy (Figure 5.14a) shows lower displacements in the $\underline{e_z}$ direction, consistent with the macroscopic regularity observed for the experimental wall.

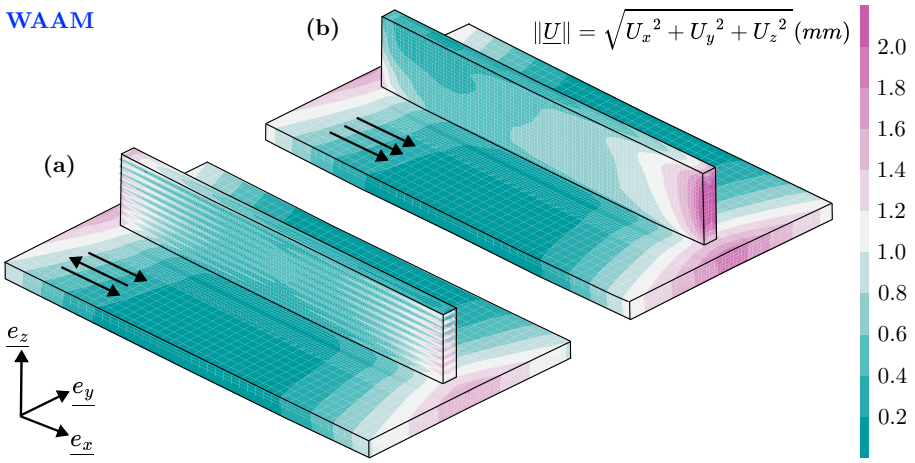

Figure 5.14. Numerical prediction of the displacement along the $\underline{e_z}$ axis at the end of the deposition, before unclamping, for two specimens manufactured by WAAM with (a) bi-directional and (b) unidirectional deposition strategy.

It was mentioned in Section 5.1.2 that two hardening models (isotropic and kinematic) were tested for mechanical resolution. Only small differences were found in predicting the displacement field with isotropic and kinematic models, which made us consider that both models can be used to estimate deformations during manufacturing with WAAM and WLAM.

5.3.3 Residual stresses

The mechanical model enables the estimation of residual stresses in the component at the end of the deposition after unclamping the substrate. The presence of residual stresses can deteriorate the mechanical behavior of the manufactured parts and, for instance, favor crack propagation [207]. Figure 5.15 presents the estimated residual stresses for the 200 mm-long single bead wall manufactured by WAAM using (a and b) isotropic and (c and d) kinematic hardening. The residual stresses are displayed at the end of the cooling of the component before (Figure 5.15b and d) and after (Figure 5.15a and c) unclamping the substrate from the testing table.

It was found that the unclamping lowers the residual stress level in the component, which is the consequence of the elastic return of the component, which is now free to deform.

For the isotropic hardening model after unclamping, the residual stresses in the wall are predominantly estimated to be around 100-300 MPa, rising to 300-400 MPa at the extremities and 400-500 MPa near the top of the wall. These values are consistent with the residual stresses measured by Elmesalamy *et al.* [208] using the contour method for multipass welds on clamped 10-mm thick substrates using laser and GTAW processes. They reported tensile residual stress values between 200-450 MPa in the welded zone for the GTAW process and slightly lower values between 100-350 MPa for the laser process, which are comparable to the experimental manufacturing carried out in this work using WLAM and WAAM.

However, even if variation trends are similar, lower residual stresses around 200-300 MPa were obtained after unclamping with the kinematic hardening law. Muransky *et al.* [148] demonstrated that an isotropic hardening model in welding tends to overestimate the residual stresses. In contrast, a kinematic hardening model tends to underestimate them. Thus, the isotropic and kinematic models can be considered as upper and lower bounds for residual stress predictions. Finally, a mixed isotropic-kinematic hardening model, such as the one developed by Chaboche [209], would have likely provided more accurate residual stress values but encountered convergence issues in this study.

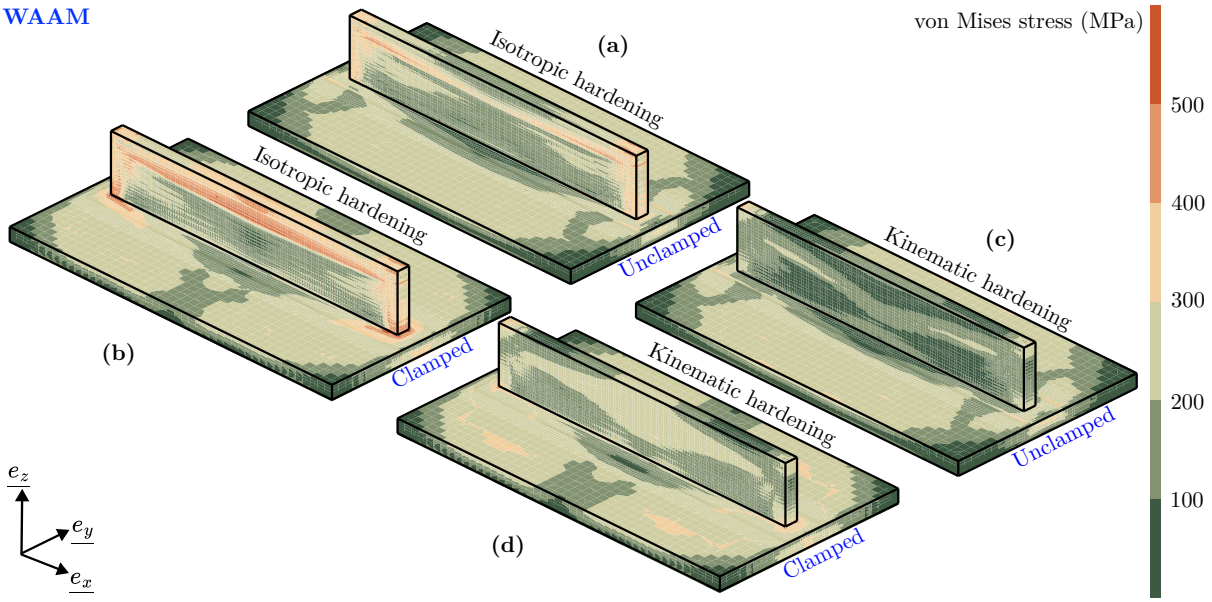

Figure 5.15. Residual von Mises stresses in a 20-layer single bead wall manufactured by WAAM. (a) Unclamped component with isotropic hardening model; (b) clamped component with isotropic hardening; (c) unclamped component with kinematic hardening; (d) clamped component with kinematic hardening.

5.4 Qualitative modeling at the fusion zone scale

The previous sections demonstrated the reliability of the numerical model at the macroscopic scale, effectively estimating heat accumulation and substrate deflection and qualitatively predicting macroscopic geometrical irregularities in the specimens. We now focus on the post-treatment of the model results at the scale of the deposited bead. At this finer scale, the model encounters limitations due to certain assumptions, such as omitting fluid dynamics in the melt pool, which affects its shape and thermal distribution [163]. Despite these limitations, the following work aims to provide qualitative insights into the microstructural homogeneity of the manufactured components.

5.4.1 Geometry of the deposited beads

The first application of the model at the mesoscopic scale was to study the shape of the fusion zone for different process parameters (Figure 5.16, where the red part represents the melted area). In particular, the aim was to establish criteria for the difference between a numerical fusion zone resulting from a set of parameters leading to a continuous bead and one leading to an irregular bead. In the case of a continuous experimental bead (Figure 5.16c), the numerical model estimates that the entire bead has been melted and that the fusion zone has a good penetration into the substrate (Figure 5.16a). In the case of a discontinuous experimental bead (Figure 5.16d), the numerical model predicts an incomplete fusion of the deposited bead (Figure 5.16b) as the red area does not cover all the added bead. This type of post-treatment allows us to determine the feasibility of the deposition based on the manufacturing conditions (power, deposition speed, wire speed) and the estimated theoretical width of the bead (based on the interpolations presented in Chapter 3).

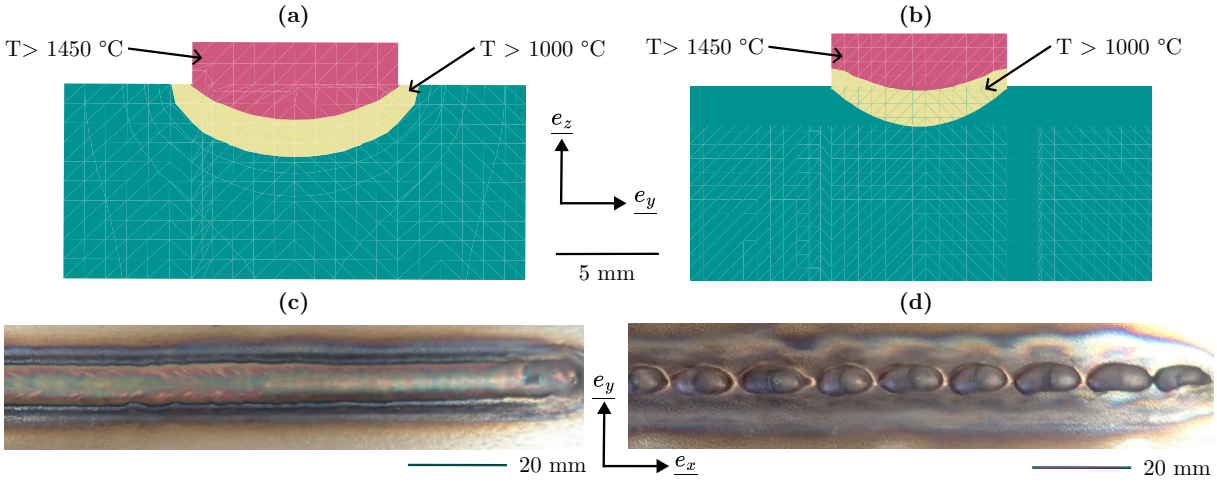

Figure 5.16. Predicted numerical shape for the fusion zone compared with single beads manufactured with WAAM process, depending on the set of parameters. (a) Transverse cross-section of the estimated numerical single bead with $Q_{exp} = 2400$ W, $s = 200$ mm.min^{-1}, $v_w = 2500$ mm.min^{-1}, resulting in the formation of the continuous single bead (c); (b) transverse cross-section of the estimated numerical single bead with $Q_{exp} = 1800$ W, $s = 150$ mm.min^{-1}, $v_w = 1875$ mm.min^{-1}, resulting in the formation of the discontinuous single bead (d). The melted area ($T > 1450$ °C) is represented in red, the area where the temperature exceeded 1000 °C is represented in yellow, while the area where the maximal temperature remained under 1000 °C is represented in green.

Our next focus was to compare the experimental shapes of the fusion zones in transverse sections of single-bead walls (colored in red in Figures 5.17a and 5.17c for WLAM and WAAM, respectively) to the model predictions (Figures 5.17b and 5.17d for WLAM and WAAM, respectively). The different numerical fusion isotherms (1450 °C) are depicted in blue, and the characterized deposited beads (first, tenth and twentieth layers) are depicted in light blue. The analyzed area corresponds to the cross-section of a bead remelted during the deposition of the next one (layers 2 and 11, respectively).

For the manufacturing of a single-bead wall using the WLAM process, the numerical model indicated that each deposited layer resulted in the complete remelting of the layer below the processed one (Figure 5.17b). In addition, the depth of the remelted zone increases as the number of deposited beads increases. For the WAAM process, a significant fraction of the previous layer was numerically observed to be remelted (Figure 5.17d). However, experimentally, only a small part of the previous layer was observed to remelt for the WAAM and WLAM processes (Figures 5.17a and 5.17d). Additionally, the experimental fusion zones exhibited a left-right alternation due to fluid movements or slight trajectory shifts, which are not captured in the numerical model.

Our model does not allow to reproduce the precise form of the fusion zones. However, trends in their changes can be identified. If one analyses the shape of the numerical melting zones, the first three layers are rounder due to their proximity to the substrate, as the heat is conducted in several directions in the substrate. In the rest of the wall, the shape of the numerical fusion zones remains regular. More accurate prediction of the experimental morphologies would require the addition of a capillarity-gravity model to estimate the shape of the deposited beads, as developed by Mohebbi *et al.* [153], and a hydrodynamic model for the melt pool shape [162]. However, this would significantly increase the computing time (around 15 days for 6 seconds of WAAM manufacturing on a 7-core, 30 GB RAM configuration, as reported by Cadiou *et al.* [163]).

Differences in final geometries were observed between the experimental and numerical walls achieved by WAAM and WLAM (Figure 5.17). The difference in height between experimental and numerical walls after the twentieth deposited layer is around 5% for WLAM and less than 1% for WAAM. Although the difference in the width of the numerical and experimental WLAM walls is acceptable at the macroscopic scale, it suggests that dimension calibration based only on the first layer is insufficient to predict the global wall dimensions for the WLAM process precisely. In contrast, the width of the first bead in the WAAM process is close to the general average width of the wall, leading to a better prediction of the final wall dimensions.

The observed geometrical differences could be corrected by measuring the wall after manufacturing and adjusting the input layer width in the model, such as calibrating a Goldak heat source to reduce fusion zone penetration in the previous layer [206]. However, this study did not perform post-manufacturing calibration to ensure that the model remains adaptable between the WAAM and WLAM processes and across various experimental conditions.

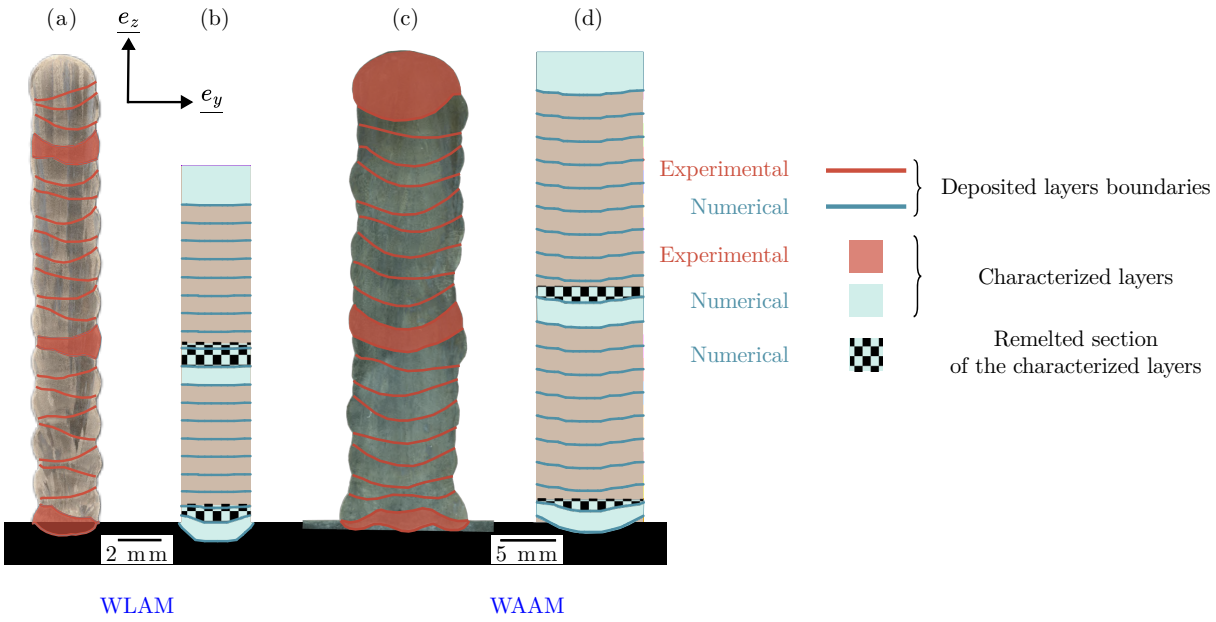

Figure 5.17. Successive fusion zones in experimental and numerical transverse cross-sections of single-bead walls manufactured by WLAM and WAAM: (a) experimental 24-layer WLAM wall after polishing and electrolytic etching; (b) numerical WLAM specimen; (c) experimental WAAM specimen after polishing and electrolytic etching; (d) numerical WAAM specimen. Fusion zones boundaries are shown in red, and the numerical successively added blocks of elements are displayed in shades of blue.

5.4.2 Cooling rates at solidification

Experimental measurements

We focused on calculating cooling rates during the solidification after reaching 1450 °C and comparing them to experimental data. The experimental cooling rates were estimated from measurements of primary dendrite arms oriented in the manufacturing direction ($\underline{e_z}$ axis) in transverse cross-sections after chemical etching. The resulting microstructures in the tenth layer of specimens manufactured by WAAM and WLAM are presented in Figures 5.18a and 5.18b, respectively. The estimated cooling rates in the first, tenth and twentieth layers of WAAM and WLAM specimens are presented in Table 5.3. These cooling rates were estimated by measuring the PDAS using Equation 2.2. The measured cooling rates are mostly in the order of magnitude of 100 °C/s for the WAAM process and approximately ten times higher (1000 °C/s) for the WLAM process. The lower cooling rate in the WAAM process results in a coarser microstructure as compared to the WLAM (Figure 5.18). These values of cooling rates are in agreement with the literature data:

- Ou *et al.* [210] estimated the solidification cooling rate in the WAAM process in the order of magnitude of 100 °C/s for the H13 steel.
- Akbari and Kovacevic [109] reported solidification cooling rates in the WLAM process in the order of magnitude of 1000 °C/s for the 316LSi steel.
- Finally, Goland *et al.* [114] reported solidification cooling rate values between around 200-400°C/s for the WAAM process and around 750-4500 °C/s for the WLAM process, based on similar measurements of the dendritic size, for the 316L steel.

Additionally, the cooling rate significantly decreases between the first and the tenth layers for both processes and between the tenth and the twentieth layers for the WLAM process. The difference in cooling rates between the first and the tenth layers is attributed to the substrate effect, as heat can quickly dissipate by conducting into the substrate. This effect diminishes as the number of deposited layers increases. The significant difference between the cooling rates in the tenth and twentieth layers of the WLAM wall is explained by heat accumulation in the component due to insufficient interlayer cooling times. Heat accumulation in the component makes energy dissipation more difficult.

Numerical post-processing

The cooling rates at solidification were also estimated with the numerical model, using the methodology illustrated in Figure 5.19 for the WAAM process[1]. For that sake, the 1450 °C isosurface corresponding to the fusion temperature of 316L steel was extracted from the geometry and remeshed (Figure 5.19a). The part of the surface located in front of the deposited bead (black surface) was not considered, as it will be remelted in the next time steps, unlike the rear part, where solidification conditions will control the microstructure formation. The thermal gradient was extracted from the thermal field and projected into the surface (Figure 5.19b). The solidification rate was computed using trigonometric relationships, assuming that the size of the melt pool does not increase during the manufacturing. The solidification speed, therefore, varies from 0 mm/s at the deepest point of the melting surface to the deposition speed at the rear of the fusion zone (3.33 m/s=200 in Figure 5.19c, corresponding to the deposition speed applied during the manufacturing of a single-bead with WAAM process). Finally, the cooling rate at solidification was determined by multiplying the thermal gradient and the solidification rate (Figure 5.19d). One can observe that the solidification cooling rate is not homogeneous across the fusion isosurface. However, the upper part of the surface will be remelted in case of stacking when depositing the bead above. For comparison purposes, we extracted one cooling rate value in the middle of the field depicted in Figure 5.19. We considered that this point is likely not to be remelted and corresponds to the position in which the experimental measurements were acquired (microstructures of Figure 5.17).

Analysis of cooling rate calculations

Following this procedure, the cooling rates were estimated for the first, tenth and twentieth layers of the single-bead walls manufactured with WAAM and WLAM, as presented in Table 5.3. The calculated cooling rates for the WAAM process are in the same order of magnitude (100 °C/s) as the experimental values. The calculated cooling rates in WLAM are underestimated (about half of the experimental values) but still five times higher than the calculated values in the WAAM process, indicating that the induced thermal gradients are the highest in WLAM.

Table 5.3. Experimental and numerical estimation of the cooling rate (°C/s) in the first, tenth and twentieth layers of the specimens manufactured using WAAM and WLAM.

Layer in the wall	**WLAM**		**WAAM**	
	Numerical	Experimental	Numerical	Experimental
Layer 1	1800	4000 ± 600	240	800 ± 300
Layer 10	550	3000 ± 1000	140	120 ± 10
Layer 20	400	1100 ± 200	110	300 ± 100

[1]The same methodology was applied for the WLAM process.

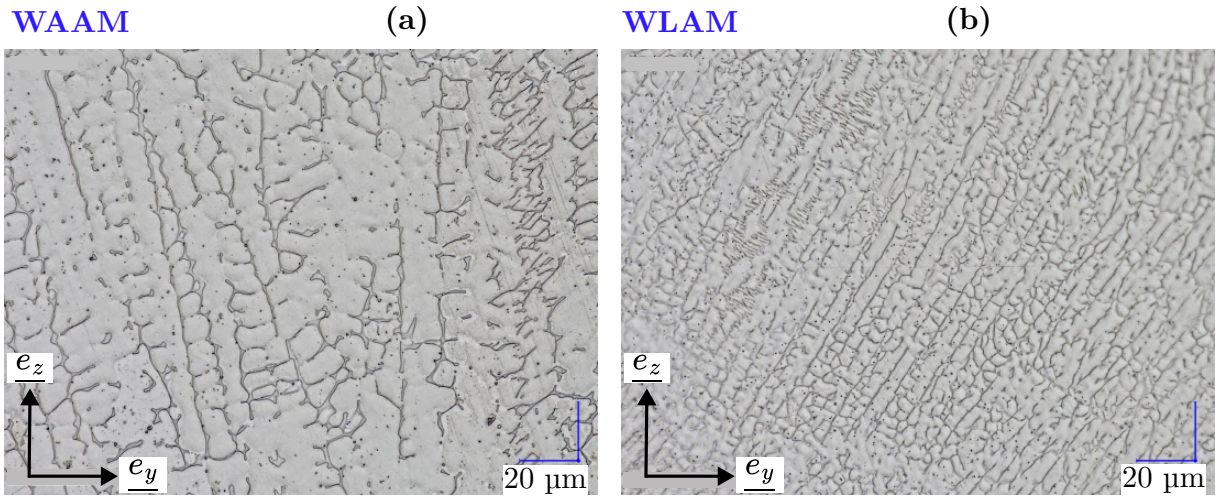

Figure 5.18. Micrographs of austeno-ferritic microstructure in transverse cross-sections of the tenth layer in specimens: (a) WAAM process; (b) WLAM process.

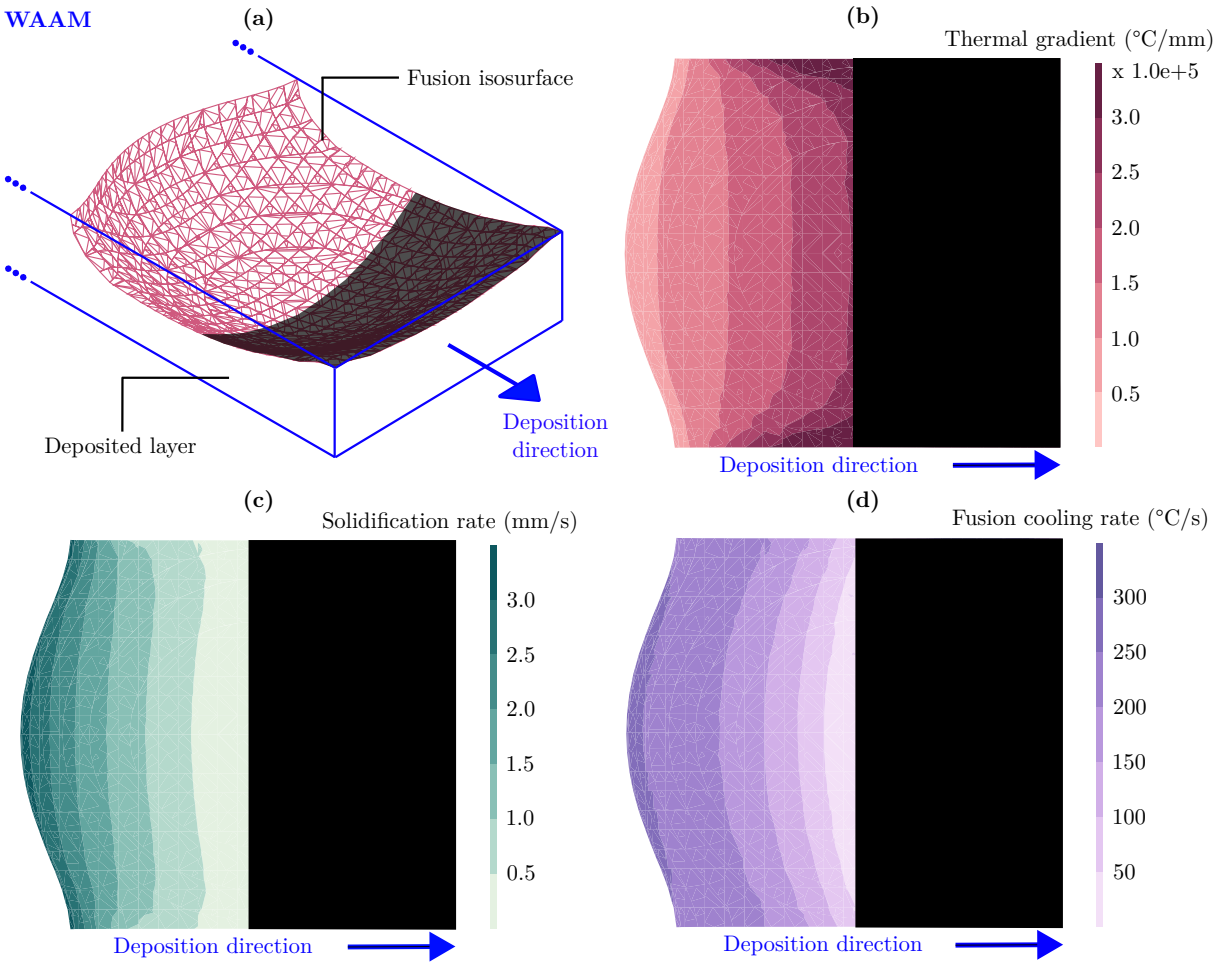

Figure 5.19. (a) Representation of the extracted fusion contour during a bead deposition with WAAM process. Numerical estimation of (b) the thermal gradient, (c) the solidification rate and (d) the fusion cooling rate at the back of the fusion contour. The front of the melt pool is blackened as it is remelted by the back of the fusion zone.

5.4.3 Interlayer cooling time control

The thermal model can be now used to optimize the interlayer cooling time during manufacturing. Too short cooling time can lead to macroscopic or microscopic heterogeneities in the produced components [155]. Conversely, excessively long cooling times are industrially undesirable as they increase the overall manufacturing time.

The WLAM manufacturing of a 100 mm-long specimen with a constant interlayer cooling time of 20 seconds was carried out experimentally and numerically. Figure 5.20a illustrates the maximum temperature reached in the wall over time. The blue curve represents the evolution of the maximum temperature at each time step during manufacturing, with the maximum temperature at the end of each interlayer cooling period indicated by dots (local numerical minima). These numerical results are compared with experimental data, with measured temperatures at the end of each cooling period shown within black error bars. For the manufacturing process shown in Figure 5.20a, the applied interlayer cooling time of 20 s was sufficient to cool down the built wall under the threshold of 200 °C for the first six layers. However, beyond the seventh layer, the temperature at the end of each cooling period exceeded 200 °C due to heat accumulation. The experimental values closely matched the numerical predictions, demonstrating a similar trend of heat accumulation in the WLAM component manufactured with a constant interlayer cooling time.

A numerical post-processing procedure was implemented to optimize the interlayer cooling time, ensuring that the components cooled to temperatures below the threshold of 200 °C. It involved conducting a new thermal simulation of the entire manufacturing process, with extended interlayer cooling times to ensure complete cooling to room temperature between layers. The post-processing step determined the required cooling time to reach 200 °C and incorporated these times into a third simulation with adapted interlayer cooling durations, as presented in Figure 5.20b. The required interlayer cooling time increases with the number of layers, reflecting the greater difficulty in dissipating heat further from the substrate.

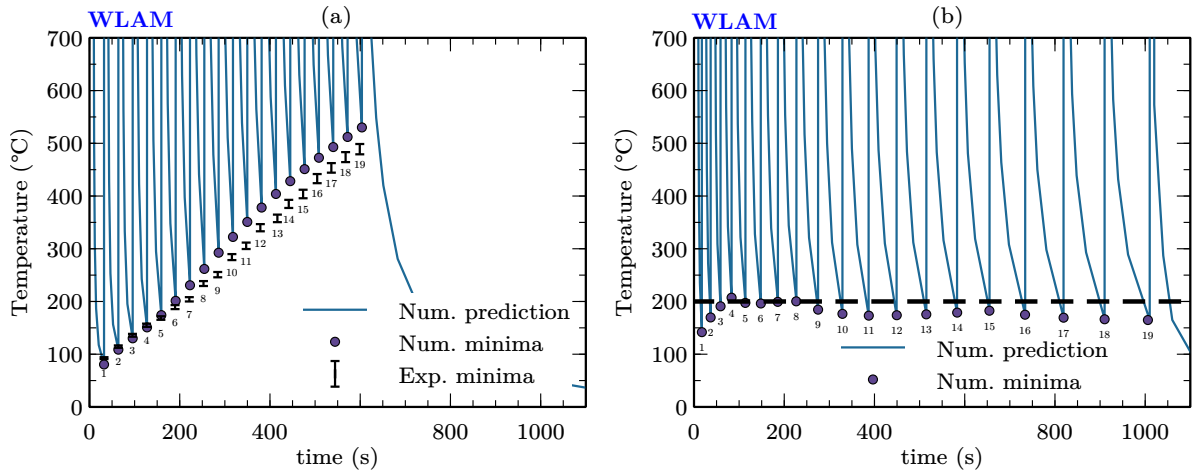

Figure 5.20. Experimental and numerical evolution of the maximum temperature reached in a 100 mm-long specimen manufactured by WLAM: (a) constant interlayer cooling time of 20 s; (b) Evolving interlayer cooling time ensuring $T < 200$ °C at the end of each cooling period. The experimental uncertainty bars are obtained by knowing the measurement precision of the thermal camera.

5.4.4 Cooling rate control

The thermal model can be further used to analyze the evolution of the cooling rate during solidification within deposited beads. In the first deposited layers, the cooling rate is affected by the substrate. However, one of the objectives of this study is to investigate the potential cooling conditions that result in constant cooling rates in the walls when the number of layers is significant and the influence of the substrate can be neglected. Maintaining a constant cooling rate throughout the manufacturing process enhances the microstructural regularity of the components by influencing dendrite size [122], which is linked to mechanical properties.

Figures 5.21a and b present the cooling rate during solidification obtained by experimental measurements and by using the thermal model, respectively, in the specimen manufactured by WLAM with different interlayer cooling time conditions: constant at 0 and 20 s, and variable interlayer cooling time ensuring $T < 200$ °C, as discussed in the previous paragraphs. Similar trends were obtained for the experimental and numerical results.

With the controlled interlayer cooling times (cyan curve), the cooling rate decreases between the first and fifth layers as the substrate still influences the cooling. However, between the fifth and twentieth layers, where the effect of the substrate becomes negligible, the cooling rate remains almost constant, as does the dendrite size (Table 5.3).

In contrast, for the walls manufactured with a constant interlayer cooling time of 20 s (blue curve), where heat accumulation was observed, the cooling rate at the fusion temperature decreases between the fifth and twentieth layers (570 °C/s versus 350 °C/s, respectively). When the interlayer cooling time is brought to zero (purple curve), the decrease in the cooling rates is amplified (530 °C/s for the fifth layer versus 100 °C/s for the twentieth layer), resulting in a variation of the dendrite spacing of almost a factor two.

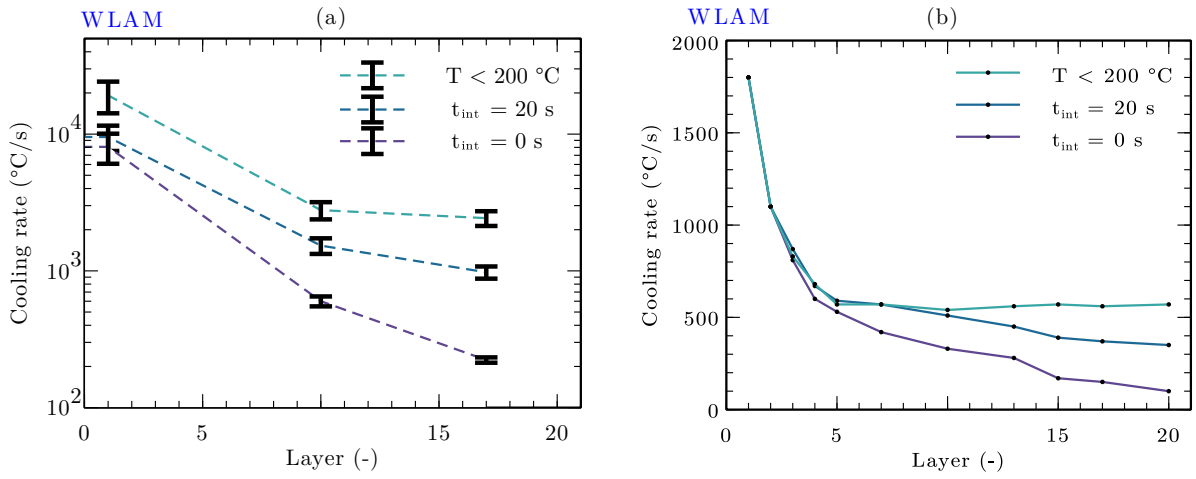

Figure 5.21. Evolution of (a) the experimental and (b) the predicted numerical cooling rate during solidification in 100 mm-long specimens manufactured by WLAM under different interlayer cooling conditions: constant interlayer cooling times of 0 s (purple) and 20 s (blue) and evolving interlayer cooling times ensuring that decreases to 200 °C before new layer deposition (cyan). Experimental uncertainty bars are obtained by taking into account errors in dendritic spacing measurements and the dispersion of the obtained values.

5.4.5 Prevention of microstructural defects

We mentioned that the exposure of 316L steel in the temperature range of 500 to 900 °C can promote the formation of carbides or σ-phase, decreasing the corrosion resistance and fracture toughness of the components [211, 212, 213]. Figures 5.22a and b illustrate the cumulative time spent within the 500-900 °C temperature range in the specimens fabricated using WAAM and WLAM, respectively. This cumulative duration increases with the height of the wall for both processes. Additionally, the time spent at the specified temperature remains constant along the deposition direction at the same wall height. The cumulative time within the 500-900 °C range reaches a maximum of 220 s for the WAAM single-bead wall and 80 s for the WLAM process. According to experimental data available in the literature [129], these durations are not long enough for phase transformation. However, other specimens fabricated using WAAM were modeled by varying the interlayer cooling times (0 s, 50 s, 100 s and 200 s), as presented in Figure 5.23. It was observed that the duration within the temperature range of 500-900 °C can extend to 15 minutes when no interlayer cooling time is applied. This duration can further increase when the number of deposited beads is more significant, for instance, in multi-layer block manufacturing. Such prolonged exposure to elevated temperatures could lead to the formation of the σ phase if the cooling control within the component is inadequate. This kind of numerical analysis can help to mitigate such a risk.

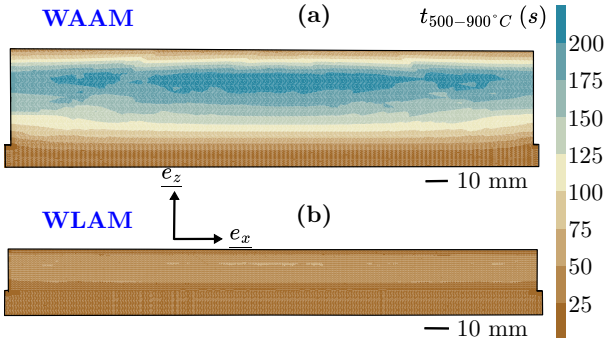

Figure 5.22. Cumulative time spent in the temperature range 500-900 °C for the specimens manufactured using (a) WAAM and (b) WLAM.

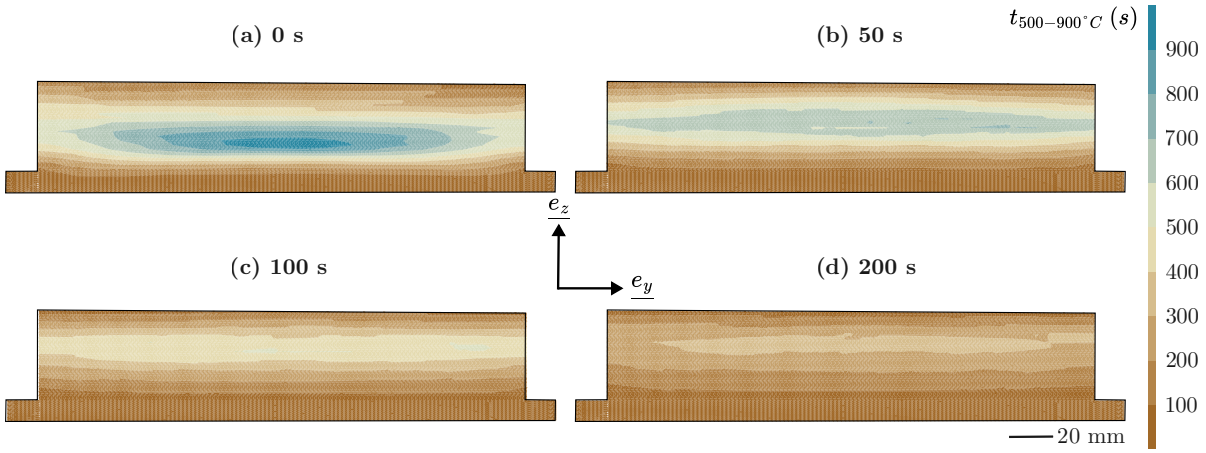

Figure 5.23. Cumulative time spent in the temperature range 500-900 °C for the specimens manufactured by WAAM applying interlayer cooling times of (a) 0 s; (b) 50 s; (c) 100 s and (d) 200 s.

5.5 Conclusion to Chapter 5

A thermomechanical model has been developed for both WAAM and WLAM processing of 316L stainless steel components. This model is based on the finite element method and incorporates a finite element addition procedure for material deposition, considering non-linear thermal and mechanical assumptions. Calibration of the thermal model was performed using experimental data at the macroscopic scale (single-bead walls) and the morphology of the first deposited bead at the mesoscopic scale to ensure agreement of total heat input and distribution. Heat distribution within the manufactured components was accurately reproduced, enabling numerical tracking of the thermal and mechanical history of the components. The model was also applied qualitatively at the scale of the deposited bead despite the strong limitations imposed by the fact that the fluid effects were not considered.

The following conclusions were obtained:

- The thermal model allowed to reveal hot areas when examining the average temperature in the component throughout manufacturing, linked to local heat accumulation. These areas correspond to the experimentally observed geometrical irregularities in height for a unidirectional deposition path.
- Interlayer cooling times based on component geometry were optimized to prevent heat accumulation while maximizing the deposition rate. It was found that constant interlayer cooling time leads to heat accumulation as the number of deposited layers increases. The evolving interlayer cooling time ensures a sufficient cooling of the component below a threshold temperature of 200 °C before each new layer deposition.
- The mechanical model also identified zones with higher displacements compared to the rest of the manufactured components, corresponding qualitatively to visually observed geometrical irregularities in height in the experimental walls.
- Residual stress distribution at the end of deposition was analyzed for a WAAM component, identifying areas with high residual stresses (up to 400 MPa) that could negatively impact the mechanical properties of the material [207]. The areas of highest residual stress are located at the start and end of the beads and the top of the finished part.
- According to experimental observations and numerical model, the WLAM process induces higher cooling rates than the WAAM process. Moreover, the cooling rate decreases with the increase in the number of layers. However, the model for the WLAM process underestimated the cooling rate due to inaccurate reproduction of the size and morphologies of the deposited beads.
- It was observed that the cooling rate during solidification decreased during the deposition of the first five layers due to the effect of the substrate. Beyond the fifth layer, the wall manufactured with controlled variable interlayer cooling times maintained a regular solidification cooling rate of about 550 °C/s, which resulted in a constant dendrite size of around 10 µm. In contrast, components produced with constant interlayer cooling times of 0 and 20 s exhibited a decrease in cooling rates of approximately 200 °C/s and 400 °C/s, respectively, between the fifth and twentieth layers.
- Finally, potential precipitation of phases detrimental to the properties, like carbides and σ-phase, can be confidently prevented by controlling the time spent by a component within the 500-900 °C temperature range. We demonstrated that for the WAAM process, this cumulative time increases as the applied interlayer cooling time decreases, insisting on the need to control this parameter.

Conclusion

The main objectives of this work were to assess the influence of the processing parameters of WAAM and WLAM used to manufacture components of 316L austenitic stainless steel on (i) their geometrical regularity, (ii) their microstructure, (iii) their mechanical properties and (iv) their thermal stability. As a typical geometrically complex component comprises thin and thick parts and angles, single beads, single-bead walls and multilayer tiles were achieved. First, the influence of the deposition speed s, the wire feed speed v_w and the power of the energy source Q_{exp} on the morphology of the beads was studied. Using the obtained results, process conditions for the manufacturing of single-bead walls and tiles were determined. It was observed that the volume energy density influences the continuity of the single beads. Moreover, an inappropriate height increment, deposition strategy, interlayer cooling time and overlap between two adjacent beads can lead to macroscopic deformations and deposition issues while manufacturing single-bead walls. The chosen deposition path should homogeneously distribute the heat in the component during manufacturing to obtain the desired geometry. The heat input should be adjusted to ensure adequate cooling time between two layers. In addition, an overlap of 70% has to be selected to obtain a surface with minimum roughness while manufacturing tile layers. We also concluded that the power used for tiles has to be 20% higher than those used for single-bead walls.

The resulting microstructure of WAAM and WLAM components consisted of elongated grains formed by epitaxial dendritic solidification. For single beads, different textures and directions of elongation of the grains were observed, as compared to WAAM and WLAM, due to the different shapes of the melt pools. Moreover, an austenitic-ferritic microstructure was formed, with ferrite fraction estimated at 8-9 vol.% for WAAM and 5-6 vol.% for WLAM for cooling rates at 10^2 °C/s for WAAM and ten times higher for WLAM.

For the single-bead walls, elongated grains throughout dozens of layers, oriented along the manufacturing direction $\underline{e_z}$, were observed for both processes, with a strong $\langle 001 \rangle_{\parallel \underline{e_z}}$ texture. The mechanical behavior during tensile tests of the single-bead wall achieved by WLAM showed some anisotropy, whereas the WAAM specimen displayed similar mechanical properties in both manufacturing and deposition directions. In addition, compared to conventionally wrought 316L steel, the components manufactured by WAAM and WLAM exhibited similar ultimate strains (around 40%) and tensile strengths.

Next, we observed that the microstructure of tiles was different from that of single-bead walls. For the WLAM tile, the center of the fusion zone (CFZ) and the side of the fusion zone (SFZ) exhibited different textures and directions of grain elongation. In the SFZ, the $\langle 011 \rangle_{\parallel \underline{e_z}}$ texture associated with elongated grains growing at a 45° angle to the manufacturing direction $\underline{e_z}$, is predominant. For the WAAM tile, the overlapped region (OR) and the center of the fusion zone (CFZ) are the two main regions in equivalent proportions. The OR has a predominant $\langle 001 \rangle_{\parallel \underline{e_z}}$ texture whereas the CFZ has a $\langle 011 \rangle_{\parallel \underline{e_z}}$ predominant texture.

Finally, the effect of post-processing heat treatment on the microstructure of single-bead walls manufactured by WAAM and WLAM was studied. One heat treatment at 1100 °C for 30 mins reduced the ferrite content in the single-bead wall. If the presence of ferrite is a limiting factor for an industrial component, this heat treatment allows the component to be re-austenitized. Another heat treatment at 1200 °C for 30 mins did not result in complete recrystallization of the single-bead wall despite the complete release of the dislocation energy. It is then assumed that the grain microstructure of single-bead walls achieved by WAAM and WLAM will remain stable under thermal exposure.

Finally, a thermomechanical model has been developed for the WAAM and WLAM processing of 316L stainless steel components to describe their thermal evolution and mechanical state. This model allowed us to obtain additional information for experimental measurements, improving our understanding of the processes. The thermal model allowed for revealing hot areas linked to local heat accumulation. Controlling interlayer cooling times based on component geometry prevented heat accumulation while maximizing the deposition rate. Conversely, constant interlayer cooling time increases heat accumulation as the number of deposited layers increases. The evolving interlayer cooling time ensures a sufficient cooling of the component below a threshold temperature of 200 °C before each new layer deposition and maintains a regular solidification cooling rate, which results in a constant dendrite size. To obtain the best microstructural homogeneity in the manufactured components, it is important to control the temperature before the deposition of each new layer, which is associated with preventing macroscopic collapses. Finally, potential precipitation of phases detrimental to the properties, like carbides and σ-phase, can be prevented by controlling the time a component spends within the 500-900 °C temperature range.

The study of single-bead walls and tiles achieved by WAAM and WLAM allowed for understanding the influence of the process parameters on their geometry, as well as understanding their microstructural specificities and their solidification cooling rate, using experimental and numerical results. The study identified the various criteria required for the production of a homogeneous component in terms of both geometry and microstructure. This study also showed that, despite a different microstructure, the components produced by WAAM and WLAM have tensile properties comparable to those of 316L in the wrought state, thus exceeding the required industrial standards.

Conclusion en français

Cette étude avait pour objectif d'évaluer l'influence des paramètres des procédés WAAM et WLAM sur des pièces fabriquées en acier inoxydable austénitique 316L, en analysant leur régularité géométrique, leur microstructure, leur propriétés mécaniques et l'évolution de leur microstructure sous l'effet de la température. L'étude paramétrique a mis en évidence l'impact de la densité volumique d'énergie sur la continuité des cordons déposés et l'importance de la calibration de la stratégie de dépôt ainsi que du temps de refroidissement interpasse afin d'éviter l'apparition de défauts géométriques (pertes de hauteur) et microstructuraux (porosité).

Les murs monocordons fabriqués par WAAM et WLAM possèdent une microstructure constituée de grains allongés dans la direction de fabrication $\underline{e_z}$, une texture selon $\langle 001 \rangle_{\parallel \underline{e_z}}$ et une fraction de ferrite de 8-9 vol.% dans le cas du WAAM et 5-6 vol.% dans le cas du WLAM. Les essais mécaniques ont révélé que, malgré les différences microstructurales, les propriétés en traction des pièces fabriquées sont comparables à celles de l'acier 316L forgé. L'effet des traitements thermiques sur la microstructure de murs monocordons a également été étudié : un traitement à 1100 °C pendant 30 min a permis de réduire la teneur en ferrite, tandis qu'un traitement à 1200 °C pendant 30 min a conduit à une stabilisation de la microstructure en entrainant une recristallisation seulement limitée au pied et aux bordures des murs fabriqués.

Les blocs multicouches fabriqués par WAAM et WLAM possèdent des microstructures distinctes, différentes de celle observée dans les murs monocordons. Au WAAM, deux zones majoritaires sont identifiées au centre et aux extrémités des cordons déposés. Au WLAM, une texture majoritaire selon $\langle 011 \rangle_{\parallel \underline{e_z}}$ est observée, due à la forme arrondie des bains de fusion.

Enfin, un modèle thermomécanique basé sur la méthode des éléments finis a été développé afin de mieux comprendre l'évolution thermique et l'état mécanique des pièces fabriquées par WAAM et WLAM, soulignant l'importance du contrôle du temps de refroidissement interpasse pour assurer une vitesse de refroidissement homogène ainsi qu'éviter la formation de phases néfastes aux propriétés du matériau, dans le cas d'accumulation de chaleur.

This page was intentionally left blank.

Perspectives

The investigation of the influence of the process parameters on the geometry of the manufactured components allowed us to establish optimal conditions for manufacturing single-bead walls and tiles of 316L steel using WAAM and WLAM. Further research could refine the threshold values leading to incorrect deposition and define precise feasibility windows by expanding the achieved dataset and experimental range. It would enable an extensive mapping of the influence of the process parameters on bead geometry, facilitating the selection of appropriate conditions adapted to each fabrication.

Porosity was observed in the tiles manufactured by WLAM. Future work is required to understand better the effect of process parameters on the formation of pores.

To validate the determined processing conditions for WAAM and WLAM, a complex component consisting of thin and thick sections and angles could be manufactured. Additional studies will be required to assess the impact of angles, junctions and crossings on the geometrical accuracy. To illustrate this perspective, we achieved an X-shaped component integrating thin and thick sections, resulting in a geometry with a thick central part and thin edges (Figure 5.24). The manufacturing parameters corresponded to those used for single-bead walls at the edges (thin sections) and those used for tiles in the central section (thick section, 20% increase in power, 70% overlap between successive beads). The deposition strategy was designed to distribute heat as evenly as possible by alternating the order of deposition of the layers and their direction, following a methodology similar to that used for the manufacturing of tiles. For the X-shaped component achieved by WLAM, we observed a height irregularity of 1 to 2 mm in the central region, where bead overlap occurs (Figure 5.25). This height variation remained constant with increasing number of layers and did not interfere with the manufacturing. However, it highlights the need for further research to assess for height irregularities at transitions between thin and thick sections.

The microstructure and mechanical properties of single-bead walls (thin sections) and the influence of heat treatments on the microstructure were analyzed. Additional tensile testing at 45° between the manufacturing $\underline{e_z}$ and deposition $\underline{e_x}$ directions could be conducted to assess the anisotropy of the material further. The heat treatment at 1200 °C for 30 minutes exhibited limited recrystallization. Future studies should investigate extended heat treatment durations to determine the potential evolution of the microstructure. For industrial applications, the findings suggest that elongated grains and inherent anisotropy in thin sections of components achieved by WLAM and WAAM are unavoidable. Alternative manufacturing strategies should be explored to promote recrystallization or limit texturing.

Although no σ-phase formation was detected in the achieved components, future research is required to determine the stability range (time and temperature) of this phase known to be negative for mechanical properties.

The microstructure of tiles (thick sections) was also examined, revealing notable differences from single-bead walls, suggesting that the mechanical properties and the behavior of the microstructure under

thermal exposure may vary. Future work should then assess the mechanical properties and the effects of heat treatments on tiles achieved using WLAM and WAAM processes and compare the results with those of single-bead walls.

The developed thermomechanical model successfully predicted thermal fields, strains, residual stresses and cooling rates in single-bead walls. Two hardening behaviors were studied for the mechanical model to estimate the upper and lower bounds of residual stresses and strains: isotropic hardening and kinematic hardening. Future work should incorporate a mixed isotropic-kinematic hardening model, such as the Chaboche model [209], to improve the accuracy of estimating the mechanical fields. Additionally, the model can be extended to simulate the manufacturing of tiles and complex components, enabling comparisons of thermal, mechanical, and cooling rate fields with those of single-bead walls. This would likely necessitate new calibrations and optimizations to reduce computational time.

Finally, one limiting factor for numerical modeling remains the generation of the mesh of the studied geometry. Developing a program that converts robot-generated trajectory files into simulation-compatible meshes would allow for evaluating a larger range of processing and geometrical conditions before manufacturing.

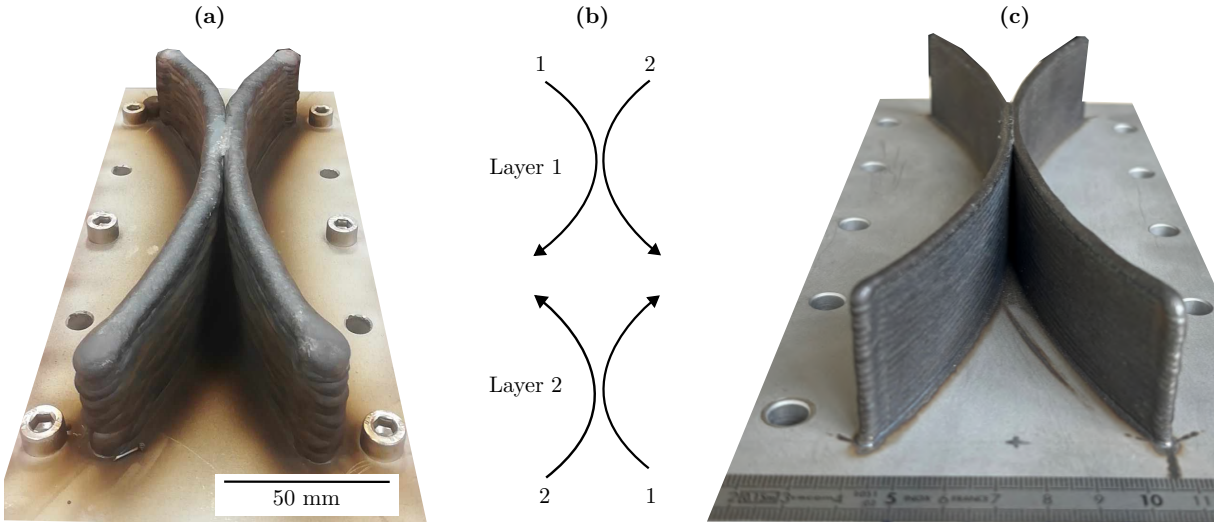

Figure 5.24. (a) X-shaped component manufactured with WAAM process. (b) Used deposition strategy. (c) X-shaped component manufactured with WLAM process.

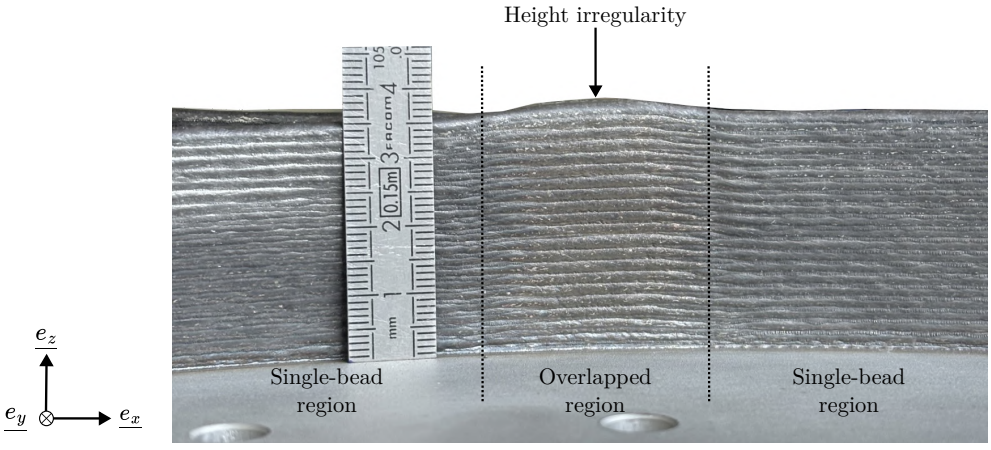

Figure 5.25. Side view of the X-shaped component elaborated with WLAM process.

Perspectives en français

L'étude de l'influence des paramètres des procédés WAAM et WLAM sur la géométrie des pièces fabriquées a permis de déterminer des conditions de fabrication de murs monocordons (sections fines) et de blocs (sections épaisses) en acier 316L. De futurs travaux permettraient d'affiner les seuils critiques d'énergie volumique conduisant à la fabrication de cordons irréguliers et ainsi définir des fenêtres de faisabilité expérimentale, facilitant le choix de conditions de fabrication.

Afin de valider les paramètres de fabrication établis dans cette étude pour les procédés WAAM et WLAM, une pièce en forme de "X" intégrant des sections fines et épaisses ainsi que des angles a été réalisée. De nouveaux travaux sont nécessaires pour évaluer l'impact de la géométrie sur la régularité de hauteur des pièces fabriquées. Dans le cas de la pièce en forme de "X" réalisée dans notre étude, une variation de hauteur est observée dans la zone centrale en comparaison aux extrémités, ne perturbant toutefois pas la fabrication.

De la porosité a été observée dans le bloc fabriqué par WLAM. Une nouvelle étude sera nécessaire pour mieux comprendre l'impact des paramètres du procédé WLAM sur la formation de ces pores.

L'analyse microstructurale des murs a montré une recristallisation limitée après un traitement thermique à 1200 °C pendant 30 minutes. Des traitements plus longs pourront être réalisés afin d'étudier l'impact du temps de traitement thermique sur l'évolution de la microstructure.

L'anisotropie de la pièce et l'élongation des grains semblent inévitables dans les murs fabriqués par WAAM et WLAM. Des stratégies alternatives de fabrication pourraient être envisagées afin de favoriser la recristallisation ou de limiter la texture et l'élongation des grains.

L'étude de la microstructure des blocs a révélé des différences notables avec la microstructure des murs, ce qui suggère des potentielles variations de propriétés mécaniques et de l'impact des traitements thermiques sur la microstructure. De nouvelles études sur les blocs, comparées aux résultats obtenus pour les murs, sont alors nécessaires.

Le modèle thermomécanique développé a permis de prédire les champs thermiques, les déformations, les contraintes résiduelles et les vitesses de refroidissement dans les murs. L'intégration d'un modèle d'écrouissage mixte (de type Chaboche) pourrait améliorer la précision des calculs mécaniques. De plus, l'extension du modèle aux blocs et aux pièces complexes pourrait être étudié. Enfin, une des limites actuelles de notre modèle numérique est la génération manuelle des géométries et des maillages. Le développement d'un programme convertissant les fichiers trajectoire générés par le robot en maillages utilisables pour la simulation permettrait d'évaluer de plus nombreuses conditions de fabrication avant leur mise en œuvre expérimentale.

This page was intentionally left blank.

Bibliography

[1] CEA, Le CEA, acteur majeur de la recherche au service de l'Etat, de l'économie et des citoyens., https://www.cea.fr/Pages/Accueil.aspx (Oct. 2024).

[2] G. N. Levy, R. Schindel, J. P. Kruth, Rapid manufacturing and rapid tooling with layer manufacturing (LM) technologies, state of the art and future perspective, CIRP Annals 52 (2) (2003) 589–609. doi:10.1016/S0007-8506(07)60206-6.

[3] T. DebRoy, H. L. Wei, J. S. Zuback, T. Mukherjee, J. W. Elmer, J. O. Milewski, A. M. Beese, A. Wilson-Heid, A. De, W. Zhang, Additive manufacturing of metallic components – Process, structure and properties, Progress in Materials Science 92 (2018) 112–224. doi:10.1016/j.pmatsci.2017.10.001.

[4] D. Ding, Z. Pan, D. Cuiuri, H. Li, A multi-bead overlapping model for robotic wire and arc additive manufacturing (WAAM), Robotics and Computer-Integrated Manufacturing 31 (2015) 101–110. doi:10.1016/j.rcim.2014.08.008.

[5] A. Dubiez, Naval Group équipe un navire de la Marine d'une hélice imprimée en 3D, https://www.lejournaldesentreprises.com/article/naval-group-equipe-un-navire-de-la-marine-dune-helice-imprimee-en-3d-849034 (2021).

[6] MX3D, Arc Bike I, https://mx3d.com/industries/design/arc-bike-i/ (2016).

[7] Meltio, Metal 3D Printing Applications - A match for your industrial needs, https://meltio3d.com/applications/ (2025).

[8] F. Dalle, M. Blat-Yrieix, S. Dubiez-Le Goff, C. Cabet, P. Dubuisson, 17 - Conventional austenitic steels as out-of-core materials for Generation IV nuclear reactors, in: P. Yvon (Ed.), Structural Materials for Generation IV Nuclear Reactors, Woodhead Publishing, 2017, pp. 595–633.

[9] T. DebRoy, T. Mukherjee, J. O. Milewski, J. W. Elmer, B. Ribic, J. J. Blecher, W. Zhang, Scientific, technological and economic issues in metal printing and their solutions, Nature Materials 18 (10) (2019) 1026–1032. doi:10.1038/s41563-019-0408-2.

[10] M. K. Thompson, G. Moroni, T. Vaneker, G. Fadel, R. I. Campbell, I. Gibson, A. Bernard, J. Schulz, P. Graf, B. Ahuja, F. Martina, Design for Additive Manufacturing: Trends, opportunities, considerations, and constraints, CIRP Annals 65 (2) (2016) 737–760. doi:10.1016/j.cirp.2016.05.004.

[11] D.-G. Ahn, Directed Energy Deposition (DED) Process: State of the Art, International Journal of Precision Engineering and Manufacturing-Green Technology 8 (2) (2021) 703–742. doi:10.1007/s40684-020-00302-7.

[12] A. Basak, S. Das, Epitaxy and Microstructure Evolution in Metal Additive Manufacturing, Annual Review of Materials Research 46 (1) (2016) 125–149. doi:10.1146/annurev-matsci-070115-031728.

[13] A. J. Pinkerton, [INVITED] Lasers in additive manufacturing, Optics & Laser Technology 78 (2016) 25–32. doi:10.1016/j.optlastec.2015.09.025.

[14] S. Liu, Y. C. Shin, Additive manufacturing of Ti6Al4V alloy: A review, Materials & Design 164 (2019) 107552. doi:10.1016/j.matdes.2018.107552.

[15] J. W. Elmer, J. Vaja, J. S. Carpenter, D. R. Coughlin, M. J. Dvornak, P. Hochanadel, P. Gurung, A. Johnson, G. Gibbs, Wire-Based Additive Manufacturing of Stainless Steel Components, Welding Journal 99 (1) (2020) S8–S24. doi:10.29391/2020.99.002.

[16] P. Bajaj, A. Hariharan, A. Kini, P. Kürnsteiner, D. Raabe, E. A. Jägle, Steels in additive manufacturing: A review of their microstructure and properties, Materials Science and Engineering: A 772 (2020) 138633. doi:10.1016/j.msea.2019.138633.

[17] T. Mukherjee, T. DebRoy, Printability of 316 stainless steel, Science and Technology of Welding and Joining 24 (5) (2019) 412–419. doi:10.1080/13621718.2019.1607061.

[18] D. Ding, Z. Pan, D. Cuiuri, H. Li, S. van Duin, N. Larkin, Bead modelling and implementation of adaptive MAT path in wire and arc additive manufacturing, Robotics and Computer-Integrated Manufacturing 39 (2016) 32–42. doi:10.1016/j.rcim.2015.12.004.

[19] Nilesh Kumar, Nilesh Kumar, Het Bhavsar, Het Bhavsar, P.V.S. Mahesh, P.V.S. Mahesh, A. K. Srivastava, Bhaskor J. Bora, Bhaskor J. Bora, A. Saxena, A. R. Dixit, Wire Arc Additive Manufacturing – A revolutionary method in additive manufacturing, Materials Chemistry and Physics (2022) 126144–126144.doi:10.1016/j.matchemphys.2022.126144.

[20] Y. Kok, X. P. Tan, P. Wang, M. L. S. Nai, N. H. Loh, E. Liu, S. B. Tor, Anisotropy and heterogeneity of microstructure and mechanical properties in metal additive manufacturing: A critical review, Materials & Design 139 (2018) 565–586. doi:10.1016/j.matdes.2017.11.021.

[21] W. E. Frazier, Metal Additive Manufacturing: A Review, Journal of Materials Engineering and Performance 23 (6) (2014) 1917–1928. doi:10.1007/s11665-014-0958-z.

[22] D. Ding, Z. Pan, D. Cuiuri, H. Li, Wire-feed additive manufacturing of metal components: technologies, developments and future interests, The International Journal of Advanced Manufacturing Technology 81 (1) (2015) 465–481. doi:10.1007/s00170-015-7077-3.

[23] D.-H. Kam, Y.-M. Kim, C. Kim, Recent Studies of Laser Metal 3D Deposition with Wire Feeding, Journal of Welding and Joining 34 (1) (2016) 35–40. doi:10.5781/JWJ.2016.34.1.35.

[24] T. Mukherjee, T. DebRoy, A digital twin for rapid qualification of 3D printed metallic components, Applied Materials Today 14 (2019) 59–65. doi:10.1016/j.apmt.2018.11.003.

[25] N. A. Rosli, M. R. Alkahari, M. F. b. Abdollah, S. Maidin, F. R. Ramli, S. G. Herawan, Review on effect of heat input for wire arc additive manufacturing process, Journal of Materials Research and Technology 11 (2021) 2127–2145. doi:10.1016/j.jmrt.2021.02.002.

[26] E. Karayel, Y. Bozkurt, Additive manufacturing method and different welding applications, Journal of Materials Research and Technology 9 (5) (2020) 11424–11438. doi:10.1016/j.jmrt.2020.08.039.

[27] O. Ojo, E. Taban, Microstructure, Mechanical and Corrosion Behavior of Additively Manufactured Steel: A Review (Part 1), Materials Testing 62 (2020) 503–516. doi:10.3139/120.111507.

[28] L. Monier, Liens procédé-microstructure-propriétés en traction de l'acier inoxydable austénitique 316L élaboré par fabrication additive, Ph.D. thesis, Université Grenoble Alpes (Dec. 2023).

[29] S. Astafurov, E. Astafurova, Phase Composition of Austenitic Stainless Steels in Additive Manufacturing: A Review, Metals 11 (7) (2021) 1052. doi:10.3390/met11071052.

[30] Q. Marsac, Modélisation de la macrostructure de soudures TIG épaisses multipasses en acier inoxydable austénitique. Application aux contrôles ultrasonores de soudures du circuit primaire des RNR-Na., Ph.D. thesis, Université Aix-Marseille (Nov. 2020).

[31] S. C. Costello, C. R. Cunningham, F. Xu, A. Shokrani, V. Dhokia, S. T. Newman, The state-of-the-art of wire arc directed energy deposition (WA-DED) as an additive manufacturing process for large metallic component manufacture, International Journal of Computer Integrated Manufacturing 36 (3) (2023) 469–510. doi:10.1080/0951192X.2022.2162597.

[32] X. Fang, C. Ren, L. Zhang, C. Wang, K. Huang, B. Lu, A model of bead size based on the dynamic response of CMT-based wire and arc additive manufacturing process parameters, Rapid Prototyping Journal 27 (4) (2021) 741–753. doi:10.1108/RPJ-03-2020-0051.

[33] T. A. Rodrigues, V. Duarte, R. M. Miranda, T. G. Santos, J. P. Oliveira, Current Status and Perspectives on Wire and Arc Additive Manufacturing (WAAM), Materials 12 (7) (2019) 1121. doi:10.3390/ma12071121.

[34] M. Chaturvedi, E. Scutelnicu, C. C. Rusu, L. R. Mistodie, D. Mihailescu, A. V. Subbiah, Wire Arc Additive Manufacturing: Review on Recent Findings and Challenges in Industrial Applications and Materials Characterization, Metals 11 (6) (2021) 939. doi:10.3390/met11060939.

[35] S. H. Mok, G. Bi, J. Folkes, I. Pashby, Deposition of Ti–6Al–4V using a high power diode laser and wire, Part I: Investigation on the process characteristics, Surface and Coatings Technology 202 (16) (2008) 3933–3939. doi:10.1016/j.surfcoat.2008.02.008.

[36] M. Schulz, F. Klocke, J. Riepe, N. Klingbeil, K. Arntz, Process Optimization of Wire-Based Laser Metal Deposition of Titanium, Journal of Engineering for Gas Turbines and Power 141 (5) (2019) 052102. doi:10.1115/1.4041167.

[37] M. Bambach, I. Sizova, F. Kies, C. Haase, Directed energy deposition of Inconel 718 powder, cold and hot wire using a six-beam direct diode laser set-up, Additive Manufacturing 47 (2021) 102269. doi:10.1016/j.addma.2021.102269.

[38] M. Shaikh, C.-C. Chen, H.-C. Chiang, J.-R. Chen, Y.-C. Chou, T.-Y. Kuo, K. Ameyama, C.-H. Chuang, Additive manufacturing using fine wire-based laser metal deposition, Rapid Prototyping Journal ahead-of-print (Nov. 2019). doi:10.1108/RPJ-04-2019-0110.

[39] A. Heralic, Monitoring and Control of Robotized Laser Metal-Wire Deposition, Ph.D. thesis, Chalmers University of Technology (2012).

[40] C. Roch, C. Tournier, S. Lavernhe, Process based modelling of power density for wire laser additive manufacturing using a coaxial head, Additive Manufacturing 73 (2023) 103648. doi:10.1016/j.addma.2023.103648.

[41] M. Motta, A. G. Demir, B. Previtali, High-speed imaging and process characterization of coaxial laser metal wire deposition, Additive Manufacturing 22 (2018) 497–507. doi:10.1016/j.addma.2018.05.043.

[42] S. W. Williams, F. Martina, A. A. Charles, A. C. Addison, J. Ding, G. Pardal, P. A. Colegrove, Wire + Arc Additive Manufacturing, Materials Science and Technology 32 (7) (2016) 641–647. doi:10.1179/1743284715y.0000000073.

[43] G. Anzalone, C. Zhang, B. Wijnen, P. Sanders, J. Pearce, A low-cost open-source metal 3-D printer, IEEE Access 1 (2013) 803–810. doi:10.1109/ACCESS.2013.2293018.

[44] B. Baufeld, R. Widdison, T. Dutilleul, K. Bridger, Electron beam additive manufacturing at the Nuclear AMRC, Electrotechnica & Electronica 51 (5-6) (2016) 25–30.

[45] G. Doumenc, Fabrication additive arc-fil en alliage d'aluminium à durcissement structural AA6061 : relations procédé, microstructures et propriétés mécaniques, Ph.D. thesis, Université de Nantes (Feb. 2021).

[46] A. Ayed, Fabrication additive par Arc-Fil et Laser-Fil de l'alliage Ti-6AL-4V : relations procédés - microstructures - propriétés, Ph.D. thesis, Université de Toulouse, INPT (May 2021).

[47] M. Valentin, C. Arnaud, R. Kling, Additive manufacturing by wire based laser metal deposition, in: Laser 3D Manufacturing VI, Vol. 10909, SPIE, 2019, pp. 86–92. doi:10.1117/12.2510074.

[48] H. Murakawa, 13 - Residual stress and distortion in laser welding, in: S. Katayama (Ed.), Handbook of Laser Welding Technologies, Woodhead Publishing Series in Electronic and Optical Materials, Woodhead Publishing, 2013, pp. 374–400e. doi:10.1533/9780857098771.2.374.

[49] J. Xiong, Y. Lei, H. Chen, G. Zhang, Fabrication of inclined thin-walled parts in multi-layer single-pass GMAW-based additive manufacturing with flat position deposition, Journal of Materials Processing Technology 240 (2017) 397–403. doi:10.1016/j.jmatprotec.2016.10.019.

[50] T. S. Senthil, S. Ramesh Babu, M. Puviyarasan, V. Dhinakaran, Mechanical and microstructural characterization of functionally graded Inconel 825 - SS316L fabricated using wire arc additive manufacturing, Journal of Materials Research and Technology 15 (2021) 661–669. doi:10.1016/j.jmrt.2021.08.060.

[51] A. R. Kannan, S. M. Kumar, R. Pramod, N. S. Shanmugam, M. Vishnukumar, S. Naveenkumar, Microstructural characterization and mechanical integrity of stainless steel 316L clad layers deposited via wire arc additive manufacturing for nuclear applications, Materialwissenschaft und Werkstofftechnik 52 (6) (2021) 617–623. doi:10.1002/mawe.202000242.

[52] A. Dass, A. Moridi, State of the Art in Directed Energy Deposition: From Additive Manufacturing to Materials Design, Coatings 9 (7) (2019) 418. doi:10.3390/coatings9070418.

[53] Avelino Zapata, C. J. Bernauer, C. Stadter, C. G. Kolb, Michael F. Zaeh, Investigation on the Cause-Effect Relationships between the Process Parameters and the Resulting Geometric Properties for Wire-Based Coaxial Laser Metal Deposition, Metals 12 (3) (2022) 455–455. doi:10.3390/met12030455.

[54] M. Akbari, Y. Ding, R. Kovacevic, Process development for a robotized laser wire additive manufacturing system, 2017. doi:10.1115/MSEC2017-2951.

[55] M. A. Chergui, Simulation Based deposition Strategies Evaluation and Optimization in Wire Arc Additive Manufacturing, Ph.D. thesis, Université Grenoble Alpes (Mar. 2021).

[56] D. Jafari, T. H. Vaneker, I. Gibson, Wire and arc additive manufacturing: Opportunities and challenges to control the quality and accuracy of manufactured parts, Materials & Design 202 (2021) 109471. doi:10.1016/j.matdes.2021.109471.

[57] W. Jin, C. Zhang, S. Jin, Y. Tian, D. Wellmann, W. Liu, Wire Arc Additive Manufacturing of Stainless Steels: A Review, Applied Sciences 10 (5) (2020) 1563. doi:10.3390/app10051563.

[58] A. Saboori, M. Toushekhah, A. Aversa, M. Lai, M. Lombardi, S. Biamino, P. Fino, Critical Features in the Microstructural Analysis of AISI 316L Produced By Metal Additive Manufacturing, Metallography Microstructure and Analysis 9 (1) (2020) 92–96. doi:10.1007/s13632-019-00604-6.

[59] T. C. Nguyen, D. C. Weckman, D. A. Johnson, H. W. Kerr, The humping phenomenon during high speed gas metal arc welding, Science and Technology of Welding and Joining 10 (4) (2005) 447–459. doi:10.1179/174329305X44134.

[60] H. Geng, J. Li, J. Xiong, X. Lin, F. Zhang, Optimization of wire feed for GTAW based additive manufacturing, Journal of Materials Processing Technology 243 (243) (2017) 40–47. doi:10.1016/j.jmatprotec.2016.11.027.

[61] A. Baghdadchi, V. Hosseini, M. A. V. Bermejo, B. Axelsson, E. Harati, M. Högström, L. Karlsson, Wire Laser Metal Deposition Additive Manufacturing of Duplex Stainless Steel Components—Development of a Systematic Methodology, Materials 14 (23) (2021) 7170. doi:10.3390/ma14237170.

[62] B. Ma, N. Zhang, Y. Zhang, X. Gao, Welding parameters effect and optimization on bead geometry during arc additive manufacturing 1986 (1) (2021) 012034, publisher: IOP Publishing. doi:10.1088/1742-6596/1986/1/012034.

[63] S. H. Oliari, A. S. C. M. D'Oliveira, M. Schulz, Additive Manufacturing of H11 with Wire-Based Laser Metal Deposition, Soldagem & Inspeção 22 (2017) 466–479. doi:10.1590/0104-9224/SI2204.06.

[64] E. Aldalur, F. Veiga, A. Suarez, J. Bilbao, A. Lamikiz, Analysis of the Wall Geometry with Different Strategies for High Deposition Wire Arc Additive Manufacturing of Mild Steel, Metals 10 (7) (2020) 892. doi:10.3390/met10070892.

[65] V. T. Le, D. S. Mai, T. K. Doan, H. Paris, Wire and arc additive manufacturing of 308L stainless steel components: Optimization of processing parameters and material properties, Engineering Science and Technology, an International Journal 24 (4) (2021) 1015–1026. doi:10.1016/j.jestch.2021.01.009.

[66] S. Mohammed, Z. Zhang, R. Kovacevic, Optimization of processing parameters in fiber laser cladding, The International Journal of Advanced Manufacturing Technology 111 (9) (2020) 2553–2568. doi:10.1007/s00170-020-06214-9.

[67] Mingpu Yao, Xi Chen, Fanrong Kong, Wei Tong, Process optimization of laser hot-wire cladding with high-power direct diode laser via the response surface methodology, The International Journal of Advanced Manufacturing Technology (May 2022). doi:10.1007/s00170-022-09300-2.

[68] V. Querard, Réalisation de pièces aéronautiques de grandes dimensions par fabrication additive WAAM, Ph.D. thesis, Ecole Centrale de Nantes (2019).

[69] F. Caiazzo, Additive manufacturing by means of laser-aided directed metal deposition of titanium wire, The International Journal of Advanced Manufacturing Technology 96 (5) (2018) 2699–2707. doi:10.1007/s00170-018-1760-0.

[70] M. Dinovitzer, X. Chen, J. Laliberte, X. Huang, H. Frei, Effect of wire and arc additive manufacturing (WAAM) process parameters on bead geometry and microstructure, Additive Manufacturing 26 (2019) 138–146. doi:10.1016/j.addma.2018.12.013.

[71] F. Caiazzo, V. Alfieri, Directed Energy Deposition of stainless steel wire with laser beam: evaluation of geometry and affection depth, Procedia CIRP 99 (2021) 348–351. doi:10.1016/j.procir.2021.03.121.

[72] J.-D. Kim, Y. Peng, Melt pool shape and dilution of laser cladding with wire feeding, Journal of Materials Processing Technology 104 (3) (2000) 284–293. doi:10.1016/S0924-0136(00)00528-8.

[73] T. E. Abioye, A. Medrano-Tellez, P. K. Farayibi, P. K. Oke, Laser metal deposition of multi-track walls of 308LSi stainless steel, Materials and Manufacturing Processes 32 (14) (2017) 1660–1666. doi:10.1080/10426914.2017.1292034.

[74] T. E. Abioye, J. Folkes, A. T. Clare, A parametric study of Inconel 625 wire laser deposition, Journal of Materials Processing Technology 213 (12) (2013) 2145–2151. doi:10.1016/j.jmatprotec.2013.06.007.

[75] D. Lindell, Process Mapping for Laser Metal Deposition of Wire using Thermal Simulations : A prediction of material transfer stability, Master's thesis, Karlstad University (2021).

[76] Y. Yehorov, L. J. da Silva, A. Scotti, Balancing WAAM Production Costs and Wall Surface Quality through Parameter Selection: A Case Study of an Al-Mg5 Alloy Multilayer-Non-Oscillated Single Pass Wall, Journal of Manufacturing and Materials Processing 3 (2) (2019) 32. doi:10.3390/jmmp3020032.

[77] P. Long, D.-X. Wen, J. Min, Z. Zheng, J. Li, Y. Liu, Microstructure Evolution and Mechanical Properties of a Wire-Arc Additive Manufactured Austenitic Stainless Steel: Effect of Processing Parameter, Materials 14 (2021) 1681. doi:10.3390/ma14071681.

[78] S. Pattanayak, S. K. Sahoo, Gas metal arc welding based additive manufacturing—a review, CIRP Journal of Manufacturing Science and Technology 33 (2021) 398–442. doi:10.1016/j.cirpj.2021.04.010.

[79] T. Feng, L. Wang, Z. Tang, S. Yu, Z. Bu, X. Hu, Y. Cheng, Effect of Trajectory Curvature on the Microstructure and Properties of Surfacing Wall Formed with the Process of Wire Arc Additive Manufacturing, Coatings 9 (12) (2019) 848. doi:10.3390/coatings9120848.

[80] G. Venturini, F. Montevecchi, A. Scippa, G. Campatelli, Optimization of WAAM Deposition Patterns for T-crossing Features, Procedia CIRP 55 (2016) 95–100. doi:10.1016/j.procir.2016.08.043.

[81] A. A. Ugla, O. Yilmaz, Deposition-Path Generation of SS308 Components Manufactured by TIG Welding-Based Shaped Metal Deposition Process, Arabian Journal for Science and Engineering 42 (11) (2017) 4701–4711. doi:10.1007/s13369-017-2582-3.

[82] K. Li, M. A. Klecka, S. Chen, W. Xiong, Wire-arc additive manufacturing and post-heat treatment optimization on microstructure and mechanical properties of Grade 91 steel, Additive Manufacturing 37 (2021) 101734. doi:10.1016/j.addma.2020.101734.

[83] E. Aldalur, F. Veiga, A. Suárez, J. Bilbao, A. Lamikiz, High deposition wire arc additive manufacturing of mild steel: Strategies and heat input effect on microstructure and mechanical properties, Journal of Manufacturing Processes 58 (2020) 615–626. doi:10.1016/j.jmapro.2020.08.060.

[84] L. Palmeira Belotti, J. A. W. van Dommelen, M. G. D. Geers, W. Ya, J. P. M. Hoefnagels, Influence of the printing strategy on the microstructure and mechanical properties of thick-walled wire arc additive manufactured stainless steels, Journal of Materials Processing Technology 324 (2024) 118275. doi:10.1016/j.jmatprotec.2023.118275.

[85] D. Svetlizky, M. Das, B. Zheng, A. L. Vyatskikh, S. Bose, A. Bandyopadhyay, J. M. Schoenung, E. J. Lavernia, N. Eliaz, Directed energy deposition (DED) additive manufacturing: Physical characteristics, defects, challenges and applications, Materials Today 49 (2021) 271–295. doi:10.1016/j.mattod.2021.03.020.

[86] N. Shamsaei, A. Yadollahi, L. Bian, S. M. Thompson, An overview of Direct Laser Deposition for additive manufacturing; Part II: Mechanical behavior, process parameter optimization and control, Additive Manufacturing 8 (2015) 12–35. doi:10.1016/j.addma.2015.07.002.

[87] S. Suryakumar, K. P. Karunakaran, A. Bernard, U. Chandrasekhar, N. Raghavender, D. Sharma, Weld bead modeling and process optimization in Hybrid Layered Manufacturing, Computer-aided Design 43 (4) (2011) 331–344. doi:10.1016/j.cad.2011.01.006.

[88] F. W. C. Farias, J. da Cruz Payão Filho, V. H. P. Moraes e Oliveira, Prediction of the interpass temperature of a wire arc additive manufactured wall: FEM simulations and artificial neural network, Additive Manufacturing 48 (2021) 102387. doi:10.1016/j.addma.2021.102387.

[89] A. Chabot, Méthodologie de monitoring multiphysique des procédés DED : développement par une démarche expérimentale, Ph.D. thesis, École centrale de Nantes (Oct. 2020).

[90] S. H. Lee, CMT-Based Wire Arc Additive Manufacturing Using 316L Stainless Steel: Effect of Heat Accumulation on the Multi-Layer Deposits, Metals 10 (2) (2020) 278. doi:10.3390/met10020278.

[91] K. Treutler, V. Wesling, The Current State of Research of Wire Arc Additive Manufacturing (WAAM): A Review, Applied Sciences 11 (18) (2021) 8619. doi:10.3390/app11188619.

[92] C. Bourlet, Développement de la fabrication additive par procédé arc-fil pour les aciers : caractérisation microstructurale et mécanique des dépôts en nuances ER100 et 316L pour la validation des propriétés d'emploi de pièces industrielles, Ph.D. thesis, Ecole nationale supérieure d'arts et métiers - ENSAM (Dec. 2019).

[93] J. Xiong, L. Yanjiang, R. Li, Y. Ziqiu, Influences of process parameters on surface roughness of multi-layer single-pass thin-walled parts in GMAW-based additive manufacturing, Journal of Materials Processing Technology 252 (2018) 128–136. doi:10.1016/j.jmatprotec.2017.09.020.

[94] S. Singh, A. N. Jinoop, G. T. A. Tarun Kumar, I. A. Palani, C. P. Paul, K. G. Prashanth, Effect of Interlayer Delay on the Microstructure and Mechanical Properties of Wire Arc Additive Manufactured Wall Structures, Materials 14 (15) (2021) 4187. doi:10.3390/ma14154187.

[95] B. L. Bramfitt, Carbon and Alloy Steels, in: Mechanical Engineers' Handbook Third Edition - Materials and Mechanical Design, John Wiley & Sons, INC., 2006, p. 43, publisher: Wiley Online Library.

[96] B. Py-Renaudie, D. Goncalves, S. Pascal, M. Sennour, V. A. Esin, T. F. Morgeneyer, Effect of Welding Microstructure on Stress Relaxation Cracking Studied by Controlled Residual Stress Generation in a 316L(N) Austenitic Stainless Steel, Metallurgical and Materials Transactions A 54 (12) (2023) 4650–4670. doi:10.1007/s11661-023-07182-x.

[97] A. Saboori, A. Aversa, G. Marchese, S. Biamino, M. Lombardi, P. Fino, Microstructure and Mechanical Properties of AISI 316L Produced by Directed Energy Deposition-Based Additive Manufacturing: A Review, Applied Sciences-Basel 10 (9) (2020) 3310. doi:10.3390/app10093310.

[98] P. Peyre, E. Charkaluk, La fabrication additive des alliages métalliques 2 – microstructures, post-traitements et propriétés d'usage, ISTE editions, 2022.

[99] A. Baumard, Prédiction des structures de grain d'un composant en acier 316L élaboré par fabrication additive fusion laser sur lit de poudre, Ph.D. thesis, Université de Montpellier (Dec. 2020).

[100] G. Ma, R. Wang, D. Liu, S. Wu, F. Niu, D. Wu, Laser-arc hybrid additive manufactured AlCu alloy for T-shaped structure: Microstructure evaluation and molten pool behavior, Journal of Manufacturing Processes 79 (2022) 442–459. doi:10.1016/j.jmapro.2022.04.042.

[101] K. Moeinfar, F. Khodabakhshi, S. F. Kashani-bozorg, M. Mohammadi, A. P. Gerlich, A review on metallurgical aspects of laser additive manufacturing (LAM): Stainless steels, nickel superalloys, and titanium alloys, Journal of Materials Research and Technology 16 (2022) 1029–1068. doi:10.1016/j.jmrt.2021.12.039.

[102] Q. Jiang, P. Zhang, Z. Yu, H. Shi, S. Li, D. Wu, H. Yan, X. Ye, J. Chen, Microstructure and Mechanical Properties of Thick-Walled Inconel 625 Alloy Manufactured by Wire Arc Additive Manufacture with Different Torch Paths, Advanced Engineering Materials 23 (1) (2021) 2000728. doi:10.1002/adem.202000728.

[103] C. Cambon, I. Bendaoud, S. Rouquette, F. Soulié, A WAAM benchmark: From process parameters to thermal effects on weld pool shape, microstructure and residual stresses, Materials Today Communications 33 (2022) 104235. doi:10.1016/j.mtcomm.2022.104235.

[104] X. Xu, G. Mi, Y. Luo, P. Jiang, X. Shao, C. Wang, Morphologies, microstructures, and mechanical properties of samples produced using laser metal deposition with 316L stainless steel wire, Optics and Lasers in Engineering 94 (2017) 1–11. doi:10.1016/j.optlaseng.2017.02.008.

[105] Z. Wang, T. A. Palmer, A. M. Beese, Effect of processing parameters on microstructure and tensile properties of austenitic stainless steel 304L made by directed energy deposition additive manufacturing, Acta Materialia 110 (2016) 226–235. doi:10.1016/j.actamat.2016.03.019.

[106] F. Khodabakhshi, M. H. Farshidianfar, A. P. Gerlich, M. Nosko, V. Trembošová, A. Khajepour, Effects of laser additive manufacturing on microstructure and crystallographic texture of austenitic and martensitic stainless steels, Additive Manufacturing 31 (2020) 100915. doi:10.1016/j.addma.2019.100915.

[107] R. Engel, Modélisation des microstructures de solidification de l'acier 316L élaboré par fabrication additive, Ph.D. thesis, Université de Montpellier (Mar. 2024).

[108] J.-z. Su, M.-z. Xiao, Z.-j. Zhang, Z.-p. Ye, X. Jin, Y.-c. Yang, Microstructural morphology and evolution of austenite stainless steel deposited using pulsed laser and wire, The International Journal of Advanced Manufacturing Technology 93 (9) (2017) 3357–3370. doi:10.1007/s00170-017-0625-2.

[109] M. Akbari, R. Kovacevic, An investigation on mechanical and microstructural properties of 316LSi parts fabricated by a robotized laser/wire direct metal deposition system, Additive Manufacturing 23 (2018) 487–497. doi:10.1016/j.addma.2018.08.031.

[110] M. Goland, Comportement en corrosion et en corrosion sous contrainte en milieu primaire REP d'un acier inoxydable 316L élaboré par fabrication additive WAAM et WLAM, Ph.D. thesis, Sorbonne université (Dec. 2024).

[111] O. Andreau, I. Koutiri, P. Peyre, J.-D. Penot, N. Saintier, E. Pessard, T. De Terris, C. Dupuy, T. Baudin, Texture control of 316L parts by modulation of the melt pool morphology in selective laser melting, Journal of Materials Processing Technology 264 (2019) 21–31. doi:10.1016/j.jmatprotec.2018.08.049.

[112] L. Palmeira Belotti, J. A. W. van Dommelen, M. G. D. Geers, C. Goulas, W. Ya, J. P. M. Hoefnagels, Microstructural characterisation of thick-walled wire arc additively manufactured stainless steel, Journal of Materials Processing Technology 299 (2022) 117373. doi:10.1016/j.jmatprotec.2021.117373.

[113] C. Wang, T. G. Liu, P. Zhu, Y. H. Lu, T. Shoji, Study on microstructure and tensile properties of 316L stainless steel fabricated by CMT wire and arc additive manufacturing, Materials Science and Engineering: A 796 (2020) 140006. doi:10.1016/j.msea.2020.140006.

[114] M. Goland, J. Nguejio, C. Guerre, M. Rousseau, F. Balbaud-Célérier, Characterization of a 316l Stainless Steel Produced by Wire Laser and Wire Arc Additive Manufacturing: Heat Treatments, Microstructural Evolution, and Tensile Properties (Jun. 2024). doi:10.2139/ssrn.4853376.

[115] A. L. Schaeffler, Constitution Diagram for Stainless Steel Weld Metal, Metal Progress 56 (11) (1949) 680.

[116] E. De sonis, Evolution microstructurale de l'acier 316L élaboré par fabrication additive (LPBF et WAAM) et influence sur son comportement à rupture, Ph.D. thesis, Université Paris sciences et lettres (Jan. 2024).

[117] D. Wen, P. Long, J. Li, L. Huang, Z. Zheng, Effects of linear heat input on microstructure and corrosion behavior of an austenitic stainless steel processed by wire arc additive manufacturing, Vacuum 173 (2020) 109131. doi:10.1016/j.vacuum.2019.109131.

[118] N. Suutala, T. Takalo, T. Moisio, The relationship between solidification and microstructure in austenitic and austenitic-ferritic stainless steel welds, Metallurgical Transactions A 10 (4) (1979) 512–514. doi:10.1007/BF02697081.

[119] N. Suutala, Effect of solidification conditions on the solidification mode in austenitic stainless steels, Metallurgical Transactions A 14 (1) (1983) 191–197. doi:10.1007/BF02651615.

[120] W. Li, X. Liu, M. Yamamoto, Y. Guo, S. Zhu, K. Sugio, G. Sasaki, Research on interface characteristics of 308L stainless steel coatings manufactured by laser hot wire cladding, Surface and Coatings Technology 427 (2021) 127822. doi:10.1016/j.surfcoat.2021.127822.

[121] T. A. Rodrigues, J. D. Escobar, J. Shen, V. R. Duarte, G. G. Ribamar, J. A. Avila, E. Maawad, N. Schell, T. G. Santos, J. P. Oliveira, Effect of heat treatments on 316 stainless steel parts fabricated by wire and arc additive manufacturing : Microstructure and synchrotron X-ray diffraction analysis, Additive Manufacturing 48 (2021) 102428. doi:10.1016/j.addma.2021.102428.

[122] S. Katayama, A. Matsunawa, Solidification microstructure of laser welded stainless steels, International Congress on Applications of Lasers & Electro-Optics 1984 (2) (1984) 60–67. doi:10.2351/1.5057623.

[123] C. Bernauer, M. E. Sigl, S. Grabmann, T. Merk, A. Zapata, M. F. Zaeh, Effects of the thermal history on the microstructural and the mechanical properties of stainless steel 316L parts produced by wire-based laser metal deposition, Materials Science and Engineering: A 889 (2024) 145862. doi:10.1016/j.msea.2023.145862.

[124] S. Gudur, V. Nagallapati, S. Pawar, G. Muvvala, S. Simhambhatla, A study on the effect of substrate heating and cooling on bead geometry in wire arc additive manufacturing and its correlation with cooling rate, Materials Today: Proceedings 41 (2021) 431–436. doi:10.1016/j.matpr.2020.10.071.

[125] J. Park, S. H. Lee, CMT-Based Wire Arc Additive Manufacturing Using 316L Stainless Steel (2): Solidification Map of the Multilayer Deposit, Metals 11 (11) (2021) 1725. doi:10.3390/met11111725.

[126] N. Rodriguez, L. Vazquez, I. Huarte, I. Arruti, I. Tabernero, P. Alvarez, Wire and arc additive manufacturing: a comparison between CMT and TopTIG processes applied to stainless steel, Welding in the World 62 (5) (2018) 1083–1096. doi:10.1007/s40194-018-0606-6.

[127] X. Chen, J. Li, X. Cheng, B. He, H. Wang, Z. Huang, Microstructure and mechanical properties of the austenitic stainless steel 316L fabricated by gas metal arc additive manufacturing, Materials Science and Engineering: A 703 (2017) 567–577. doi:10.1016/j.msea.2017.05.024.

[128] F. Hejripour, F. Binesh, M. Hebel, D. K. Aidun, Thermal modeling and characterization of wire arc additive manufactured duplex stainless steel, Journal of Materials Processing Technology 272 (2019) 58–71. doi:10.1016/j.jmatprotec.2019.05.003.

[129] X. Chen, J. Li, X. Cheng, H. Wang, Z. Huang, Effect of heat treatment on microstructure, mechanical and corrosion properties of austenitic stainless steel 316L using arc additive manufacturing, Materials Science and Engineering: A 715 (2018) 307–314. doi:10.1016/j.msea.2017.10.002.

[130] L. Pryce, K. Andrews, Practical estimation of composition balance and ferrite content in stainless steels, Iron and Steel Institute Journal 195 (4) (1960) 415.

[131] V. Laghi, M. Palermo, L. Tonelli, G. Gasparini, L. Ceschini, T. Trombetti, Tensile properties and microstructural features of 304L austenitic stainless steel produced by wire-and-arc additive manufacturing, The International Journal of Advanced Manufacturing Technology 106 (9) (2020) 3693–3705. doi:10.1007/s00170-019-04868-8.

[132] K. M. Bertsch, G. Meric de Bellefon, B. Kuehl, D. J. Thoma, Origin of dislocation structures in an additively manufactured austenitic stainless steel 316L, Acta Materialia 199 (2020) 19–33. doi:10.1016/j.actamat.2020.07.063.

[133] ASTM A473-15 Standard Specification for Stainless Steel Forgings, https://www.astm.org/a0473-15.html.

[134] A. Suárez, E. Aldalur, F. Veiga, T. Artaza, I. Tabernero, A. Lamikiz, Wire arc additive manufacturing of an aeronautic fitting with different metal alloys: From the design to the part, Journal of Manufacturing Processes 64 (2021) 188–197. doi:10.1016/j.jmapro.2021.01.012.

[135] M. Ziętala, T. Durejko, M. Polański, I. Kunce, T. Płociński, W. Zieliński, M. Łazińska, W. Stępniowski, T. Czujko, K. J. Kurzydłowski, Z. Bojar, The microstructure, mechanical properties and corrosion resistance of 316L stainless steel fabricated using laser engineered net shaping, Materials Science and Engineering: A 677 (2016) 1–10. doi:10.1016/j.msea.2016.09.028.

[136] J. Yu, M. Rombouts, G. Maes, Cracking behavior and mechanical properties of austenitic stainless steel parts produced by laser metal deposition, Materials & Design 45 (2013) 228–235. doi:10.1016/j.matdes.2012.08.078.

[137] K. Wandtke, D. Schroepfer, R. Scharf-Wildenhain, A. Haelsig, T. Kannengiesser, A. Kromm, J. Hensel, Influence of the WAAM process and design aspects on residual stresses in high-strength structural steels, Welding in the World 67 (4) (2023) 987–996. doi:10.1007/s40194-023-01503-9.

[138] W. Li, K. Sugio, X. Liu, M. Yamamoto, Y. Guo, S. Zhu, G. Sasaki, Microstructure evolution and mechanical properties of 308L stainless steel coatings fabricated by laser hot wire cladding, Materials Science and Engineering: A 824 (2021) 141825. doi:10.1016/j.msea.2021.141825.

[139] K. Li, D. Li, D. Liu, G. Pei, L. Sun, Microstructure evolution and mechanical properties of multiple-layer laser cladding coating of 308L stainless steel, Applied Surface Science 340 (2015) 143–150. doi:10.1016/j.apsusc.2015.02.171.

[140] W. E. Luecke, J. A. Slotwinski, Mechanical Properties of Austenitic Stainless Steel Made by Additive Manufacturing, Journal of Research of the National Institute of Standards and Technology 119 (2014) 398–418. doi:10.6028/jres.119.015.

[141] C. Wang, P. Zhu, Y. H. Lu, T. Shoji, Effect of heat treatment temperature on microstructure and tensile properties of austenitic stainless 316L using wire and arc additive manufacturing, Materials Science and Engineering: A 832 (2022) 142446. doi:10.1016/j.msea.2021.142446.

[142] R. F. V. Sampaio, J. P. M. Pragana, I. M. F. Bragança, C. M. A. Silva, C. V. Nielsen, P. A. F. Martins, Modelling of wire-arc additive manufacturing – A review, Advances in Industrial and Manufacturing Engineering 6 (2023) 100121. doi:https://doi.org/10.1016/j.aime.2023.100121.

[143] C. Cambon, Étude thermomécanique du procédé de fabrication métallique arc-fil : approche numérique et expérimentale, Ph.D. thesis, Université de Montpellier (May 2021).

[144] S. Hilal, Thermo-mechanical modelling of the Wire Arc Additive Manufacturing process (WAAM), Ph.D. thesis, Université Paris sciences et lettres (May 2022).

[145] A. Chergui, N. Beraud, F. Vignat, F. Villeneuve, Finite Element Modeling and Validation of Metal Deposition in Wire Arc Additive Manufacturing, in: L. Roucoules, M. Paredes, B. Eynard, P. Morer Camo, C. Rizzi (Eds.), Advances on Mechanics, Design Engineering and Manufacturing III, Lecture Notes in Mechanical Engineering, Springer International Publishing, Cham, 2021, pp. 61–66. doi:10.1007/978-3-030-70566-4_11.

[146] L. Depradeux, J.-F. Jullien, Experimental and numerical simulation of thermomechanical phenomena during a TIG welding process, Journal de Physique IV (Proceedings) 120 (2004) 697–704. doi:10.1051/jp4:2004120080.

[147] J. Goldak, A. Chakravarti, M. Bibby, A new finite element model for welding heat sources, Metallurgical Transactions B 15 (2) (1984) 299–305. doi:10.1007/BF02667333.

[148] O. Muránsky, C. J. Hamelin, M. C. Smith, P. J. Bendeich, L. Edwards, The effect of plasticity theory on predicted residual stress fields in numerical weld analyses, Computational Materials Science 54 (2012) 125–134. doi:10.1016/j.commatsci.2011.10.026.

[149] J. L. Chaboche, A review of some plasticity and viscoplasticity constitutive theories, International Journal of Plasticity 24 (10) (2008) 1642–1693. doi:10.1016/j.ijplas.2008.03.009.

[150] K. P. Prajadhiama, Y. H. Manurung, Z. Minggu, F. H. Pengadau, M. Graf, A. Haelsig, T.-E. Adams, H. L. Choo, Development of Bead Modelling for Distortion Analysis Induced by Wire Arc Additive Manufacturing using FEM and Experiment, MATEC Web of Conferences 269 (2019) 05003. doi:10.1051/matecconf/201926905003.

[151] S. Pascal, S. Gounand, Modélisation thermomécanique d'un cas d'étude de fabrication additive arc-fil, in: 15ème colloque national en calcul des structures, Université Polytechnique Hauts-de-France [UPHF], 83400 Hyères-les-Palmiers, France, 2022.

[152] A. Kiran, J. Hodek, J. Vavrik, M. Urbanek, J. Dzugan, Numerical Simulation Development and Computational Optimization for Directed Energy Deposition Additive Manufacturing Process, Materials 13 (11) (2020) 2666. doi:10.3390/ma13112666.

[153] M. S. Mohebbi, M. Kühl, V. Ploshikhin, A thermo-capillary-gravity model for geometrical analysis of single-bead wire and arc additive manufacturing (WAAM), The International Journal of Advanced Manufacturing Technology 109 (3) (2020) 877–891. doi:10.1007/s00170-020-05647-6.

[154] N. P. Gokhale, P. Kala, Thermal analysis of TIG-WAAM based metal deposition process using finite element method, Materials Today: Proceedings 44 (2021) 453–459. doi:10.1016/j.matpr.2020.09.756.

[155] Y. Lee, Y. Bandari, P. Nandwana, B. T. Gibson, B. Richardson, S. Simunovic, Effect of Interlayer Cooling Time, Constraint and Tool Path Strategy on Deformation of Large Components Made by Laser Metal Deposition with Wire, Applied Sciences 9 (23) (2019) 5115. doi:10.3390/app9235115.

[156] M. P. Mughal, R. A. Mufti, H. Fawad, The mechanical effects of deposition patterns in welding-based layered manufacturing, Proceedings of the Institution of Mechanical Engineers, Part B: Journal of Engineering Manufacture 221 (10) (2007) 1499–1509. doi:10.1243/09544054JEM783.

[157] M. Biegler, A. Marko, B. Graf, M. Rethmeier, Finite element analysis of in-situ distortion and bulging for an arbitrarily curved additive manufacturing directed energy deposition geometry, Additive Manufacturing 24 (2018) 264–272. doi:10.1016/j.addma.2018.10.006.

[158] C. Cambon, S. Rouquette, I. Bendaoud, C. Bordreuil, R. Wimpory, F. Soulie, Thermo-mechanical simulation of overlaid layers made with wire + arc additive manufacturing and GMAW-cold metal transfer, Welding in the World 64 (8) (2020) 1427–1435. doi:10.1007/s40194-020-00951-x.

[159] W. Huang, Q. Wang, N. Ma, H. Kitano, Distribution characteristics of residual stresses in typical wall and pipe components built by wire arc additive manufacturing, Journal of Manufacturing Processes 82 (2022) 434–447. doi:10.1016/j.jmapro.2022.08.010.

[160] X. Wang, A. Wang, Finite element analysis of clamping form in wire and arc additive manufacturing, in: 2017 7th International Conference on Modeling, Simulation, and Applied Optimization (ICMSAO), 2017, pp. 1–5. doi:10.1109/ICMSAO.2017.7934926.

[161] M. Brochard, Modèle couplé cathode-plasma-pièce en vue de la simulation du procédé de soudage à l'arc TIG, Ph.D. thesis, Université Aix-Marseille (2009).

[162] W. Ou, G. L. Knapp, T. Mukherjee, Y. Wei, T. DebRoy, An improved heat transfer and fluid flow model of wire-arc additive manufacturing, International Journal of Heat and Mass Transfer 167 (2021) 120835. doi:10.1016/j.ijheatmasstransfer.2020.120835.

[163] S. Cadiou, M. Courtois, M. Carin, W. Berckmans, P. Le masson, 3D heat transfer, fluid flow and electromagnetic model for cold metal transfer wire arc additive manufacturing (Cmt-Waam), Additive Manufacturing 36 (2020) 101541. doi:10.1016/j.addma.2020.101541.

[164] A. Herbeaux, H. Aboleinein, A. Villani, C. Maurice, J.-M. Bergheau, H. Klöcker, Combining Phase Field Modeling and Deep Learning for Accurate Modeling of Grain Structure in Solidification, Additive Manufacturing (2024) 103994doi:10.1016/j.addma.2024.103994.

[165] H. Rosso, Assessment of the feasibility of a complex part using the WLAM process, Tech. rep., CEA Paris-Saclay (Sep. 2024).

[166] C. A. Terrazas-Nájera, A. Fernández, R. Felice, R. Wicker, On the thermal emissive behavior of four common alloys processed via powder bed fusion additive manufacturing, Additive Manufacturing 82 (2024) 104023. doi:https://doi.org/10.1016/j.addma.2024.104023.

[167] P. Pichler, B. J. Simonds, J. W. Sowards, G. Pottlacher, Measurements of thermophysical properties of solid and liquid NIST SRM 316L stainless steel, Journal of Materials Science 55 (9) (2020) 4081–4093. doi:10.1007/s10853-019-04261-6.

[168] M. Balat-Pichelin, J. L. Sans, E. Bêche, Spectral directional and total hemispherical emissivity of virgin and oxidized 316L stainless steel from 1000 to 1650 K, Infrared Physics and Technology 123 (2022) 104156. doi:10.1016/j.infrared.2022.104156.

[169] P. Barnett, P. Gentry, J. Jackson, D. Tong, Emissivity measurements of liquid sodium and some sodium contaminated steel surfaces (1986).

[170] H. Kraus, Experimental Measurement of Stationary SS 304, SS 316 L and 8630 GTA Weld Pool Surface Temperatures, Weld. J. 68 (7) (1989) 269.

[171] T. Fu, P. Tan, M. Zhong, Experimental research on the influence of surface conditions on the total hemispherical emissivity of iron-based alloys, Experimental Thermal and Fluid Science 40 (2012) 159–167. doi:10.1016/j.expthermflusci.2012.03.001.

[172] Norme NF EN 10088-1, https://www.boutique.afnor.org/fr-fr/norme/nf-en-100881/aciers-inoxydables-partie-1-liste-des-aciers-inoxydables/fa173619/44456.

[173] J. H. Park, Y. Kang, Youngjo Kang, Inclusions in Stainless Steels - A Review, Steel Research International 88 (12) (2017) 1700130. doi:10.1002/srin.201700130.

[174] J. H. Park, H. Todoroki, Control of MgO·Al2O3 Spinel Inclusions in Stainless Steels, Isij International 50 (10) (2010) 1333–1346. doi:10.2355/isijinternational.50.1333.

[175] G. Li, J. S. Li, S. F. Yang, Y. J. Wang, N. S. Li, Study on the Cleanliness of 316L Stainless Steel, Advanced Materials Research 311-313 (2011) 881–885. doi:10.4028/www.scientific.net/AMR.311-313.881.

[176] X. Yin, Y. H. Sun, Y. D. Yang, X. F. Bai, X. X. Deng, M. Barati, A. McLean, Inclusion evolution during refining and continuous casting of 316L stainless steel, Ironmaking & Steelmaking 43 (7) (2016) 533–540. doi:10.1080/03019233.2015.1125599.

[177] L. Sun, F. Jiang, R. Huang, D. Yuan, Y. Su, C. Guo, J. Wang, Investigation on the process window with liner energy density for single-layer parts fabricated by wire and arc additive manufacturing, Journal of Manufacturing Processes 56 (2020) 898–907. doi:10.1016/j.jmapro.2020.05.054.

[178] S. Ji, F. Liu, T. Shi, G. Fu, S. Shi, Effects of Defocus Distance on Three-Beam Laser Internal Coaxial Wire Cladding, Chinese Journal of Mechanical Engineering 34 (1) (2021) 45. doi:10.1186/s10033-021-00560-9.

[179] B. Ateba, Influence du temps de refroidissement sur les caractéristiques de pièces en acier 316L obtenues par fabrication additive laser-fil (WLAM), Tech. rep., CEA Paris-Saclay (Sep. 2023).

[180] P. Deng, M. Karadge, R. B. Rebak, V. K. Gupta, B. C. Prorok, X. Lou, The origin and formation of oxygen inclusions in austenitic stainless steels manufactured by laser powder bed fusion, Additive Manufacturing 35 (2020) 101334. doi:10.1016/j.addma.2020.101334.

[181] G. Murry, Transformations dans les aciers, Techniques de l'ingénieur (1998). doi:10.51257/a-v2-m1115.

[182] H. Dong, Analysis of Grain Selection during Directional Solidification of Gas Turbine Blades., in: World Congress on Engineering, 2007, pp. 1257–1262.

[183] K. Andrews, The calculation of transformation temperatures and austenite-ferrite equilibria in steels, Journal of Iron and Steel Institute 184 (12) (1956) 414–427.

[184] D. R. H. Jones, M. F. Ashby, Engineering Materials 2: An Introduction to Microstructures and Processing, Butterworth-Heinemann, 2012.

[185] J. W. Elmer, S. M. Allen, T. W. Eagar, Microstructural development during solidification of stainless steel alloys, Metallurgical Transactions A 20 (10) (1989) 2117–2131. doi:10.1007/BF02650298.

[186] J. Chen, H. Wei, X. Zhang, Y. Peng, J. Kong, K. Wang, Flow behavior and microstructure evolution during dynamic deformation of 316 L stainless steel fabricated by wire and arc additive manufacturing, Materials & Design 198 (2021) 109325. doi:10.1016/j.matdes.2020.109325.

[187] M. Pan, J. Xu, N. Liang, Y. Peng, Q. Zhou, K. Wang, Microstructure and mechanical properties of the laminated heterostructured material with 316L stainless steel/18Ni300 maraging steel fabricated by WAAM, Materials Science and Engineering: A 881 (2023) 145300. doi:10.1016/j.msea.2023.145300.

[188] E. de Sonis, S. Dépinoy, P.-F. Giroux, H. Maskrot, P. Wident, O. Hercher, F. Villaret, A.-F. Gourgues-Lorenzon, Microstructure – Toughness relationships in 316L stainless steel produced by laser powder bed fusion, Materials Science and Engineering: A 877 (2023) 145179. doi:10.1016/j.msea.2023.145179.

[189] H. Inoue, T. Koseki, S. Ohkita, M. Fuji, Formation mechanism of vermicular and lacy ferrite in austenitic stainless steel weld metals, Science and Technology of Welding and Joining 5 (6) (2000) 385–396. doi:10.1179/136217100101538452.

[190] W. Zhai, Naien Wu, W. Zhou, Effect of Interpass Temperature on Wire Arc Additive Manufacturing Using High-Strength Metal-Cored Wire, Metals 12 (2) (2022) 212–212. doi:10.3390/met12020212.

[191] H. Inoue, T. Koseki, Solidification mechanism of austenitic stainless steels solidified with primary ferrite, Acta Materialia 124 (2017) 430–436. doi:10.1016/j.actamat.2016.11.030.

[192] E. de Sonis, S. Dépinoy, P.-F. Giroux, H. Maskrot, L. Lemarquis, O. Hercher, F. Villaret, A.-F. Gourgues-Lorenzon, Dependency of recrystallization kinetics on the solidification microstructure of 316L stainless steel processed by laser powder bed fusion (LPBF), Materials Characterization 194 (2022) 112370. doi:10.1016/j.matchar.2022.112370.

[193] J. Suryawanshi, K. G. Prashanth, U. Ramamurty, Mechanical behavior of selective laser melted 316L stainless steel, Materials Science and Engineering: A 696 (2017) 113–121. doi:10.1016/j.msea.2017.04.058.

[194] D. Goncalves, Modélisation polycristalline du comportement élasto-viscoplastique des aciers inoxydables austénitiques 316L(N) sur une large gamme de chargements : application à l'étude du comportement cyclique à température élevée, Ph.D. thesis, Sorbonne Université (May 2018).

[195] I. Tolosa, F. Garciandía, F. Zubiri, F. Zapirain, A. Esnaola, Study of mechanical properties of AISI 316 stainless steel processed by "selective laser melting", following different manufacturing strategies, The International Journal of Advanced Manufacturing Technology 51 (5) (2010) 639–647. doi:10.1007/s00170-010-2631-5.

[196] S. Dépinoy, Influence of solidification conditions on chemical heterogeneities and dislocations patterning in additively manufactured 316L stainless steel, Materialia 24 (2022) 101472. doi:10.1016/j.mtla.2022.101472.

[197] T. Ishimoto, S. Wu, Y. Ito, S.-H. Sun, H. Amano, T. Nakano, Crystallographic Orientation Control of 316L Austenitic Stainless Steel via Selective Laser Melting, ISIJ International 60 (8) (2020) 1758–1764. doi:10.2355/isijinternational.ISIJINT-2019-744.

[198] T. P. S. Gill, M. Vijayalaxshmi, J. B. Gnamamoorthy, K. A. Padmanabhan, Transformation of delta-ferrite during the postweld heat treatment of type 316L stainless steel weld metal, Welding Journal 65 (5) (1986) 122s–128s.

[199] Cast3M, http://www-cast3m.cea.fr/.

[200] L. Depradeux, simulation numérique du soudage -acier 316L validation sur cas tests de complexité croissante, Ph.D. thesis, INSA Lyon (2004).

[201] T. Charras, F. Di Paola, La procédure PASAPAS (2011).

[202] K. C. Mills, Recommended Values of Thermophysical Properties for Selected Commercial Alloys, Woodhead Publishing, 2002.

[203] N. Collings, K. Wong, A. Guile, Efficiency of tungsten-inert-gas arcs in very-high-speed welding, Proceedings of the Institution of Electrical Engineers 126 (3) (1979) 276–280. doi:10.1049/piee.1979.0071.

[204] A. P. Tadamalle, Y. P. Reddy, E. Ramjee, V. Reddy, Evaluation of Nd: YAG Laser Welding Efficiencies for 304L Stainless Steel, Procedia Materials Science 6 (2014) 1731–1739. doi:10.1016/j.mspro.2014.07.160.

[205] J. W. Elmer, K. Fisher, G. Gibbs, J. Sengthay, D. Urabe, Post-build thermomechanical processing of wire arc additively manufactured stainless steel for improved mechanical properties and reduction of crystallographic texture, Additive Manufacturing 50 (2022) 102573. doi:10.1016/j.addma.2021.102573.

[206] A. Baumard, D. Ayrault, O. Fandeur, C. Bordreuil, F. Deschaux-Beaume, Numerical prediction of grain structure formation during laser powder bed fusion of 316 L stainless steel, Materials & Design 199 (2021) 109434. doi:10.1016/j.matdes.2020.109434.

[207] P. Colegrove, C. Ikeagu, A. Thistlethwaite, S. Williams, T. Nagy, W. Suder, A. Steuwer, T. Pirling, Welding process impact on residual stress and distortion, Science and Technology of Welding and Joining 14 (8) (2009) 717–725. doi:10.1179/136217109X406938.

[208] A. Elmesalamy, J. A. Francis, L. Li, A comparison of residual stresses in multi pass narrow gap laser welds and gas-tungsten arc welds in AISI 316L stainless steel, International Journal of Pressure Vessels and Piping 113 (2014) 49–59. doi:10.1016/j.ijpvp.2013.11.002.

[209] J. L. Chaboche, Constitutive equations for cyclic plasticity and cyclic viscoplasticity, International Journal of Plasticity 5 (3) (1989) 247–302. doi:10.1016/0749-6419(89)90015-6.

[210] W. Ou, T. Mukherjee, G. L. Knapp, Y. Wei, T. DebRoy, Fusion zone geometries, cooling rates and solidification parameters during wire arc additive manufacturing, International Journal of Heat and Mass Transfer 127 (2018) 1084–1094. doi:10.1016/j.ijheatmasstransfer.2018.08.111.

[211] N. Moslemi, N. Redzuan, N. Ahmad, T. N. Hor, Effect of Current on Characteristic for 316 Stainless Steel Welded Joint Including Microstructure and Mechanical Properties, Procedia CIRP 26 (2015) 560–564. doi:10.1016/j.procir.2015.01.010.

[212] E. L. Hall, C. L. Briant, Chromium depletion in the vicinity of carbides in sensitized austenitic stainless steels, Metallurgical Transactions A 15 (5) (1984) 793–811. doi:10.1007/BF02644554.

[213] Y. H. Kim, D. J. Lee, J. C. Byun, K. H. Jung, J. I. Kim, H. J. Lee, Y. T. Shin, S. H. Kim, H. W. Lee, The effect of sigma phases formation depending on Cr/Ni equivalent ratio in AISI 316L weldments, Materials & Design 32 (1) (2011) 330–336. doi:10.1016/j.matdes.2010.06.044.

[214] V. Kumar, A. Mandal, A. K. Das, S. Kumar, Parametric study and characterization of wire arc additive manufactured steel structures, The International Journal of Advanced Manufacturing Technology 115 (5) (2021) 1723–1733. doi:10.1007/s00170-021-07261-6.

Appendix A

Complements for Chapter 3

A.1 Detailed parameters for single bead manufacturing

Table A.1. Considered parameters and geometry for single bead manufacturing with WAAM and WLAM. Red highlighting corresponds to the parameters leading to an irregular/discontinuous deposition, and green indicates the optimized parameters.

N°	Q_{exp}	s	v_w	E_l	d_{rate}	S	w	h	$\bar{h}$	$\bar{p}$	$\frac{w}{h}$ ratio	Dilution
-	W	mm/min	mm/min	J/mm	g/min	mm^2	mm	mm	mm	mm	-	%
WAAM process												
1	2400	200	2500	720.0	22.6	14.14	8.56	2.20	1.48	0.30	**3.89**	**16.9**
2	2400	200	1875	720.0	17.0	10.60	9.15	1.68	1.14	0.38	5.45	**25.1**
3	2400	200	1250	720.0	11.3	7.07	8.86	1.21	0.85	0.68	7.35	44.4
4	2400	200	3125	720	28.3	17.67	(-)	(-)	(-)	(-)	(-)	(-)
5	2400	200	3750	720	33.9	21.21	(-)	(-)	(-)	(-)	(-)	(-)
6	2400	150	1875	960.0	17.0	14.14	10.26	1.92	1.36	0.55	5.35	**28.7**
7	2400	250	1875	576.0	17.0	8.48	8.68	1.49	1.01	0.43	5.83	**29.7**
8	2400	100	1875	1440.0	17.0	21.21	12.07	2.41	1.78	0.87	5.00	**32.9**
9	2400	300	1875	480.0	17.0	7.07	7.85	1.34	0.94	0.37	5.88	**28.2**
10	1800	200	1875	540.0	17.0	10.60	(-)	(-)	(-)	(-)	(-)	(-)
11	3000	200	1875	900.0	17.0	10.60	11.61	1.39	0.97	0.80	8.38	45.2
12	3600	200	1875	1080.0	17.0	10.60	13.03	1.22	0.84	1.52	10.68	64.3
13	2400	150	3125	960.0	28.3	23.56	9.48	3.23	2.40	0.39	**2.93**	**13.9**
14	2400	150	2500	960.0	22.6	18.85	10.64	2.36	1.74	0.40	4.51	**18.8**
15	1800	150	1875	720.0	17.0	14.14	(-)	(-)	(-)	(-)	(-)	(-)
16	3000	150	1875	1200.0	17.0	14.14	12.51	1.61	1.17	0.93	7.76	44.3
17	3000	250	1875	720.0	17.0	8.48	10.85	1.21	0.85	0.77	9.00	47.7
18	3000	200	3125	900.0	28.3	17.67	10.84	2.15	1.58	0.52	5.05	**24.7**
19	2400	150	1250	960.0	11.3	9.42	10.28	1.47	1.03	0.74	7.00	42.0
20	3000	200	2500	900.0	22.6	14.14	10.71	1.84	1.34	0.57	5.81	**30.0**
21	2400	250	2500	576.0	22.6	11.31	(-)	(-)	(-)	(-)	(-)	(-)
22	1800	100	1875	1080.0	17.0	21.21	(-)	(-)	(-)	(-)	(-)	(-)
23	3000	200	3750	900.0	33.9	21.21	10.39	2.67	1.98	0.46	**3.89**	**18.8**
24	3600	200	3750	1080.0	33.9	21.21	13.38	2.19	1.62	0.84	6.12	**34.1**
WLAM process												
1	1000	500	700	120.0	6.3	1.58	2.88	0.74	0.52	0.02	**3.87**	3.5
2	1000	700	900	85.7	8.1	1.45	2.74	0.69	0.48	0.02	**3.97**	3.4
3	1000	300	500	200.0	4.5	1.88	3.07	0.84	0.57	0.08	**3.66**	**12.8**
4	1000	700	500	85.7	4.5	0.81	2.86	0.40	0.27	0.03	7.19	9.1
5	1000	300	900	200.0	8.1	3.39	3.08	1.39	0.97	0.02	**2.22**	1.7
6	2400	1400	1000	102.9	9.0	0.81	3.27	0.34	0.25	0.29	9.53	54.4
7	2400	1600	1200	90.0	10.9	0.85	3.22	0.40	0.26	0.25	8.06	49.2
8	2400	1200	800	120.0	7.2	0.75	3.42	0.39	0.27	0.33	8.71	55.4
9	2400	1600	800	90.0	7.2	0.57	3.28	0.31	0.21	0.26	**10.44**	56.0
10	2400	1200	1200	120.0	10.9	1.13	3.36	0.46	0.32	0.30	7.26	48.3

11	2400	1000	1400	144.0	12.7	1.58	3.35	0.67	0.45	0.33	4.98	42.2
12	2400	1200	1600	120.0	14.5	1.51	3.42	0.64	0.43	0.26	5.36	38.3
13	2400	800	1200	180.0	10.9	1.70	3.26	0.72	0.48	0.41	4.55	46.2
14	2400	800	1600	180.0	14.5	2.26	3.74	0.92	0.57	0.33	4.06	36.2
15	1000	700	1100	85.7	9.9	1.78	2.84	0.68	0.45	0.01	4.20	1.2
16	1000	100	500	600.0	4.5	5.65	(-)	(-)	(-)	(-)	(-)	(-)
17	2400	1400	1800	102.9	16.3	1.45	(-)	(-)	(-)	(-)	(-)	(-)
18	2400	1400	2200	102.9	19.9	1.78	3.27	0.67	0.43	0.20	4.90	**31.4**
19	2400	1200	2400	120.0	21.7	2.26	3.34	0.84	0.53	0.26	**4.00**	**32.7**
20	2400	1200	2000	120.0	18.1	1.88	3.30	0.84	0.54	0.27	**3.91**	**33.4**
21	2400	1000	1800	144.0	16.3	2.04	3.37	0.93	0.59	0.32	**3.64**	**35.4**
22	2400	1000	2200	144.0	19.9	2.49	3.27	0.98	0.66	0.36	**3.33**	**35.1**
23	2400	800	2000	180.0	18.1	2.83	3.30	1.19	0.81	0.30	**2.78**	**26.9**
24	2400	800	2400	180.0	21.7	3.39	3.16	1.41	0.99	0.32	**2.23**	**24.3**
25	2400	600	2200	240.0	19.9	4.15	3.42	1.63	1.17	0.40	**2.11**	**25.5**
26	2400	600	1800	240.0	16.3	3.39	3.62	1.31	0.92	0.42	**2.78**	**31.2**
27	2400	400	1600	360.0	14.5	4.52	3.63	1.62	1.23	0.65	**2.24**	**34.4**
28	2400	400	2000	360.0	18.1	5.65	3.35	2.02	1.61	0.57	1.66	**26.0**
29	3500	1600	3000	131.3	27.1	2.12	3.22	0.86	0.59	0.38	**3.74**	39.6
30	3500	1400	2800	150.0	25.3	2.26	3.36	0.95	0.62	0.44	**3.53**	41.5
31	3500	1400	3200	150.0	28.9	2.59	3.31	0.98	0.64	0.45	**3.38**	41.1
32	3500	1200	3000	175.0	27.1	2.83	3.23	1.16	0.81	0.46	**2.80**	36.5
33	3500	1200	3400	175.0	30.7	3.20	3.33	1.13	0.79	0.51	**2.94**	39.2
34	3500	1200	2600	175.0	23.5	2.45	3.35	1.10	0.75	0.39	**3.05**	**34.2**
35	3500	1000	2800	210.0	25.3	3.17	3.47	1.24	0.88	0.47	**2.79**	**34.8**
36	3500	1000	3200	210.0	28.9	3.62	3.34	1.42	1.00	0.46	**2.36**	**31.5**
37	3500	800	2600	262.5	23.5	3.68	3.85	1.44	1.05	0.52	**2.67**	**33.0**
38	3500	800	3400	262.5	30.7	4.81	3.54	1.62	1.16	0.54	**2.19**	**31.5**
39	3500	800	3000	262.5	27.1	4.24	3.53	1.55	1.16	0.51	**2.27**	**30.6**
40	3500	600	2800	350.0	25.3	5.28	3.91	1.81	1.33	0.67	**2.16**	**33.4**

A.2 Interpolation setup using ANOVA

An interpolation was developed using Python (Statsmodels module) to approximate a relationship between the geometrical features of the manufactured single beads, the process parameters (Q_{exp}, s, and v_w), the applied linear energy E_l, and the surface of the cross-section above the substrate S, as expressed in Equation A.1 where a_0 to a_5 are the coefficients to calibrate. The interpolation allows for the estimation of geometrical ratios (width/height and dilution) for a given set of parameters.

$$param = a_0 + a_1.\frac{Q_{exp}}{s} + a_2.\frac{v_w}{s} + a_3.s + a_4.v_w + a_5.Q_{exp} \tag{A.1}$$

This equation only considers physical terms, giving it some physical meaning, unlike conventional quadratic interpolations [214], though at the expense of interpolation precision. To later assess its validity, two sets of parameters were not taken into account to create the interpolation:

WAAM – 7. $s = 250$ mm/min; $v_w = 1875$ mm/min; $Q_{exp} = 2400$ W and
WLAM – 11. $s = 1000$ mm/min; $v_w = 1400$ mm/min; $Q_{exp} = 2400$ W.

These sets of parameters will be used as reference points to compare the predicted geometrical ratios from the interpolation and the experimentally measured values.

An analysis of variance (ANOVA) was conducted on the geometrical features to enhance the accuracy of the interpolation. This ANOVA analysis aimed to assess the contribution of each term in the interpolation and identify non-significant terms, which could then be excluded from the model. Furthermore, the ANOVA was designed to ensure that the order of terms in the equation does not impact the coefficients a_0 to a_5. To achieve this, the relative contribution of each term was calculated using a calibrated equation that accounts for all the other terms rather than sequentially adding terms as done previously. This approach is based on the methodologies outlined by Mohammed *et al.* [66], who conducted a similar study on the influence of process parameters on the geometrical features of cobalt-based alloy single beads manufactured by WLAM, and Kumar *et al.* [214], who investigated the effect of process parameters in WAAM manufacturing for 304L stainless steel. Several statistical parameters were then employed to perform the ANOVA and assess the significance of each term:

- The "sequential sum of squares" for each parameter is computed. This value corresponds to the correction due to the introduction of a given parameter in the residual error of the model, which is expressed as $\sum_{i=0}^{n}(y_i - \hat{y}_i)^2$, where y_i is the experimental value and $\hat{y}_i$ is the estimated value using the model in its current state.
- The "degrees of freedom" represent the amount of independent variables available for estimating each parameter. In our case, each process parameter contributes to 1 degree of freedom, such that the model has five degrees of freedom, corresponding to the five terms in the interpolation. The residual degrees of freedom, which reflect the remaining independent information after fitting the model, are calculated as the difference between the total number of experimental data points (38 for WLAM and 17 for WAAM) and the total number of model parameters (five process parameters plus the geometrical feature, totaling six). Thus, the residual degrees of freedom are 31 for WLAM and 11 for WAAM.
- The F-value is an indicator of the statistical meaning of each parameter. Its value is obtained by dividing the "mean squares" (*i.e.* the ratio between the sum of squares and the degrees of freedom) of the introduced parameter and the residual associated with this parameter introduction in the model. For instance, we can check that the F value of the last parameter is equal to the ratio

between the mean squares of $s \cdot v_w$ and the mean squares of the residual of the model.

- The p-value is the probability of finding a similar F-value if the parameter does not influence the model fit. According to Mohammed *et al.* [66], the parameter is significant if the p-value is lower than $5 \cdot 10^{-2}$ and not significant if it is higher than $1 \cdot 10^{-2}$. Some parameters might simultaneously be significant and non-significant and can be kept in the model fit.
- Finally, the relative contribution of each term in the equation is obtained by dividing the sum of squares of each term by the total sum of squares of the model. This value is linked to the p-value, as a term with a high p-value will have a low contribution to the equation.

Each of these statistical terms was then computed using the ANOVA to assess the contribution of each term to the width/height ratio for the WAAM (Table A.2) and WLAM (Table A.4) processes, and the dilution ratio (Tables A.3 and A.5 for WAAM and WLAM, respectively). The non-significant terms are highlighted in red, while the most significant ones are in blue. Finally, Equations A.2, A.3, A.4 and A.5 correspond to the estimated width/height and dilution ratios for single beads produced via WAAM and WLAM processes, respectively, depending on the process parameters. These equations estimate the expected geometrical features for single beads manufactured with a given set of parameters within the experimental range.

For the WAAM process, the ANOVA indicated that the interpolation of the width/height ratio and the dilution ratio is mainly governed by both E_l and S, which is consistent with the experimental observations showing that the applied linear energy mainly affects the width of the bead. At the same time, the cross-sectional section above the substrate influences its height.

For the WLAM process, it indicated that S and v_w contributed the most to interpolating the width/height ratio. Changes in the volume of supplied metal (or the wire feed speed) will lead to a variation in the width/height ratio, as it will mainly modify the height. In addition, the ANOVA indicated that E_l is not significant, which was expected as we mentioned that the diameter of the pool melted by the laser does not significantly change with its applied energy, and so does the width of the beads. Finally, we reported that the deposition speed s is the most influential factor in interpolating the dilution ratio, likely because a lower deposition speed increases the time the laser spends in a given area, enabling it to create a deeper melt pool. In contrast, the width of the melt pool mainly stays unchanged.

Table A.2. ANOVA of the width/height ratio of the beads manufactured using the WAAM process.

Source	Sum of squares	Degrees of freedom	F value	p value $Prob > F$	Contribution (%)
Model	64.0	5	101.1	8.18e-09	-
E_l	27.5	1	217.3	1.37e-08	43
S	40.6	1	320.4	1.75e-09	**63**
s	9.8	1	77.5	2.60e-06	15
Q_{exp}	6.8	1	54.0	1.45e-05	11
v_w	2.9	1	23.3	5.33e-04	5
Residual	1.4	11	-	-	-

Table A.3. ANOVA of the dilution ratio of the beads manufactured using the WAAM process.

Source	Sum of squares	Degrees of freedom	F value	p value $Prob > F$	Contribution (%)
Model	2777.2	5	49.8	3.48e-07	-
E_l	1414.9	1	126.8	2.23e-07	51
S	1849.2	1	165.7	5.63e-08	**67**
s	337.1	1	30.2	1.87e-04	12
Q_{exp}	220.1	1	19.7	9.92e-04	8
v_w	97.7	1	8.8	1.30e-02	4
Residual	122.7	11	-	-	-

$$\left(\frac{w}{h}\right)_{\text{WAAM}} \approx 2.97 \cdot 10^{-1} \cdot S - 5.13 \cdot 10^{-3} \cdot E_l + 6.68 \cdot 10^{-4} \cdot s + 5.81 \cdot 10^{-3} \cdot Q_{exp} - 4.21 \cdot 10^{-3} \cdot v_w + 4.35 \cdot 10^{-2}$$
$$\text{while } s \in [100, 300]\ mm/min,\ v_w \in [1250, 3750]\ mm/min,\ P \in [1800, 3600]\ W \tag{A.2}$$

$$(d)_{\text{WAAM}} \approx 1.35 \cdot S - 1.29 \cdot 10^{-2} \cdot E_l + 1.33 \cdot 10^{-2} \cdot s + 3.30 \cdot 10^{-2} \cdot Q_{exp} - 2.43 \cdot 10^{-2} \cdot v_w - 12.5$$
$$\text{while } s \in [100, 300]\ mm/min,\ v_w \in [1250, 3750]\ mm/min,\ P \in [1800, 3600]\ W \tag{A.3}$$

Table A.4. ANOVA of the width/height ratio of the beads manufactured using the WLAM process. The non-significant terms are highlighted in red, while the most significant ones are in blue.

Source	Sum of squares	Degrees of freedom	F value	p value $Prob > F$	Contribution (%)
Model	159.6	5	59.3	6.03e-15	-
E_l	1.3	1	2.5	**1.26e-01**	1
S	27.7	1	51.5	4.52e-08	**17**
s	8.6	1	16.0	3.63e-04	5
Q_{exp}	3.9	1	7.2	1.15e-02	2
v_w	15.5	1	28.9	7.38e-06	10
Residual	16.7	31	-	-	-

Table A.5. ANOVA of the dilution ratio of the beads manufactured using the WLAM process. The non-significant terms are highlighted in red, while the most significant ones are in blue.

Source	Sum of squares	Degrees of freedom	F value	p value $Prob > F$	Contribution (%)
Model	6434.8	5	43.6	4.07e-13	-
E_l	1642.3	1	55.6	2.12e-08	26
S	1047.7	1	35.5	1.39-06	16
s	5319.6	1	180.1	1.87e-14	**83**
Q_{exp}	184.0	1	6.2	1.81e-02	3
v_w	166.3	1	5.6	2.40e-02	3
Residual	915.6	31	-	-	-

$$\left(\frac{w}{h}\right)_{\text{WLAM}} \approx 1.76 \cdot 10^{-1} \cdot S - 2.90 \cdot 10^{-3} \cdot v_w + 4.27 \cdot 10^{-3} \cdot s + 1.00 \cdot 10^{-3} \cdot Q_{exp} + 2.68$$
$$\text{while } s \in [500, 1600]\ mm/min,\ v_w \in [500, 3400]\ mm/min,\ P \in [1000, 3500]\ W \tag{A.4}$$

$$(d)_{\text{WLAM}} \approx 2.87 \cdot 10^{-2} \cdot s + 1.05 \cdot 10^{-1} \cdot E_l - 1.97 \cdot S + 1.44 \cdot 10^{-2} \cdot Q_{exp} - 1.29 \cdot 10^{-2} \cdot v_w - 20.3$$
$$\text{while } s \in [500, 1600]\ mm/min,\ v_w \in [500, 3400]\ mm/min,\ P \in [1000, 3500]\ W \tag{A.5}$$

Moreover, Figures A.1a and b present a comparison between the experimentally measured values and the predicted values based on Equations A.2 and A.3 for WAAM and A.4 and A.5 for WLAM, for the width/height and the dilution ratios, respectively. The geometrical features of single beads manufactured by WAAM are depicted in red, while the ones of single beads manufactured by WLAM are in blue. The data points somehow align along the $y = x$, indicating a satisfactory fit. The R^2 values of the fit for the WAAM process are 0.98 for the width/height ratio and 0.96 for the dilution ratio, showing the robustness and significance of the interpolations, as these values exceed 0.95. For the WLAM process, lower R^2 were found (0.89 for the width/height ratio and 0.87 for the dilution ratio). However, it was observed that the interpolation resulted in an error of at maximum ±1 for the width/height ratio and ±10% for the dilution ratio, which we assumed to be sufficient to determine the general geometrical features of the single beads to assess for the feasibility of the manufacturing. In practice, we can estimate that a single bead with a predicted width/height ratio above 5 or below 1 or a predicted dilution ratio above 40% is likely to have a geometry outside our selection criteria.

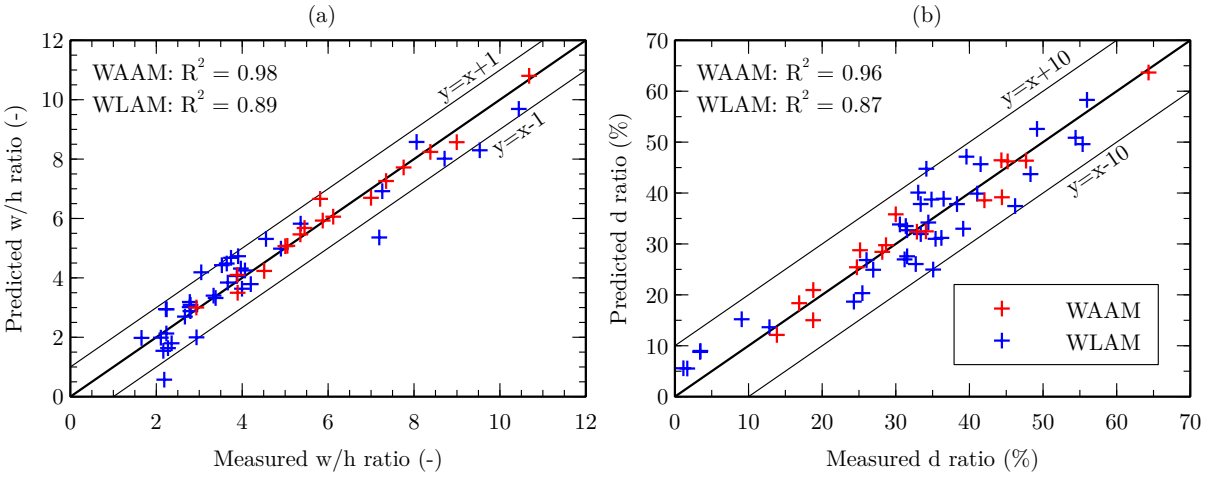

Figure A.1. Comparison between the experimental (a) width/height ratio and (b) dilution ratio and their computed values using the interpolation (Equations A.2, A.3, A.4 and A.5). Red crosses represent the WAAM process conditions, blue crosses the WLAM conditions.

As mentioned earlier, one set of parameters for WAAM ($s = 250$ mm/min; $v_w = 1875$ mm/min; $Q_{exp} = 2400$ W) and one for WLAM ($s = 1000$ mm/min; $v_w = 1400$ mm/min; $Q_{exp} = 2400$ W) were excluded from the interpolation to assess for its robustness. The comparison between the predicted width/height ratio and dilution ratio and the experimental measurements are compared in Table A.6. For the WAAM process, a good coincidence is found between the predicted and the measured ratios (+0 for w/h and +1 for d). The difference is slightly higher for the single bead manufactured by WLAM (-0.6 for w/h and +5 for d). However, we considered that this precision is sufficient to estimate the magnitude ranges of the geometrical features of the manufactured single beads with WAAM and WLAM, demonstrating the good accuracy of the interpolation for values taken inside the experimental amplitude range.

Table A.6. Comparison of the measured and estimated (ANOVA) geometrical ratio for single beads manufactured with WLAM and WAAM.

	$(\frac{w}{h})_{\text{ANOVA}}$	$(\frac{w}{h})_{\text{measured}}$	$(d)_{\text{ANOVA}}$	$(d)_{\text{measured}}$
WAAM	5.8	5.8	28	29
WLAM	5.6	5.0	37	42

A.3 Microstructural defects

The presence of microstructural heterogeneities in the manufactured tiles was investigated. For the block produced by WAAM, an X-ray scan confirmed the absence of porosity within the part. However, numerous pores were detected in the tile manufactured by WLAM, as seen in the transverse section shown in Figure A.2a. These pores appeared between the layers, forming straight lines aligned with the deposited beads. Such interlayer porosity indicates incorrect process calibration and recovering issues, primarily due to insufficient applied volume energy [52].

However, upon examining a micrograph of an etched transverse section of the tile, it was observed that all these pores are not located at the fusion boundaries visible on the micrograph (Figure A.2b). Another hypothesis is that these pores may be attributed to irregularities in the wire unwinding process or the entrapment of fumes from the manufacturing process within the molten pool. Due to time constraints and the focus of the thesis, we have decided not to address this issue. We, however, observed in Figure A.2b that the presence of pores does not seem to affect the shape of the grains, allowing the microstructure to be studied.

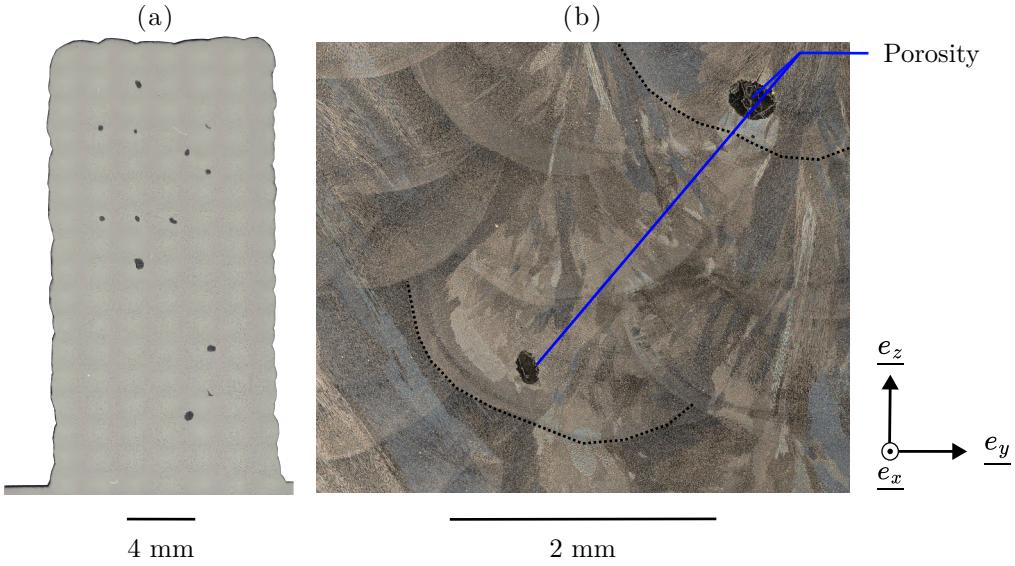

Figure A.2. Pores in a 6 × 20 tile produced with WLAM: (a) transverse cross-section presenting intra- and interlayer porosity; (b) Intralayers pores.

This page was intentionally left blank.

Appendix B

Complements for Chapter 4

B.1 Single beads

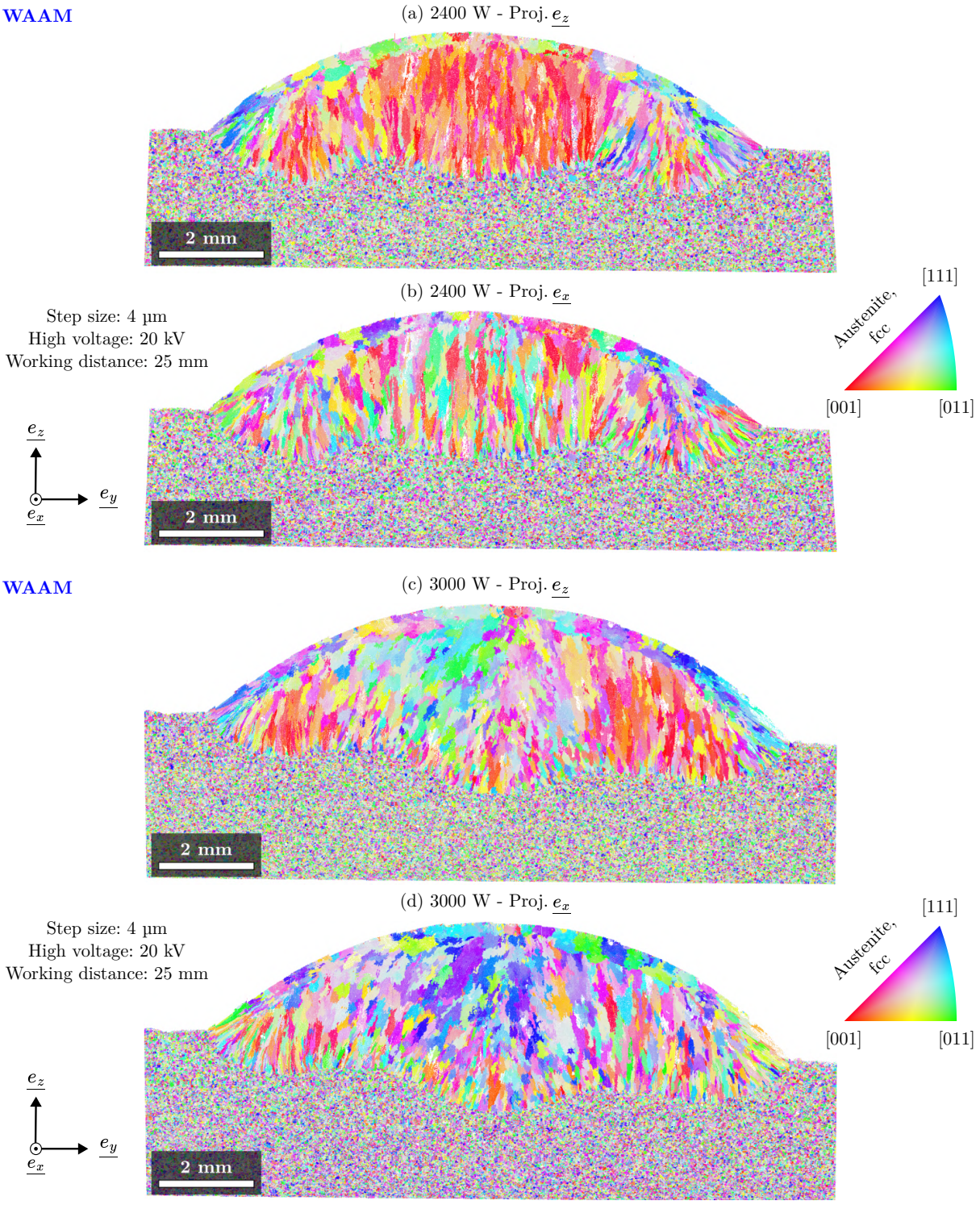

Figure B.1. EBSD orientation maps of transverse cross-sections of single beads manufactured with WAAM using (a) and (b) Set 1 and (c) and (d) Set 3 (Table 3.5). (a) and (c) projection along the manufacturing direction $\underline{e_z}$. (b) and (d) projection along the deposition direction $\underline{e_x}$.

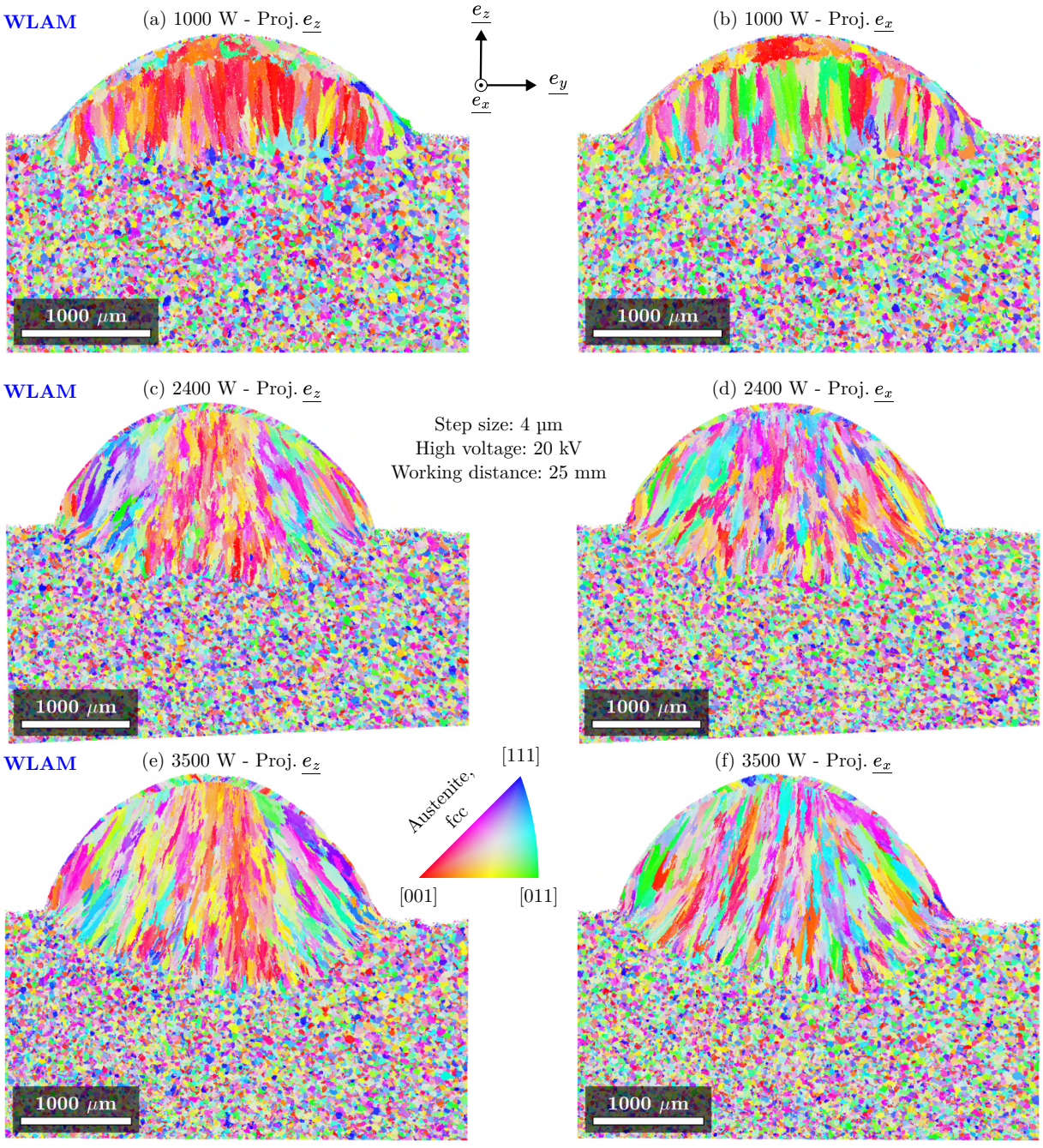

Figure B.2. EBSD orientation maps of transverse cross-sections of single beads manufactured with WLAM using (a) and (b) Set 1, (c) and (d) Set 2 and (e) and (f) Set 3 (Table 3.4). (a), (c) and (e) projection along the manufacturing direction $\underline{e_z}$. (b), (d) and (f) projection along the deposition direction $\underline{e_x}$.

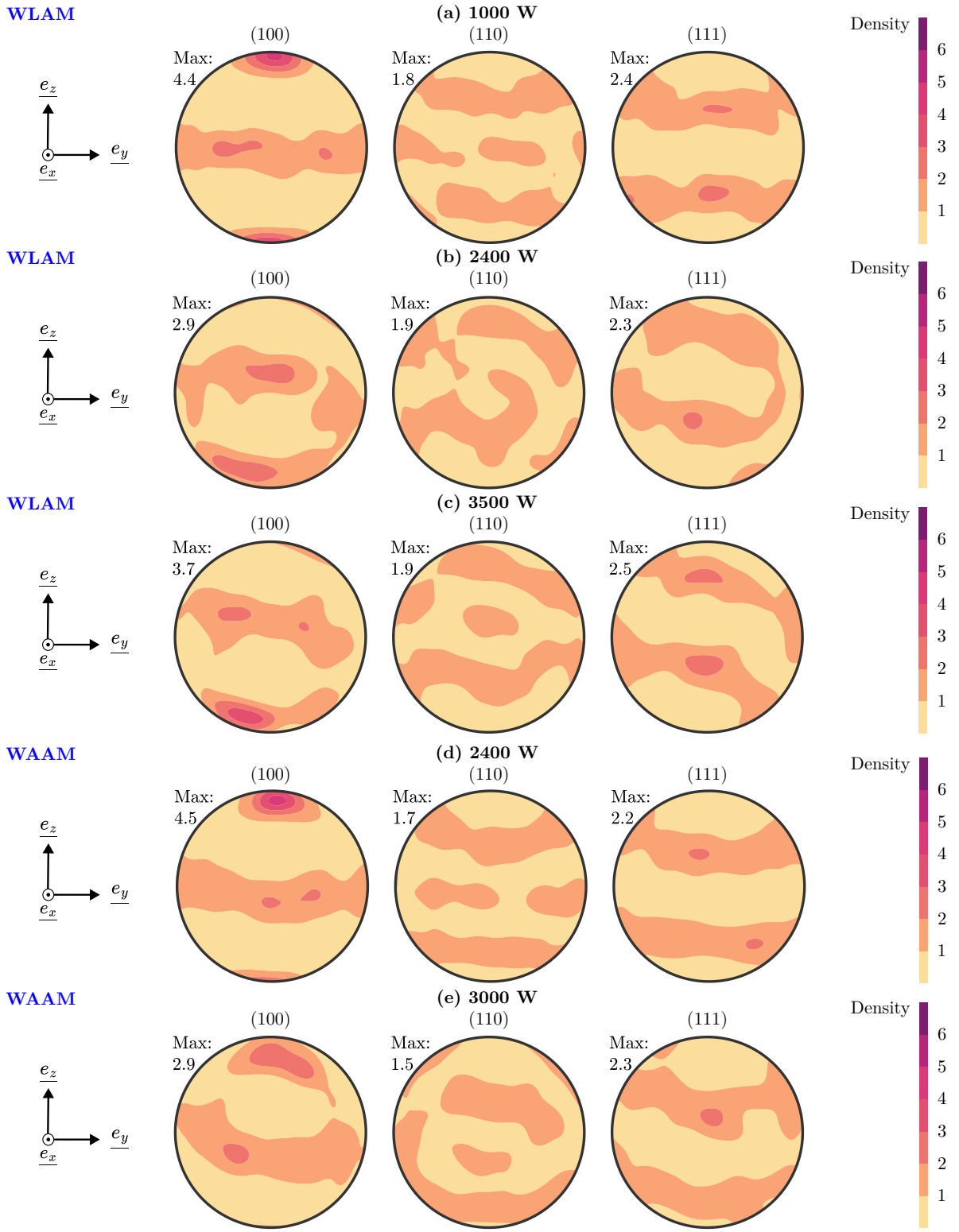

Figure B.3. Pole figures associated with EBSD maps of transverse cross-sections of single beads produced by WLAM using (a) Set 1, (b) Set 2 and (c) Set 3 (Table 3.4) and by WAAM using (a) Set 1 and (b) Set 3 (Table 3.5).

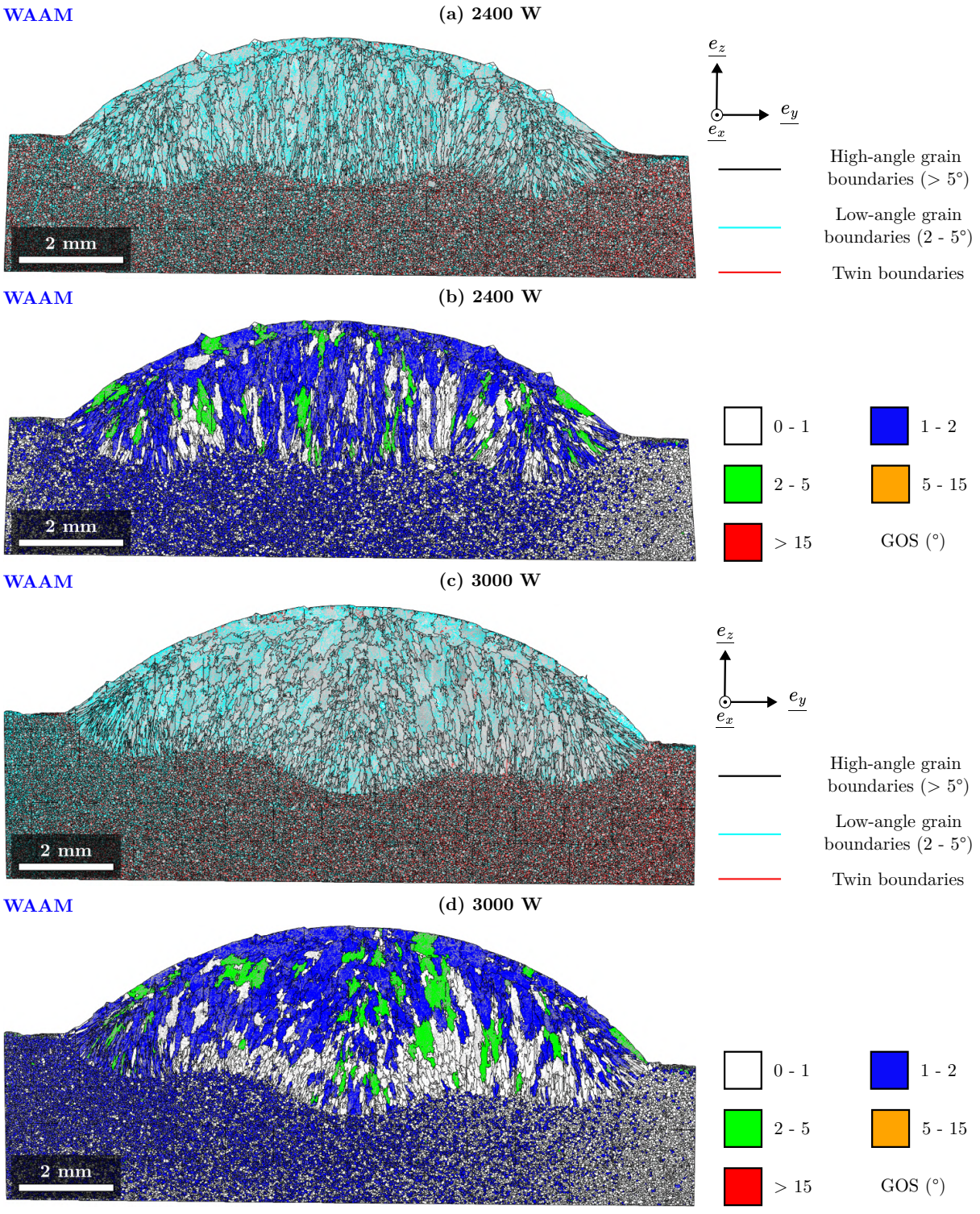

Figure B.4. Grain boundary (GB) and grain orientation spread (GOS) maps from EBSD of transverse cross-sections of single beads manufactured by WAAM using (a) and (b) Set 1 and (c) and (d) Set 3 (Table 3.5). In GB maps (a) and (c), high-angle grain boundaries (HAGBs) are depicted in black, low-angle grain boundaries (LAGBs) in cyan and Σ3-twin boundaries in red. In GOS maps (b) and (d), HAGBs are represented by black lines while LAGBs are depicted in grey.

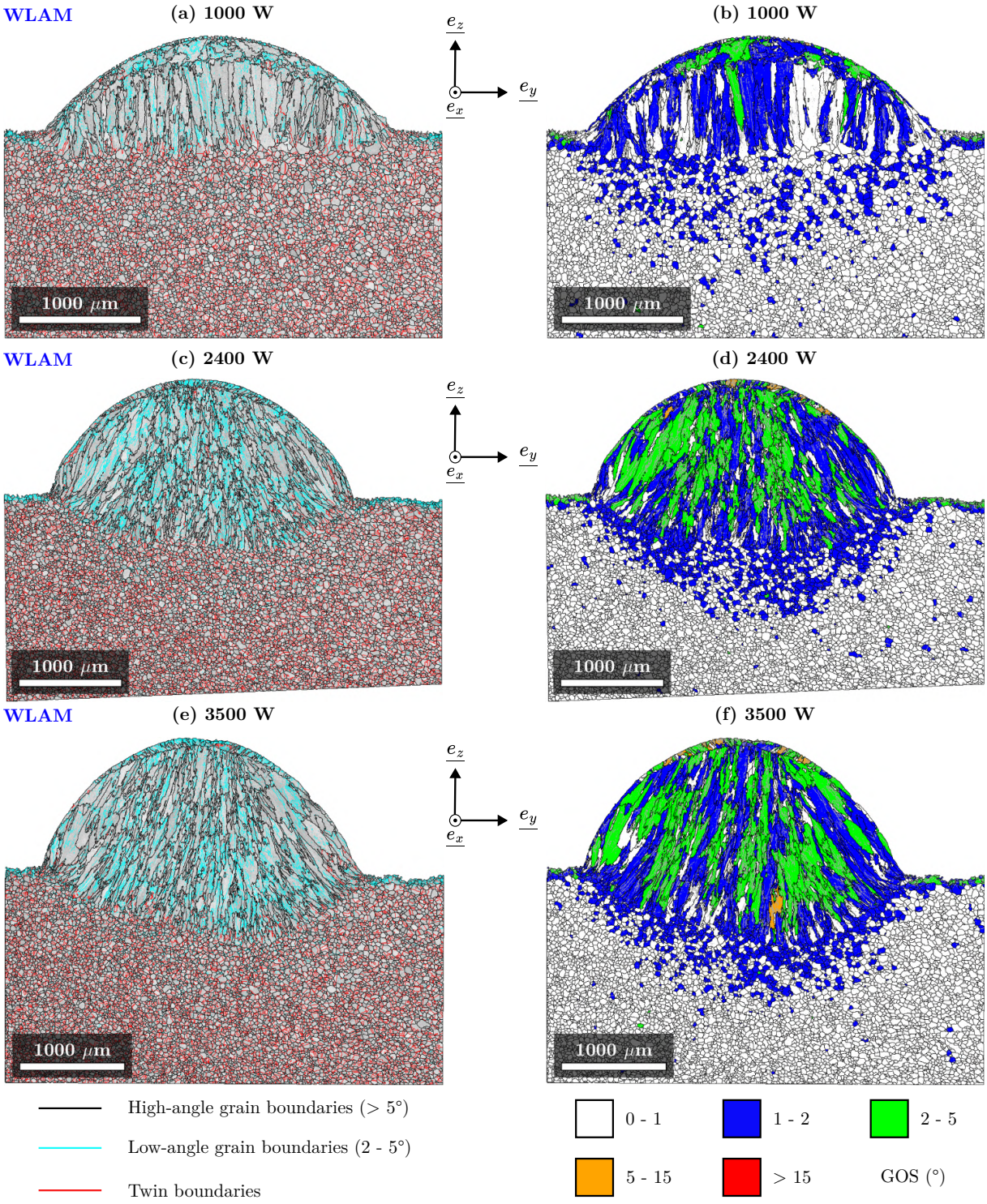

Figure B.5. Grain boundary (GB) and grain orientation spread (GOS) maps from EBSD of transverse cross-sections of single beads manufactured by WLAM using (a) and (b) Set 1, (c) and (d) Set 2 and (e) and (f) Set 3 (Table 3.4). In GB maps (a), (c) and (e), high-angle grain boundaries (HAGBs) are depicted in black, low-angle grain boundaries (LAGBs) in cyan and Σ3-twin boundaries in red. In GOS maps (b), (d) and (f), HAGBs are represented by black lines while LAGBs are depicted in grey.

B.2 Single-bead walls

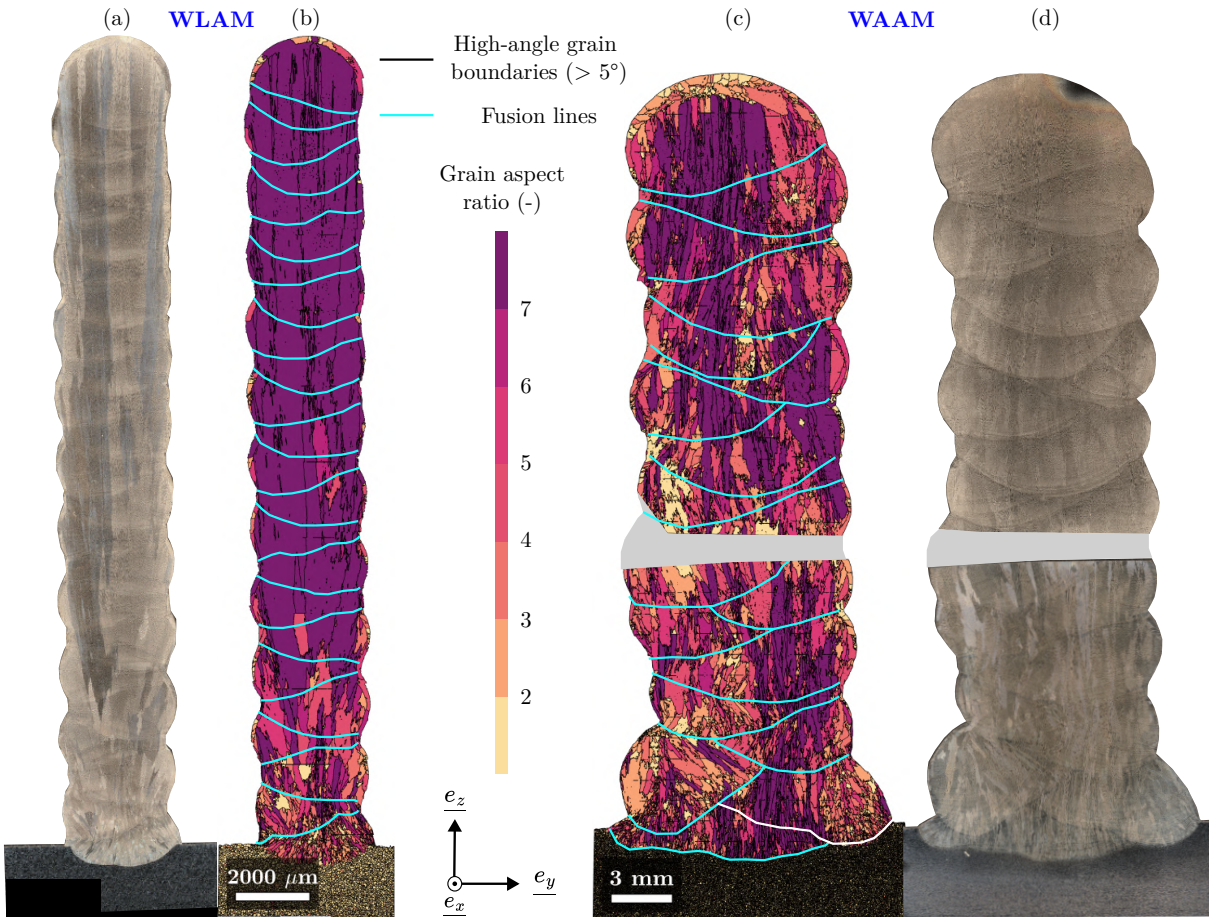

Figure B.6. Transverse cross-sections and grains aspect ratio maps of single-bead walls manufactured by (a) and (b) WLAM using Set 2 (Table 3.4) and (c) and (d) WAAM using Set 3 (Table 3.5). The cross-sections (a) and (d) were polished and chemically etched. The grains on the grain aspect ratio maps (b) and (c) were identified using EBSD. The cyan lines indicate the boundaries of the successive melt pools, determined by visual identification on the transverse cross-sections.

B.3 Tiles

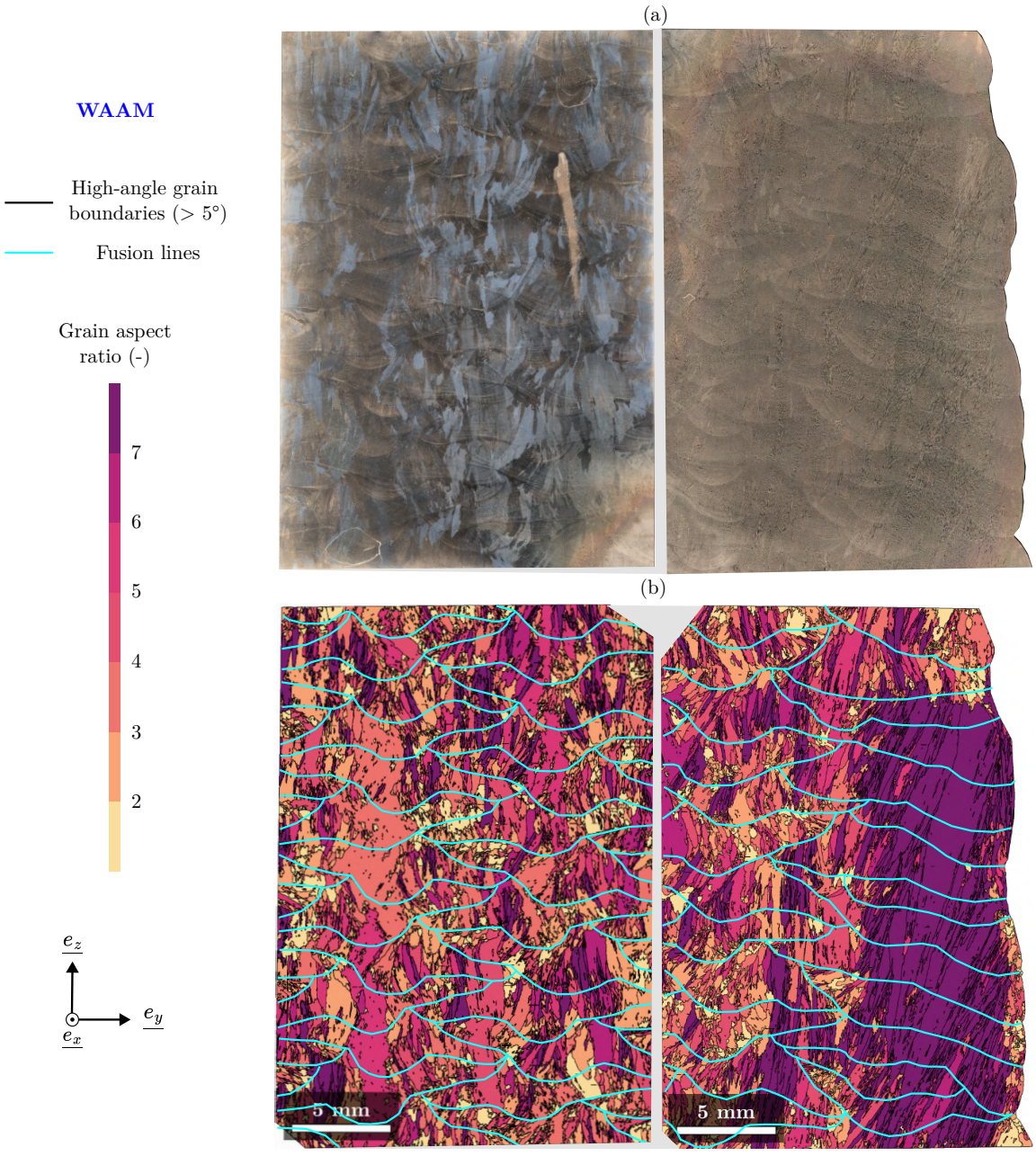

Figure B.7. (a) Transverse cross-section and (b) grain aspect ratio map of the tile manufactured by WAAM. The left part of the map corresponds to the upper middle part of the transverse cross-section of the tile. The right part of the map corresponds to the upper right part of the transverse cross-section of the tile. The cross-section was polished and chemically etched. The grains on the grain aspect ratio map were identified using EBSD. The cyan lines indicate the boundaries of the successive melt pools, determined by visual identification on the transverse cross-section.

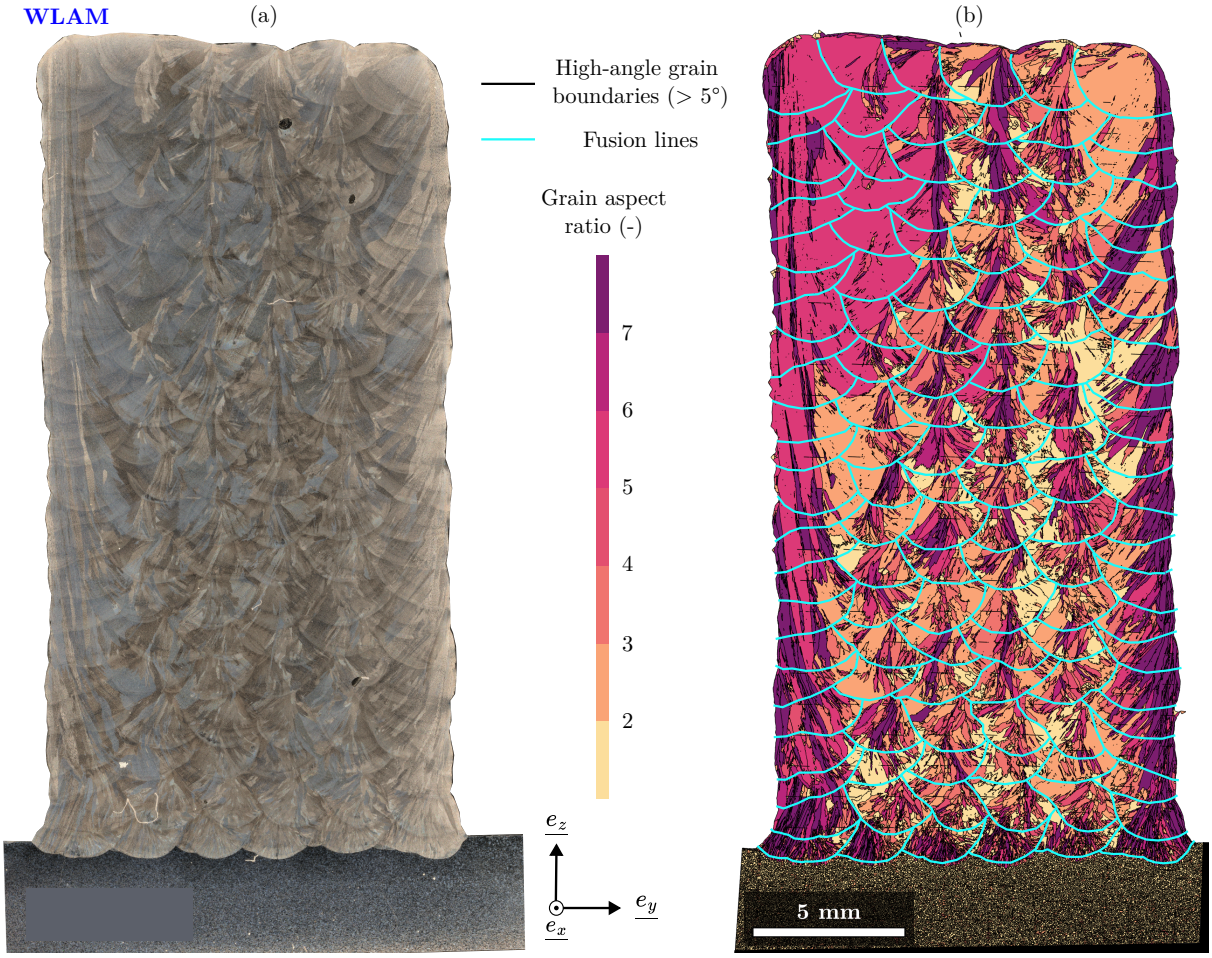

Figure B.8. (a) Transverse cross-section and (b) grain aspect ratio map of the tile manufactured by WLAM. The cross-section was polished and chemically etched. The grains on the grain aspect ratio map were identified using EBSD. The cyan lines indicate the boundaries of the successive melt pools, determined by visual identification on the transverse cross-section.

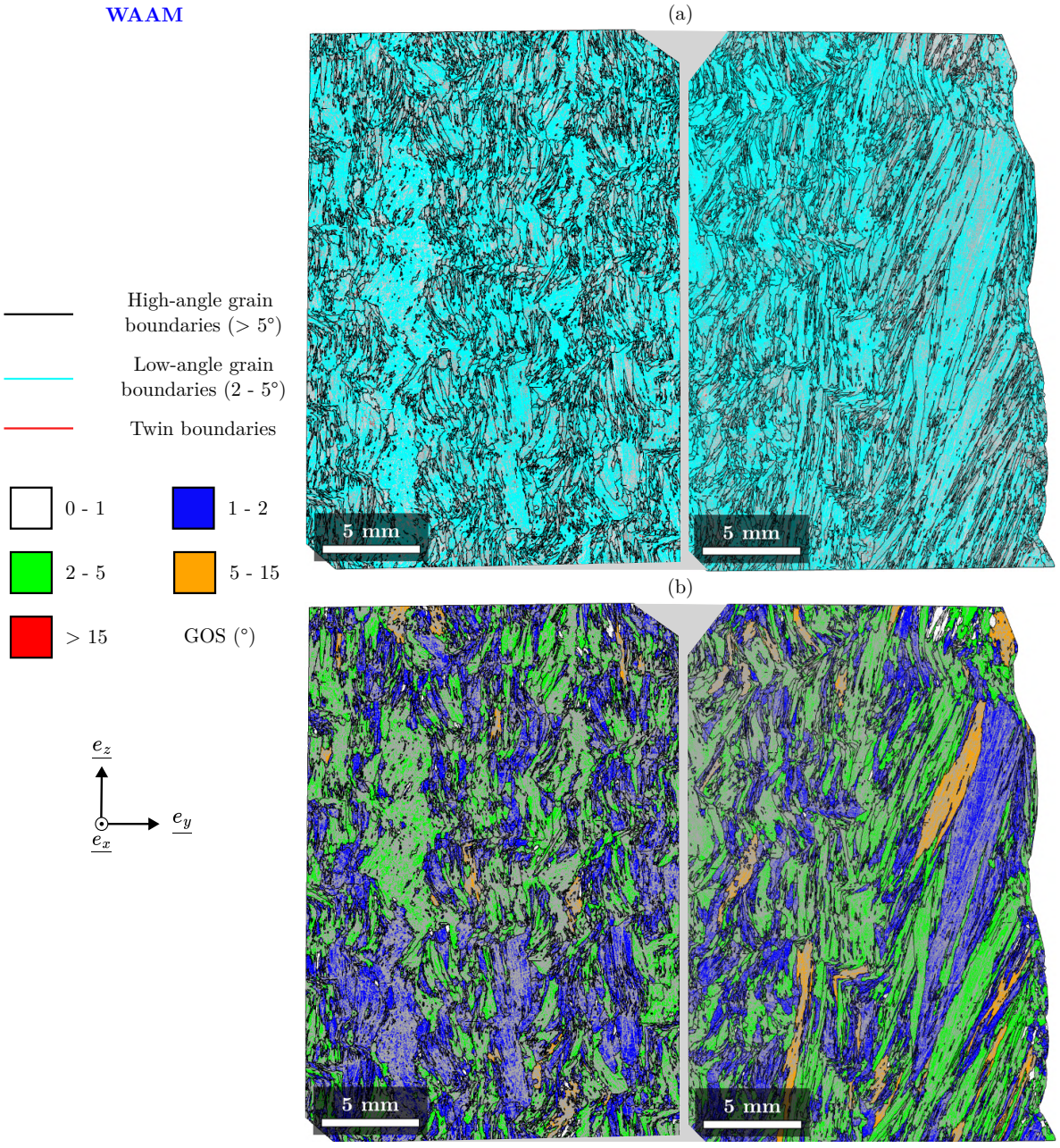

Figure B.9. Grain boundary (GB) and grain orientation spread (GOS) maps from EBSD of the transverse cross-section of the tile manufactured by WAAM. The left part of the map corresponds to the upper middle part of the transverse cross-section of the tile. The right part of the map corresponds to the upper right part of the transverse cross-section of the tile. In GB map (a), high-angle grain boundaries (HAGBs) are depicted in black, low-angle grain boundaries (LAGBs) in cyan and Σ3-twin boundaries in red. In GOS map (b), HAGBs are represented by black lines while LAGBs are depicted in grey.

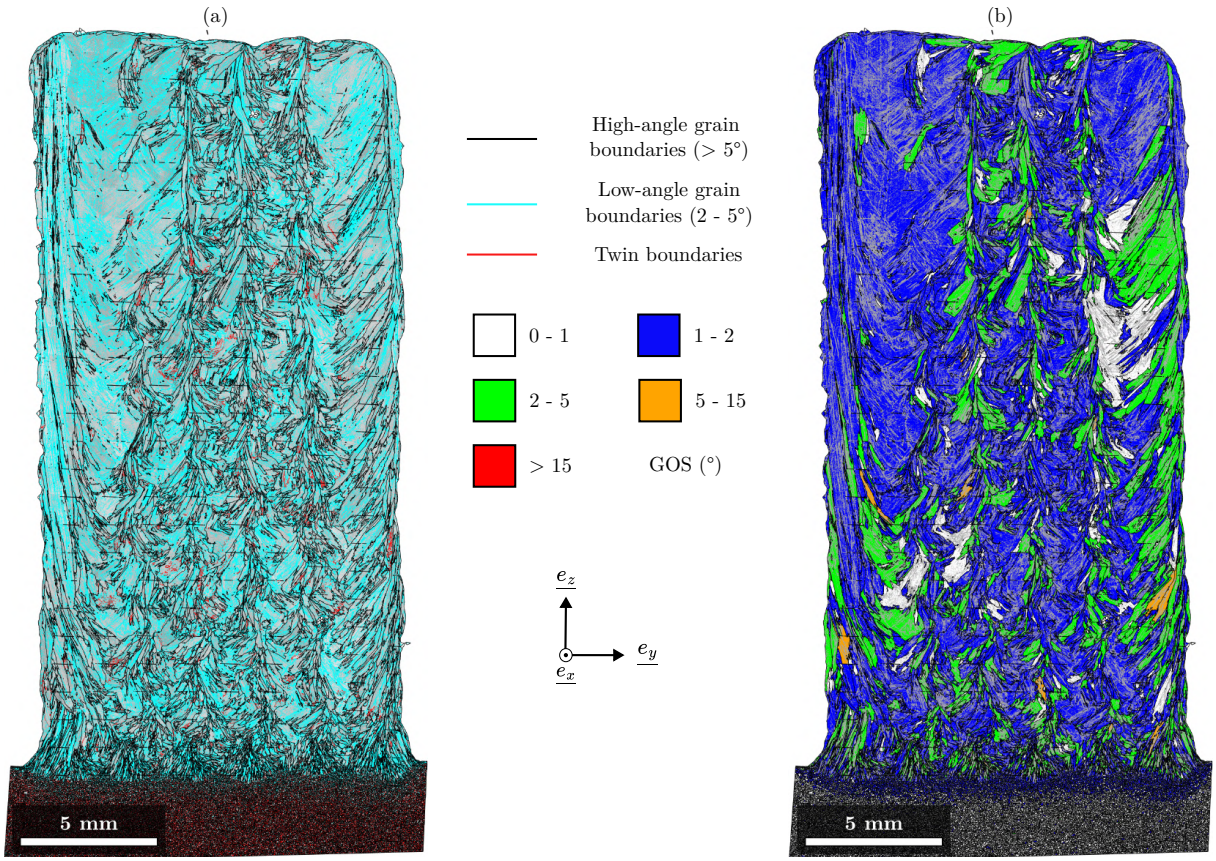

Figure B.10. Grain boundary (GB) and grain orientation spread (GOS) maps from EBSD of the transverse cross-section of the tile manufactured by WLAM. In GB map (a), high-angle grain boundaries (HAGBs) are depicted in black, low-angle grain boundaries (LAGBs) in cyan and Σ3-twin boundaries in red. In GOS map (b), HAGBs are represented by black lines while LAGBs are depicted in grey.

This page was intentionally left blank.

Appendix C

Complements for Chapter 5

C.1 Non conformous nodes

When applying a non-conformal transition between the fine and coarse mesh zones, several hanging nodes are left. These nodes are treated by applying linear relationships between unknowns of the fine and coarse meshes. In practice, the value of an arbitrary nodal field θ_i at a hanging node $\underline{x}_i \in \mathcal{A}_{\mathrm{NC}}$, where $\mathcal{A}_{\mathrm{NC}}$ is the set of the hanging nodes, is linearly linked to the nodal values of the adjacent coarse finite element by using the interpolation functions and the barycentric coordinates of the hanging node in that element, as presented in Equation C.1, where θ^j are the values of the nodal field in the adjacent coarse finite element and β^j the barycentric coordinates of the hanging point $\underline{x}_i$ in this element. This relation between unknowns is added to the linear system of equations that represents the thermal or mechanical equilibrium.

$$\theta_i - \sum_j \theta^j \beta^j(\underline{x}_A) = 0 \tag{C.1}$$

C.2 Energy conservation during finite elements addition.

When finite elements are added to a given mesh to simulate material deposition during the thermal analysis, the two mesh parts do not have the same temperature at their interface in the general case. The developed model satisfies the equation of energy conservation to set the temperatures at the nodes of the interface between the two mesh parts. In finite element modeling, the energy stored at the nodes of a mesh is given by the product of the heat capacity matrix by the temperature field. The energy conservation is written in Equation C.2a. In this equation, $\underline{\underline{C}}^d$ and $\underline{\underline{C}}^{d+1}$ are respectively the heat capacity matrices before and after the addition of finite elements, $\underline{\underline{C}}^{add}$ that of the added part, and $\underline{T}^d$, $\underline{T}^{d+1}$ and $\underline{T}^{add}$ their respective temperature fields. Thanks to the fact that the heat capacity matrix of the assembled mesh is equal to the assembled heat capacity matrices, we can then compute the temperature field $\underline{T}^{d+1}$ that ensures the energy conservation of the system after addition of finite elements, as expressed in the Equation C.2b.

$$\begin{aligned} \underline{\underline{C}}^{d+1}.\underline{T}^{d+1} &= \underline{\underline{C}}^{d}.\underline{T}^{d} + \underline{\underline{C}}^{add}.\underline{T}^{add} && \text{(a)} \\ \underline{T}^{d+1} &= \left[\underline{\underline{C}}^{d} + \underline{\underline{C}}^{add}\right]^{-1} \left(\underline{\underline{C}}^{d}.\underline{T}^{d} + \underline{\underline{C}}^{add}.\underline{T}^{add}\right) && \text{(b)} \end{aligned} \tag{C.2}$$

The temperature field $\underline{T}^{d+1}(t)$ does not comply with the local thermodynamic equilibrium, but it is only used to initialize the resolution of the next time step. At last, only the temperature field computed at the current time step t before the addition of elements, $\underline{T}^{d}(t)$, and that after this addition and the resolution of the next time-step,$\underline{T}^{d+1}(t+\delta t)$ are saved.

For the mechanical analysis, adding finite elements seems more straightforward to handle. There is no kinetic energy since static analysis is performed, and the internal mechanical energy of the added part is zero since it is stress-free. Energy conservation is then trivially satisfied. The initialization of the mechanical fields after adding elements is straightforward. The fields of stresses and state variables are set to zero in the added part, whereas they remain identical elsewhere. A similar approach is used for the displacement field, in which the nodes at the interface between the initial and the added parts get the values of the initial part, $\underline{U}_{int}$, whereas they are set to zero in the rest of the added part.

However, initializing the displacement field in the added part prescribes non-zero displacements on its boundary with the initial mesh, inducing strains and stresses in this part and potentially the evolution of other state variables. Moreover, the thermal field $\underline{T}^{d+1}$ computed from Equation C.2b generates non-homogeneous thermal strains in the added part, which contradicts the previous analysis assuming that material deposition is stress-free. To circumvent this problem, a field of eigenstrains $\underline{\underline{\varepsilon}}^{L}$ is prescribed in the added part to annihilate the strains generated by the displacements $\underline{U}_{int}$ and the temperature field $\underline{T}^{d+1}$. This field of eigenstrains is defined in Equation C.3a. The expression of Hook's law then verifies that the added part is stress-free, as expressed in Equation C.3b, where $\underline{\underline{\underline{\underline{\mathcal{C}}}}}^{e}(T)$ is the Hook's tensor. It is expressed using the Poisson's ratio ν and the Young modulus of the 316L stainless steel $E(T)$, depending on the temperature.

$$\begin{aligned} \underline{\underline{\varepsilon}}^{L} &= \underline{\underline{\varepsilon}}\left(\underline{U}_{int}\right) - \underline{\underline{\varepsilon}}^{th}\left(\underline{T}^{d+1}\right) && \text{(a)} \\ \underline{\underline{\sigma}} &= \underline{\underline{\underline{\underline{\mathcal{C}}}}}^{e}(T) : \left[\underline{\underline{\varepsilon}}\left(\underline{U}_{int}\right) - \underline{\underline{\varepsilon}}^{th}\left(\underline{T}^{d+1}\right) - \underline{\underline{\varepsilon}}^{L}\right] = 0 && \text{(b)} \end{aligned} \tag{C.3}$$

Finally, if the interface between the initial and the added parts experiences strong displacements, nodes of the added part may be susceptible to going through some of its elements since the other nodes have zero displacements. In the frame of a "small displacement analysis," this does not influence the previous definition since the equilibrium is satisfied in the reference configuration of the mesh, in which it is not deformed. In the frame of a "large displacement analysis", the equilibrium is satisfied in the deformed configuration: the problem can occur at the first iteration of the resolution loop if the numerical scheme is based on an "updated lagrangian formulation." To circumvent this problem, we can do a first resolution in "small displacement" to get a displacement field consistent in all the added parts or either perform the "large displacement analysis" according to a "total lagrangian formulation." However, this problem does not occur in practice since manufactured pieces are generally firmly clamped: they undergo minimal displacements unless there is a significant manufacturing defect [144], which justifies carrying out the mechanical analysis in the frame of this hypothesis.

List of Figures

This page was intentionally left blank.

List of Tables

RÉSUMÉ

L'un des défis des procédés de fabrication additive métallique par dépôt de fil tels que le WAAM (*Wire Arc Additive Manufacturing*) et le WLAM (*Wire Laser Addititive Manufacturing*) est de maîtriser les paramètres de fabrication pour produire des pièces aux géométries complexes et aux propriétés homogènes. En effet, des paramètres procédés mal contrôlés peuvent engendrer des hétérogénéités thermiques, mécaniques et microstructurales. Cette thèse a pour objectif d'évaluer l'effet des paramètres des procédés WAAM et WLAM utilisés pour fabriquer des pièces en acier austénitique inoxydable 316L (monocordons, murs ou blocs) sur (i) leur régularité géométrique, (ii) leur microstructure, (iii) leurs propriétés mécaniques et (iv) leur stabilité microstructurale sous l'effet de la température.

L'influence des paramètres des procédés WAAM et WLAM sur des critères géométriques (largeur/hauteur, dilution) a été établie et des pièces aux géométries régulières et sans porosité ont été obtenues, à l'exception du bloc WLAM possédant quelques pores. L'étude de la microstructure des monocordons a révélé (i) une solidification dendritique et épitaxiale perpendiculaire à la ligne de fusion et (ii) des bandes de ferrite orientées selon $\underline{e_z}$ au sein de l'austenite dans une fraction de 5 vol.% pour le WLAM et 8 vol.% pour le WAAM. La microstructure des murs est caractérisée par une forte texture cristallographique selon $\langle 001 \rangle_{\| \underline{e_z}}$ et des grains allongés sur plusieurs dizaines de passes. Le WLAM produit des grains plus fins et des dendrites deux fois plus petites comparé au WAAM en raison de vitesses de refroidissement plus rapides, estimées à 10^3 °C/s contre 10^2 °C/s au WAAM. Les essais mécaniques ont montré une anisotropie et une dureté plus importante pour les pièces élaborées par WLAM que par WAAM. Toutefois, la résistance à la traction et la déformation à rupture des murs obtenus par WAAM et WLAM restent similaires à celles de l'acier 316L à l'état forgé. Des traitements thermiques effectués sur les murs ont permis de dissoudre la ferrite et ont entrainé une recristallisation partielle, limitée aux bordures et pied des murs. Les blocs sont caractérisés par des grains plus fins et moins allongés que les murs, avec des différences microstructurales notables pour chaque procédé due à des formes de bains de fusion différentes.

Enfin, un modèle thermomécanique a été développé avec le logiciel Cast3M. En s'appuyant sur la géométrie des murs expérimentaux, il permet d'estimer correctement le champ de température en cours de la fabrication et la déformation finale du substrat. Le modèle a ensuite été appliqué pour ajuster les temps de refroidissement interpasse et les paramètres opératoires pour (i) éviter l'accumulation de chaleur, (ii) contrôler la vitesse de refroidissement et (iii) minimiser l'apparition de phases néfastes aux propriétés du matériau.

MOTS CLÉS

Fabrication additive par dépôt de fil, Optimisation paramétrique, Acier 316L, Caractérisation microstructurale, Traitements thermiques, Propriétés mécaniques, Méthode des éléments finis, Modélisation thermomécanique

ABSTRACT

One of the main challenges in metallic wire additive manufacturing, particularly the WAAM (Wire Arc Additive Manufacturing) and WLAM (Wire Laser Additive Manufacturing) processes, is controlling the manufacturing parameters to achieve components with complex geometries and homogeneous properties. Indeed, inadequate control of the parameters can lead to thermal, mechanical and microstructural heterogeneities. This thesis aims to assess the influence of the parameters of WAAM and WLAM processes used to manufacture 316L austenitic stainless steel components (single beads, single-bead walls and tiles) on (i) their geometrical regularity, (ii) their microstructure, (iii) their mechanical properties and (iv) their thermal stability.

The influence of the process parameters on defined geometric criteria (width/height, dilution) was established and porosity-free components with regular geometries were obtained, with the exception of the tile manufactured by WLAM which exhibited some pores. The study of the microstructure of single beads revealed the presence of (i) dendritic and epitaxial solidification perpendicularly to the fusion line and (ii) bands of ferrite oriented along $\underline{e_z}$ within the austenite in a fraction of 5 vol.% for WLAM and 8 vol.% for WAAM. The microstructure of the single-bead walls is characterized by a strong crystallographic texture along $\langle 001 \rangle_{\| \underline{e_z}}$ and elongated grains over dozens of layers. The WLAM process produced dendrites twice smaller than the WAAM process in single-bead walls due to the faster cooling rates, estimated at 10^3 °C/s versus 10^2 °C/s for WAAM. Mechanical testing showed increased anisotropy and hardness in components manufactured by WLAM rather than by WAAM. Still, the tensile stress and ultimate strain of single-bead walls elaborated with WAAM and WLAM processes remain similar to those of 316L steel in its forged state. Heat treatments of the walls resulted in the dissolution of the ferrite and limited recrystallization at the edges and bottom of the walls. The tiles are characterized by finer and less elongated grains than the walls, with notable microstructural differences between each process due to the different shapes of the melt pools.

Finally, a thermomechanical model was developed with the Cast3M software. Based on the geometry of the experimental walls, this model proved to correctly estimate the temperature field during manufacturing and the final deformation of the substrate. The model was then applied to adjust the interlayer cooling times and the process parameters to (i) avoid heat accumulation, (ii) control the cooling rate and (iii) minimize the probability of the appearance of phases detrimental to the properties of the material.

KEYWORDS

Wire additive manufacturing, Parametric optimization, 316L steel, Microstructural characterization, Heat treatments, Mechanical properties, Finite element method, Thermomechanical modeling